Institut für Geowissenschaften
Mathematisch-Naturwissenschaftliche Fakultät
Universität Potsdam

Cenozoic foreland-basin evolution in the northern Andes: insights from thermochronology and basin analysis in the Eastern Cordillera, Colombia.

Mauricio Parra

Dissertation
zur Erlangung des akademischen Grades
Doktor der Naturwissenschaften (Dr. rer. nat.)
in der Wissenschaftsdisziplin Geologie

eingereicht an der
Mathematisch-Naturwissenschaftlichen Fakultät der Universität Potsdam

Potsdam, Oktober 2008

Published online at the
Institutional Repository of the University of Potsdam:
http://opus.kobv.de/ubp/volltexte/2009/2933/
urn:nbn:de:kobv:517-opus-29333
[http://nbn-resolving.de/urn:nbn:de:kobv:517-opus-29333]

Abstract

The modern foreland basin straddling the eastern margin of the Andean orogen is the prime example of a retro-arc foreland basin system adjacent to a subduction orogen. While widely studied in the central and southern Andes, the spatial and temporal evolution of the Cenozoic foreland basin system in the northern Andes has received considerably less attention. This is in part due to the complex geodynamic boundary conditions, such as the oblique subduction and accretion of the Caribbean plates to the already complex interaction between the Nazca and the South American plates. In the Colombian Andes, for example, a foreland basin system has been forming since ~80 Ma over an area previously affected by rift tectonics during the Mesozoic. This setting of Cenozoic contractile deformation superposed on continental crust pre-strained by extensional processes thus represents a natural, yet poorly studied experimental set-up, where the role of tectonic inheritance on the development of foreland basin systems can be evaluated. However, a detailed documentation of the early foreland basin evolution in this part of the Andes has thus far only been accomplished in the more internal sectors of the orogen. In this study, I integrate new structural, sedimentological and biostratigraphic data with low-temperature thermochronology from the eastern sector of the Colombian Andes, in order to provide the first comprehensive account of mountain building and related foreland basin sedimentation in this part of the orogen, and to assess as to what extent pre-existent basement anisotropies have conditioned the locus of foreland deformation in space and time.

In the Medina Basin, along the eastern flank of the Eastern Cordillera, I integrated detailed structural mapping and new sedimentological data with a new chronostratigraphic framework based on detailed palynology that links an eastward-thinning early Oligocene to early Miocene syntectonic wedge containing rapid facies changes with an episode of fast tectonic subsidence starting at ~30 Ma. This record represents the first evidence of topographic loading generated by slip along the principal basement-bounding thrusts in the Eastern Cordillera to the west of the basin and thus constrains the onset of mountain building in this area. A comprehensive assessment of exhumation patterns based on zircon fission-track (ZFT), apatite fission-track (AFT) analysis and thermal modelling reveals the location of these thrust loads to have been located along the contractionally reactivated Soapaga Fault in the axial sector of the Eastern Cordillera. Farther to the east, AFT and ZFT data also document the onset of thrust-induced exhumation associated with contractional reactivation of the main range-bounding Servita Fault at ~20 Ma. Associated with this episode of orogenic growth, peak burial temperature estimates based on vitrinite reflectance data in the Cenozoic sedimentary record of the adjacent Medina Basin documents earlier incorporation of the western sector of the basin into the advancing fold and thrust belt.

I combined these new thermochronological data with published AFT analyses and known chronologic indicators of brittle deformation in order to evaluate the patterns of orogenic-front migration in the Andes of central Colombia. This spatiotemporal analysis of deformation reveals an

episodic pattern of eastward migration of the orogenic front at an average rate of 2.5-2.7 mm/yr during the Late Cretaceous-Cenozoic. I identified three major stages of orogen propagation. First, following initiation of mountain building in the Central Cordillera during the Late Cretaceous, the orogenic front propagate eastward at slow rates (0.5-3.1 mm/yr) until early Eocene times. Such slow orogenic advance would have resulted from limited accretionary flux related to slow and oblique (SW-NE-oriented) convergence of the Farallon and South American plates during that time. A second stage of rapid orogenic advance (4.0-18.0 mm/yr) during the middle-late Eocene, and locally of at least 100 mm/yr in the middle Eocene, resulted from initial tectonic inversion of the Eastern Cordillera. I correlate this episode of rapid orogen-front migration with an increase in the accretionary flux triggered by acceleration in convergence and a rotation of the convergence vector to a more orogen-perpendicular direction. Finally, stagnation of the Miocene deformation front along former rift-bounding reactivated faults in the eastern flank of the Eastern Cordillera led to a decrease in the rates of orogenic advance. Post-late Miocene-Pliocene thrusting along the actively deforming front of the Eastern Cordillera at this latitude suggests averaged Miocene-Holocene orogen propagation rates of 1.2-2.1 mm/yr. In addition, ZFT data suggest that exhumation along the eastern flank of the orogen occurred at moderate rates of ~0.3 mm/yr during the Miocene, prior to an acceleration of exhumation since the Pliocene, as suggested by recently published AFT data

In order to evaluate the relations between thrust loading and sedimentary facies evolution in the foreland, I analyzed gravel progradation in the foreland basin system. In particular, I compared one-dimensional Eocene to Pliocene sediment accumulation rates in the Medina basin with a three-dimensional sedimentary budget based on the interpretation of ~1800 km of industry-style seismic reflection profiles and borehole data tied to the new chronostratigraphic framework. The sedimentological data from the Medina Basin reveal rapid accumulation of fluvial and lacustrine sediments at rates of up to ~ 0.5 mm/yr during the Miocene. Provenance data based on gravel petrography and paleocurrents reveal that these Miocene fluvial systems were sourced by Upper Cretaceous and Paleocene sedimentary units exposed to the west, in the Eastern Cordillera. Peak sediment-accumulation rates in the upper Carbonera Formation and the Guayabo Group occur during episodes of gravel progradation in the proximal foredeep in the Early and Late Miocene. I interpreted this positive correlation between sediment accumulation and gravel deposition as the direct consequence of thrust activity in the Servita-Lengupá Fault. This contrasts with current models relating gravel progradation to episodes of tectonic quiescence in more distal portions of foreland basin systems and calls for a re-evaluation of tectonic history interpretations inferred from sedimentary units in other mountain belts.

In summary, my results document a late Eocene-early Miocene eastward advance of the topographic loads associated with the leading edge of deformation in the northern Andes of Colombia. Crustal thickening of the Eastern Cordillera associated with initiation of thrusting along the Servitá Fault illustrates that this sector of the Andean orogen acquired ~90% of its present width already by

the early Miocene (~20 Ma). My data thus demonstrate that inherited crustal anisotropies, such as the former rift-bounding faults of the Eastern Cordillera, favour a non-systematic progression of foreland basin deformation through time by preferentially concentrating accommodation of slip and thrust-loading. These new chronology of exhumation and deformation associated with specific structures in the Colombian Andes also constitutes an important advance towards the understanding of models for hydrocarbon maturation, migration and trap formation along the prolific petroleum province of the Llanos Basin in the modern foredeep area.

Zusammenfasung

Das Vorlandbecken, das sich an der östlichen Flanke der Anden erstreckt, ist ein prototypisches Beispiel für ein Retro-Arc-Vorlandbecken eines Subduktionszonenorogens. Im Gegensatz zu den südlichen und zentralen Anden, wurde die zeitliche und räumliche Entwicklung dieses känozoischen Systems im nördlichen Teil des Orogens weit weniger untersucht. Dies liegt unter anderem an den komplexen geodynamischen Randbedingungen, wie der schrägen Subduktion und Anlagerung der karibischen Plattengrenzen an die südamerikanische und Nazca-Platte, deren Interaktion ebenfalls komplex ist und durch unterschiedliche Konvergenzrichtungen und –geschwindigkeiten gekennzeichnet ist. Aufgrund dieser Verhältnisse hat auch die Oberplatte eine sehr differenzierte tektonische Entwicklung erfahrens. In den kolumbianischen Anden hat sich zum Beispiel seit ca. 80 Milllionen Jahren ein Vorlandbeckensystem in einem Gebiet gebildet, das während des Mesozoikums durch Rifttektonik geprägt war. Dieses Gebiet, in dem kompressive Deformation die Strukturen vorheriger extensionaler Prozesse z.T. reaktiviert und überlagert, ist daher ein natürliches, wenn auch bisher wenig erforschtes Naturlabor, um zu untersuchen, wie sich tektonische bedingte Anisotropien auf die Entwicklung von Vorlandbeckensystemen auswirken können und Änderungen in den Ablagerungsräumen und in der Faziesverteilung von Sedimenten hervorrufen. In dieser Arbeit präsentiere ich neue strukturelle, sedimentologische und biostratigraphische Daten zusammen mit neuen Informationen zur Exhumationsgeschichte mit Hilfe von Niedrigtemperatur-Thermochronologie aus dem östlichen Teil der kolumbianischen Anden, um zum ersten Mal eine vollständige Darstellung der Gebirgsbildung und zugehöriger Vorlandbeckensedimentation in diesem Teil der Anden zu liefern. Zusätzlich wird untersucht, zu welchem Ausmaß bereits existierende krustale Anisotropien den Ort der Vorlanddeformation in Raum und Zeit bestimmt haben.

Im Medina Becken, an der östlichen Flanke der östlichen Kordillere, habe ich detaillierte strukturelle Kartierungen und neue sedimentologische Daten mit einem neuen chronostratigraphischen Rahmen, der auf detaillierter Palynologie basiert, verknüpft. Dieser Bezugsrahmen verbindet einen nach Osten hin ausdünnenden, syntektonischen früholigozänen bis frühmiozänen Keil, welcher rasche Faziesänderungen enthält, mit einer Phase schneller tektonischer Subsidenz, die vor ca. 30 Millionen Jahren beginnt. Dieser hier erarbeitete Datensatz stellt den ersten Beweis einer tektonisch bedingten Subsidenz dar, die durch Bewegungen entlang der Haupüberschiebungen an der Westgrenze des Vorlandes stattfanden. Dadurch wird das Einsetzen der Gebirgsbildung in diesem Gebiet zeitlich eingegrenzt. Eine umfassende Auswertung von Exhumationsmustern, die auf Zirkon- (ZFT) und Apatit-Spaltspuraltern (AFT) sowie thermischen Modellierungen beruhen, zeigt, daß diese Überschiebungsbahnen und die bedeutende Aufschiebungstätigkeit und tektonische Auflast entlang der reakivierten, vormals extensionalen Servita-Störung, im zentralen Bereich der östlichen Kordillere liegen. Weiter östlich dokumentieren AFT und ZFT Daten den Einsatz einer durch Überschiebungen hervorgerufenen Exhumation, die mit einer kompressiven Reaktivierung der großen Servita-Störung

vor ca. 20 Millionen Jahren zusammenhängt. Vitrinitreflexionsdaten aus dem känozoischen Sedimentationsdatensatz des benachbarten Medina Beckens zeigen eine bedeutende Absenkung in dieser Region, bei der der westliche Sektor des Beckens schon im Anfangsstadium der orogenen Entwicklung in den nach Osten wandernden Falten- und Überschiebungsgürtel einbezogen wurde.

Ich verbinde diese neuen thermochronologischen Daten mit veröffentlichten AFT Analysen und bekannten chronologischen Indikatoren für Spröddeformation, um die räumlich-zeitlichen Muster in der Entwicklung der Gebirgsfront in den Anden Zentralkolumbiens zu charakterisieren. Diese Analyse der Deformation zeigt ein episodisches Muster in der östlich gerichteten Migration der Gebirgsfront, mit einer durchschnittlichen Rate von 1.8-3.4 mm/a am Übergang von der späten Kreide zum frühen Känozoikum. Ich habe dabei drei Hauptabschnitte des lateralen Orogenwachstums identifiziert. Zuerst wandert die Gebirsfront, nach dem Beginn der Gebirgsbildung in den Zentralkordilleren während der späten Kreidezeit, ostwärts mit niedrigen Raten (0.3-3.3 mm/a) bis ins frühe Eozän. Ein solches langsames laterales Wachstum des Orogens resultiert aus Akkretionsprozessen im Zuge einer langsamen und schrägen (SW-NO orientiert) Konvergenz der Farallon- mit der südamerikanischen Platte. Eine zweite Phase schnellen Fortschreitens der Gebirgsfront mit Raten von 5.3-13.3 mm/a, lokal sogar bis zu 100 mm/a, fand während des mittleren/späten Eozäns statt und resultierte aus einer beginnenden tektonischen Inversion der östlichen Kordillere. Ich verbinde diese Phase rascher Gebirgsfrontmigration mit einem erhöhten Akkretionsfluß, der durch eine Beschleunigung der Konvergenz sowie einer Rotation des Konvergenzvektors in eine mehr rechtwinklige Richtung ausgelöst wurde. Letztlich führte eine Stagnation der Deformationsfront im Miozän entlang von ehemals riftbegrenzenden, reaktivierten Störungen an der östlichen Flanke der östlichen Kordillere zu einer Abschwächung der Raten der Gebirgsfrontmigration. Aus Überschiebungen des späten Miozän/Pliozän entlang der aktiv deformierten Front der östlichen Kordillere kann man auf durchschnittliche Bewegungsraten der Gebirgsfront von etwa 1.5-2.1 mm/a im Zeitraum Miozän bis Holozän schließen. Außerdem deuten ZFT Daten darauf hin, daß Exhumation entlang der östlichen Flanke des Orogens mit mittleren Raten von ungefähr 0.3 mm/a während des Miozäns stattfand. Im Pliozän erfolgte daraufhin eine Beschleunigung der Exhumation, wie kürzlich veröffentlichte AFT Daten nahelegen.

Um die Beziehung zwischen tektonischer Auflast aufgrund der Verkürzung im Orogen und Evolution der sedimentären Fazies im Vorland zu untersuchen, habe ich die Progradation von Konglomeraten im Vorlandbeckensystem detailliert analysiert. Insbesondere habe ich eindimensionale Raten von Sedimentakkumulation vom Eozän bis zum Pliozän im Medina Becken mit einem dreidimensionalen Sedimenthaushalt verglichen. Dieser wurde aus der Interpretationen mit einer Gesamtlänge von ~2500 km seismischer Reflexionsprofile sowie Bohrlochdaten, verbunden mit dem neuen chronostratigraphischen Bezugssystem der sedimentären Ablagerungen, gewonnen. Die sedimentologischen Daten aus dem Medina Becken zeugen von rascher Akkumulation von fluviatiler und lakustriner Sedimente mit Raten von bis zu 0.5 mm/a während des Miozäns. Provenienzanalysen

mittels Konglomerat-Petrographie und Paläoströmungsmessungen belegen, daß diese miozänen fluviatilen Systeme des Miozäns durch die Erosion sedimentärer Einheiten aus der oberen Kreide und dem Paläozän generiert wurden, die im Westen der östlichen Kordillere aufgeschlossen sind. Die höchsten Sedimentationsraten in der oberen Carbonera Formation und der Guayabo Gruppe finden sich während Episoden von Konglomeratprogradation der proximalen Vortiefe im frühen und späten Miozän. Ich interpretiere diese positive Korrelation zwischen Sedimentakkumulation und Konglomeratablagerung als direkte Konsequenz von Überschiebungstektonik an der Servita-Lengupá-Störung. Diese Interpretation ist allerdings im Gegensatz zu gängigen Sedimentationsmodellen Modellen, die eher eine tektonische Ruhephase mit der Progradation grober Schüttungen in den distalen Bereichen der Vorlandbecken in Verbindung bringen. Dies bedeutet, daß Interpretationen der aus Faziesverteilungen gewonnenen tektonischen Entwiklungsschritte eines Orogens auch in andeen Regionen neu bewertet werden müssen.

Zusammengefaßt dokumentieren meine Ergebnisse, daß die Überschiebungsfront sowie die durch Einengung generierte Topographie und Auflast der Überschiebungsblöcke in den nördlichen kolumbianischen Anden während des späten Miozäns bis zum frühen Miozän ostwärts gewandert ist. Einengung und Krustenverdickung der östlichen Kordillere, verbunden mit beginnender Aktivität entlang der Servitá Störung, deutet an, daß dieser Bereich der Anden schon nahezu 90% seiner derzeitigen Breite bereits im Miozän (20 Ma) erreicht hattte. Die hier vorgestellten Daten zeigen also, daß ererbte krustale Anisotropien ein diachrones Voranschreiten der Vorlandbeckendeformation begünstigen. Dies geschieht durch Konzentration der Bewegungsverteilung an ererbten Störungen sowie lokalen Spannungsänderung im Vorland durch tektonische induzierte Auflasten. Diese neue Charakterisierung der Deformationsabfolge im Vorland der Anden bedeutet auch einen großen Schritt vorwärts in Richtung des Verstehens von Modellen, die das Reifen und die Wanderung von Kohlenwasserstoffen sowie die Entstehung von Ölfallen entlang der produktiven Petroleumprovinz im Llanos Becken der rezenten Vortiefe beschreiben.

Contents

List of Figures

List of Tables

Acknowledgements

There are numerous individuals deserving of thanks for the successful completion of my doctoral research. I would first like to thank my advisor Manfred Strecker for having facilitated my education while at the University of Postdam. His guidance and continuous encouragement have helped me develop the capability to conduct scientific research. Manfred has also generously supported my investigations in Colombia and has motivated my interaction with various other scientists. I am especially indebted to my great friend and colleague Andrés Mora, with whom I share most of my research time in Potsdam and during our long field seasons in Colombia. Many of the ideas in this dissertation and the strategies for accomplishing our research objectives were developed as a work team. I thank also him for his positiveness during difficult times. I am also thankful to Ed Sobel for his rigorous teaching of the fission track method, for continuously providing stimulus for scientific discussions and for his constructive criticism of ideas and manuscripts.

My research also greatly benefited from stimulating discussions on foreland basin dynamics and various other aspects of Andean geology held with Brian Horton during his sabbatical year at Potsdam. Carlos Jaramillo, first in the Instituto Colombiano del Petróleo, and later in the Smithsonian Tropical Research Institute, generously provided support biostratigraphical dating. A first, unsuccessful attempt for establishing a chronology of sediment accumulation with magnetostratigraphy was possible thanks to the kind help of Norbert Nowaczyk at the GFZ-Potsdam.

This research benefited from scientific cooperation with many institutions to whom I am indebted. I am very thankful to Vladimir Torres, Milton Rueda and the group of palynologsts at the ICP for palynological age determinations. Hocol S.A kindly provided us with apatite fission track analyses. Germán Reyes from INGEOMINAS, Bogotá kindly allowed vitrinite reflectance analyses in his laboratory.

My work in Potsdam has greatly benefited from fruitful discussions held in our weekly seminar on Tectonics and Earth Surface Processes. I am especially thankful to Paolo Ballato, Cornelius Uba and Gerold Zeilinger. My life as a doctoral student in Potsdam was more enjoyable thanks to all friends and colleagues from the Institute of Geosciences. I would especially thank my officemates Gaetan Rimmele, Dietrich Lange, Nicolas Kühn, and Lydia Olaka.

During field work in Colombia, my work greatly benefited from discussions with many colleagues. I would like to especially thank Andreas Kammer, Eduardo López, Germán Bayona, Tatiana Gaona, Martín Cortés, and Antonio Velásquez. I also shared enjoyable field campaigns with many geologists and students. Thanks goes to Yuri Garcia, Juan G Vargas, Gabriel Veloza, Luis Quiroz, Rafaél López,, Oscar Romero, Sara Morón and Andrés Pizzas.

This study was supported by grants and fellowships from the German Academic Exchange Service (DAAD), A/02/11325 to M. Parra, the German Research Foundation (DFG), Str 373/19-1 to M. Strecker, funds from the Leibniz Center for Earth Surface and Climate Studies at Potsdam University, and Universidad Nacional de Colombia (Beca de Honor to M. Parra). I am also grateful to

the Instituto Colombiano del Petróleo and to the Smithsonian Tropical Research Institute (STRI) for additional support.

Finally, my deepest gratitude goes to Alvaro, Cecilia, Leonor, Alvarito and Natalia, for making easier my life far from them with their continuous love and support, and very especially to Camila, my love, fiancée and best friend. Thanks to her I am writing these final lines of my dissertation.

Chapter 1
Introduction

Foreland basins are outstanding, first-order registers that record Earth's evolution regarding climatic and tectonic forcing factors of orogenic evolution. Because of their dimensions, spanning thousands of kilometers in length and hundreds of kilometers in width, as well as their exceptionally thick sedimentary fills, foreland basins may contain a virtually complete record of the tectonic and climatic processes that operate both in the basins themselves and in the adjacent mountain belts.

Foreland basins are integral features of tectonically active and dormant mountain belts and have been associated with plate tectonic processes since the earliest manifestations of mountain building during the Precambrian (e.g., Rivers, 1997; Zhao et al., 2002). These basins thus furnish important information, which helps decipher the overall geodynamic and climatic factors and possible feedback mechanisms between tectonics and climate during various stages of crustal evolution in Earth's history. Apart from their importance as geologic archives, foreland basins are also the locus of innumerable natural resources that are crucial to modern societies, from fossil fuels and water to various types of raw materials. Field observations, numerical- and analog models have long documented the dynamic interaction between crustal shortening, thrust loading, exhumation, lithospheric flexure, surface processes, sediment routing, and loading by the deposited sediments themselves, which ultimately determine the characteristics of foreland basins and adjacent fold-and-thrust belts (Dickinson, 1974; Beaumont, 1981; Jordan, 1981; Flemings and Jordan, 1989; Sinclair et al., 1991; Willett et al., 1993; Jordan, 1995; Catuneanu et al., 1997; Storti et al., 2000; McClay and Whitehouse, 2005). Given the inherent interdependence between these processes, a major remaining challenge in the study of foreland basins is the deconvolution of the sedimentary signal in search of discrimination among multiple forcing factors that, simultaneously operating at various magnitudes and spatiotemporal scales, may have resulted in similar responses in the basin. Such discrimination largely relies on the acquisition of independent chronologies for thrust deformation, related information on exhumation in the orogen, and foreland sediment accumulation (Jordan et al., 1988). For this reason, this study investigates the interplay of some of these factors in the medium to late stages of the Cenozoic evolution of the active retroarc foreland basin in the northern Andes of Colombia. By developing a new chronological framework of exhumation and sediment accumulation, I provide a first comprehensive study linking the mode and tempo of exhumation with foreland-basin partitioning in the eastern Colombian Andes.

The overall mechanics of foreland-basin formation and the idealized stratigraphic response to variations in thrust loading, lithospheric rheology, and erosional processes are reasonably well understood (e.g., Flemings and Jordan, 1989; Flemings and Jordan, 1990; Sinclair et al., 1991). In nature, however, crustal inhomogeneities (e.g., Waschbusch and Royden, 1992; Cardozo and Jordan,

2001) and mechanical variations (Allmendinger et al., 1983; DeCelles and Mitra, 1995) in the lithosphere, as well as spatially and temporally variable configurations of both thrust loads (e.g., Whiting and Thomas, 1994; Boyer, 1995) and climate conditions (e.g., Horton, 1999; Montgomery et al., 2001; Strecker et al., 2007) generate basins that deviate from ideal models. Episodic foreland-basin evolution is thus a common phenomenon, rather than the exception in the orogens of many convergent margins.

Retroarc foreland basins straddle the eastern flanks of the Andean orogen along most of their 7500 km length. Despite their topographic continuity as an important merdionally oriented climate barrier, the Andes exhibit a marked along-strike variation in morphology, tectonic style, crustal structure and climatic gradients (e.g., Gansser, 1973; Pilger, 1981; Jordan et al., 1983). This has been attributed to the competing roles of changes in subduction geometry (e.g., Pilger, 1981; Jordan et al., 1983), the inherited pre-Andean structure (e.g., Allmendinger et al., 1983; Kley et al., 1999) and climatic gradients (e.g., Horton, 1999; Montgomery et al., 2001). North of ~ 4°S, additional mechanisms have contributed to shape the Andean margin. In particular, episodes of oblique accretion of oceanic crust along the western margin since ~ 85 Ma (e.g., Kerr and Tarney, 2005) have been invoked as triggers of Cenozoic deformation (e.g., Cooper et al., 1995). In addition, a pronounced crustal heterogeneity inherited form Mesozoic lithospheric stretching and the formation of wide rift-basins bounded by steep normal faults (e.g., Sarmiento-Rojas et al., 2006) may have fundamentally influenced the spatial and temporal trends of deformation. However, the precise role of these kinematic and structural imprints on the Cenozoic evolution of the northern Andean margin remains largely unexplored in the eastern Colombian Andes. Specific open question that motivated the undertaking of this research are: (1) How have the inherited structural fabrics influenced the loci and tempo of orogen growth? (2) How did a Cenozoic change in plate kinematics from oblique to sub-perpendicular convergence (e.g., Pardo-Casas and Molnar, 1987) affect the growth of the northern Andean orogen? (3) Is there a hierarchy in the controlling factors that contributed to foreland basin accumulation in this province? (4) Can we correlate patterns of exhumation and sediment accumulation with deformation and activity of specific structures? This last question is of great relevance for applied geological aspects, in particular in Colombia, because of exploration strategies for energy resources.

The following chapters of this dissertation are devoted to the investigation of these fundamental problems. In particular, In Chapter 2, I integrated the results of detailed geologic mapping and interpretation of selected industry seismic reflection data from the modern wedge-top Medina Basin with sedimentary, provenance, and thermal maturation data in order to identify the oldest synorogenic strata that register initial tectonic inversion of the Eastern Cordillera. Based on a new chronology of sediment accumulation derived from a detailed palynological study, I identify the onset of thrusting along major east-verging reactivated faults along the eastern flank of the range as having occurred at ~30 Ma. I compare the subsidence signal of the basin with published data on the

distribution and tempo of sediment accumulation in the interior of the range and discuss potential mechanisms of foreland basin unsteadiness.

One fundamental unknown aspect of the Eastern Cordillera is the pattern of long-term exhumation and its relation with the inherited structures related to extensional processes during the Mesozoic. In Chapter 3, I therefore address this problem by combining my newly developed extensive thermochronological apatite- and zircon fission-track database with published ages of exhumation and brittle deformation. I identified an episodic pattern of orogenic advance that largely results from the virtually simultaneous tectonic inversion of both flanks of the Eastern Cordillera in middle-late Eocene time. My data also provide additional support for previous hypotheses regarding the post-Pliocene acceleration in exhumation that ultimately resulted in the present-day asymmetry in topography and exhumation patterns of the Eastern Cordillera. I discuss the role of plate kinematics and the inherited crustal structure in determining the locus and mode of orogenic advance and foreland basin partitioning.

Chapter 4 focuses on the Miocene to Holocene foredeep evolution. I use an extensive grid of seismic reflection profiles and data from my own surface mapping to refine the time constraints for thrusting along one of the principal long-lived reactivated faults in the east of the Eastern Cordillera. On the basis of new sedimentological, palynological data, I reconstruct the chronology and spatial distribution of foredeep sedimentation, and the unroofing history of the source areas. I compare one- and three-dimensional estimates of sediment accumulation rates with available data on time-series of various potential forcing factors. My results emphasize the prime role of intensified in tectonics determining the trends of sedimentary facies in proximal foredeep areas.

The chapters that constitute the main body of this dissertation have been submitted to peer-reviewed journals. Chapter 2 (“Orogenic wedge advance in the northern Andes: evidence from the Oligo-Miocene sedimentary record of the Medina basin, Eastern Cordillera, Colombia” by Mauricio Parra, Andrés Mora, Carlos Jaramillo, Manfred R. Strecker, Edward R. Sobel, Luis Quiroz, Milton Rueda, Vladimir Torres) is in press in the *Geological Society of America Bulletin*; Chapter 3 (“Episodic orogenic-front migration in the northern Andes: constraints from low-temperature thermochronology in the Eastern Cordillera, Colombia”, by Mauricio Parra, Andrés Mora, Edward R. Sobel, Manfred R. Strecker and Román González) is in revision in the journal *Tectonics*; Chapter 4 (“Tectonic controls on Cenozoic foreland basin development in the northeastern Andes, Colombia” by Mauricio Parra, Andrés Mora, Carlos Jaramillo, Vladimir Torres, Silane da Silva, Gerold Zeilinger and Manfred R. Strecker) has been submitted to the journal *Basin Research*.

Chapter 2

Orogenic wedge advance in the northern Andes: Evidence from the Oligocene-Miocene sedimentary record of the Medina basin, Eastern Cordillera, Colombia

ABSTRACT

Foreland basin development in the Andes of central Colombia has been suggested to have started in the Late Cretaceous through tectonic loading of the Central Cordillera. Eastward migration of the Cenozoic orogenic front has also been inferred from the foreland basin record west of the Eastern Cordillera. However, farther east, limited data provided by foreland basin strata and the adjacent Eastern Cordillera complicate any correlation between mountain building, exhumation, and foreland basin sedimentation. In this study we present new data from the Medina basin in the eastern foothills of the Eastern Cordillera of Colombia. We report sedimentological data and palynological ages that link an eastward-thinning early Oligocene to early Miocene syntectonic wedge containing rapid facies changes with an episode of fast tectonic subsidence starting at ca.31 Ma. This record may represent the first evidence of topographic loading generated by slip along the principal basement-bounding thrusts in the Eastern Cordillera to the southwest of the basin. Zircon fission-track ages and paleocurrent analysis reveal the location of these thrust loads and illustrate a time lag between the sedimentary signal of topographic loading and the timing of exhumation (~18 Ma). This lag may reflect the period between the onset of range uplift and significant removal of overburden. Vitrinite reflectance data document northward along-strike propagation of the deformation front and folding of the Oligocene syntectonic wedge. This deformation was coupled with a non-uniform incorporation of the basin into the wedge-top depozone. Thus, our dataset constitutes unique evidence for the early growth and propagation of the deformation front in the Eastern Cordillera, which may also improve our understanding of spatiotemporal patterns in foreland evolution in other mountain belts.

2.1 INTRODUCTION

The stratigraphic record of foreland basins yields an important archive of the tectonic and climatic evolution of mountain belts. A close link among shortening, thrust loading and the flexural response of continental lithosphere, as well as associated changes in topography is ultimately reflected in the creation of accommodation space for large volumes of sediments (Beaumont, 1981; DeCelles and Giles, 1996; Flemings and Jordan, 1989; Jordan, 1981). As a result, spatiotemporal variations in the magnitude of these parameters can be inferred from trends in the three-dimensional evolution of sedimentary facies and the geometry (i.e., wavelength) of foreland basins (Flemings and Jordan, 1990). For example, observations from many mountain belts and deduced conceptual models of orogenic evolution illustrate that migration of thrust loading and the development of characteristic facies belts are directed toward the foreland (e,g., DeCelles, 2004; DeCelles et al., 1998; Horton, 2005; Ramos et al., 2002; Sinclair, 1997). However, changes in the sense of propagation of the foreland basin depozones may follow changes in the distribution of thrust loading, with out-of-sequence faulting (e.g., DeCelles and Giles, 1996) and deceleration and thickening of the thrust wedge (e.g., Sinclair et. al., 1991) promoting orogenward migration of the foreland basin depozones. Alternatively,

episodic deformation along a stationary deformation front, reflected in alternating stages of thrust-loading and either quiescence or erosional unloading, may account for spatial shifts of the foreland basin depositional environments (Catuneanu et al., 1997; Catuneanu et al., 1998; Flemings and Jordan, 1990). A long-term stagnation of the foreland basin system may also result from lateral variations in flexural rigidity of the flexed plate (Waschbusch and Royden, 1992). Alternatively, its internal structure may be fundamentally influenced by inherited basement inhomogeneities, along which deformation is preferentially accommodated during subsequent orogenic processes (e.g., Hilley et al., 2005). Testing such models in natural settings is thus important and requires a multidisciplinary approach that allows identification of trends in sedimentary facies and subsidence rates in the basin, and of the location of thrust-loads through time (e.g., Jordan, 1995).

The Cenozoic Andes constitute one of the best suited settings to closely examine these issues. The Andes orogen is the type example of a retro-arc foreland basin (e.g., Jordan, 1995; Ramos et al., 2002). Along different sectors of the southern and central Andes of Argentina and Bolivia, the onset of mountain building during contractional deformation has been widely documented using the architectural characteristics of depositional foreland sequences and provenance data (e.g., Coutand et al., 2001; Damanti, 1993; Dávila and Astini, 2003; Echavarria et al., 2003; Horton et al., 2001; Jordan et al., 1993; Uba et al., 2006). A long-term pattern of cratonward migration of the orogenic-wedge leading to the formation of fold-and thrust belts (e.g., Coutand et al., 2001; Echavarria et al., 2003; Ramos et al., 2002) has been explained as the result of deformation acting on a relatively mechanically homogeneous crust, largely controlled by critical Coulomb wedge mechanics (e.g., Hilley et al., 2004; Horton, 1999). However, a non-systematic pattern of lateral orogenic growth or the absence of typical wedge geometries may occur in those settings, where favorably oriented basement anisotropies in front of an orogenic wedge may absorb shortening. This is apparently the case in the Santa Barbara system and the northern Sierras Pampeanas of NW Argentina, where deformation tends to be accommodated along basement inhomogeneities inherited from previous tectonic events (e.g., Allmendinger et al., 1983; Hilley et al., 2005; Mortimer et al., 2007; Ramos et al., 2002).

In contrast to these morphotectonic provinces of the southern central Andes, in the northern Andes of Colombia, a detailed documentation of foreland basin evolution has thus far only been accomplished in the more internal sectors of the orogen (Fig. 2.1), such as the Central Cordillera and the Magdalena Valley basin (Cooper et al., 1995; Gómez et al., 2005; Gómez et al., 2003; Montes et al., 2005; Ramon and Rosero, 2006). Uplift of the Central Cordillera since the late Cretaceous and episodic deformation (Gómez et al., 2005) have been inferred to account for the Paleogene facies distribution and basin geometry in this region. Also, an episode of orogenward progression of the foreland basin system has been identified for the early stages of basin development during the late Paleocene (Gómez et al., 2005). Despite these recent improvements in our understanding of foreland development in this part of the Andes, details of the tectonic and stratigraphic expressions of the advance of the orogenic front farther to the east remain ambiguous and largely unidentified.

Particularly due to a lack of timing constraints for deformation in the eastern sectors of the Eastern Cordillera, the spatiotemporal evolution of thrust systems, the associated creation of topography, and the chronology of denudation and sedimentation are not very well known in this region. Along both flanks of the Eastern Cordillera, the presence of basement inhomogeneities associated with Mesozoic normal faults reactivated during Cenozoic compressional tectonics (e.g., Mora et al., 2006; Mora et al., 2008a) offer the possibility of assessing their role in the localization of deformation during orogenic evolution.

In this paper we unravel the early history of mountain building along the eastern border of the Eastern Cordillera of Colombia through analysis of the sedimentary record preserved in the Medina basin, along the eastern foothills of the range between 4°20'-5°00' N latitude. We integrate new detailed geologic mapping of an area of ~1500 km^2 and structural interpretation of approximately 50 km of 2D industry-style seismic reflection profiles with new sedimentologic and biostratigraphic information. We combine these results with new thermal maturation data based on vitrinite reflectance from the foreland basin sediments, and new zircon fission- track (ZFT) ages from bedrock in the hinterland to provide a detailed account of the evolution of the northern Andean orogenic front in central Colombia. This approach helps document the effects of tectonic loading along individual thrust sheets, illustrates along-strike propagation of faulting, and documents the advance of the orogenic front toward the foreland beginning in early Oligocene time. Collectively, our new data allow a more robust evaluation of the different mechanisms influencing the development of the Colombian foreland-system through time.

2.2 TECTONIC SETTING AND GEOLOGICAL BACKGROUND

The Colombian Andes comprise three principal, northeast-southwest oriented geologic provinces (Fig. 2.1): (1) an allochthonous sector of accreted oceanic paleo-Pacific crust west of the Romeral Suture constitutes the Western Cordillera and the Baudo Range; (2) a central zone, defined by Proterozoic continental basement covered by upper Paleozoic platformal sequences, rift-related Mesozoic sediments, and Cenozoic marine and nonmarine sedimentary rocks, which underwent significant Cenozoic shortening and now constitutes the Central and Eastern Cordilleras and the intermontane Magdalena Valley basin; and (3) The Guyana Shield province to the east, where crystalline Proterozoic basement, lower to upper Paleozoic, Mesozoic (post-Cenomanian), and Cenozoic strata occur below a veneer of Quaternary sediments (e.g., Cooper et al., 1995).

East of the Central Cordillera, a foreland basin system has evolved in response to shortening and uplift of this range since the Late Cretaceous (Cooper et al., 1995; Gómez et al., 2003). Oblique accretion of oceanic rocks in the Western Cordillera (McCourt et al., 1984) has been suggested as the driving mechanism for the Late Cretaceous initiation of uplift, loading, and foreland basin development (Cooper et al., 1995). In contrast, the Eastern Cordillera is a north-northeast-oriented bivergent inversion orogen related to Cenozoic reactivation of Cretaceous rift structures during E-W

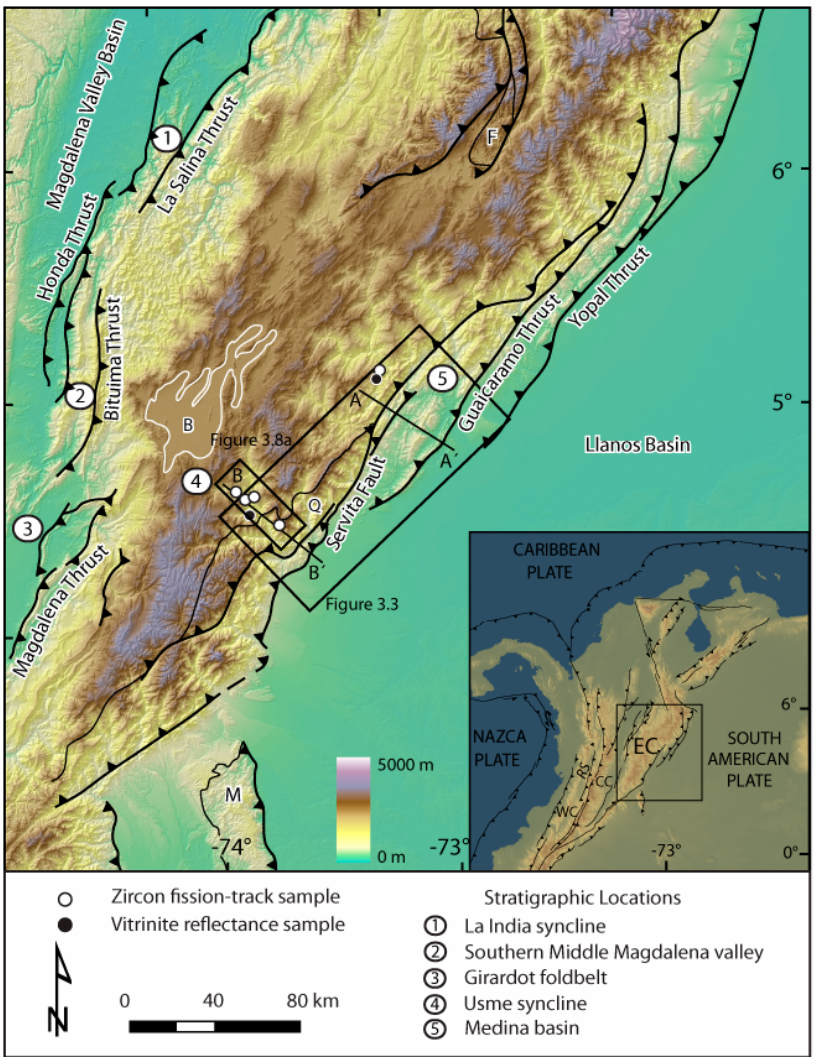

Figure 2.1: (a) 90-m STRM digital elevation model (DEM) showing the major thrusts of the Eastern Cordillera of Colombia. The black lines mark the boundary of the Floresta (F) and Quetame (Q) basement highs and the Macarena Range (M). White line shows the extent of the High Plain of Bogotá (B). Locations of vitrinite reflectance and zircon fission-track samples in the area of the Quetame massif are indicated. Stratigraphic locations referred in the text are shown with numbers 1 to 5. Inset shows the geodynamic setting of the Western (WC), Central (CC) and Eastern (EC) Cordilleras, and the Romeral Suture (*RS*) within the northern Andes. Black frame denotes area covered by Figures 3.3 and 3.8. Box in inset indicates the location of the main map.

oriented compression (Colletta et al., 1990; Cooper et al., 1995; Mora et al., 2006). The Eastern Cordillera constitutes the eastern limit of the Colombian Andes, abutting the virtually undeformed lowlands of the Llanos basin (Fig. 2.1). Tectonic inversion compartmentalized a once contiguous foreland province including areas east of the Central Cordillera, the present-day intermontane Magdalena Valley basin and the Llanos basin to the east. The principal phase of tectonic inversion in the Eastern Cordillera is thought to have started in the Miocene (Cooper et al., 1995; Van der Hammen, 1958) and has been attributed to the collision of the Baudó-Panama arc with the western active margin of South America (Duque-Caro, 1990). The appearance of post-middle Miocene alluvial sediments in the Llanos basin has been linked to the onset of uplift and exhumation in the Eastern Cordillera (Cooper et al., 1995; Dengo and Covey, 1993; Van der Hammen, 1958). Direct indicators of Cenozoic deformation in the Eastern Cordillera are known for the western and, to lesser extent, central and northeastern parts of the mountain range. To the west, in the middle Magdalena Valley basin (La India syncline, number 1 in Fig. 2.1), middle Eocene strata rest unconformably over folded early Paleocene units associated with west-verging thrust sheets. This constrains an episode of late Paleocene to early Oligocene deformation (Restrepo-Pace et al., 2004). Approximately 120 km to the

south (number 2 in Fig. 2.1), middle Eocene to Oligocene nonmarine growth strata associated with west-verging, thrust-related folding (Gómez et al., 2003) document initial deformation of the Eastern Cordillera. Farther to the south (number 3 in Fig. 2.1), the local unconformable relationship between upper Cretaceous and Oligocene-Miocene deposits in the Girardot fold belt (e.g., Montes et al., 2005; Raasveldt, 1956) has been interpreted to reflect pre-Oligocene to Miocene erosion as a response to folding along the western flank of the Eastern Cordillera (Gómez et al., 2003; Montes et al., 2005). In the axial part of the Eastern Cordillera, the structural configuration of an Upper Cretaceous to Oligocene sedimentary sequence from the eastern flank of the Usme syncline (Julivert, 1963; number 4 in Fig. 2.1) has been interpreted as growth strata related to folding and the resultant creation of subdued topography (Gómez et al., 2005). Finally, along the northeastern margin of the Eastern Cordillera, subsurface data has been used to infer late Eocene to late Oligocene thin-skinned deformation (Corredor, 2003; Martínez, 2006). However, the surficial sedimentological and structural expression of this inferred deformation episode remains ambiguous. Furthermore, the exact timing of initial deformation and spatiotemporal variations along strike are still poorly resolved.

Despite these problems and limitations, integrated regional reconstructions and geodynamic modeling have attempted constraining the onset of mountain building in the Eastern Cordillera. Despite evidence for a pre-middle Miocene onset of thrust loading, the inferred timing and locus of thrusting differ significantly among these models. For instance, at approximately 4.5°N latitude, tectonic loading in the present-day axial sector of the mountain range has been inferred to have started in the late Cretaceous (Bayona et al., 2006; Ojeda et al., 2006). Conversely, Sarmiento-Rojas (2001) suggested initial loading during the late Paleocene in the eastern foothills region. Here, a minor contribution of remaining thermal subsidence inherited from Mesozoic rifting is also suggested for the late Paleocene by this author. Finally, Gomez et al. (2005) modeled loading along the axial Eastern Cordillera as having started in the late Eocene-early Oligocene. These temporal disparities in the initiation of loading along the Eastern Cordillera call for a direct assessment of the tectono-sedimentary evolution of the range and the adjacent basins, involving the integration of the uplift history of the hinterland with an analysis of the response of the basin with respect to crustal thickening and exhumation.

The record of foreland basin evolution is preserved in the Late Cretaceous to Holocene deposits east of the Central Cordillera. These strata consist of an up to 7-km-thick succession evolving from estuarine and coastal plain to proximal fluvial deposits (Gómez et al., 2003). Cenozoic uplift of the Eastern Cordillera caused either erosional removal or non-deposition in this part of the succession. Consequently, an incomplete record of foreland basin sedimentation is preserved in the internal sectors of the mountain range and is exposed mainly along syncline inliers. In the area surrounding the High Plain of Bogotá, for example, upper Miocene alluvial deposits (Tilatá and Marichuela Formations; Helmens and Van der Hammen, 1994) rest uncomformably on middle Eocene to lower Oligocene nonmarine sediments (Usme and Regadera Formations; Gómez et al., 2005; Hoorn et al., 1987;

Kammer, 2003; Fig. 2.2). In contrast, a complete record of Cenozoic sedimentation is exposed in elongated basins along fold-and-thrust belts on either side of the Eastern Cordillera (e.g., Cooper et al., 1995). Along the eastern margin of the range at 4.5-5° N latitude, the Medina basin is particularly well suited for determining the initial stages of orogenesis in this part of the Andes (Fig. 2.1). First, it is located within the present-day wedge-top depozone of the foreland basin system between the deeply exhumed basement high of the Quetame massif to the west and the presently deforming mountain front demarcated by the Guaicaramo thrust to the east. Second, approximately 5 km of shallow marine and nonmarine syntectonic sediments are well exposed and preserved within the fold-and-thrust belt and thus offer an unrestricted view of Cenozoic orogenic processes (Fig. 2.2).

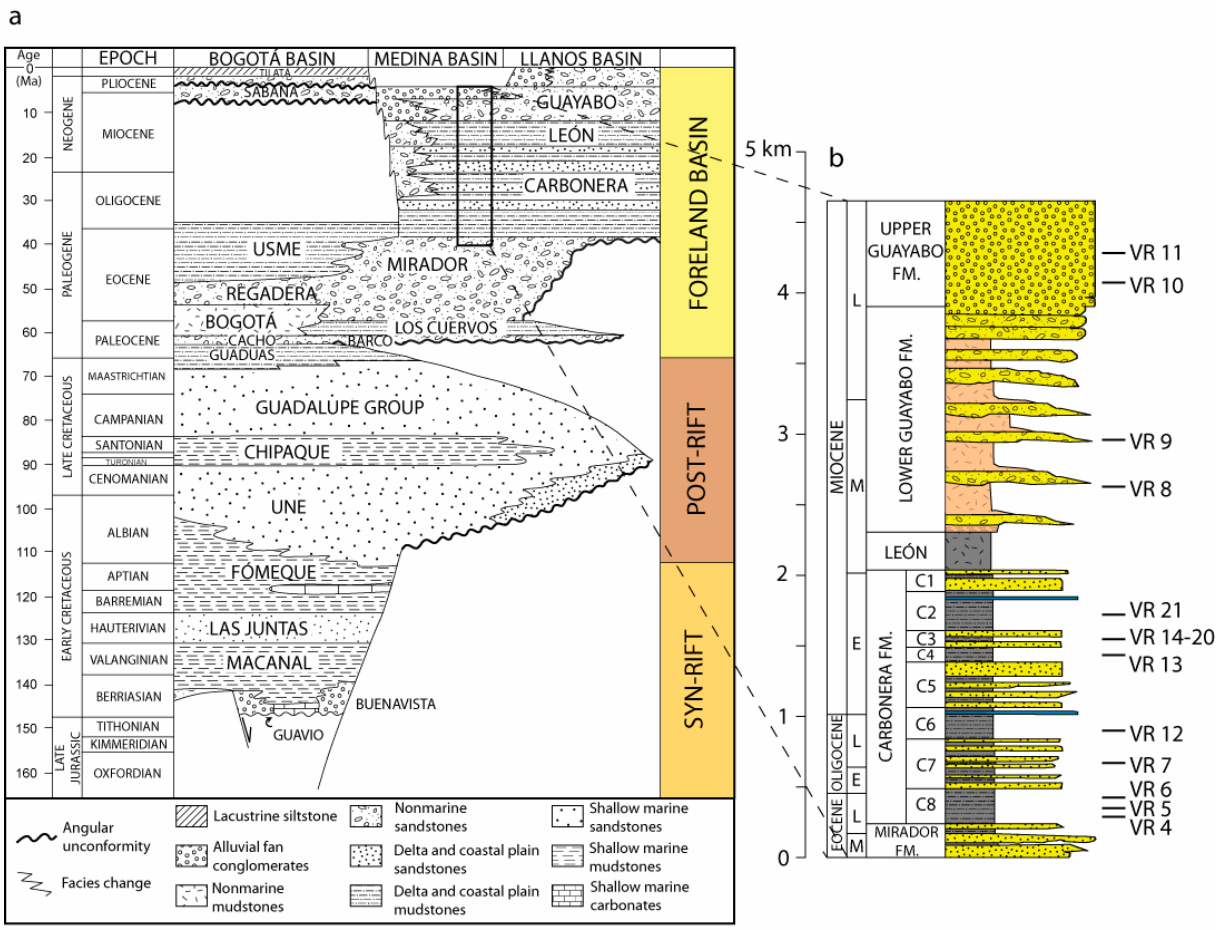

Figure 2.2: (a) Generalized stratigraphy of the eastern margin of the Eastern Cordillera and the Llanos basin showing the spatiotemporal distribution of Cretaceous rift-related and Cenozoic foreland basin sedimentary units. (b) The Upper Eocene - Miocene stratigraphy of the Medina basin comprises a ~4.5 km thick first-order coarsening upward succession. Location of samples for vitrinite reflectance analyses is indicated.

2.3 METHODS

The apparent discrepancies in the early spatiotemporal localization of the leading edge of deformation in the Eastern Cordillera led us to employ a multidisciplinary approach aimed at linking the uplift and exhumation in the Quetame massif with the creation of accommodation space and the depositional history in the adjacent Medina basin. In order to identify variations in thickness and

lithology within laterally equivalent lithostratigraphic units across the Medina basin, we mapped an area of about 1500 m^2 at a scale of 1:10,000. Field observations were integrated with the interpretation of two-dimensional industry-style seismic reflection profiles to better document the lateral continuity and geometry of sedimentary units. We analyzed stratigraphic sections and facies along three sections to document lithofacies variations at different positions within the basin. Approximately 180 measurements of paleocurrent indicators (e.g., DeCelles et al., 1983) were carried out to reveal patterns of sediment dispersal. To better constrain the depositional history, we provide a new palynological biozonation based on analysis of 125 samples. We identified 169 palynomorph species and counted a total of 16,379 grains (Appendix A, Parra et al., 2008). All samples were collected from unoxidized, organic mudstone beds along stratigraphic profiles 1, 2 and 3 (18, 71 and 36 samples, respectively, Fig. 2.4). Sample preparation followed standard procedures (Traverse, 1988), further detailed in the Data Repository.

Our new stratigraphic results were combined with published data in order to investigate the mechanisms and patterns of subsidence in the basin. We performed one-dimensional backstripping following the procedure described by (Allen and Allen, 2005), aimed at estimating the changing depth of the basin floor through time. Regional changes in accommodation patterns were assessed by comparing our results from the Medina basin with published data from the Magdalena Valley (Gómez et al., 2005), ~170 km to the west (Fig. 2.1).

Spatial comparison of the degree of sediment burial across the Medina basin was conducted through vitrinite reflectance analysis (e.g., Guidish et al., 1985). Vitrinite reflectance (Ro) values have been shown to correlate with the maximum temperature reached by organic-matter bearing sediments during heating, allowing for burial assessment in basin analysis (e.g., Tissot et al., 1987). We sampled sediments rich in organic matter and coal beds at different stratigraphic levels within the Cenozoic sedimentary units of the Medina basin and analyzed 26 samples following standard procedures (e.g., Barker and Pawlewicz, 1993), and references therein). Ro values were converted to maximum paleo-temperatures using the kinetic model of Burnham and Sweeney (1989) for heating rates of 0.5 and 50°C/Myr. These values represent maximum temperatures attained during burial and, when evaluated for lateral equivalent units across the basin, allow for spatial comparison of the degree of burial within the basin.

In order to obtain information on the initial exhumation of the Eastern Cordillera in response to Cenozoic Andean uplift, we performed bedrock thermochronology using the high-temperature zircon fission track (ZFT) system, targeting upper structural levels within Lower Cretaceous, syn-rift shallow marine rocks from the Quetame massif area. Fission-track thermochronology is based on the accumulation of linear damage zones (i.e., fission tracks) in the crystal lattice of uranium-bearing minerals caused by the spontaneous fission decay of ^{238}U (Wagner and van den Haute, 1992). Fission tracks are unstable and are progressively erased with time and temperature (e.g., Green et al., 1986), and therefore are useful for extracting the thermal history of the rocks containing the analyzed mineral.

The range of temperatures at which fission tracks are partially stable constitutes the partial annealing zone (PAZ; e.g., Tagami and O'Sullivan, 2005). The zircon PAZ corresponds to a temperature range of 250 ± 40°C (e.g., Tagami et al., 1998). Here, we present five ZFT ages obtained from the western flank of the Quetame massif (Fig. 2.1). Mineral separation and analytical procedures followed conventional methods (e.g., Bernet and Garver, 2005) and are summarized in Table 3.3.

2.4 STRUCTURAL SETTING AND STRATIGRAPHY OF THE EASTERN FOOTHILLS REGION

The Medina basin is an integral part of the modern wedge-top depozone (DeCelles and Giles, 1996) of the northern Andean foreland basin system. The sedimentary succession of the eastern flank of the Eastern Cordillera encompasses up to 12 km of Mesozoic rift-related and Cenozoic foreland basin deposits that taper eastward onto the pre-Mesozoic basement of the Guyana Shield (Fig. 2.2). In the following sections we provide a general background on the structural configuration of the eastern foothills area and the Mesozoic and Cenozoic stratigraphy.

2.4.1 Structural configuration

The Medina basin separates the northern termination of the Quetame massif, west of the west-dipping reverse Servitá fault, from the virtually undeformed Llanos plains east of the Guaicaramo thrust (Fig. 2.1).

The Quetame massif is a basement high, where pre-Devonian phyllitic basement and upper Paleozoic shallow marine strata are overlain by Cretaceous syn-rift and post-rift deposits (Fig. 2.3). Contractile deformation in the Quetame massif is thick-skinned and has been mainly accommodated by reactivation of inherited Mesozoic normal faults (e.g., Mora et al., 2006). In this context, the Farallones anticline is a broad hanging-wall fold associated with the tectonic inversion along the Servitá and Lengupá-Tesalia fault systems (Fig. 2.3). At about 4°50’ N latitude, the Farallones anticline plunges northward and displacement along the Tesalia fault decreases. As a result, shortening in the forelimb of the Farallones anticline is accommodated only by folding (Fig. 2.3a).

Farther east, the Medina basin constitutes the hanging wall of a thin-skinned thrust sheet that extends ~40 km east of the Tesalia fault. Here, the Guavio anticline is a broad fault-bend fold related to the Guaicaramo thrust. In the northern part of the basin, west of the Guavio anticline, the Nazareth syncline is a highly asymmetric, east-verging fold that forms the westernmost structure in the area. Its western limb is overturned and constitutes the northern extent of the western Medina syncline. The steepening of the western limb of the Medina syncline occurs where the surficial expression of deformation in the western margin of the Quetame massif changes. In the south, deformation at the surface is mainly accommodated by the Servitá fault, whereas in the north, deformation has resulted in fault-propagation folding (Fig. 2.3).

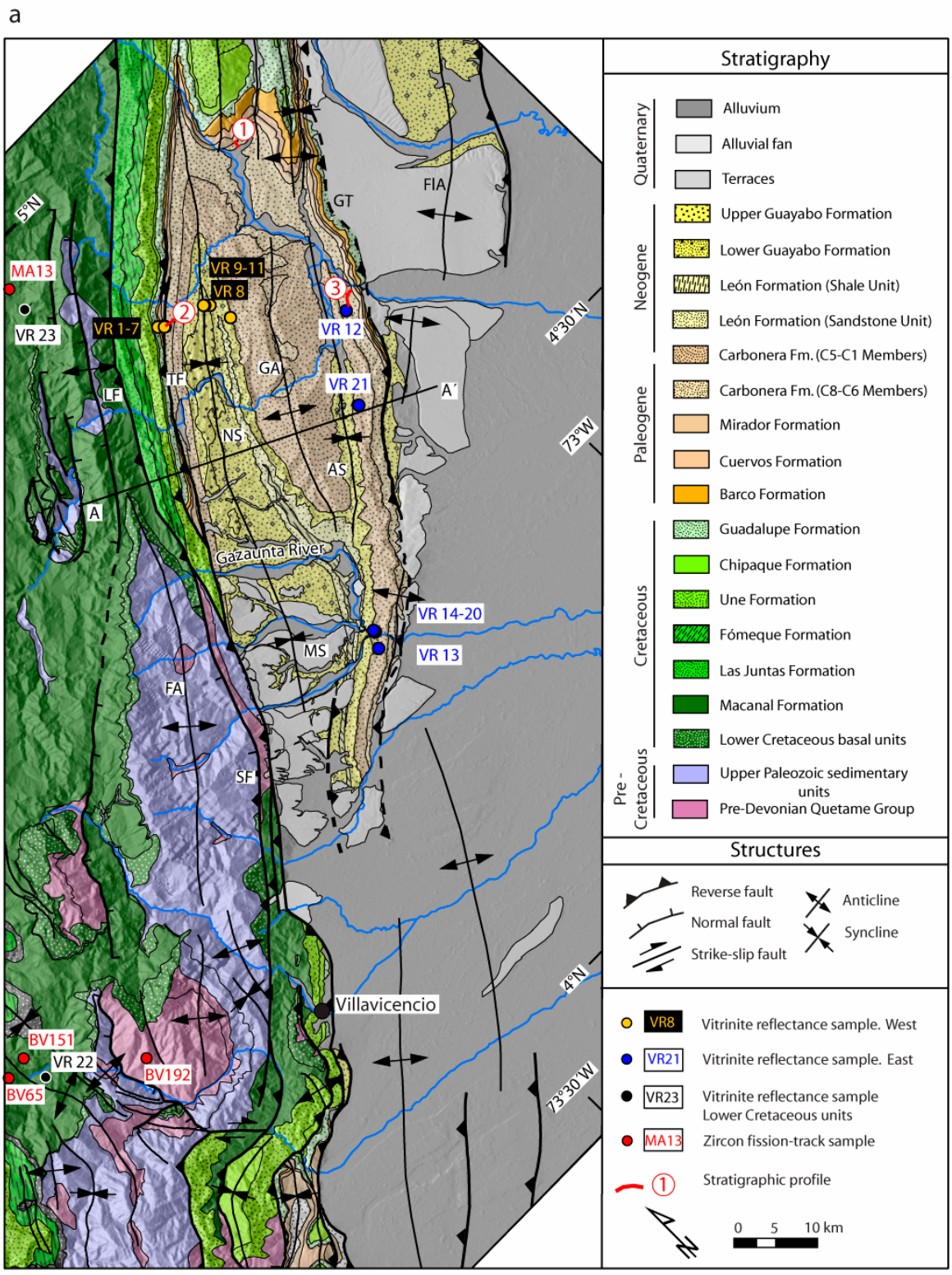

Figure. 2.3:. Geological map and cross section of the Medina basin and the northern termination of the Quetame massif (location shown in Fig. 2.1). (a) Map depicting main stratigraphic units and structures. Location of three stratigraphic profiles and sampling sites for zircon fission-track and vitrinite reflectance analyses are indicated. Abbreviations are as follows: AS, Río Amarillo syncline; FA, Farallones anticline; FlA, La Florida anticline; GA, Guavio anticline; GT, Guaicaramo thrust; LF, Lengupá fault; MS, Medina syncline; NS, Nazareth syncline; SF, Servitá fault; TF, Tesalia fault. (b) Balanced cross section along structural profile A-A´ (location indicated in Fig. 2.3a) based on detailed surface mapping and interpretation of seismic reflection profiles. An eastward-thinning sedimentary wedge made up of the Carbonera Formation is shown.

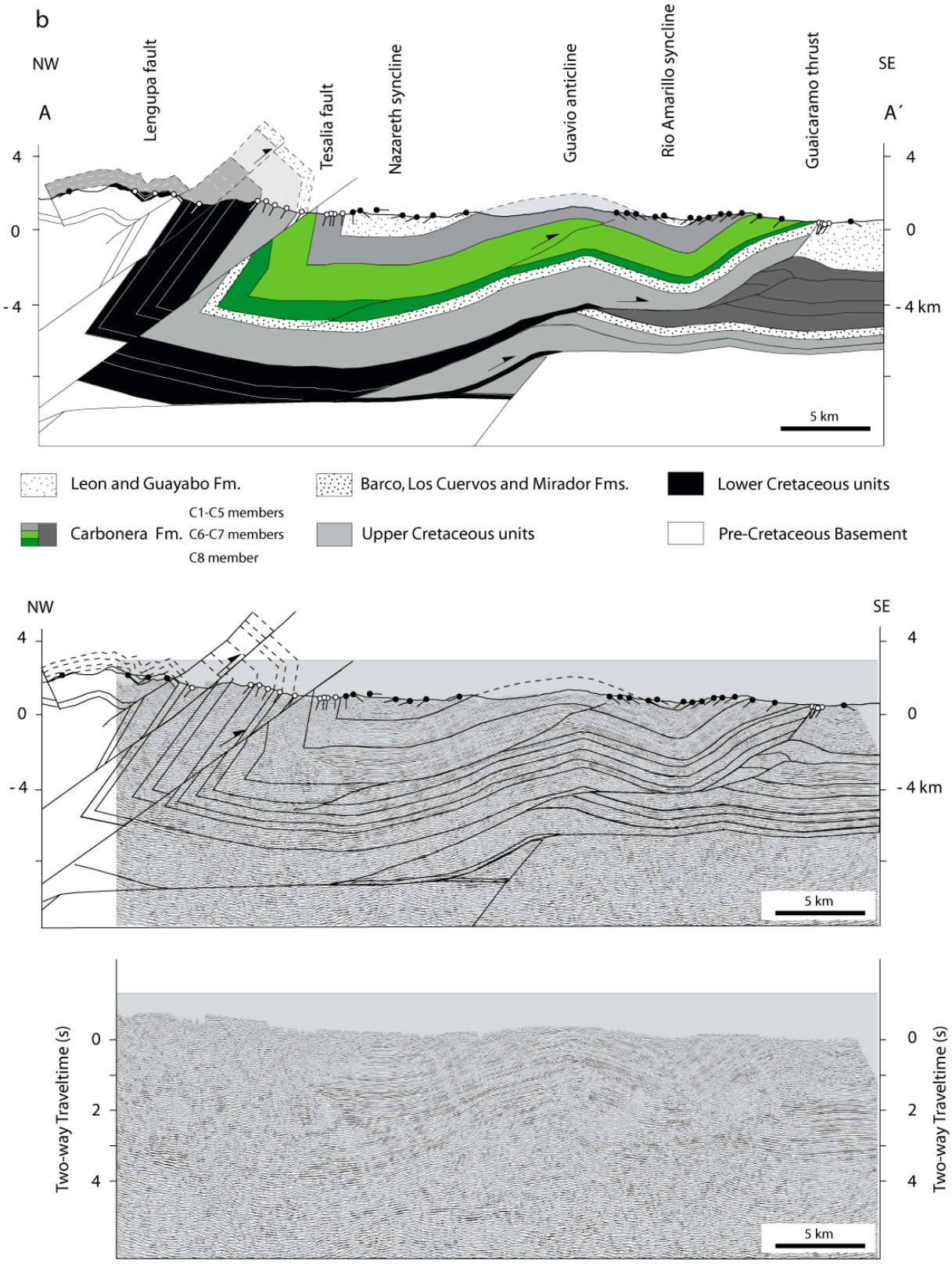

Finally, southeast of the Guaicaramo thrust, the Llanos Plain constitutes the modern foredeep. Here, deformation is very minor and mainly results from the southward propagation of the Yopal thrust and the associated hanging wall, the La Florida anticline, a structure corresponding to a more frontal depocenter within the en echelon segments of the eastern fold-and-thrust belt.

2.4.3 Stratigraphy

The stratigraphy of the eastern flank of the Colombian Eastern Cordillera comprises three principal subdivisions (Fig. 2.2): (1) a Lower Cretaceous, shallow marine sedimentary sequence associated with rifting, up to 5 km thick, is exposed in the internal, elevated areas of the Eastern Cordillera (Mora et al., 2006). These units unconformably overlie either localized back-arc Jurassic volcanoclastic sediments (Kammer and Sánchez, 2006; Mojica et al., 1996), an upper Paleozoic shallow marine sequence or pre-Devonian phyllites (Campbell and Bürgl, 1965; Mora et al., 2006; Sarmiento-Rojas et al., 2006); (2) Up to 3-km-thick Upper Cretaceous platformal deposits that register the onset of post-rift thermal subsidence (Fabre, 1983; Sarmiento-Rojas et al., 2006); and (3) Maastrichtian to Holocene marginal marine to nonmarine foreland basin-related units that reach a thickness of up to ~7 km. These foreland basin units comprise three sedimentary sequences bounded by two major unconformities that merge into a single composite unconformity toward the east (Fig. 2.2; Cooper et al., 1995; Gómez et al., 2005).

2.5 EARLY SYNOROGENIC STRATA OF THE MEDINA BASIN

We present a new stratigraphic framework for the early Eocene to early Miocene foreland basin sediments in the Medina basin. First, we describe the spatial distribution of sedimentary units and their major lithological and thickness variations, based on our surface and subsurface data. Second, we present facies analyses and paleocurrent data from the lower members of the Carbonera Formation along three stratigraphic profiles across the basin (Fig. 2.4). Third, we present new biostratigraphic data that allow estimation of depositional ages, and finally we integrate the stratigraphic results to better assess basin evolution during the initial stages of orogenesis in the Eastern Cordillera.

Combined surface mapping and seismic interpretation document the presence of an eastward thinning sedimentary wedge comprising the C8-C6 members of the Carbonera Formation (Figs. 2.3b and 2.4). The thickness of the C8 Member in the northern axial portion of the basin reaches approximately 250 m (profile 1; Fig. 2.4). Seismic interpretation tied to detailed geological mapping suggests rapid thickening of this unit to the west (Fig. 2.3). A varying stratigraphy within the interval delineated by the base of the sandstone-dominated C7 Member and a bivalve-rich horizon found at the top of the C6 member across the basin is illustrated based on description along profiles 2 and 3, where a complete record of the C7-C6 members is described (Fig. 2.4). Due to lithological variations, we subdivided the equivalent interval into units G1, G2, G3, and G4 in the western profile (Fig. 2.4). These sections were also sampled for palynology in order to constrain depositional ages and environments. In the following section we present the facies analysis for the profiled sections.

2.5.1 Depositional systems

Based on lithology and sedimentary structures, fifteen lithofacies (Table 3.1) and four facies associations were recognized within the C8, C7, and C6 members of the Carbonera Formation. A

summary of the facies analysis and the spatial distribution of the facies associations is presented in Table 3.2 and Figure. 2.4.

Our results show a reversal of paleocurrents from initially westward transport directions in the Mirador Formation, associated with eastern sources on the Guyana Shield (Cazier et al., 1997; Cooper et al., 1995), to a northeastward sediment dispersal pattern. The switch occurs in the C7 and C6 members in the northern and eastern parts of the basin (Fig. 2.4). This reversal thus documents a change in the main sediment source to the southwest, along the present-day Eastern Cordillera. Limited paleocurrent indicators in the alluvial G4 unit of the western section suggest a polymodal dispersion pattern (Fig. 2.4), interpreted to reflect episodes of avulsion in the alluvial system. Our analysis and lithostratigraphic correlation indicate that the C8-C6 Members constitute an eastward-thinning syntectonic wedge in the Medina basin. In the western part, the interval equivalent to the C7-C6 Members reaches a thickness of 1150 m. It evolves from coastal plain and deltaic deposits in the G1-G3 units (Facies Associations 1 and 2; Table 3.2) to braided fluvial deposits in the G4 unit (Facies Associations 3 and 4). Equivalent deposits ~20 km to the east are only 455 m thick and are exclusively dominated by deltaic Facies Associations 1 and 2. Taken together, the rapid facies changes from tidally-influenced coastal plain to fluvial deposits to the west, and the changeover to northeastward paleocurrent directions documents the initial existence of elevated topography in the area of the present-day Eastern Cordillera in early Oligocene time. Furthermore, the thickness variations in the basin clearly illustrate enhanced subsidence in the west, suggesting tectonic loading in the location of the present-day Eastern Cordillera during the late Eocene-late Oligocene.

2.5.2 Age constraints

Our new chronostratigraphic framework for the C8-C6 Members of the Carbonera Formation, based on palynomorphs, facilitates the evaluation of spatiotemporal trends in basin evolution. In our analysis we follow the biostratigraphic zonal scheme developed by Jaramillo et al. (2005), Jaramillo and Rueda (2004) and Jaramillo et al. (2008). Palynological biozones from northern South America have been calibrated using foraminifera and nanoplankton from Venezuela (Germeraad et al., 1968; Muller et al., 1987), and stable carbon isotopes ($\delta^{13}C$) from Colombia and Venezuela (Jaramillo et al., 2007; Jaramillo et al., 2006). The calibration data provided by these authors suggest that uncertainties in the time-assignments of the individual biozones are relatively minor, although the published data are insufficient to further quantify the uncertainty.

Both the eastern and western intervals of the syntectonic wedge corresponding to the C8-C6 members of the Carbonera Formation were deposited within the palynological zones T-05 to Ca-07, corresponding to early Eocene to early Miocene time (Fig. 2.6). Based on the key taxa for the zonal scheme (Fig. 2.6), the limits of the biozones in the composite section are assigned to the midpoint between samples belonging to contiguous biozones (Appendix A, Table A1).

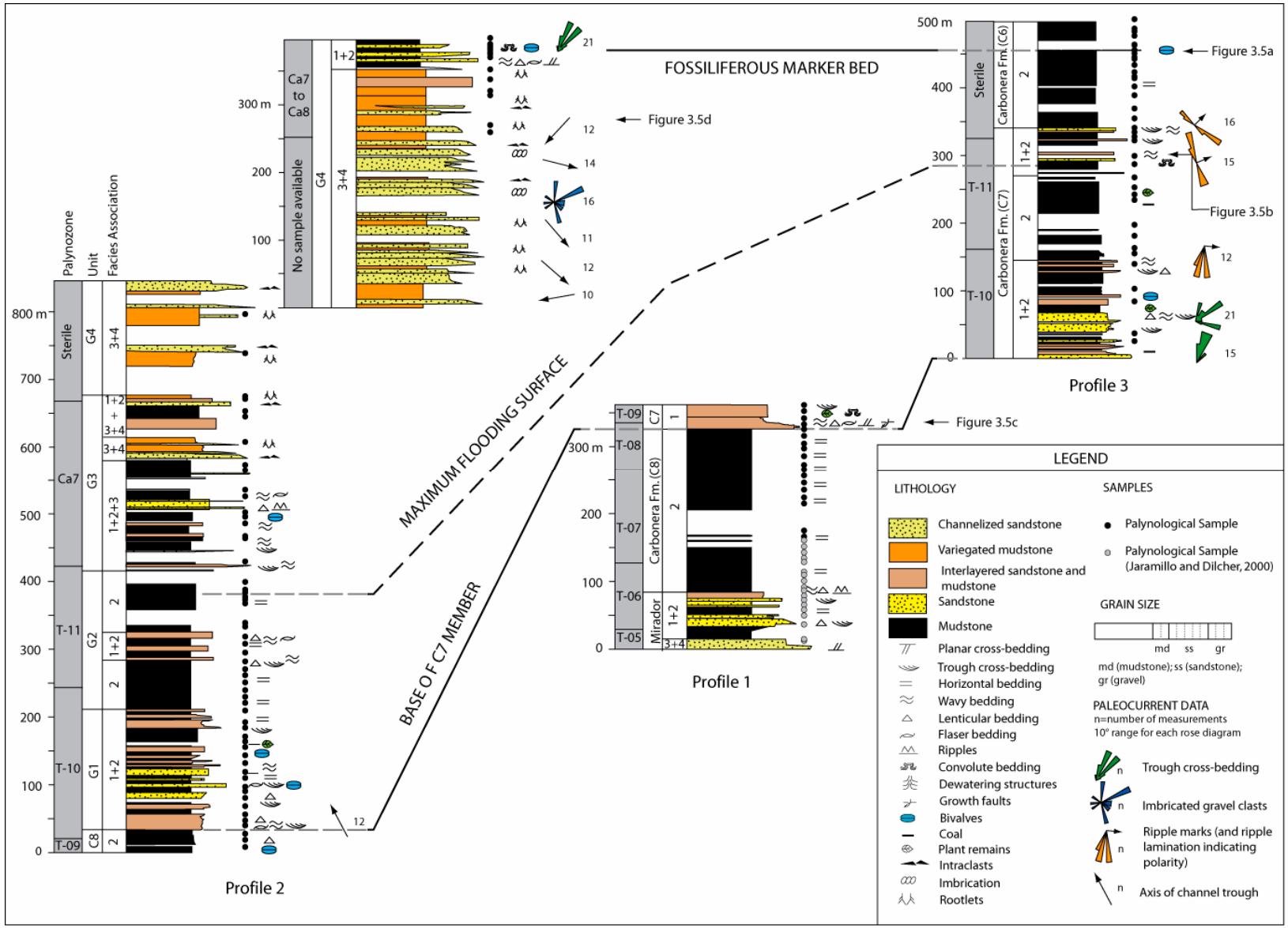

Figure. 2.4: Measured stratigraphic profiles of the C8-C6 members of the Carbonera Formation in the Medina basin (location in Fig. 2.3a), including lithostratigraphic correlations, interpreted facies associations, palynological zonations and paleocurrent measurements. A southwesterly sourced, eastward-thinning clastic wedge corresponding to the C7-C6 members is identified based on lithostratigraphic correlation along distinct marker horizons. Thickness between the base of the C7 Member of the Carbonera Formation and a fossiliferous, bivalve-rich marker bed at the top of C6 Member diminishes from ~1150 to ~450 m over a distance of ~20 km.

TABLE 2.1: DESCRIPTION AND INTERPRETATION OF LITHOFACIES (after Miall,1996; Einsele, 2000)

Code	Description	Interpretation
Gcd	Disorganized clast-supported conglomerates, cobbles and pebbles	Clast-rich non cohesive debris flow
Gco	Organized, clast-supported conglomerates, cobbles and pebbles. Weak imbrication	Longitudinal bedforms, lag deposits
St	Trough cross-stratified sandstone, fine to coarse	3D dunes
Sp	Planar cross-stratified sandstone, fine to very coarse, often pebbly	Transverse and linguoid bedforms (2D dunes)
Sr	Ripple marks and small-scale cross stratification	Ripples (lower flow regime)
Sf	Flaser bedded sandstone	Alternating suspension settling and lower flow regime
Sw	Wavy bedded sandstone	Alternating suspension settling and lower flow regime
Slc	Lenticular bedded sandstone	Alternating suspension settling and lower flow regime
Sc	Convoluted bedded sandstone	Deformation by diferential loading or dewatering
Sm	Massive sandstone	Sediment gravity-flow deposits
Fl	Laminated mudstone and siltstone	Suspension-load deposits.
Fm	Massive mudstone and siltstone	Suspension deposits, overbank or abandoned channels
Fs	Disorganized shell-dominated mudstone	Upper flow regime
Fb	Variegated mudstone and siltstone. Commonly sandy, intense mottling	Overbank or abandoned channels
Fo	Mudstone and siltstone with organic matter-rich laminae	Suspension settling deposits
C	Coal	Organic-rich swamp deposits

The base of the early Eocene Zone T-05 is defined by the first appearance datum (FAD) of *Tetracolporites maculosus*. The FAD of *Cicatricosisporites dorogensis* defines the top of the early Eocene Zone T-05. The last appearance datum (LAD) of *Spinizonocolpites grandis* defines the top of the middle Eocene Zone T-06. The top of the late Eocene Zone T-07 is marked by the the LAD of *Echitriporites trianguliformis orbicularis*. The top of the early Oligocene Zone T08 is defined by the LAD of *Nothofagidites huertasii.* The FAD of combined acme of *Jandufouria seamrogiformis, Magnastriatites grandiosus, Mauritiidites franciscoi minutus* and *Verrucatosporites usmensis* defines the top of the early to middle Oligocene Zone T 09. The LAD of the combined acme of *Jandufouria seamrogiformis, Magnastriatites grandiosus, Mauritiidites franciscoi minutus* and *Verrucatosporites usmensis* defines top of the middle Oligocene Zone T 10. The top of the late Oligocene Zone T-11 is defined by the LAD of *Cicatricosisporites dorogensis*. Finally, the FAD of *Echitricolporites maristellae* defines top of Zone Ca07, corresponding to early Miocene.

TABLE 2.2. SUMMARY OF FACIES ASSOCIATIONS

Facies Association	Description	Stratigraphic occurrence (see Figure. 2.4)	Interpretation
FA 1 (coarsening-upward laminated sandstone)	Up to 8 m thick thickening- and coarsening-upwards intervals of tabular sandstone with minor thin interbeds of mudstone. Sandstone beds present non-erosive basal contacts and are frequently bioturbated. Laminae rich in organic-matter, plant remains. Thin pebble conglomerate commonly cap intervals at top. Typical lithofacies pattern includes, from base to top, Fm, Fl, Sw, Sf, Slc, Sr and Gco. Dewatering structures, convolute bedding and growth faults (Figs. 2.5b and 2.5c) occur. Sandstone-mudstone couplets with wavy (Sw), lenticular (Slc), flaser (Sf) and oscillatory current ripple lamination (Sr)	In upper 70 m of Mirador Formation (Profile 1), in the G1, G2, G3 and uppermost 40 m of G4 units of the Carbonera Formation in the western part of the basin (Profile 2), and in C7 member of the eastern section (Profile 3)	Thickening and coarsening upward intervals suggest progradational succession in a tidally-influenced deltaic environment (e.g., Tye and Coleman,1989; Coleman et al., 1998). Growth faults, convolute bedding and water-escape structures suggest rapid accumulation (Lowe, 1975; Owen, 1996). Possible allogenic control
FA 2 (massive and laminated dark mudstone)	Thick intervals (up to 100 m) of dark-gray to greenish mudstone. Occasional minor bioturbation. Limited interbeds of trough cross-laminated sandstone, and up to 30-cm-thick coal seams. Occasional thin, disorganized bivalve-bearing shell-beds. Local microforaminiferal linings and dinoflagellates. Fragmented and disarticulated bivalves belonging to the genus *Pachydon* (CORBULIDAE; Fig. 2.5a). Best preserved specimens resemble the species *P. tenuis, P. trigonalis, and P. Cuneatus*. Discrete levels with microforaminiferal linings and dinoflagellates including *Homotryblium floripes, Cordosphaeridium inodes, Polysphaeridium subtile, Achomosphaera, and Spiniferites*	Dominant facies in C8 and C6 members. Interlayered with FA1in G1, G2 and G3 units in the western Medina Basin (Profile 2)	Mud flat in a deltaic plain. Coal indicates humid climate. Fragmented bivalves belonging to genus *Pachydon* suggest a high-energy, freshwater environment (e.g., Nuttall, 1990; Wesselingh et al., 2002). Dinoflagellates and microforaminiferal linings indicate local marine influence
FA 3 (interbedded fluvial sandstones and conglomerates)	Medium- to thick-bedded, medium-to coarse grained, and pebbly sandstone. Gravel lags and mudstone intraclasts common at base of individual beds. Beds have erosive bases (Fig. DR1d above mottled sandy mudstones and siltstones, and extend laterally up to few tens of meters. Commonly floating pebble clasts occur. Granule and pebble stringers loosely defining large-scale planar cross stratification occur rarely. Frequently, strata grade upward into variegated mudstone (FA4)	Occurs in the lower 15 m of measured section of Mirador Formation in Profile 1. Occur interlayered with FA4 in G4 unit (western Medina Basin)	Stream flow deposits. Loosely defined large-scale, low-angle planar cross-stratification, absence of well defined normal grading and frequent floating pebbles suggest deposition in braided fluvial channels
FA 4 (overbank fines)	Reddish to brown, massive to crudely stratified sandy mudstone and siltstone. Ubiquitous mottling and root traces (Fig 3.5d). Lenticular, normally graded, thin sandstone interbeds	Major facies of G4 unit. Also in the lower part of Mirador Formation, subordinate to FA3.	Laterally continuous variegated mudstone with pervasive mottling and root traces indicate deposition in an alluvial-plain environment

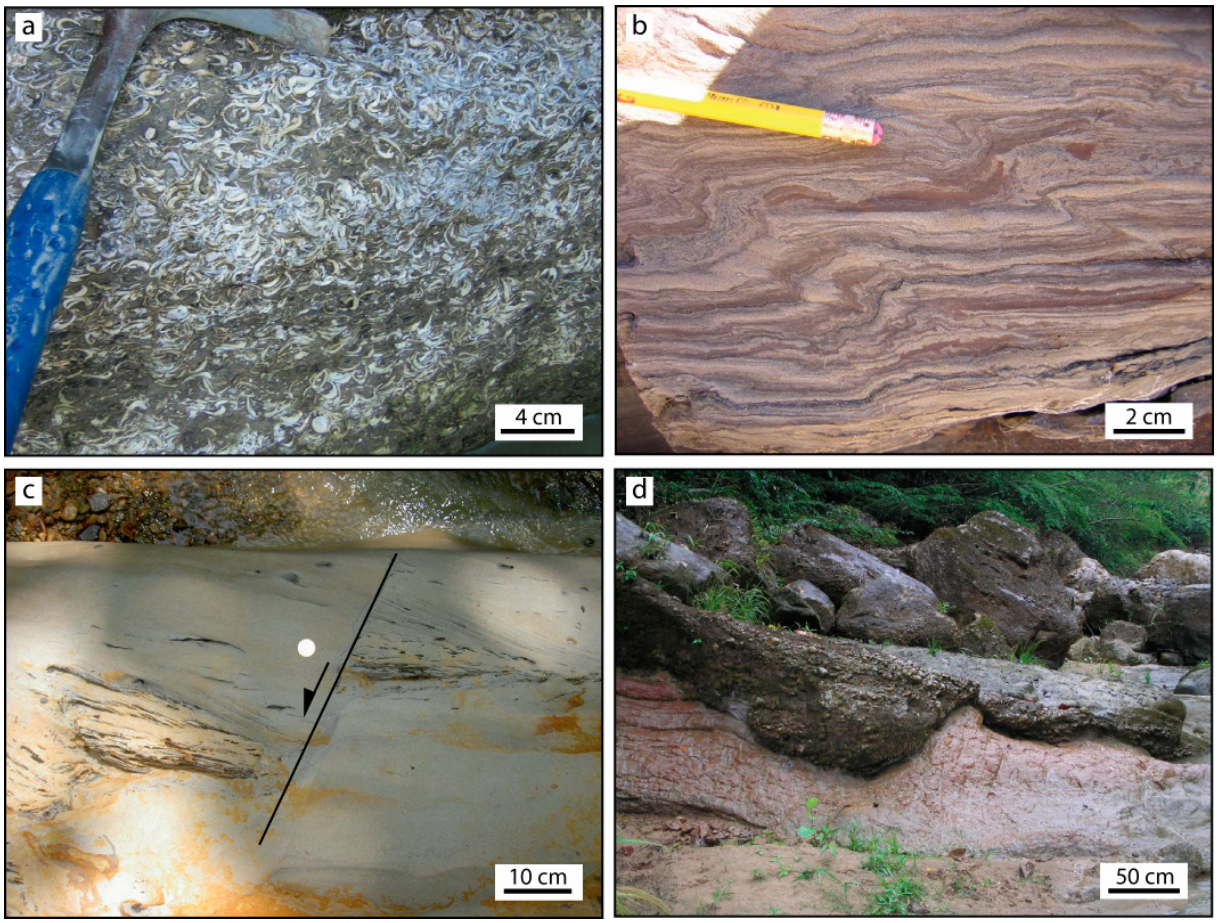

Figure. 2.5: Photographs of selected outcrops within the C7 and C6 members of the Carbonera Formation (location in Fig. 2.4); (a) shell bed formed by disarticulated, closely packed bivalves including specimens belonging to genus *Pachydon* at the top of the C6 member in profile 3; (b) thin-bedded mudstone-sandstone couplets at the top of the C7 Member in profile 3 with convolute bedding; (c) growth fault in ~ 30-cm-thick sandstone bed at the base of C7 Member in profile 1. Soft-sediment deformation shown in (b) and (c) is interpreted to result from rapid sediment accumulation; (d) channelized sandy cobble conglomerates, ~0.8 m thick overlying variegated mudstone with pervasive mottling within interval G4 along profile 3. Prominent basal scour surface results from incision of meandering fluvial channels into alluvial floodplain deposits.

2.6 GEOHISTORY ANALYSIS

The Paleocene-early Miocene tectonic subsidence history of the Medina basin was assessed using one-dimensional backstripping of a composite stratigraphic section from the Medina basin constructed using the stratigraphic data presented in this study for the lower part of the Carbonera Formation (profiles 1 and 2; Fig. 2.4), and published data from Paleogene foreland sediments in the basin (Jaramillo and Dilcher, 2000; Jaramillo and Dilcher, 2001; see Figs. 2.4 and 2.6). Here, we used thicknesses and age constraints for biostratigraphic units based on the palynological biozonation for the Paleocene-early Miocene composite section. Vertical error bars were defined by the stratigraphic separation between the younger and older samples of contiguous biozones. Water-depth estimates were assigned according to the interpreted depositional environments of coastal plain deposits (see methods in Data Repository). Since constraints on Paleogene and Neogene paleoelevations are poor, we assumed a maximum altitude of 300 m, which corresponds to the present maximum altitude of the

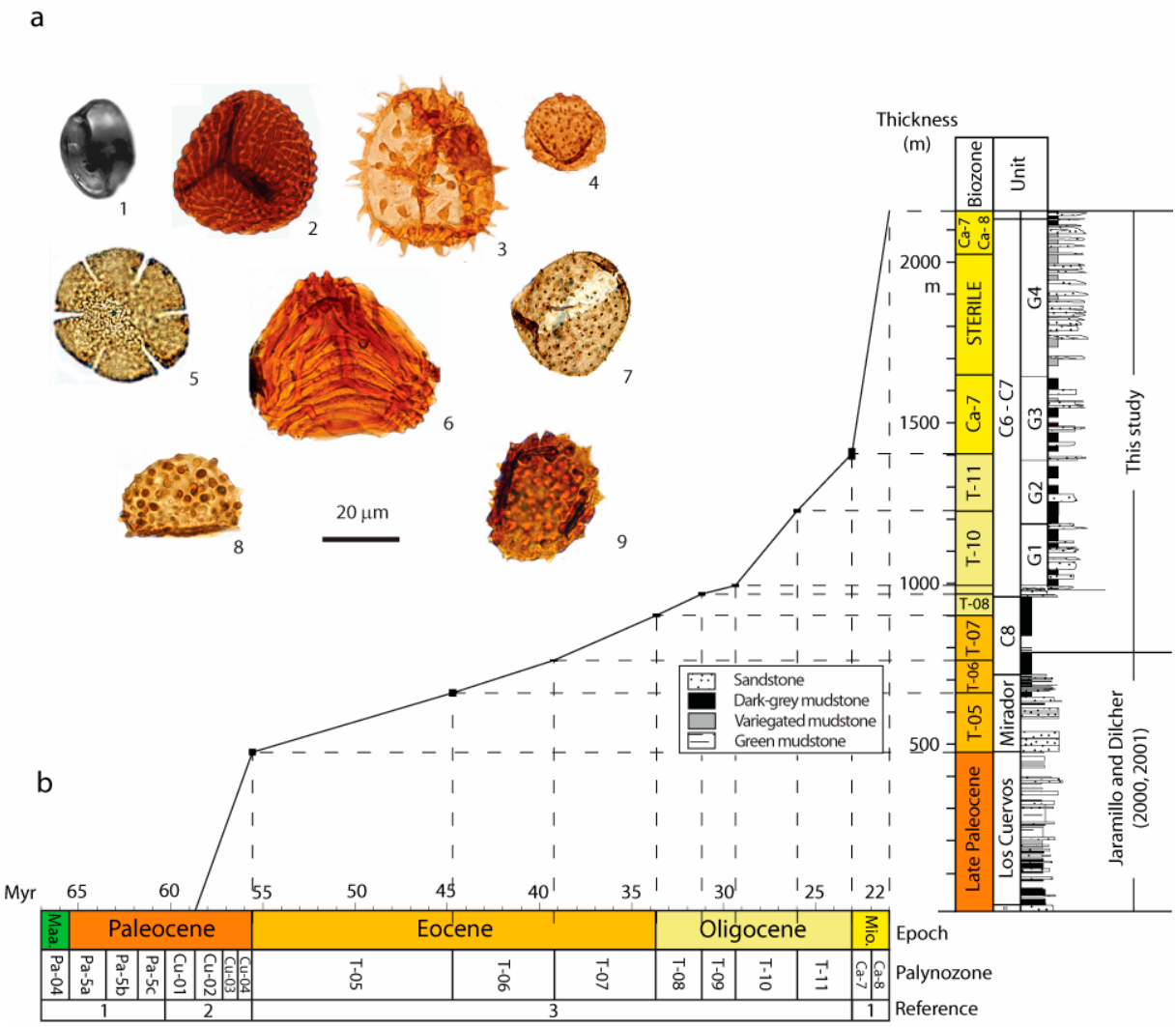

Figure. 2.6: Palynological biozonation and composite stratigraphic section for the Upper Paleocene-lower Miocene strata of the Medina basin. (a) Photographs of key taxa used in this study; 1. *Tetracolporites maculosus*. 2. *Cicatricosisporites dorogensis*. 3. *Spinizonocolpites grandis*. 4. *Echitriporites trianguliformis orbicularis*. 5. *Jandufouria seamrogiformis*. 6. *Magnastriatites grandiosus*. 7. *Mauritiidites franciscoi minutus*. 8. *Verrucatosporites usmensis*. 9. *Echitricolporites maristellae*. See explanation in text. (b). Composite stratigraphic section for the Paleogene strata of the Medina basin. The composite section is constructed based on thickness, lithology, and biozonation after Jaramillo and Dilcher (2000) for the Los Cuervos and Mirador Formations, and data obtained in this study from profiles 1 and 2 of the Carbonera Formation. The biozonal scheme utilizes the geological time scale of (Gradstein et al., 2004). Assignment of biozones is based on Jaramillo and Rueda (2004), Jaramillo et al. (2005) and Jaramillo et al. (2008) (references coded in zonal scheme with numbers 1, 2 and 3, respectively).

Llanos basin alluvial plain. The early to late Miocene sediments of the Upper Carbonera, the León and Guayabo Formations were treated as a single unit for the analysis. Global long-term eustatic sea-level values (Haq et al., 1987) were averaged over the time span represented by each biostratigraphic unit. A summary of the different parameters used in the geohistory analysis is presented in Table A1 (Appendix A).

In order to evaluate the spatial and temporal variations in the subsidence pattern of the foreland basin system, we also plot an early Paleocene-middle Miocene backstripped section from the southern Middle Magdalena Valley basin (SMMV) using published data (Gómez et al., 2005). Although

geohistory analysis is a powerful method for identifying the components of subsidence, it entails important assumptions that must be taken into consideration when interpreting trends in subsidence patterns. Specifically, local (Airy) compensation of the sediment load neglects lateral flexural strength of the lithosphere and hence results in overestimation of the contribution of the weight of the sediment column to the subsidence of the basin (Watts et al., 1982). Furthermore, in our analysis (Fig. 2.7) we

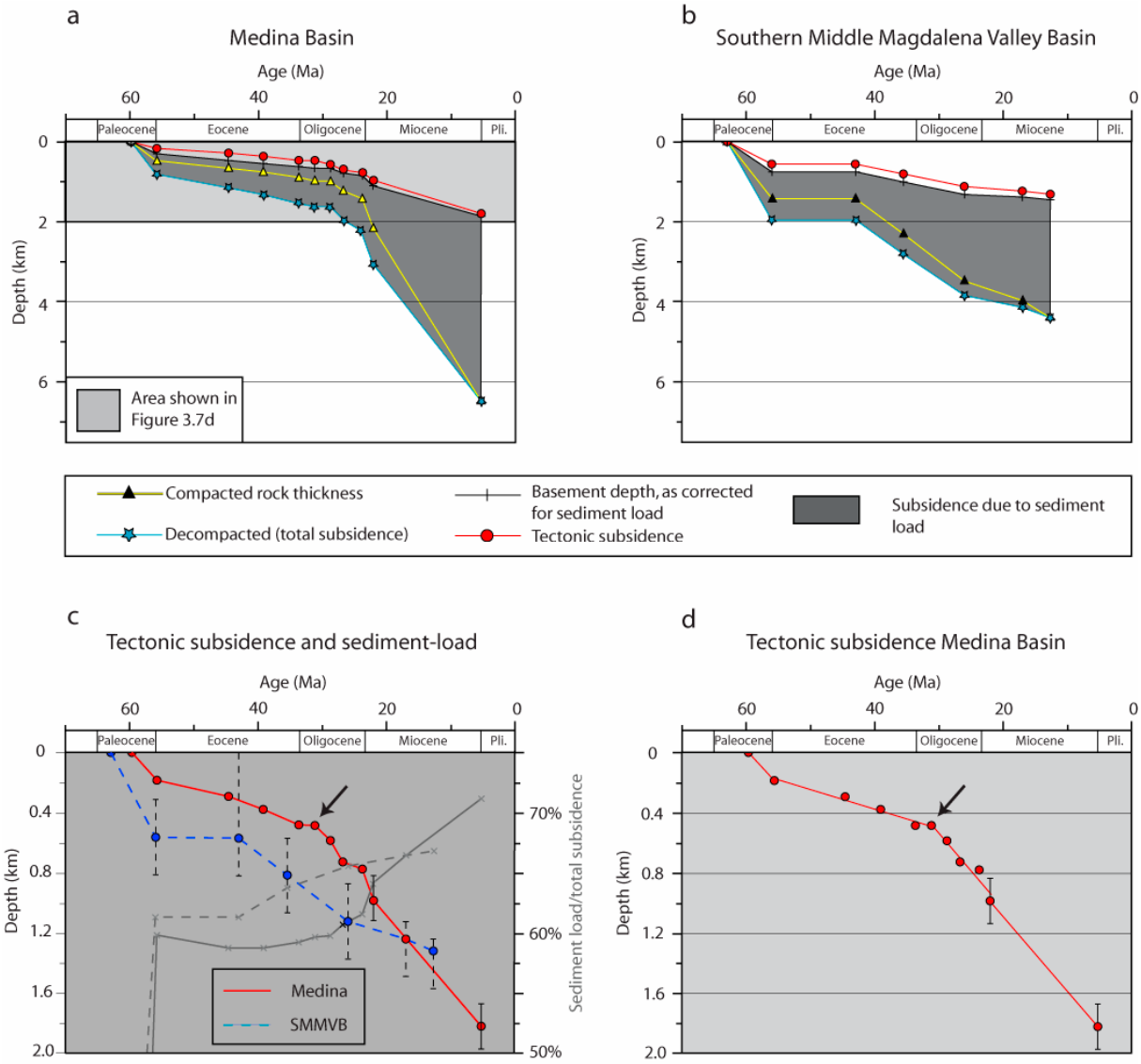

Figure. 2.7: Geohistory analysis for the Upper Paleocene-Miocene stratigraphic sections of the Medina and Southern Middle Magdalena Valley basins. (a) Medina basin. (b) Southern Middle Magdalena Valley (SMMV) basin [data from (Gómez et al., 2005)]. Details on parameters used for analyses are shown in Table A5 (Appendix A). (c) Tectonic subsidence curves (red and blue lines) and temporal evolution of the sediment-load contribution to the total (decompacted) subsidence (gray lines) for Medina and SMMV basins. Rapid subsidence in the SMMV basin during Paleocene time result from tectonic loading of the Central Cordillera (Gómez et al., 2005). Enhanced subsidence since ca. 31 Ma (arrow) in the Medina basin results from initiation of loading along the present-day eastern border of the Eastern Cordillera. See text for discussion. (d) Tectonic subsidence curve of the Medina basin depicting a sigmoidal, three-stage pattern interpreted as the vertical stacking of distal foredeep, forebulge and proximal foredeep resulting from the Eocene retreat and subsequent Oligocene advance of the foreland basin system. Vertical error bars represent uncertainties in paleoaltitude (water depth) for continental (marine) units. Bars are only visible for the two youngest points representing continental deposits with larger uncertainty in paleoelevation (see Table A1 and text for discussion).

do not extract subsidence rates, since backstripping only the Cenozoic strata implies that underlying units underwent no compaction during the Cenozoic. Since the pre-Cenozoic substratum in both the Medina and SMMV basins comprises ~6-7 km of Mesozoic sedimentary rocks (Gómez et al., 2005; Mora et al., 2008b), the total Cenozoic decompacted thickness is overestimated. Consequently, the decompaction curves (Figs. 2.7a and 2.7b) are forced to meet the compacted-thickness curves at our time zero (Angevine et al., 1993). Nevertheless, our geohistory analysis is sufficient to allow for comparisons between the western and eastern foothills sections, as we applied the same procedure to a corresponding time interval in both areas.

The Paleocene-Miocene subsidence curves for the Medina and SMMV basins (Fig. 2.7) furnish a means to evaluate and compare regional accommodation patterns across the entire foreland basin system. The total subsidence signal for both areas (lowest curves in Figs. 2.7a and 2.7b) display a similar sigmoidal pattern resulting from a period of reduced subsidence (or even uplift in the case of the SMMV, as suggested by the regional Late Cretaceous-Cenozoic unconformity) that separates two episodes with higher accommodation rates. Importantly, the curve for the Medina basin suggests (1) that the onset of faster subsidence occurred at ca. 31 Ma, at least 30 Myr after an equivalent episode in the SMMV, and (2) that this episode, starting in the early Oligocene, was responsible for most of the basin subsidence, ultimately leading to a larger amount of total Cenozoic subsidence in the Medina basin compared to the Magdalena Valley (Fig. 2.7c). The analysis for the Medina and SMMV basins shows that the contribution of the sedimentary load to the total subsidence increases through time (Fig. 2.7c). Since middle Miocene time (ca. 12 Ma), sedimentary loads have accounted for ~70% of the total subsidence in both areas (Fig. 2.7c). As cautioned earlier, this result is an overestimation due to the simplification introduced by using local (Airy) isostatic compensation. However, the results indicate a different temporal evolution for the sedimentary-load contribution for each area. Mimicking the pattern of the total subsidence curve, the sediment-load contribution in the Medina basin was minor in the early stages of the foreland basin development. Since early Oligocene time, sedimentary loads have increased until their contribution to the total subsidence reached a similar amount (~70%), compared to the backstripped foreland strata in the Magdalena Valley.

Larger amounts of total and normalized sediment-load driven subsidence during the Paleocene-early Oligocene (between 65 and 31 Ma; Fig. 2.7c) in the Middle Magdalena basin relative to the Medina basin are compatible with a basin located closer to the orogenic front. Such a basin would have undergone faster subsidence and received a greater load of sediments from the source areas in the hinterland. Maastrichtian to Oligocene tectonic subsidence in the MMVB has been explained by loading of the Central Cordillera between the Maastrichtian and late Paleocene (Cooper et al., 1995; Gómez et al., 2005; Gómez et al., 2003) and by loading of the western front of the Eastern Cordillera in the late Eocene-early Oligocene (Gómez et al., 2005; Gómez et al., 2003). The increase in accommodation rates in the Medina basin since the late Oligocene suggests that the tectonic load, and hence the main source of sediments, has migrated closer to the eastern foothills of the Eastern

Cordillera. Despite the limitations of the backstripping method, the analyzed section in the Medina basin allows identification of changes in the pattern of tectonic subsidence rates (Fig. 2.7d). We conclude that the late Paleocene to early Miocene accommodation history in this region is characterized by a three-stage evolution: an initial late Paleocene episode of moderate subsidence; limited subsidence from Eocene through early Oligocene time; and rapid subsidence from early Oligocene through early Miocene time. We correlate the first two stages with a late Paleocene eastward advance, and subsequent Eocene to early Oligocene westward retreat of the foreland basin system. These episodes have also been documented in the foreland basin record of the Magdalena Valley basin where they were interpreted as the response to a phase of tectonic activity followed by tectonic quiescence in the Central Cordillera (Gómez et al., 2005; Gómez et al., 2003). Similarly, we interpret the second episode of faster tectonic subsidence registered in the late Oligocene-early Miocene sedimentary record of the Medina basin to result from the eastward advance of the deformation front. Rapid subsidence in the Medina basin starting at ca. 31 Ma and the concomitant deposition of an eastward-thinning sedimentary wedge are compatible with initial deposition in a foredeep depozone, and hence are strong evidence for an eastward advance of the orogenic front.

2.7 ZIRCON FISSION TRACK THERMOCHRONOLOGY

Apatite fission track (AFT) data from in situ bedrock samples from the Quetame massif area show rapid cooling below ~120°C since ca. 3 Ma and thus reflect fast rock exhumation of 3 to 5 km since the late Pliocene (Mora et al., 2008b). These data suggest that any older record of exhumation potentially detectable with AFT has been erosionally removed from the deeply incised eastern margin of the mountain range. Thus, in order to obtain information on the earlier stages of exhumation, we conducted zircon fission-track (ZFT) analysis. A comprehensive analysis of exhumation patterns is beyond the scope of this paper and will be presented elsewhere. However, although limited, we present data from five samples obtained from the Quetame massif area (Figs. 2.3 and 2.8) in order to document the timing of thrust-induced exhumation in this sector of the range. Four samples were collected along a longitudinal profile running across the pre-Devonian to Lower Cretaceous section of the western flank of the Quetame massif. Sampling covered different structural levels in order to determine the limits of the ZFT partial annealing zone in this part of the mountain range. A fifth sample (MA 13) was collected from a similar structural position to that of the uppermost sample (Sample BV 121) in the longitudinal profile. However, sample MA 13 is located approximately 80 km to the northwest along strike. Table 3.3 shows the individual ages for the five analyzed samples. The three structurally deepest samples pass the χ^2 test (Galbraith, 1981; Green, 1981) with values of $P(\chi^2) > 5\%$ (Samples BV 151, BV 192 and MA13) indicating that the single-grain age distribution corresponds to a single component (Fig. 2.8d). We analyze the significance of the ZFT cooling ages using an approximation to an age-elevation profile. Age-elevation profiles exploit differences in topographic elevation of samples along relatively steep profiles; if the profile includes part of an

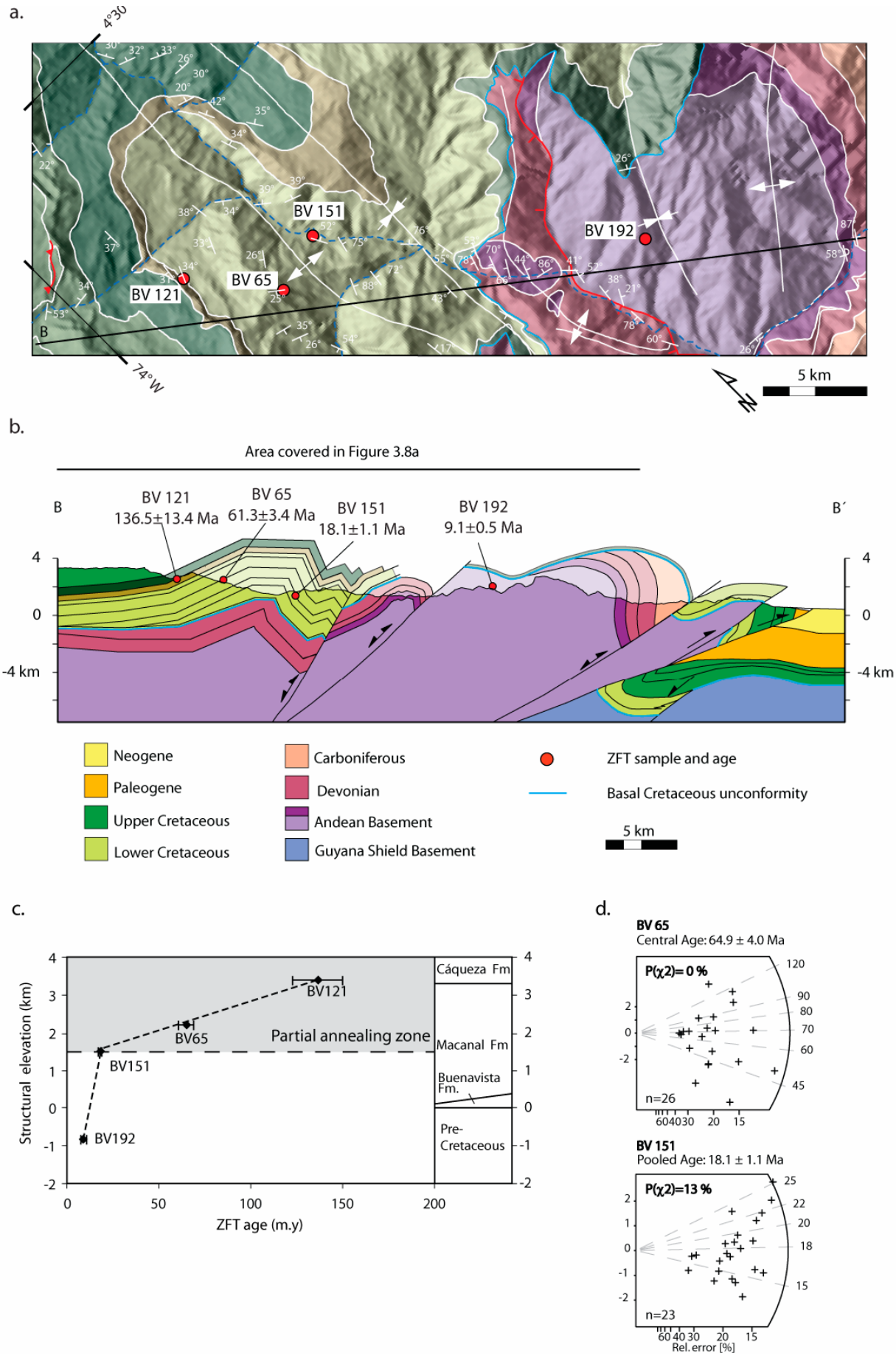
a.
4°30'
74°W
BV 151
BV 192
BV 65
BV 121
B
5 km
b.
Area covered in Figure 3.8a
B
B´
BV 121
136.5±13.4 Ma
BV 65
61.3±3.4 Ma
BV 151
18.1±1.1 Ma
BV 192
9.1±0.5 Ma
4
0
-4 km
Neogene
Paleogene
Upper Cretaceous
Lower Cretaceous
Carboniferous
Devonian
Andean Basement
Guyana Shield Basement
ZFT sample and age
Basal Cretaceous unconformity
5 km
c.
Structural elevation (km)
ZFT age (m.y)
BV121
BV65
BV151
BV192
Partial annealing zone
Cáqueza Fm
Macanal Fm
Buenavista Fm.
Pre-Cretaceous
d.
BV 65
Central Age: 64.9 ± 4.0 Ma
P(χ2)= 0 %
n=26
BV 151
Pooled Age: 18.1 ± 1.1 Ma
P(χ2)=13 %
n=23
Rel. error [%]

exhumed partial annealing zone, it is possible to derive the timing of initiation of exhumation (Huntington et al., 2007; Wagner and Reimer, 1972). In the Quetame massif, the absence of deeply incised canyons cutting through the entire Lower Cretaceous to pre-Devonian section prevents such an approach. Instead, we use detailed structural mapping and a structural cross-section (Mora et al., 2006) to project the four samples collected in the southwestern part of the Quetame Masssif onto a profile. We relate the samples to a datum which is defined by the angular unconformity at the base of the rift-related Cretaceous sedimentary sequence (Fig. 2.8). The stratigraphic elevation of the samples with respect to this datum is plotted versus the zircon fission-track age. The resulting plot illustrates the approximate position of the base of an exhumed partial annealing zone between sample BV65 ($P(\chi^2)$ equals 0.0; central age = 61.3 ± 6.4 Ma) and sample BV151 ($P(\chi^2) > 5\%$; pooled age = 18.5 ± 1.0 Ma; Table 3.3 and Fig. 2.8c). Furthermore, the total annealing for the ZFT system of the Lower Cretaceous section is also supported by vitrinite reflectance data constraining the maximum post-depositional paleo-temperature of the Lower Cretaceous rift-related rocks. Regional Ro values for the shales of the Macanal Formation along the Eastern Cordillera vary between 3.5% and 5% (e.g., (Toro et al., 2004) and represent maximum paleo-temperatures > 250°C, according to the standard correlation model (Burnham and Sweeney, 1989). Two Ro analyses of samples obtained from the western flank of the Quetame massif (Mora et al., 2008b; location in Fig. 2.3) yielded results similar to the regional trend (Table 3.4, samples VR22 and VR23).

Sample MA13, from the northern part of the Quetame massif, adjacent to the Medina basin, yields a ZFT age of 17.9 ± 1.0 Ma. This age overlaps within 2σ error with the age of the structurally equivalent sample BV 151 from the south (18.5 ± 1.0 Ma). We interpret these early Miocene ZFT ages to represent cooling ages resulting from thrust-induced exhumation of the Quetame massif. However, these ZFT ages postdate the onset of thrust-related exhumation, likely by a small amount, as this information would only be provided by the structurally uppermost rocks just beneath the zircon partial annealing zone. More precise identification of this limit requires more detailed sampling and, ideally, ZFT investigations along near-vertical profiles. However, our results constrain the stratigraphic interval within the upper part of the Macanal Formation along which future studies should be focused.

Early Miocene exhumation and rock uplift in the Quetame massif area contrasts with subsidence in the Medina basin, a few kilometers to the east. Geohistory analysis of the thick

Figure. 2.8: Zircon-fission track data. (a) Geologic map and (b) structural cross section along profile B-B´ (see location also in Fig 3.1) illustrating the location of zircon fission-track samples (red dots) and the unconformity at the base of the Lower Cretaceous sedimentary units (blue line; modified from Mora et al., 2006). (c) Structural elevation – age profile for the analyzed samples. The upper part of the Macanal Formation, between samples BV65 and BV 151, delimits the base of an exhumed partial annealing zone. (d) Radial plots for two samples from the Lower Cretaceous rift-related deposits of the Macanal Formation in the Quetame massif. Sample BV-151 passes chi squared test [$P(\chi 2) > 5\%$; see Galbraith (1981), Green (1981)] and thus represent a single age population. Therefore, the reported pooled age of ca. 18 Ma can be interpreted as reflecting early Miocene, thrust-induced exhumation. Sample BV 65 fails chi squared test, reflecting a mixed age population as a result of only partial annealing.

sedimentary wedge corresponding to the C8-C6 Members of the Carbonera Formation suggests that enhanced tectonic subsidence in the Medina basin started in the early Oligocene. Combined, the thermochronological results help to better constrain the position of the deformation front of the orogenic wedge, which by the early Oligocene coincided with the inverted Servitá fault.

TABLE 2.3: ZIRCON FISSION-TRACK DATA

Sample Number	Long. (W)	Lat. (N)	Elevation (m)	Stratigraphic Age (Ma)	# Grains	U (ppm)	Rho-S (NS)†	Rho-I (NI)†	P(χ2)‡ (%)	Rho-D (ND)§	ZFT age	±1σ
BV 121	73° 57.199′	4° 23.808′	2091	133.2 ± 3.2	26	241	186.495 (4485)	33.515 (806)	0	4.181 (2089)	136.5	13.4
BV 65	73° 55.594′	2382	2382	135.1 ± 5.1	21	212	75.722 (2318)	24.958 (764)	0	3.528 (3388)	61.3	6.4
BV151	73° 54.044′	4° 22.229′	1451	135.1 ± 5.1	46	251	23.600 (2870)	32.464 (3948)	24	4.178 (3924)	18.5	1.0
BV 192	73° 48.015′	4° 16.044′	2224	> 416	34	317	14.717 (1726)	42.174 (4946)	9.3	4.254 (3924)	9.0	0.5
MA13	73° 18.803′	4° 57.516′	1428	138.4 ± 1.8	58	270	25.476 (1835)	38.402 (2766)	44	4.442 (3924)	17.9	1.0

Zircon used for the analysis was concentrated from sandstone samples following conventional heavy liquid and magnetic separation procedures. Individual zircon samples were split into two aliquots and each aliquot etched separately in eutectic mixture of NaOH/KOH at 228°C for periods between 11 and 25 h. Analytical procedures followed the external detector method (Gleadow, 1981). Samples were irradiated at the Oregon State University research reactor. Following irradiation, induced tracks were etched with 40% hydrofluoric acid at 21°C for 45 min. Samples were counted at a magnification of 1600 X (dry objective) using a Leica DMRM microscope with drawing tube located above a digitizing tablet, and a Kinetec ™ computer-controlled strage driven by the FTStage program (Dumitru, 1993). Ages and errors were calculated using the zeta calibration method (Hurford and Green, 1983) with the software Trackkey (Dunkl, 2002), and are reported at the 1σ level. Zeta calibration factor 121.8 ± 5.2 for zircon (CN2 glass; M.Parra)

† RhoS and Rho I are the measured spontaneous and induced tracks density respectively (x 10^5 tracks/cm^2). NS and NI are the number of spontaneous and induced tracks counted for estimating RhoS and RhoI, respectively

‡ (χ2) (%) is the chi-square probability (Galbraith, 1981; Green, 1981). Values greater than 5% are considered to pass this test and represent a single population of ages

§ RhoD is the induced track density measured in the external mica detector attached to CN2 dosimetry glass (x 10^5 tracks/cm^2). ND is the number of induced tracks counted in the mica for estimating RhoD.

2.8 VITRINITE REFLECTANCE

Observed mean Ro values in the Paleocene to Miocene sedimentary rocks of the basin vary between 0.16 and 0.49%, corresponding to maximum paleo-temperatures of up to ~80°C. Interestingly, the results cluster at different ranges when grouped according to basin locality. First, VR values for samples from the western part (Samples VR1 to VR11; Table 2.4) vary between 0.22 and 0.32%, corresponding to temperatures of up to 60°C (Burnham and Sweeney, 1989). No significant differences in maximum paleo-temperature are observed between the lowermost Paleocene and the youngest Miocene samples. Estimated burial temperatures of up to 60°C for sedimentary units as old

as early Paleocene have rather low values considering the maximum overburden of 4 to 5 km, equivalent to the full preserved stratigraphic thickness of the Oligocene to Miocene units younger than the sampled interval. On the other hand, in the eastern part of the Medina basin, younger units corresponding to the upper members of the Carbonera Formation (C6-C3 members; samples VR12-VR21, Table 2.4) yield VR values ranging between 0.35 and 0.45%, corresponding to temperatures of up to 95°C. The results suggest that strata from the eastern part of the Medina basin were subjected to higher burial paleo-temperatures, not only compared to their lateral equivalents but also in comparison to older units to the west, suggesting non-uniform burial across the basin.

TABLE 2.4: VITRINITE REFLECTANCE DATA

Sample number	Stratigraphic level	Lithology	Elevation (m)	Longitude (W)	Latitude (N)	Ro (%)	s.d †	Maximum paleo-temperature (°C)‡
Eastern Medina Basin								
VR1	Guaduas Fm	coal	683	73°13.670′	4°48.545′	0.43	0.03	60-89
VR2	Cuervos Fm	coal	633	73°13.584′	4°48.696′	0.31	0.04	33-57
VR3	Cuervos Fm	coal	624	73°13.466′	4°48.512′	0.28	0.03	<50
VR4	Carbonera Fm. (C8)	coal	624	73°13.458′	4°48.523′	0.28	0.03	<50
VR5	Carbonera Fm. (C8)	coal	621	73°13.429′	4°48.572′	0.30	0.03	31-55
VR6	Carbonera Fm. (C8)	coal	618	73°13.404′	4°48.600′	0.29	0.03	30-52
VR7	Carbonera Fm (C7)	coal	615	73°13.435′	4°48.496′	0.26	0.02	<50
VR8	Lower Guayabo Fm	coal-intraclast	491	73°10.049′	4°45.850′	0.38	0.05	48-77
VR9	Lower Guayabo Fm	coal	455	73°10.409′	4°47.372′	0.26	0.02	<50
VR10	Upper Guayabo Fm	coal	499	73°10.656′	4°47.621′	0.24	0.02	<50
VR11	Upper Guayabo Fm	coal	517	73°10.710′	4°47.664′	0.22	0.04	<50
Western Medina Basin								
VR12	Carbonera Fm (C6)	coal	375	73°04.444′	4°40.725′	0.40	0.03	53-82
VR13	Carbonera Fm (C4)	coal	478	73°18.693′	4°23.850′	0.32	0.03	36-60
VR14	Carbonera Fm (C3)	coal	311	73°18.060′	4°24.757′	0.44	0.05	62-92
VR15	Carbonera Fm (C3)	coal	304	73°18.066′	4°24.767′	0.35	0.04	43-70
VR16	Carbonera Fm (C3)	coal	304	73°18.071′	4°24.776′	0.45	0.03	64-94
VR17	Carbonera Fm (C3)	coal	301	73°18.073′	4°24.817′	0.45	0.04	64-94
VR18	Carbonera Fm (C3)	coal	301	73°18.078′	4°24.830′	0.43	0.04	61-90
VR19	Carbonera Fm (C3)	coal	301	73°18.085′	4°24.863′	0.42	0.03	59-88
VR20	Carbonera Fm (C3)	coal	300	73°18.087′	4°24.921′	0.42	0.03	59-88
VR21	Carbonera Fm (C2)	coal	468	73°08.280′	4°35.846′	0.42	0.05	58-87
Quetame Massif								
VR22	Macanal Fm	shale	1351	73°52.072′	4°19.861′	4.45	0.88	>250
VR23	Macanal Fm	shale	1146	73°20.941′	4°53.215′	3.25	0.42	>250

All samples had 100 VR measurements except VR22, which had 69 measurements
† s.d: standard deviation of VR measurements
‡ Based on Burnham and Sweeney (1989)

Considering the maximum overburden, the estimated maximum paleo-temperatures suggest a mean paleo-geothermal gradient of only ~7 to 9°C/km for the western area (maximum paleo-

temperature = ~60°C; full stratigraphic thickness equals ~4-5 km; present surface temperature equals 25°C), a much lower value than the present geothermal gradient of ~22 °C/km, obtained from oil wells in the proximal foredeep of the Llanos basin (e.g., (Bachu et al., 1995). As suggested for similar foreland settings, such as the southeastern margin of the Puna Plateau in NW Argentina (e.g., (Coutand et al., 2006), two possible scenarios may explain such an extremely low geothermal gradient. Either it could be related to thermal perturbations driven by expulsion of pore fluids during compaction, caused by rapid syntectonic sedimentation (Deming et al., 1990) or the cooling effects of groundwater recharge driven by an adjacent orographic barrier intercepting moisture (e.g., Forster and Smith, 1989). However, the present geothermal gradient of ~22°C in an analogous foredeep setting of the Llanos basin (Bachu et al., 1995) rules out both of these scenarios from having significantly affected the maximum paleo-temperature.

Conversely, uneven burial between the eastern and western sectors of the basin, as suggested by the Ro data, constitutes compelling evidence for earlier incorporation of the western sector of the basin into the fold-and-thrust belt. This earlier deformation prevented the western Medina basin from undergoing further burial beneath the stratigraphic thickness as observed farther east, where VR values suggest greater burial. Thus, a previously subsiding area in the western Medina basin, where the stratigraphic thickness of the C8-C6 members reaches a maximum, became an area of limited accommodation space through structural incorporation into the eastern Andean fold and thrust belt.

2.9 DISCUSSION AND CONCLUSIONS

2.9.1 Late Eocene-Oligocene history of the eastern flank of the Eastern Cordillera

Our dataset provides new insights into different evolutionary stages of a foreland fold and thrust belt, the compartmentalization of the foreland, and the resulting thermal history of the basin. In particular, we furnish new constraints on the propagation of the northern Andes deformation front during the early stages of Cenozoic mountain building in this part of the orogen. A southwesterly sourced lower Oligocene-lower Miocene eastward-thinning syntectonic wedge comprised of the C8-C6 Members of the Carbonera Formation was deposited in the Medina basin during an episode of rapid tectonic subsidence starting at ca. 31 Ma. Rapidly eastward thinning deposits constituting the upper part of this sedimentary wedge change their character in an eastward direction from alluvial to tidal-influenced coastal plain lithofacies. The age at the top of this stratigraphic interval is biostratigraphically constrained at approximately 22 Ma (Ca7-Ca8 palynozones; Figs. 2.4 and 2.6). On the other hand, our ZFT data reveal ongoing early Miocene (ca. 18 Ma) exhumation along the northern termination of the Quetame massif, ~30 km to the west of the Medina basin. ZFT ages determined from different structural levels on the western flank of the Quetame massif and burial estimates from this area based on vitrinite reflectance data suggest that the ~18 Ma ZFT ages obtained from the upper part of the Lower Cretaceous Macanal Formation at least slightly postdate the onset of exhumation. Roughly simultaneous exhumation in the Quetame massif and rapid tectonic subsidence recorded in

the upper portion of the syntectonic sedimentary wedge of the Medina basin thus delineate the position of the orogenic front along the fault system separating the two areas (i.e., the Lengupá-Tesalia fault system) since at least the early Miocene. Furthermore, the apparent disparity between the onset of rapid subsidence at ca. 31 Ma in the Medina basin and the younger initiation of exhumation during the early Miocene in the Quetame massif can be explained by the following scenarios: (1) tectonic loads located west of the Quetame massif triggered the stage of rapid subsidence between ca. 31 Ma and the initial exhumation of the Quetame massif shortly before 18 Ma; (2) tectonic loads that caused such a rapid subsidence were located in the area of the present-day Quetame massif and, hence, a significant lag time of as much as 13 m.y occurred between the emplacement of the thrust loads at ca. 31 Ma and the onset of significant exhumation of the Quetame massif.

Although geodynamic modeling must be conducted to better define the location of the tectonic loads, regional structural and stratigraphic considerations permits to hypothesize about the most favorable among the two scenarios outlined above. Along the axial Eastern Cordillera, an incomplete Cenozoic sedimentary record (see Fig. 2.2) and incomplete palynological sampling prevent a well constrained westward extrapolation of sediment accommodation patterns. West of the Medina basin, the easternmost locality where the Paleogene record has been described is in the Usme syncline, south of the High Plain of Bogotá (Fig. 2.1). There, the Usme Formation comprises 300 m of deltaic deposits (Hoorn et al., 1987) unconformably underlying upper Miocene strata. The available palynological data (Hoorn et al., 1987) reveal that the uppermost 200 m of the Usme Formation correspond to the biozone T08 (early Oligocene, ca. 34 Ma to 31 Ma). In the composite stratigraphic section of the Medina basin, the coeval interval in the C8 Member of the Carbonera Formation is only ~70 m thick and corresponds to the uppermost part of the Eocene-early Oligocene interval that registers limited tectonic subsidence (see Table A1 and Fig. 2.6). These results document faster sediment accumulation and subsidence in the axial part of the Eastern Cordillera than in the eastern foothills and support a scenario of tectonic loading west of the axial part of the Eastern Cordillera prior to 31 Ma. Whether this pattern continued throughout the Oligocene cannot be evaluated due to the incomplete record. However, between the High Plain of Bogotá and the Servitá-Lengupá-Tesalia faults, the structural configuration of the Eastern Cordillera does not involve major faults which could have caused significant tectonic loading (Mora et al, 2006; see also Fig. 2.1). Thus, we favor the second scenario, in which tectonic loading at ca. 31 Ma was generated by slip along the basement-bounding faults of the Quetame massif, which then caused proximal foredeep deposition in the Medina basin. In this context, the absence of observable direct indicators of deformation (i.e., growth strata or unconformities) in the fore- and the backlimbs of the Farallones anticline (Fig. 2.3) could be explained by poor seismic imaging in the steeply dipping, overturned western limb of the Nazareth syncline and/or subsequent erosion resulting from protracted exhumation and uplift along this structure.

However, despite absence of such direct indicators, a combination of observed changes in sedimentary facies, thickness and subsidence patterns in the basin, and the localization of areas with contemporaneous ongoing exhumation enable us to identify the Lengupá-Servitá faults as the most likely locus of the orogenic front since the Early Oligocene. Furthermore, the structural configuration of the Lengupá fault and our paleocurrent data from the syntectonic wedge help place more detailed constraints on the proposed location of the tectonic loads that triggered the earlier phase of subsidence at ca. 31 Ma. The structural cross section across the northern part of the Guavio anticline (Figs. 2.3b and 2.9) reveals that the overturned western margin of the basin corresponds to the forelimb of a fault-propagation anticline associated with the northern termination of the Lengupá fault. However, south of the Gazaunta River, deformation along this thrust sheet has been accommodated by faulting (Fig. 2.3a). This configuration documents a deformation gradient. Nucleation of this fault system appears to have started first in the south, where the fault has attained maximum structural relief. There, pre-Devonian basement rocks have been thrust over Upper Cenozoic strata. In contrast, farther north this fault system only causes folding and the fault has not yet cut the surface. As illustrated in Figure. 2.9, we suggest that rapid subsidence and increased accommodation in the western part of the basin at ca. 31 Ma would have resulted from loading in the hanging wall of the Servitá-Lengupá thrust sheet to the southwest of the basin. This is further supported by paleocurrent data from the C7-C6 members of the Carbonera Formation, which indicate that the main source for these sediments was located to the southwest of the basin. Subsequent deformation within this thrust sheet propagated northward via fault-propagation folding, which incorporated the western part of the sedimentary wedge into the thrust belt (Fig. 2.9). The propagation of the structure is also supported by the northward plunge of the Quetame massif. As a result of these processes, the change from subsidence and burial to folding prevented further thermal maturation of organic matter, as revealed by VR data from the C8 Member of the Carbonera Formation and younger units in the western Medina basin. In this context, a difference of ~13 Ma between the onset of rapid subsidence and the older exhumation ages may result from a combination of (1) an incomplete thermochronologic database preventing precise identification of the onset of exhumation (thus only representing a minimum age for this process) and (2) a potential temporal lag between thrust loading and exhumation, reflecting the period between the onset of range uplift and significant removal of overburden. More detailed thermochronological investigations in the future might resolve this issue.

2.9.2 Migration of the foreland basin system

Our plots of Cenozoic sediment accumulation and tectonic subsidence display a similar three-stage pattern in the SMMV and Medina basins, resulting from two episodes of rapid subsidence separated by an interval of slower subsidence (Figs. 2.7a and 2.7b). In other foreland basins such

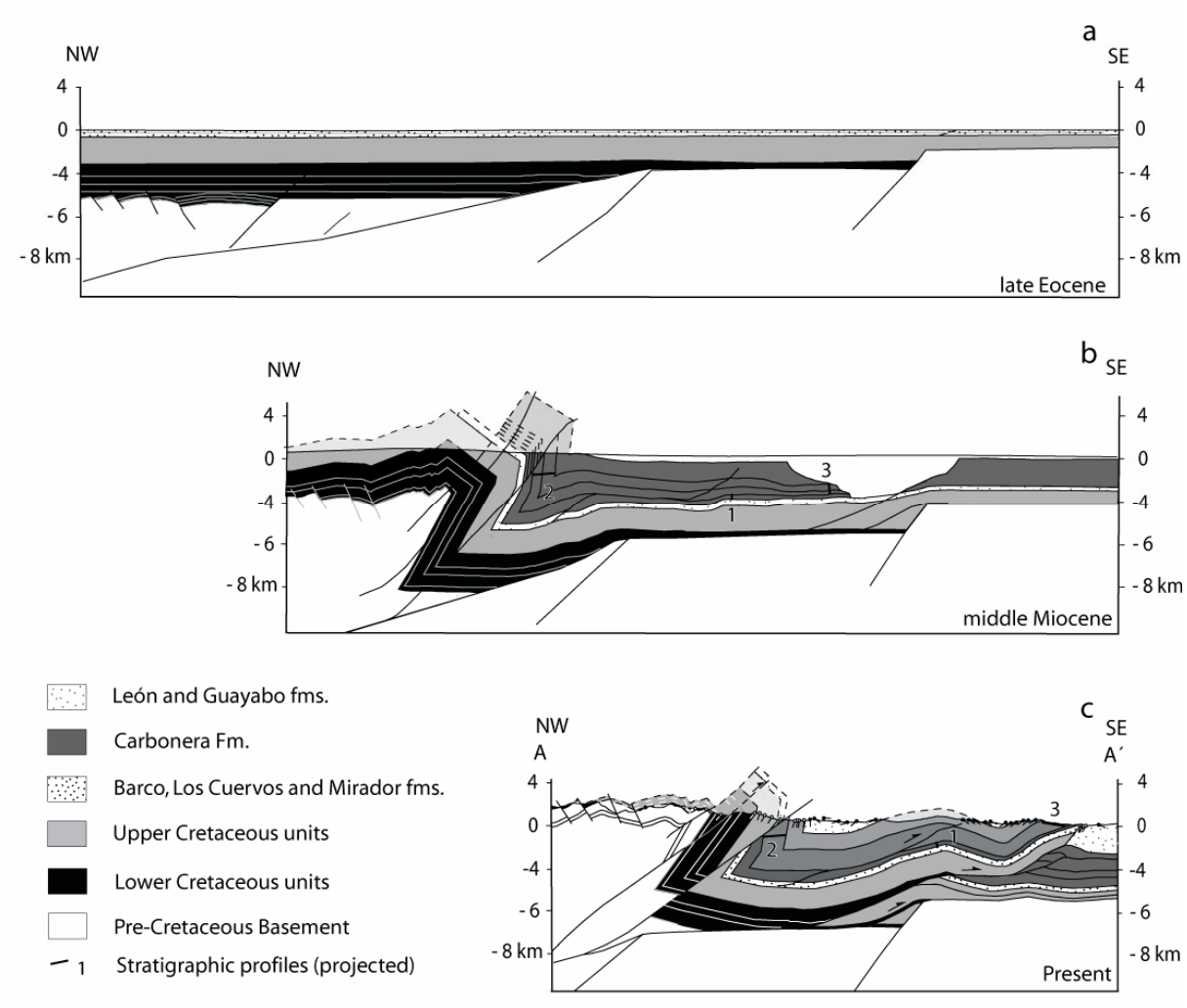

Figure. 2.9: Retrodeformed cross section across the Medina basin during (a) late Eocene, (b) early Miocene time, and (c) present time, respectively (location of cross section in Fig. 2.2). Projected location of stratigraphic sections and samples for vitrinite reflectance and zircon fission-track analysis are indicated for each time slice. Thrust-induced exhumation along of the Quetame massif during early Miocene incorporated the western part of the syntectonic clastic wedge of the Medina basin into the fold-and-thrust belt. This resulted in the interruption of the thermal maturation of strata rich in organic matter in the western Medina basin.

three-stage sigmoidal patterns have been explained by vertical superposition of foreland-basin depozones resulting from redistribution of thrust loads and progradation of the orogenic wedge (DeCelles and Currie, 1996; Horton et al., 2001). In such a scenario, a cratonward migration of the orogenic wedge results in the superposition of the foredeep, forebulge, and back-bulge depozones. Alternatively, orogenward retreat of the foreland system may lead to vertical stacking of distal (i.e., back-bulge and forebulge) over proximal foreland basin depozones (i.e., foredeep and wedge-top). This latter scenario may result from internal thickening of the orogenic wedge via out-of-sequence reactivation of thrusts in the hinterland (e.g., (DeCelles and Giles, 1996), underplating (e.g., Sinclair et al., 1991) or from a decrease in the wavelength of the flexural profile of the basin. Such a decrease can be related to episodic deformation associated with alternating episodes of thrust loading following

tectonic quiescence, erosional unloading (Burbank, 1992; Catuneanu et al., 1998; Flemings and Jordan, 1990) or lateral variations in the rigidity of the flexed plate (Waschbuch and Royden, 1992).

Concerning the late Paleocene episode of rapid subsidence during deposition of the Los Cuervos Formation in the Medina basin, accumulation in a back-bulge depozone can be ruled out in light of the regional distribution of foreland basin deposits. In particular, late Paleocene back-bulge deposition in the Medina basin would imply that a forebulge would have been located to the west of the basin. However, Paleogene subsidence patterns in the SMMV to the west of the basin do not indicate limited accommodation, such as expected in a forebulge depozone. Instead, late Paleocene rapid subsidence in the SMMV basin (Fig. 2.7b) and a thick upper Paleocene sedimentary section in the axial Eastern Cordillera (Cacho Bogotá and Lower and Upper Socha Formations, Fig. 2.2) result from foredeep deposition related to tectonic loading in the Central Cordillera (Gómez et al., 2005; Gómez et al., 2003). We hence suggest that the rapid accumulation recorded by the Los Cuervos deposits in the Medina basin as reflecting deposition in the eastern reaches of this foredeep depozone. However, as noted by Sarmiento-Rojas (2001), minor contribution of remaining thermal subsidence from the Mesozoic rifting event may account for part of the observed rapid tectonic subsidence in the basin. As pointed out by Gomez et al. (2005), eastward onlapping of the late Paleocene Barco and Los Cuervos Formations onto the Cenozoic and Mesozoic substratum of the Llanos basin suggests an increase in the wavelength of the foreland basin (i.e., basin widening; see Figs. 2.2 and 2.10c) that may correlate with a diminished load exerted by the Central Cordillera. The adjustment of the flexural profile of the basin to such episodes of erosional unloading is characterized by an increase in subsidence in the distal foreland basin system (i.e., in the forebulge) that correlates with diminished subsidence or flexural uplift in the foredeep (e.g., Burbank, 1992; Catuneanu et al., 1997; Catuneanu et al., 1998). Although limited, data from the northern part of the Middle Magdalena Valley basin (Pardo-Trujillo et al., 2003) suggest a decrease in sediment accumulation rates toward the top of the upper Paleocene units. This may represent reduction in subsidence within a proximal foredeep coeval with the increase in subsidence rates that allowed the accumulation and eastward onlapping of the Barco and Los Cuervos Formations over more distal foredeep areas previously subjected to erosion in the Llanos basin (Gómez et al., 2005; Fig. 2.10).

We interpret the intermediate stage of reduced accumulation in the Medina basin during the Eocene-early Oligocene (ca. 56 to 31 Ma) by a regional comparison of accommodation patterns across the foreland-basin system. This stage of moderate subsidence rates in the Medina basin is partially coeval with late Paleocene to middle Eocene unconformity development in the Middle Magdalena Valley basin (Gómez et al., 2005; Restrepo-Pace et al., 2004). In the southern part of the SMMVB, such an episode is represented by the flat segment in the subsidence curve (Fig. 2.7b). Subsequent uplift in the western part of the Eastern Cordillera documented by AFT modeling and middle Eocene-Oligocene growth strata in the southern part of the basin also overlaps in time with the episode of limited accommodation recorded by accommodation, subsequent to a late Paleocene episode of rapid

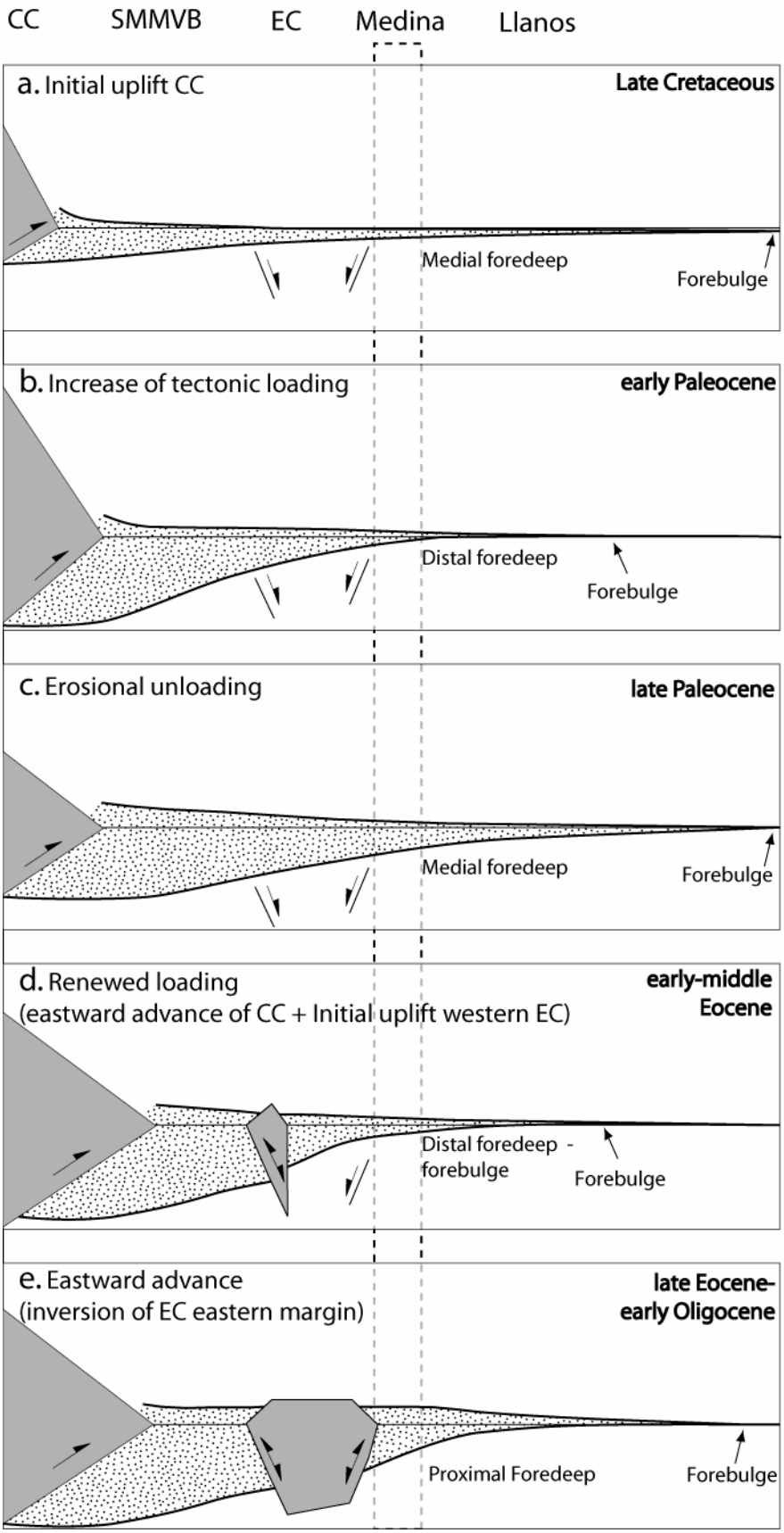

Figure. 2.10: Cartoon illustrating the Maastrichtian-early Oligocene evolution of the foreland basin system in response to uplift of the Central (CC) and Eastern (EC) cordilleras of the Colombian Andes. SMMVB refers to the southern Middle Magdalena Valley basin. See text for discussion.

subsidence that we interpret to have occurred in a foredeep depozone, is compatible with a distal foredeep setting. In this context, we invoke that a reduction in tectonic subsidence reveals an episode of basin narrowing and westward retreat of the foreland-basin system (Fig. 2.10d). Moreover, in the east, the development of an unconformity with an eastward-increasing chronostratigraphic gap beneath the middle Eocene Mirador Formation (Jaramillo et al., 2008) suggests the existence of a forebulge in the Llanos basin at that time. Following the late Paleocene episode of faster subsidence in the course of erosional unloading, limited Eocene accumulation in the eastern foothills can be interpreted as a flexural response of the basin to a renewed episode of thrust loading. This may have resulted from the eastward migration of the Central Cordillera thrust front as well as the onset of thrusting along the western flanks of the Eastern Cordillera (Fig 3.10d). Interestingly, available palynological data from the northern Magdalena Valley basin (Pardo-Trujillo et al., 2003) show a coeval, yet opposite pattern of increased sediment accommodation between the Paleocene and Eocene, which is in line with asymmetric subsidence as a response to renewed thrust loading and basin narrowing. This long-lasting (ca. 25 Ma) episode of slower subsidence and narrowing of the Medina basin may also suggest protracted stationary foredeep and fore-bulge depozones. Such stagnation of the foreland-system may have been the consequence of tectonic loading acting over a less rigid part of the foreland lithosphere (e.g., Waschbusch and Royden, 1992). In this case, the weakened lithosphere could correspond to a pre-strained area affected by Mesozoic rifting, which now delimits the extent of the Eastern Cordillera (Fabre, 1983; Sarmiento-Rojas et al., 2006). However, a comprehensive regional documentation of Cenozoic exhumation patterns and geodynamical modeling is required to further test the validity of these hypotheses.

Finally, the second stage of rapid subsidence in the Medina basin, starting in the early Oligocene, documents proximal foredeep deposition due to loading through initial inversion of the Servitá fault (Figs. 2.9 and 2.10e). This episode thus reveals a stage of basinward migration of the foreland basin system, which involved the reactivation of inherited Cretaceous extensional faults. Moreover, this early initiation of thrusting along the Servitá-Lengupá fault in the early Oligocene documents protracted deformation located along this reactivated fault. This is in line with active thrust-induced exhumation throughout the Miocene, suggested by the ZFT data, and rapid exhumation during the last ~3 Ma, as indicated by apatite fission-track data in the Quetame massif (Mora et al., 2008b). Our data thus provide compelling evidence for the fundamental role exerted by inherited basement anisotropies in accommodating contractional deformation during Cenozoic orogeneis in the northern Andes. The Eastern Cordillera of the Colombian Andes hence constitutes a natural testing ground for numerical models predicting that the locus of active deformation in an orogen is determined to a great extent by weak zones in the crust that accommodate shortening. However, as predicted by Allmendinger et al. (1983), more straightforward time/space patterns of deformation associated with an orogenic wedge may develop in those areas where the role of such anisotropies is

reduced or where pre-existing basin fills provide a much more homogenous material to develop new detachment systems that promote systematic lateral orogenic growth.

In summary, our new data from the Medina basin provide evidence for the initial stages of mountain building and foreland-basin development along the eastern margin of the Eastern Cordillera of the Colombian Andes. Our model of foreland basin development provides a consistent hypothesis for a variety of observations, including the spatiotemporal patterns of subsidence, sediment dispersal in the basin, and exhumation patterns in the hinterland. Our multidisciplinary study has identified the early Eocene to early Miocene locus of deformation and flexural loading in the Eastern Cordillera of the central Colombia Andes, and correlates the response of the foreland basin to the tectonic activity of individual thrust sheets. Our data support previous hypotheses suggesting episodic deformation in this environment as the principal mechanism that controlled foreland dynamics up to late Paleocene time. Likewise, we suggest that this mechanism is gradually replaced by a combination of renewed loading in the Central Cordillera and eastward migration of the deformation front to the western foothills of the Eastern Cordillera during Eocene-early Oligocene time. Finally, approximately 31 m.y. ago, the orogenic front would have shifted eastward and deformation would have been accommodated along an inherited Mesozoic extensional structure. The behavior of the foreland basin of the Colombian Andes thus resembles other foreland regions of the Andean orogen (Carrera et al., 2006; Hain and Strecker, 2008; Hilley et al., 2005; Mon and Salfity, 1995) where predicted patterns of gradual, foreland-directed migration of deformation are modified by the effects of loading of inherited crustal weak zones, whose activation generates a much more complex pattern of thrust-belt evolution.

ACKNOWLEDGMENTS

This research was supported by grants and scholarships from the DAAD (German Academic Exchange Service, Scholarships A/02/11325 and A/01/12054 to M. Parra and A. Mora, respectively), Deutsche Forschungsgemeinschaft (Str 373/19-1 to M. Strecker), funds from the DFG-Leibniz Center for Earth Surface and Climate Studies at Potsdam University, and the Universidad Nacional de Colombia (Beca de Honor to M. Parra). We also thank the Instituto Colombiano del Petróleo and the Smithsonian Tropical Research Institute for financial support. Seismic profiles were kindly provided by the ANH (Agencia Nacional de Hidrocarburos) of Colombia. We thank B. Horton, G. Bayona and C. Uba for discussion that helped improve the manuscript. We also greatly appreciate discussions with A. Kammer and E. López on the Cenozoic stratigraphy of the area. N. Cardozo generously provided us with his program OSXBackstrip for one dimensional backstripping. A. Gómez kindly identified fossils. G. Veloza and R. López are thanked for their assistance in the field. We are grateful for thorough reviews by D. Barbeau, M. Giovanni and E. Gómez, and helpful suggestions by Associate Editor J. Schmitt.

Chapter 3

Episodic orogenic-front migration in the northern Andes: constraints from low-temperature thermochronology in the Eastern Cordillera, Colombia

ABSTRACT

New thermochronometric data from the Eastern Cordillera of the Colombian Andes provide information on the timing of erosional exhumation associated with Cenozoic contractional deformation in this sector of the northern Andes. We present a comprehensive account of exhumation patterns along a 150 km-long, across strike transect between ~4° and 6° N by integrating 29 new apatite fission-track ages and 17 new zircon-fission track ages with sparse published thermochronological data from this area. Diachronous exhumation is documented by an eastward younging of the ages for the onset of thrust-induced cooling. This pattern and regional evaluation of published brittle deformation markers suggest episodic eastward migration of the orogenic front at an average rate of 2.5-2.7 mm/yr during the Late Cretaceous-Cenozoic. We identify three major stages of orogen propagation. First, following initiation of mountain building in the Central Cordillera during the Late Cretaceous, the orogenic front propagated eastward at slow rates (0.5-3.1 mm/yr) until early Eocene times. Such slow orogenic advance would have resulted from limited accretionary flux related to slow and oblique (SW-NE-oriented) convergence of the Farallon and South American plates during that time. A second stage of rapid orogenic advance (4.0-18.0 mm/yr) during middle-late Eocene, and locally of at least 100 mm/yr in the middle Eocene, resulted from initial tectonic inversion of the Eastern Cordillera. By the end of this stage, the central Colombian Andes had achieved ~86% of its actual width. We correlate this episode with an increase in the accretionary flux triggered by acceleration in plate convergence and a rotation of the convergence vector to a more orogen-perpendicular, eastward direction. Finally, stagnation of the Miocene deformation front along former rift-bounding reactivated faults in the eastern flank of the Eastern Cordillera led to a decrease in the rates of orogenic advance. Post-late Miocene-Pliocene thrusting along the actively deforming front of the Eastern Cordillera at this latitude suggests averaged Miocene-Holocene orogen propagation rates of 1.2-2.1 mm/yr. Our data demonstrate that, in the course of changes in plate kinematics, the presence of inherited crustal anisotropies, such as the former rift-bounding faults of the Eastern Cordillera, favor a non-systematic progression of foreland basin deformation through time by preferentially concentrating accommodation of slip and thrust-loading along these zones of weakness.

3.1 INTRODUCTION

The large-scale kinematics of faulting in thrust belts has been successfully reproduced by theoretical and analog models that consider that deformation of such belts resembles that of critically tapered wedges (e.g., Dahlen, 1990; Dahlen and Barr, 1989; Dahlen et al., 1984; Davis et al., 1983; Hoth et al., 2005). These models predict a complex interaction between tectonically accreted mass to the orogen, mass removed by erosion, and the internal strength and frictional resistance along the base of such a wedge. These factors largely determine the geometry and spatiotemporal evolution of deformation in the thrust belt. While successfully applied to isotropic materials (e.g., Dahlen, 1990; DeCelles and Mitra, 1995), the geometry of deformation in thrust belts developed over pre-strained segments of continental crust may be strongly guided by pre-existing anisotropies that absorb and

guide upper crustal deformation (e.g., Allmendinger et al., 1983; Jordan and Allmendinger, 1986; Marshak et al., 2000; Pfiffner et al., 2000). In such an environment, inherited zones of crustal weakness that are favorably oriented with respect to the ambient crustal stresses will fail, resulting in deformation and generation of topography. Such topographic loading may in turn lead to an increase in the lithostatic stresses and subsequent reactivation of other structures in the vicinity (Hilley et al., 2005). The flexural response of the lihosphere to the topographic load exerted by this kind of thick-skinned thrust belt also leads to the formation of a foreland basin (e.g., Jordan, 1981). However, instead of the continuous, laterally extensive basin associated with large-scale thin-skinned thrust belts of other mountain belts, a broken foreland basin is formed where the spatial configuration of the pre-existing anisotropies determine the areal extent and compartmentalization of an otherwise contiguous basin (e.g., Allmendinger et al., 1983; Jordan and Allmendinger, 1986; Strecker et al., 2008). As convergence and deformation progress, a non-systematic, spatially disparate and diachronous pattern of orogenic advance and incorporation of these depocenters into the fold-and-thrust belt is expected for these orogens (e.g., Hilley et al., 2005; Strecker et al., 2008).

The timing and rates of tectonic deformation, uplift, and associated exhumation during orogenesis can be assessed through low-temperature thermochronology in areas where significant amounts of material have been removed from the uplifting ranges either by tectonic processes (e.g., Ring et al., 1999; Stockli, 2005) or protracted, focused erosion (e.g., Batt et al., 2000; Blythe et al., 2007; Mora et al., 2008b; Thiede et al., 2004; Tippett and Kamp, 1993). However, in orogens with moderate exhumation where ancient sedimentary basins are still partially preserved in the orogen interior, erosion may have resulted in a low degree of preservation of critically needed indicators of brittle deformation and rock uplift, such as growth strata or cross-cutting structural relations (e.g., Sobel and Strecker, 2003). In the absence of such indicators, however, quantification of the timing of range uplift relies either on ductile deformation markers (Godin et al., 2001; Hubbard and Harrison, 1989) or on indirect methods, such as reconstructing the subsidence history of adjacent basins (e.g., Echavarría et al., 2003; Jones et al., 2004). The character and timing of basin subsidence can provide first-order proxies for crustal thickening, and potentially rock uplift, in orogens where thrust-related loads are in flexural isostatic equilibrium with the adjacent basin (e.g., Jordan et al., 1988; Sinclair, 1995). On the other hand, direct indicators of brittle deformation and uplift tend to be better preserved in areas with minor to moderate exhumation, especially in sedimentary basins (e.g., Burbank et al., 1992). In these environments, direct quantification of long-term denudation may be limited to the youngest exhumation history of the uppermost crustal levels, whose evolution can only be evaluated through low-temperature thermochronology methods, such as apatite (U-Th)/He (e.g., Bertotti et al., 2006; Crowhurst et al., 2002; Richardson et al., 2008) or apatite fission-track dating, especially when combined with other thermal history indicators such as vitrinite reflectance (Bray et al., 1992; O'Sullivan, 1999). In the case where thermochronometers were not reset during burial, unraveling

older exhumation events often requires indirect, less precise methods, such as inverse modeling of apatite fission-track data (e.g., Steinmann et al., 1999).

Here, we present a case study of late Cretaceous-Cenozoic episodic lateral growth of an inversion orogen in the northern Andes of Central Colombia. In this setting, Cenozoic inversion and moderate exhumation of a Mesozoic rift basin that occupied the area of the present-day Eastern Cordillera between 4°-5°30´ N (Fig. 3.1) offers a unique opportunity to study the style of orogenic growth in a subduction orogen developed over a region of significantly pre-strained crust in a foreland setting. Here, the close proximity of various morphotectonic provinces characterized by different degrees of exhumation over an across-strike distance of only ~150 km, constitutes an ideal, yet poorly studied, natural experimental set-up, where rock uplift and exhumation can be evaluated. These morphotectonic provinces include: (1) a slightly exhumed Cenozoic central fold belt, including the 2.5-km-high intraorogenic Bogotá plateau; (2) the Quetame and Floresta massifs constitute deeply exhumed basement highs located to the east and northeast of the plateau, respectively, where Paleozoic, low- and medium-grade metamorphic continental basement rocks, and Cretaceous rift-related sedimentary rocks were uplifted through contractional reactivation of west-dipping reverse faults (Kammer and Sánchez, 2006; Mora et al., 2008a; Mora et al., 2006); (3) the moderately exhumed Villeta Anticlinorium, located to the west of the Bogotá Plateau, where west-verging reverse faults caused uplift and exhumation of Lower Cretaceous rift-related sedimentary units; and (4) fold-and-thrust belts on either side, involving basins with up to 7 km of Cenozoic foreland deposits.

Available data (see below) on the spatiotemporal tectonic evolution of the northern Andes indicate a Late Cretaceous age for initiation of deformation in the Colombian Andes, in areas that constitute the present-day Central Cordillera (Gómez et al., 2003). A Paleocene-early Oligocene eastward advance of the orogenic front toward the Eastern Cordillera is supported by cross-cutting relationships and growth strata in the western and axial sectors of the Eastern Cordillera (Gómez et al., 2005; Gómez et al., 2003; Restrepo-Pace et al., 2004), and by an increase in tectonic subsidence in basins to the east [(Parra et al., 2008); see Section 3.3]. However, despite this information, little is known about whether deformation was coupled with exhumation, due to the lack of thermochronologic studies constraining the early denudational history. AFT ages and thermal modeling from the western flank of the Eastern Cordillera illustrate an older cooling event that began sometime between 65 and 30 Ma, and a younger cooling episode between 15 and 5 Ma (Gómez, 2001; Gómez et al., 2003; see Table 3.1). On the other hand, published AFT data from the eastern flank of the Eastern Cordillera indicate that (1) exhumation had already begun by ~20 Ma in the Santander Massif (Shagam et al., 1984), and (2) rapid exhumation of 3 to 5 km of crust has been active during the last 3-4 Ma (Mora et al., 2008b). Thus, these data do not furnish information on the earliest exhumation history of the range.

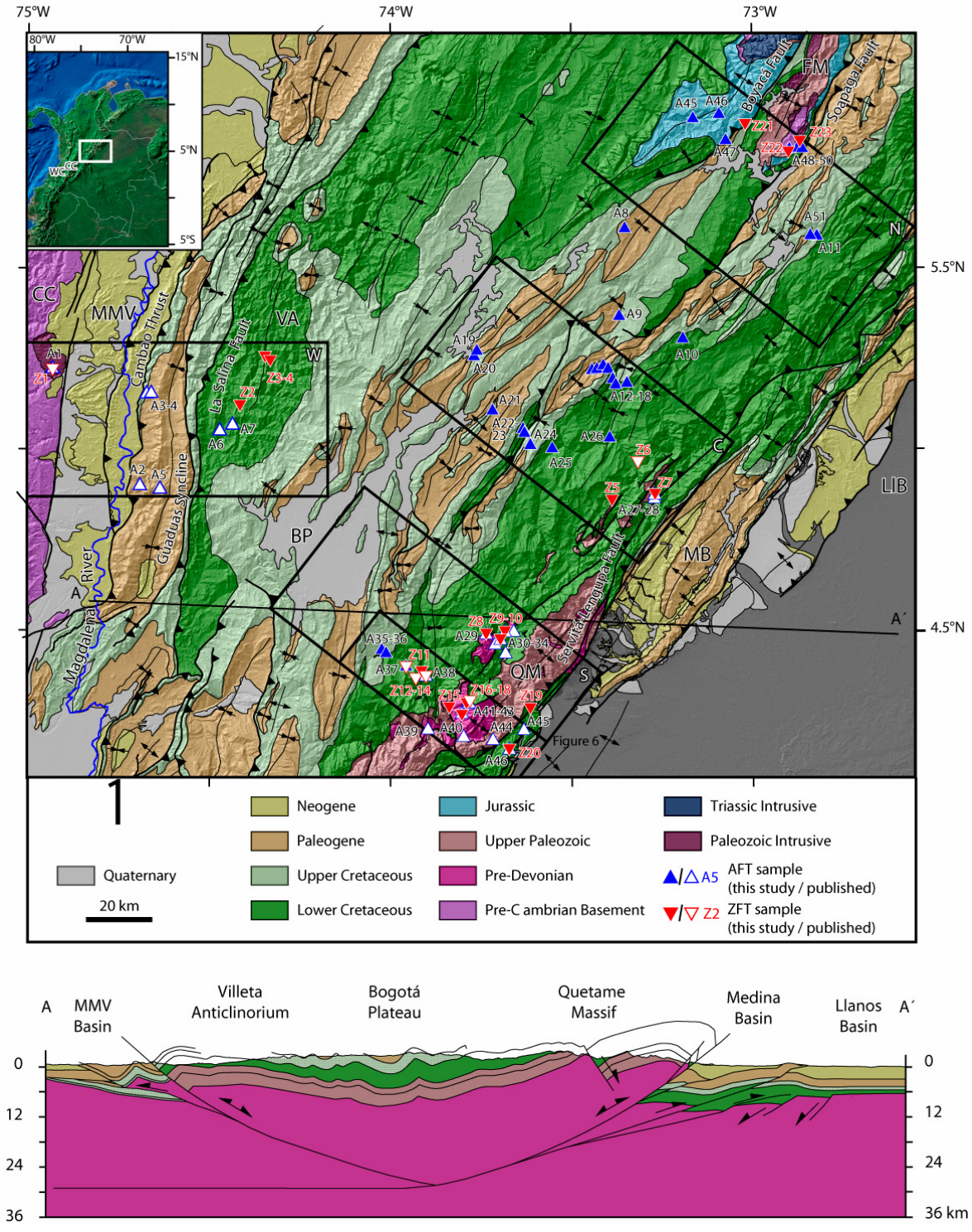

Figure 3.1. **a**. Geologic map of the Eastern Cordillera modified from Gómez et al., (2007), Mora et al., (2006) and Parra et al.; (2008) showing main structures, morphotectonic domains and location of fission-track samples. Symbols: CC – Central Cordillera, MMV – Middle Magdalena Valley Basin, VA – Villeta Anticlinorium, BP – Bogotá Plateau, QM – Quetame Massif, FM – Floresta Massif, MB – Medina Basin. Boxes denote location of four fission-track transects [Western (W), Northern (N) Central (C) and Southern (S) transects] shown in figures 3.3-3.6. **b**. Structural cross section showing the former rift-bounding La Salina and Servitá-Lengupá faults, reactivated as reverse faults during Cenozoic deformation (after Mora et al., 2008b).

In this study, our primary goals are to (1) investigate the spatial and temporal pattern of exhumation in the Eastern Cordillera across a ~150-km-long transect by integrating 46 new AFT and ZFT analyses with published AFT and ZFT data; (2) evaluate the temporal correlation between these exhumation patterns with published direct and indirect indicators of rock uplift throughout the Central and Eastern cordilleras; and (3) correlate the uplift and exhumation patterns with kinematic models for the evolution of the Eastern Cordillera.

3.2 REGIONAL SETTING, STRATIGRAPHY AND TECTONIC EVOLUTION

In the course of an absolute westward movement of the South American Plate over the Pacific ocean basin (Coney and Evenchick, 1994; Russo and Silver, 1996), contractional deformation along the tectonically active northwestern margin of the South American continent results from oblique convergence and accretion of oceanic crust of Pacific affinity since late Cretaceous time (e.g., Cooper et al., 1995; Taboada et al., 2000). Late Cretaceous initial accretion of oceanic crust along the western margin of Ecuador and Colombia (e.g., Kerr and Tarney, 2005; Spikings et al., 2001; Vallejo et al., 2006; Villagómez et al., 2008) triggered initial orogeny in the northern Andes (e.g., McCourt et al., 1984). Regional kinematic reconstructions of the Farallon-Nazca and South American plates illustrate a major change in convergence direction from a N-S to a ~WNW-ESE at ca. 49 Ma (Pilger, 1984; Pardo-Casas and Molnar, 1987). Associated with this kinematic regime, paleostress determinations in the eastern Colombian Andes indicate a coeval shift in the direction of the main horizontal stress, which rotated clockwise from a SW-NE orientation prevailing until early Eocene to a WNW-ESE direction during middle Eocene-Miocene time (Cortés et al., 2005), similar to the neotectonic orientation (Colmenares and Zoback, 2003; Cortés and Angelier, 2005; Dimaté et al., 2003; Mora, 2007; Taboada et al., 2000). The protracted plate convergence along the western margin of South America has generated a Cenozoic orogen in the northern Andes which comprises three NE-SW striking ranges north of 2° N. These include (1) the Western Cordillera, formed by relicts of oceanic basement sliced off an oceanic plateau associated with a Late Cretaceous mantle plume (e.g., Burke, 1988; Kerr and Tarney, 2005); (2) the Central Cordillera, an exhumed, Mesozoic to Recent magmatic arc that intruded Proterozoic and Paleozoic continental basement; and (3) the Eastern Cordillera, an inverted Mesozoic rift with east and west dipping reverse faults, which abuts the foredeep basin that extends eastward toward the Guyana craton (e.g., Cooper et al., 1995).

Structural models illustrate that at ~4-5° N the main range-bounding faults of the Eastern Cordillera merge into a subhorizontal detachment at a depth between 20 and 25 km (e.g., Cortés et al., 2006; Mora et al., 2006; Restrepo-Pace et al., 2004); Fig 3.1b). Mora et al. (2006; 2008b) inferred a mid-crustal detachment in the Eastern Cordillera based on structural area balancing and the presence of a zone of focused seismicity. These authors model the Servitá fault with a listric geometry because of the documented exhumation pattern, which is reminiscent of that simulated for inverted listric normal faults (e.g., Erslev, 1986). Shortening estimates in their model amount to 58 km. However, this

value should be considered as a conservative end-member calculation for the Eastern Cordillera, in contrast to models arguing for higher shortening values (e.g., 150 km, Dengo and Covey, 1993; 200 km, Roeder and Chamberlain, 1995), where the hanging-wall transport above sub-horizontal detachments occurs over longer distances. While the latter mechanism may produce more crustal thickening when multiple crustal-scale sheets are involved, it does not honor most of the observations supporting the listric fault geometry of Mora et al. (2008b).

Along the axial and eastern sectors of the Eastern Cordillera, in the Quetame and Floresta massifs, the exhumed basement constitutes up to ~4 km of low- and medium-grade metamorphic rocks and Paleozoic intermediate to acid intrusives (Segovia, 1965; Ulloa and Rodríguez, 1979; Ulloa and Rodríguez 1982). The disconformably overlying rocks of late Paleozoic age comprise up to ~4 km of a clastic platformal sequence, including the Devonian Tibet, Floresta and Cuche Formations in the Floresta area (Mojica and Villarroel, 1984) and the Devonian to Carboniferous Farallones Group in the Quetame Massif (Ulloa and Rodríguez, 1979). The inverted crust in the Eastern Cordillera has been heavily influenced by Mesozoic rifting. Rifting was associated with two main transtensional events during the Late Triassic-Middle Jurassic, and latest Jurassic-Cretaceous time (e.g., Kammer and Sánchez, 2006; Sarmiento-Rojas et al., 2006). Triassic-Middle Jurassic rift-related accumulation of mainly nonmarine and volcanoclastic sediments occurred in narrow asymmetric graben straddling the western flank of the present-day Eastern Cordillera from the southern Magdalena Basin in the south to the Santa Marta Massif in the north (e.g., Sarmiento-Rojas et al. 2006, and references therein). In the Floresta Massif, at ~ 6°N, a minimum of up to 1.8 km of Lower to Upper Jurassic lacustrine and fluvial sediments with tuffaceous interbeds accumulated within halfgraben basins limited by west-dipping faults (Kammer and Sánchez, 2006). These units comprise the Palermo, Montebel and Rusia Formations in the western hanging wall of the Boyacá fault, and the Girón Formation in the hanging wall of the Soapaga fault (Kammer and Sánchez, 2006; Fig. 3.2). Unlike the narrow geometry of the early Mesozoic depocenters, regional reconstructions of the extent of Lower Cretaceous sediments in the Eastern Cordillera reveal that the second Mesozoic rifting episode generated a wider extensional basin system bounded by the east-dipping La Salina fault system, to the west, and the west-dipping Servitá-Lengupá fault system, to the east (e.g., Mora et al., 2006; Sarmiento-Rojas et al., 2006). Along the footwall of these normal faults, rift shoulder erosion led to the partial or total removal of Paleozoic sequences (e.g., Mora et al., 2006). The resulting paleotopography was preserved beneath Lower Cretaceous shallow marine units, deposited during the active stage of rifting. As a result, drastic facies and thickness changes (4.5-6 km) characterize the Lower Cretaceous sediments (Mora et al., 2008a; Mora et al., 2006; see Fig. 3.2). These units are covered by ~1.5–2 km of Upper Cretaceous units (Une and Chipaque Formations and the Guadalupe Group), deposited during a stage of post-rift thermal subsidence (Sarmiento-Rojas et al., 2006).

Associated with deformation and crustal thickening in the Central Cordillera since the Late Cretaceous, a foreland basin system began to develop east of this range, in areas that include the

present-day Magdalena Valley Basin, the Eastern Cordillera and the Llanos Basin (e.g., Cooper et al., 1995; Gómez et al., 2005). Continued Cenozoic convergence and deformation prompted eastward orogenic growth and caused tectonic inversion of the Mesozoic rift basin (e.g., Bayona et al., 2008; Cooper et al., 1995; Mora et al., 2006; Parra et al., 2008). This initial deformation and uplift in the Eastern Cordillera fragmented the foreland basin, shifted the foredeep eastward to the region occupied by the modern wedge-top basins of the eastern foothills, and ultimately resulted in the formation of intermontane basins in the Bogotá Plateau and the Magdalena Valley (Fig. 3.1). The Cenozoic sedimentary record associated with such foreland basin development comprise a Paleocene to late Miocene coarsening-upward sequence, approximately 6.5 km thick (Fig.3.2). In the Medina Basin, along the eastern foothills of the range (see Fig 3.1 for location), this sequence evolves from coastal plain and tidally-influenced lacustrine deposits of the Barco, Los Cuervos, Mirador, Carbonera and León Formations, to the distal and proximal alluvial deposits of the Guayabo Group (e.g., Cooper et al., 1995; Parra et al., 2008). Paleocurrent directions and sandstone petrography suggest that the main sediment source for the Lower Oligocene to Miocene deposits coincides with the present-day Eastern Cordillera (Bayona et al., 2008; Parra et al., 2008).

3.3 DEFORMATION AND EXHUMATION IN THE CENTRAL AND EASTERN CORDILLERAS

In this section we provide a brief synopsis of available data on the chronology of deformation and exhumation in the central Colombian Andes. This provides the data base that guided us in obtaining additional thermocrhonological data to better understand the early tectonic and depositional history of the Eastern Cordillera region. Provenance data and sedimentary facies distribution along the western fold-and-thrust belt of the Eastern Cordillera and the Magdalena Valley Basin have been used to constrain the onset of contractional deformation of the Central Cordillera to late Cretaceous time (Campanian to Maastrichtian, ~80-65 Ma; Cooper et al., 1995; Gómez et al., 2003; Ramon and Rosero, 2006). Associated with this episode of mountain building, ongoing exhumation since ~ 80 Ma has been documented with a limited number of bedrock apatite and zircon fission-track data from the Central Cordillera (Gómez et al., 2003). To the east of this range, the timing of Cenozoic deformation along a NW-SE transect at 4°-6°N has been determined using various indicators within a biostratigraphically dated foreland-basin record (Bayona et al., 2008; Gómez et al., 2005; Gómez et al., 2003; Parra et al., 2008; Restrepo-Pace et al., 2004). These data illustrate the Cenozoic eastward advance of the deformation front from its late Cretaceous position in the Central Cordillera toward the present-day Eastern Cordillera. First, along its western fold-and-thrust belt, regional biostratigraphic correlation and surface cross-cutting relations provided by an angular unconformity at the base of middle Eocene nonmarine units (Gómez et al., 2003; Restrepo-Pace et al., 2004) constrain the age of initial deformation to late Paleocene -middle Eocene (~56-43 Ma). Second, growth strata imaged on industry-style seismic-reflection profiles along the eastern margin of the Guaduas syncline document initial nucleation of the Villeta Anticlinorium through contractional reactivation of the extensional La

Salina fault system during the middle Eocene-early Oligocene (43-30 Ma; Gómez et al., 2003). Farther east, middle Eocene-lower Oligocene (48-30 Ma) growth strata south of the Bogotá Plateau (Gómez et al., 2005; Julivert, 1963) reflect initial deformation in the axial Eastern Cordillera. Finally, even farther to the east, in the Medina Basin, detailed palynological data document a late Oligocene (~31 Ma) increase in subsidence rates, which has been associated with initial thrust loading in the Eastern Cordillera (Parra et al., 2008).

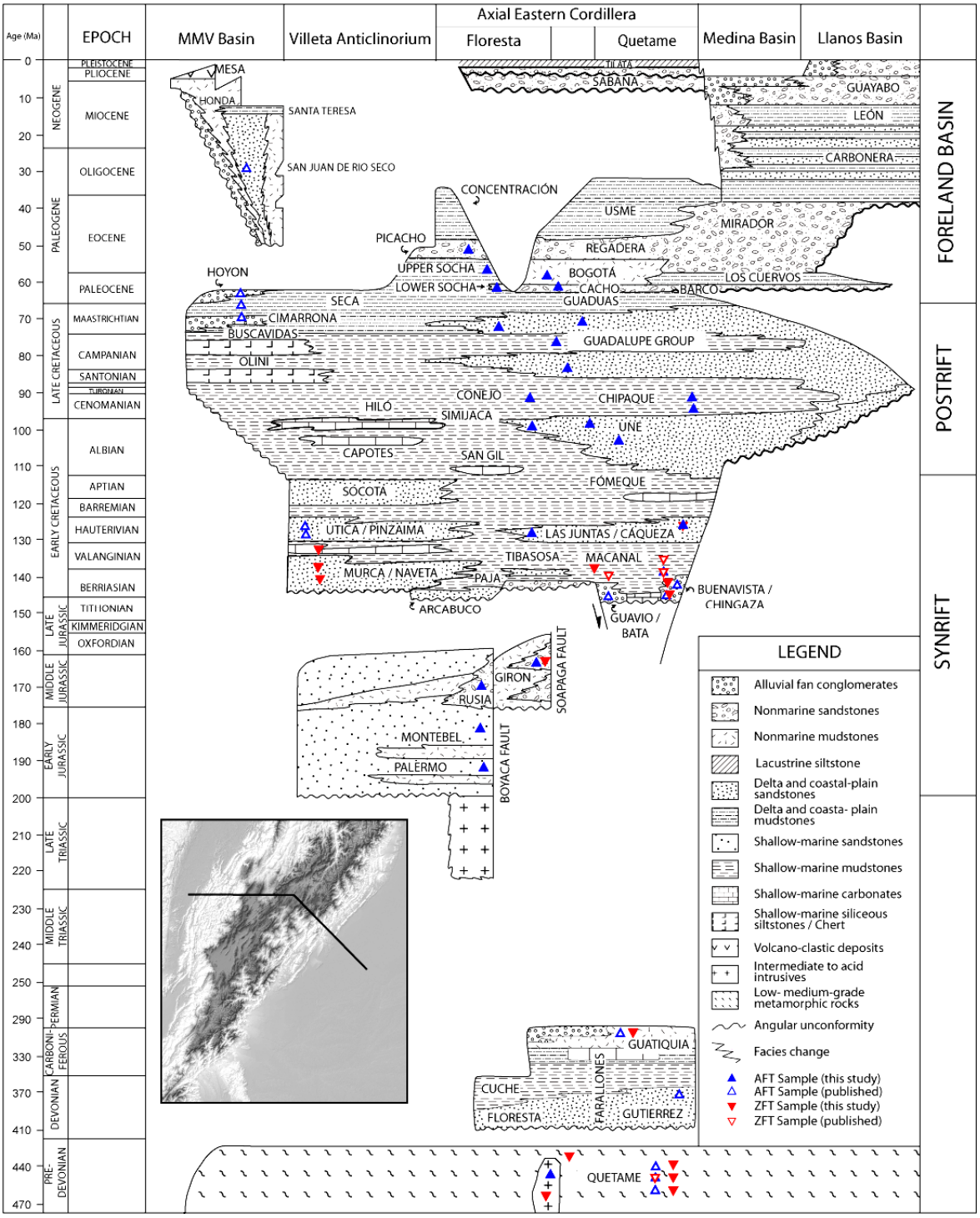

Figure 3.2. Generalized stratigraphy of the western, axial and eastern sectors of Eastern Cordillera. The stratigraphic locations of fission-track samples are indicated.

Despite this regional-scale information on the late Cretaceous-Oligocene spatiotemporal pattern of deformation, details about the Neogene pattern of orogenic growth as well as on the exhumation patterns associated with the eastward advance of the Colombian Andes are poorly known. Published thermochronological data include thermal modeling of apatite fission-track data from the Guaduas syncline, in the Eastern Cordillera´s western foothills, which has been used to suggest initiation of thrust-driven exhumation sometime between 65 and 30 Ma (Gómez et al., 2003). In the Floresta Massif, late Oligocene-early Miocene exhumation has been suggested based on a limited number of AFT ages (Toro, 1990; Toro et al., 2004). Approximately ~100-150 km to the north, in the Santander Massif, AFT ages obtained in Proterozoic and Triassic intrusives are as old as 20 Ma, suggesting that exhumation in the axial sector and eastern margin of the Eastern Cordillera had already begun in the early Miocene (Shagam et al., 1984). Finally, in the Quetame Massif, AFT ages younger than 4 Ma reveal rapid Pliocene-Pleistocene exhumation (Mora et al., 2008b).

These available thermochronological data provide an initial, yet incomplete picture of the exhumation of the range. This is particularly the case in the axial and eastern sectors, where the age for initiation of thrust-induced exhumation is unknown.

3.4 METHODS

In order to unravel the early exhumation history of the Eastern Cordillera we employed apatite and zircon fission-track thermochronology (AFT and ZFT, respectively). Fission-track dating exploits the thermally sensitive accumulation of linear damage trails (i.e., fission tracks) in the crystal lattice of uranium-rich minerals due to the spontaneous nuclear fission of ^{238}U nuclei (e.g., Tagami and O'Sullivan, 2005). Apatite fission-tracks are formed with a nearly constant track length. The range of temperatures at which tracks are progressively shortened defines the partial-annealing zone (PAZ), typically corresponding to ~60° - 110-140°C (e.g., Ketcham et al., 1999). The upper temperature limit of the PAZ, referred as to the total annealing temperature, depends on the cooling rate and has been shown to correlate with both the chemical composition of the apatites (e.g., Gleadow et al., 1986) and the etching parameter Dpar (Donelick et al., 1999; Donelick et al., 2005; Ketcham et al., 1999). Commonly, apatites with larger Dpar are chlorine rich and anneal at higher temperatures (Donelick et al., 2005). The distribution of track lengths provides information on the portion of the cooling history that the sample has experienced within the PAZ. A full reconstruction of the thermal history of a sample based on AFT data is thus achieved by inverse modeling of time-temperature (*t-T*) paths based on grain-age, track-lengths and kinetic parameters (chlorine content or Dpar; e.g., (Ketcham, 2005), as well as additional constraints based on the geology of the study area. In the case of sedimentary samples, such additional information usually includes depositional age and, when available, proxies for maximum burial temperatures such as vitrinite reflectance (e.g., Burnham and Sweeney, 1989) or ZFT data. In the case of ZFT, the fission-track annealing kinetics largely depends on the degree of radiation damage of zircon crystals (Garver et al., 2005; Rahn et al., 2004). Accordingly, estimates of

the total annealing temperature for ZFT are in the range of 250 ± 40 °C (e.g., Bernet and Garver, 2005; Brandon et al., 1998).

In the Eastern Cordillera of Colombia, spatially uneven burial related to the Mesozoic rifting history caused laterally variable peak burial temperatures. Our sampling strategy was guided by paleoburial-temperature estimates derived from published vitrinite reflectance (Ro) analyses (Table B2). In the axial part of the Eastern Cordillera at the latitude of our transect, vitrinite reflectance (Ro) values of 0.6-0.7 % occur in the Upper Cretaceous sedimentary units (Guadalupe Group). For normal heating rates of 1°-5°C/Myr, these Ro values are equivalent to the total annealing temperatures of the AFT system according to the kinetic model of Burnham and Sweeney (1989). Within the Lower Cretaceous synrift sediments of the Macanal Formation, ~ 5-6 km deeper within the stratigraphic section, Ro values > 3.5% indicate maximum burial temperatures corresponding to the total annealing temperature for ZFT. Consequently, in order to decipher the Cenozoic exhumation patterns in the central sector of the mountain range, we conducted AFT analysis of 29 samples, mostly from sedimentary rocks ranging in age from Jurassic to Paleocene. AFT ages were obtained by Apatite to Zircon, Inc., using the LA-ICPMS method (see Appendix B). In addition, we present ZFT data from 17 samples collected in the Villeta Anticlinorium and the Quetame Massif from pre-Devonian low-grade meta-arenites and sedimentary units ranging in age from Upper Paleozoic to Lower Cretaceous (Figs 3.1 and 3.2). ZFT analyses were conducted at the University of Potsdam, following the external detector method (Gleadow, 1981). Based on individual grain-age distributions, we differentiate concordant (*discordant*) ages for samples that pass (*fail*) the $\chi 2$ test (Galbraith, 1981; Green, 1981). FT age errors are reported at 68% confidence. Further analytical details for the AFT and ZFT measurements are described in Appendix B.

Our dataset includes samples that were exhumed from both above and below the depths of total annealing temperatures for the AFT and ZFT systems. For each thermochronological system, we identify samples that were above such an isotherm, and hence resided within the PAZ prior to Cenozoic exhumation, by integrating data on (1) paleoburial temperatures based on vitrinite reflectance, (2) the comparison between cooling and depositional ages, (3) the statistical distribution of individual grain ages (concordant vs. discordant ages according to the $\chi 2$ test, e.g., Galbraith, 1981; Green, 1981), and (4) the distribution of FT ages with respect to burial depth, as indicated by the stratigraphic depth of the samples (e.g., Brandon et al., 1998; O'Sullivan and Wallace, 2002). Following these criteria, we identify three types of FT ages. (1) Reset ages result from samples that attained peak burial temperatures hotter than the total annealing isotherm before the last cooling event; reset cooling ages are younger than depositional ages and, depending on the homogeneity in the annealing properties of the mineral, may be concordant [$P(\chi 2) > 5\%$] or discordant [$P(\chi 2) < 5\%$]. (2) Partially reset ages occur in samples with peak burial temperatures similar to or cooler than the total annealing temperature, thus indicating exhumation from within the fission track PAZ. Partially reset cooling ages may overlap with depositional age and may be concordant or discordant. Partially reset

ages have no direct geological meaning since they reflect the penultimate cooling event modified by partial annealing. Finally, (3) detrital ages are obtained from samples with burial temperatures similar to or less than the lower temperature limit of the PAZ and thus preserved an inherited age from the source area. Detrital ages are distinguished by having a cooling age significantly older than the depositional age and are usually discordant.

In order to extract cooling histories from AFT partially reset and detrital samples, we modeled AFT ages, track-lengths and kinetic data following the annealing kinetic model of Ketcham et al. (2007b) implemented in the program HeFTy (Ketcham, 2005). We present thermal models for three Paleocene and one Upper Cretaceous samples from the moderately exhumed areas in the axial sector of the range. In addition, we include one partially reset Upper Cretaceous sample presented by Gómez (2001) in our thermal history modeling. Finally, we also modeled AFT data for two reset samples with available peak burial temperature estimates. For these reset samples, thermal modeling extrapolates back in time the cooling patterns allowed by the AFT data in the younger (cooler) portion of the *t-T* path, in order to investigate the approximate age for initiation of cooling. Further analytical details for AFT thermal modeling are described in detail in Appendix B.

3.5 THERMOCHRONOLOGY

We present results from 29 new AFT samples and 17 new ZFT age determinations from samples collected from a wide range of elevations, mostly from sedimentary units, across the Eastern Cordillera (see Fig. 3.1 and Tables 3.2 and 3.3). In order to provide a more regionally meaningful evaluation of the exhumation patterns, we integrate our new data with 24 published AFT and 6 published ZFT ages from areas to the east of the Central Cordillera at a similar latitude (Gómez, 2001; Gómez et al., 2003; Mora et al., 2008b; Parra et al., 2008). For clarity, we subdivided this thermochronological dataset into four transects: the western, northern, central, and southern transects (Fig. 3.1). Raw data and methodology details for the published AFT analyses are presented in Table 3.1. Also, available vitrinite reflectance (Ro) data used to constrain peak burial temperatures are shown in Table B2. In the following section we present the results and interpretations according to the different morphotectonic provinces, moving eastward from the Central Cordillera and Middle Magdalena Valley basin to the Villeta Anticlinorium, the axial Eastern Cordillera, and finally the Quetame Massif.

3.5.1 Central Cordillera and Magdalena Valley Basin

Thermochronological data from the Central Cordillera at the latitude of our transect are sparse. Gómez et al (2003) reported a ZFT age of 77.6 ± 3.9 Ma and an AFT age of 32.0 ± 3.1 Ma from a granodioritic pluton from the eastern Central Cordillera (Samples Z01, A01; Fig. 3.3a, Table 3.1).

TABLE 3.1 Published fission-track data used in this study

ID #	Sample Number	Long (W)	Lat (N)	Elev. (m)	Unit	Strat. Age (Ma)	# Gr	U (ppm)	Rho-S (NS) [a]	Rho-I (NI) [a]	Rho-D (ND) [b]	P(χ2) (%) [c]	Age (Ma) [d]	±1 σ error	Dpar (μm)	Cl (%wt)	±1 σ	#	Length (μm)	error (μm)	1s	# length	Data Source [e]
Apatite fission-track data																							
Western Transect																							
A01	MIGN-1	74° 55.723′	5° 13.455′	737	Mariquita Stock	-	20	31	1.70 (150)	3.00 (1322)	11.86 (4472)	80.0	**31.8**	**3.1**	-	-	-	-	-	-	-	-	1
A02	660-40	74° 40.006′	5° 9.292′	443	Cimarrona Fm	70 ± 5	20	6	1.914 (96)	8.334 (418)	14.74 (2277)	16.0	**66.2**	**7.7**	-	0.78	0.27	20	11.73	0.34	2.43	50	1
A03	660-41	74° 39.494′	5° 9.279′	598	Seca Fm.	65 ± 2	20	5	1.482 (57)	6.996 (269)	14.84 (2277)	90.0	**61.5**	**9.1**	-	0.63	0.19	20	11.72	0.35	1.47	18	1
A04	660-43	74° 41.335′	4° 53.946′	578	Hoyon Fm.	60 ± 4	20	13	1.547 (51)	17.65 (582)	15.02 (2350)	42.0	**25.8**	**3.8**	-	0.52	0.45	20	10.75	0.94	3.86	17	1
A05	660-49	74° 37.902′	4° 53.326′	1515	San Juan Rio Seco Fm.	31 ± 5	20	16	0.879 (29)	21.20 (699)	14.93 (2250)	15.0	**12.2**	**2.3**	-	0.06	0.15	20	-	-	-	-	1
A06	726-25	74° 28.067′	5° 3.034′	979	Útica Fm	144 ± 2	20	42	1.01 (36)	47.76 (1698)	12.96 (2063)	< 1	**6.6**	**1.8**	-	0.14	0.21	20	12.36	2.17	4.85	5	1
A07	726-24	74° 26.000′	5° 4.000′	847	Pinzaima Fm	138 ± 3	18	10	0.36 (7)	11.52 (224)	12.89 (2063)	72.0	**7.9**	**3.0**	-	0.06	0.14	18	11.57	-	-	1	1
Central Transect																							
A27	MA18	73° 16.075′	4° 51.844′	851	Bata Fm.	138 ± 2	24	30.5	0.234 (15)	33.20 (2132)	1.360 (5557)	9.5	**1.7**	**0.4**	2.35	-	0.30	36	-	-	-	-	2
A28	MA16	73° 16.035′	4° 52.393′	990	Farallones Gr.	388 ± 28	21	34.7	0.334 (38)	38.20 (4349)	1.378 (5557)	13.8	**2.2**	**0.4**	2.46	-	0.24	28	-	-	-	-	2
Southern Transect																							
A29	FT-1	73° 43.870′	4° 29.308′	3660	Chingaza Fm.	143 ± 2	20	37	0.422 (12)	35.34 (1006)	1.193 (4850)	6.2	**2.7**	**0.7**	2.33	-	0.33	6	-	-	-	-	3
A30	FT-6	73° 42.500′	4° 27.591′	2866	Quetame Gr.	>416	30	45.7	0.492 (14)	45.93 (1307)	1.263 (5089)	79.0	**2.4**	**0.7**	2.01	-	0.26	9	-	-	-	-	3
A31	SJ-5	73° 41.586′	4° 28.296′	2251	Quetame Gr.	>416	20	26.3	0.216 (15)	29.17 (2022)	1.388 (5748)	0.0	**2.3**	**0.8**	2.46	-	0.11	7	-	-	-	-	3
A32	SJ-1	73° 40.851′	4° 29.628′	2748	Quetame Gr.	>416	21	38.6	0.474 (48)	44.17 (4470)	1.432 (5748)	35.6	**2.8**	**0.4**	2.33	-	0.12	31	-	-	-	-	3
A33	SJ-3	73° 39.416′	4° 29.695′	1893	Buenavista Fm.	143 ± 2	30	28	0.948 (9)	31.54 (2995)	1.406 (5748)	97.7	**0.8**	**0.3**	2.41	-	0.25	2	-	-	-	-	3
A34	SJ-2a	73° 40.809′	4° 25.822′	1630	Macanal Fm.	135 ± 5	27	31.4	0.170 (10)	35.64 (2092)	1.419 (5748)	54.5	**1.2**	**0.4**	2.39	-	0.17	5	-	-	-	-	3
A38	BV-151	73° 54.044′	4° 22.229′	1451	Macanal Fm.	135 ± 5	29	29.4	0.495 (31)	28.50 (1784)	1.213 (4926)	49.7	**3.8**	**0.7**	2.28	-	0.19	12	-	-	-	-	3
A39	BV-90	73° 53.628′	4° 13.507′	1446	Quetame Gr.	>416	40	37	0.452 (54)	36.03 (4307)	1.217 (4926)	74.2	**2.8**	**0.4**	2.6	-	0.23	55	-	-	-	-	3
A40	BV-423	73° 48.015′	4° 16.044′	942	Quetame Gr.	>416	30	47.5	0.334 (13)	45.30 (1762)	1.193 (4926)	97.8	**1.6**	**0.4**	2.11	-	0.18	7	-	-	-	-	3
A41	BV-192	73° 47.705′	4° 12.171′	2224	Quetame Gr.	>416	30	30.8	0.312 (16)	35.98 (1845)	1.460 (5089)	57.9	**2.3**	**0.6**	2.18	-	0.29	9	-	-	-	-	3

TABLE 3.1 Published fission-track data used in this study (continued from previous page)

ID #	Sample Number	Long (W)	Lat (N)	Elev. (m)	Unit	Strat. Age (Ma)	# Gr	U (ppm)	Rho-S (NS) [a]	Rho-I (NI) [a]	Rho-D (ND) [b]	P(χ2) (%) [c]	Age (Ma) [d]	±1 σ error	Dpar (μm)	Cl (%wt)	±1 σ	#	Length (μm)	error (μm)	1s	# length	Data Source [e]
A27	MA18	73° 16.075′	4° 51.844′	851	Bata Fm.	138 ± 2	24	30.5	0.234 (15)	33.20 (2132)	1.360 (5557)	9.5	**1.7**	**0.4**	2.35	-	0.30	36	-	-	-	-	2
A28	MA16	73° 16.035′	4° 52.393′	990	Farallones Gr.	388 ± 28	21	34.7	0.334 (38)	38.20 (4349)	1.378 (5557)	13.8	**2.2**	**0.4**	2.46	-	0.24	28	-	-	-	-	2
Southern Transect																							
A42	BV-196	73° 47.002′	4° 17.550′	2862	Quetame Gr.	>416	20	26.8	0.305 (6)	26.05 (513)	1.214 (5089)	86.0	**2.6**	**1.1**	1.89	-	0.15	5	-	-	-	-	3
A43	BV-195	73° 46.969′	4° 17.599′	2905	Quetame Gr.	>416	30	36.7	0.416 (24)	36.40 (2101)	1.239 (5089)	76.6	**2.6**	**0.5**	2.04	-	0.27	14	-	-	-	-	3
A44	WPT	73° 42.743′	4° 11.772′	857	Farallones Gr.	388 ± 28	10	12.6	0.163 (2)	12.05 (148)	1.195 (4850)	86.8	**2.9**	**2.1**	-	-	-	-	-	-	-	-	3
A45	BV-279	73° 40.141′	4° 9.743′	870	Buenavista Fm.	143 ± 2	40	29.3	0.338 (75)	28.06 (6228)	1.198 (4926)	15.7	**2.6**	**0.3**	2.48		0.2	36					3
A46	BV-427	73° 38.682′	4° 11.916′	617	Buenavista Fm.	143 ± 2	30	20.6	0.272 (56)	22.77 (4695)	1.195 (4850)	41.2	**3.0**	**0.4**	2.61		0.36	35					3
Zircon fission-track data																							
Western Transect																							
Z01	MIGN-1	74° 55.723′	5° 13.455′	737	Mariquita Stock	-	20	759	103.1 (2911)	17.18 (2425)	2.90 (4010)	70.0	**77.6**	**3.9**	-	-	-	-	-	-	-	-	1
Central Transect																							
Z06	MA 13	73° 18.803′	4° 57.516′	1428	Macanal Fm.	138.4 ± 1.8	58	270	25.476 (1835)	38.402 (2766)	4.4423 (3924)	44.0	**17.9**	**1.0**	-	-	-	-	-	-	-	-	4
Southern Transect																							
Z11	BV 121	73° 57.199′	4° 23.808′	2090	Caqueza Fm.	133.2 ± 3.2	26	241	186.495	33.515 (806)	4.1814 (2089)	0.0	**136.5**	**13.4**	-	-	-	-	-	-	-	-	4
Z12	BV 65	73° 55.594′	4° 21.760′	2382	Macanal Fm	135.1 ± 5.1	21	212	75.722 (2318)	24.958 (764)	3.5283 (3388)	0.0	**61.3**	**6.4**	-	-	-	-	-	-	-	-	4
Z14	BV 151	73° 54.044′	4° 22.229′	1451	Macanal Fm.	135.1 ± 5.1	46	251	23.600 (2870)	32.464 (3948)	4.178 (3924)	24.3	**18.5**	**1.0**	-	-	-	-	-	-	-	-	4
Z16	BV 192	73° 48.015′	4° 16.044′	2224	Quetame Gr.	> 416	34	317	14.717 (1726)	42.174 (4946)	4.2541 (3924)	9.3	**9.0**	**0.5**	-	-	-	-	-	-	-	-	4

[a] RhoS and Rho I are the spontaneous and induced tracks density measured, respectively (x 10^5 tracks/cm^2). NS and NI are the number of spontaneous and induced tracks counted for estimating RhoS and RhoI, respectively

[b] RhoD is the induced track density measured in the external mica detector attached to CN2 dosimetry glass (x 105 tracks/cm2). ND is the number of induced tracks counted in the mica for estimating RhoD.

[c] (χ2) (%) is the chi-square probability (Galbraith, 1981; Green, 1981). Values greater than 5% are considered to pass this test and represent a single population of ages

[d] Pooled (central) age reported for ages that pass (fail) the χ2 test

[e] 1 - Gómez (2001); 2 - Mora (2007); 3 - Mora et al (2008); 3 - Parra et al. (2008)

TABLE 3.2: Apatite fission-track data

ID #	Sample Number	Long (W)	Lat (N)	Elev. (m)	Unit	Strat. Age (Ma)	# Gr.	NS	$\Sigma(P\Omega)$ (cm^2)	$1\sigma\ \Sigma(P\Omega)$ (cm2)	ξ_{MS}	$1\sigma\ \xi_{MS}$	^{43}Ca	^{238}U	$P(\chi2)$ [c]	**Age (Ma)**	**± 1 σ error**	Dpar (μm)	± 1 s	#	Length (μm)	error (μm)	Stdev (μm)	# length
Northern Transect																								
A11	RW-2	72° 49.084′	5° 35.167′	3096	Chipaque Fm.	88 ± 5	**30**	55	2.21E-05	1.51E-07	1.17E+01	3.32E-01	3.89E-02	1.01E-01	0.0%	**14.1**	**2.0**	1.62	0.17	30	13.71	0.54	1.52	9
A45	RG 05	73° 9.719′	5° 54.630′	2600	Palermo Fm.	188 ± 12	**13**	40	2.63E-05	6.73E-07	1.38E+01	4.93E-01	3.81E-02	9.40E-03	7.5%	**10.5**	**1.7**	1.50	0.27	12	12.73	1.22	1.73	3
A46	RG 04	73° 5.294′	5° 55.501′	3574	Montebel Fm.	168 ± 7	**38**	77	3.63E-05	1.35E-07	1.59E+01	3.94E-01	3.48E-02	4.63E-02	76.5%	**19.9**	**2.1**	1.59	0.15	37	13.61	0.22	1.6	53
A47	RG 01	73° 4.255′	5° 50.999′	2911	Rusia Fm.	154 ± 8	**14**	25	1.89E-05	1.25E-07	1.60E+01	4.06E-01	3.73E-02	9.29E-02	15.5%	**10.6**	**2.1**	1.57	0.26	13	14.12	0.43	1.23	9
A48	AM 12	72° 53.717′	5° 49.446′	2541	Busbanza Gneiss	>542	**31**	29	1.46E-05	7.90E-08	1.61E+01	4.16E-01	2.73E-02	4.32E-02	72.8%	**16.0**	**3.0**	1.59	0.15	30	13.89	0.21	1.55	55
A49	AM 10	72° 52.061′	5° 49.948′	2542	Girón Fm.	161 ± 15	**33**	108	4.45E-05	2.34E-07	1.63E+01	4.33E-01	3.78E-02	2.31E-01	3.4%	**19.8**	**2.0**	1.66	0.23	32	14.22	0.19	1.42	54
A50	AM 09	72° 51.608′	5° 49.699′	2525	Une Fm.	103 ± 9	**30**	162	5.21E-05	2.34E-07	1.66E+01	4.52E-01	2.68E-02	4.78E-02	5.6%	**25.9**	**2.2**	1.59	0.20	74	12.91	0.21	1.84	75
A51	RW 3b	72° 50.293′	5° 35.348′	3330	Guadalupe Gr.	68 ± 3	**18**	60	3.66E-05	3.49E-07	1.16E+01	3.21E-01	4.77E-02	4.60E-02	0.0%	**9.6**	**2.5**	1.53	0.22	17	12.66	0.62	1.64	8
Central Transect																								
A08	RG-06	73° 20.907′	5° 36.650′	3121	Bogotá Fm.	54 ± 5	18	291	4.27E-05	6.65E-07	1.38E+01	4.79E-01	3.53E-02	4.94E-03	0.0%	**46.8**	**3.3**	1.51	0.13	17	13.50	0.82	2.58	11
A09	M4-04	73° 21.874′	5° 22.084′	2147	Lower Socha Fm.	59 ± 3	40	614	4.78E-05	3.59E-07	1.15E+01	3.04E-01	3.42E-02	8.22E-03	11.3%	**73.2**	**3.6**	2.60	0.52	40	14.18	0.1	1.47	203
A10	T4-032	73° 11.008′	5° 18.428′	1815	Une Fm.	103 ± 9	38	51	4.42E-05	2.54E-07	1.14E+01	2.92E-01	4.12E-02	1.86E-02	97.9%	**6.6**	**0.9**	1.71	0.39	38	13.00	0.48	2.05	19
A12	AM-01	73° 26.273′	5° 13.112′	2097	Picacho Fm.	46 ± 2	13	51	3.81E-05	5.06E-07	1.75E+01	5.23E-01	2.72E-02	8.32E-02	0.0%	**11.7**	**1.7**	1.59	0.22	12	12.90	0.53	2.05	16
A13	AM-03	73° 25.517′	5° 13.244′	2025	Upper Socha Fm.	54 ± 5	37	134	3.03E-05	1.80E-07	1.74E+01	5.14E-01	1.43E-02	6.39E-02	0.0%	**38.3**	**3.5**	2.15	0.49	35	13.53	0.14	1.79	156
A14	AM-04	73° 24.472′	5° 13.808′	1901	Upper Socha Fm.	54 ± 5	37	297	4.84E-05	2.11E-07	1.72E+01	4.99E-01	1.97E-02	2.13E-02	2.5%	**52.5**	**3.4**	2.55	0.47	34	13.19	0.16	2.05	163
A15	AM-05	73° 23.723′	5° 13.260′	1928	Guadalupe Gr.	68 ± 3	25	63	2.52E-05	1.01E-07	1.70E+01	4.88E-01	3.67E-02	1.64E-01	0.0%	**21.2**	**2.7**	1.68	0.3	24	13.03	0.37	2.05	32
A16	AM-06	73° 22.921′	5° 11.569′	1711	Une Fm.	103 ± 9	35	14	2.22E-05	1.06E-07	1.68E+01	4.72E-01	2.35E-02	5.44E-02	0.0%	**5.3**	**1.4**	1.54	0.16	28	12.06	0.66	1.63	7
A17	T3-004	73° 22.463′	5° 10.754′	1884	Une Fm.	103 ± 9	24	62	4.55E-05	2.93E-07	1.53E+01	3.49E-01	2.96E-02	1.34E-02	45.3%	**10.4**	**1.3**	1.60	0.2	23	11.96	0.35	1.91	30
A18	T3-003	73° 20.562′	5° 11.039′	2396	Une Fm.	103 ± 9	12	13	9.78E-06	1.11E-07	1.54E+01	3.57E-01	2.47E-02	4.75E-02	95.0%	**10.2**	**2.8**	1.69	0.19	11	9.67	1.21	3.21	8
A19	RG-16	73° 45.493′	5° 16.269′	2595	Upper Socha Fm.	54 ± 5	39	595	1.01E-04	4.95E-07	1.57E+01	3.79E-01	2.68E-02	3.40E-02	0.3%	**45.9**	**2.2**	1.88	0.23	35	12.74	0.17	2.06	156

TABLE 3.2: Apatite fission-track data (continued from previous page)

ID #	Sample Number	Long (W)	Lat (N)	Elev. (m)	Unit	Strat. Age (Ma)	# Gr.	NS	$\Sigma(P\Omega)$ (cm^2)	$1\sigma\ \Sigma(P\Omega)$ (cm2)	ξ_{MS}	$1\sigma\ \xi_{MS}$	^{43}Ca	^{238}U	$P(\chi2)$ [c]	**Age (Ma)**	**± 1 σ error**	Dpar (μm)	± 1 s	#	Length (μm)	error (μm)	Stdev (μm)	# length
A20	RG-14	73° 45.958′	5° 15.500′	2600	Cacho Fm.	59 ± 3	14	83	3.23E-05	6.51E-07	1.37E+01	4.62E-01	4.14E-02	7.01E-03	4.6%	**17.6**	**2.0**	1.54	0.27	13	13.30	2.42	4.19	4
A21	T2-018	73° 42.897′	5° 6.472′	2630	Guadalupe Gr.	68 ± 3	8	68	1.85E-05	4.55E-07	1.33E+01	3.94E-01	4.03E-02	7.59E-01	0.0%	**24.4**	**3.1**	1.57	0.25	7	13.45	3.8	3.8	2
A22	T2-660	73° 37.762′	5° 3.110′	2275	Une Fm.	103 ± 9	29	16	8.50E-06	6.69E-08	1.55E+01	3.68E-01	2.93E-02	1.95E-01	0.0%	**14.6**	**3.7**	1.61	0.21	14	14.04	0.33	0.8	7
A23	T2-013	73° 37.563′	5° 2.545′	2255	Une Fm.	103 ± 9	21	55	3.80E-05	7.31E-07	1.34E+01	4.18E-01	3.49E-02	4.20E-02	27.3%	**9.7**	**1.4**	1.51	0.19	19	10.37	1.41	3.16	6
A24	T2-012	73° 36.602′	5° 0.794′	2687	Guadalupe Gr	77 ± 6	20	232	6.50E-05	1.01E-06	1.36E+01	4.41E-01	4.20E-02	3.42E-03	0.0%	**24.2**	**1.8**	1.59	0.19	20	12.97	0.6	2.69	21
A25	T2-019	73° 32.976′	5° 0.158′	1868	Une Fm.	103 ± 9	5	3	3.69E-06	6.98E-08	1.32E+01	3.79E-01	3.88E-02	5.64E-02	66.8%	**5.4**	**3.1**	1.64	0.15	5	-	-	-	no lengths
A26	AM-07	73° 23.441′	5° 1.925′	1341	Las Juntas Fm.	117 ± 3	11	8	3.58E-05	3.14E-07	1.67E+01	4.59E-01	2.92E-02	6.81E-02	57.0%	**1.9**	**0.7**	1.52	0.23	11	12.10	0.29	0.77	8
Southern Transect																								
A35	BV-MP3-F	74° 1.239′	4° 26.561′	2275	Chipaque Fm.	85 ± 5	18	28	1.13E-05	1.37E-07	1.11E+01	2.68E-01	4.02E-02	7.21E-02	23.8%	**13.8**	**2.6**	1.64	0.13	17	12.35	1.64	3.27	5
A36	BV-MP7-F	74° 0.561′	4° 26.094′	2022	Chipaque Fm.	85 ± 5	10	14	5.43E-06	9.06E-08	1.11E+01	2.62E-01	2.86E-02	2.63E-02	0.1%	**14.3**	**3.8**	1.68	0.25	9	12.28	0.51	0.72	3
A37	BV 120-F	73° 57.256′	4° 23.872′	2123	Cáqueza Fm.	133 ± 2	39	8	2.24E-05	3.04E-07	1.12E+01	2.77E-01	4.03E-02	4.92E-01	99.9%	**2.0**	**0.7**	1.62	0.22	28	13.06	0.95	0.95	2

[a] RhoS and Rho I are the spontaneous and induced tracks density measured, respectively (x 10^5 tracks/cm^2). NS and NI are the number of spontaneous and induced tracks counted for estimating RhoS and RhoI, respectively

[b] (c^2) (%) is the chi-square probability (Galbraith, 1981; Green, 1981). Values greater than 5% are considered to pass this test and represent a single population of ages

[c] RhoD is the induced track density measured in the external mica detector attached to CN2 dosimetry glass (x 10^5 tracks/cm^2). ND is the number of induced tracks counted in the mica for estimating RhoD.

[d] Pooled (*central*) age for samples passing (*failing*) the c^2test

TABLE 3.3: Zircon fission-track data

ID #	Sample Number	Long (W)	Lat (N)	Elev. (m)	Unit	Strat. Age (Ma)	# Gr.	U (ppm)	Rho-S (NS) [a]	Rho-I (NI) [a]	Rho-D (ND) [b]	P(χ^2) (%)	Age Dispersion	Age [d]	±1σ error
Western Transect															
Z02	Villeta	74° 24.724′	5° 7.096′	737	Villeta Gr.	135 ± 5	26	84	10.597 (1406)	12.564 (1667)	4.6803 (3924)	8.7	11%	**24.0**	**1.4**
Z03	Murca 1	74° 20.607′	5° 15.257′	1114	Murca Fm.	138 ± 2	21	224	21.759 (2252)	29.817 (3086)	4.3912 (4082)	14.7	6%	**19.5**	**1.0**
Z04	Murca 2	74° 19.715′	5° 14.675′	1085	Murca Fm.	138 ± 2	20	248	27.739 (1769)	38.244 (2439)	4.4023 (4082)	11.0	9%	**19.4**	**1.1**
Northern Transect															
Z21	FS 17	73° 0.190′	5° 53.606′	2975	Girón Gr	161 ± 15	25	330	112.508 (2846)	46.529 (1177)	4.597 (2370)	0.0	42%	**68.2**	**7.0**
Z22	FS 15	72° 53.812′	5° 49.010′	2515	Gneiss	>542	21	209	110.987 (2333)	30.732 (646)	4.6245 (2370)	0.0	105%	**68.3**	**16.4**
Z23	FS 11A	72° 51.869′	5° 50.925′	2789	Granite	>542	13	270	141.762 (1229)	41.064 (356)	4.6521 (2370)	0.0	44%	**89.2**	**13.0**
Central Transect															
Z05	Soescol	73° 23.065′	4° 51.205′	1858	Macanal Fm.	135 ± 5	8	474	45.929 (240)	77.697 (406)	4.3763 (4082)	90.8	0%	**15.7**	**1.5**
Z07	MA 16	73° 16.035′	4° 52.393′	990	Farallones Gr.	388 ± 28	35	219	26.236 (2354)	28.543 (2561)	4.4485 (2370)	9.5	10%	**24.9**	**1.4**
Southern Transect															
Z08	FT 1	73° 43.870′	4° 29.308′	3660	Chingaza Fm.	143 ± 2	46	402	26.654 (2401)	55.351 (4986)	4.4272 (3924)	0.0	28%	**13.1**	**0.9**
Z09	SJ 5	73° 41.586′	4° 28.296′	2251	Quetame Gr.	> 416	43	322	19.038 (1473)	47.097 (3644)	4.6695 (3924)	88.1	0%	**11.5**	**0.6**
Z10	SJ 1	73° 40.851′	4° 29.628′	2748	Quetame Gr.	> 416	14	544	51.06 (1519)	16.942 (504)	2.9134 (2766)	6.2	15%	**5.9**	**0.4**
Z13	BV 126	73° 54.523′	4° 22.629′	1582	Macanal Fm.	135 ± 5	11	322	22.887 (458)	37.379 (748)	3.5714 (3388)	5.1	16%	**13.3**	**1.0**
Z15	BV 86	73° 50.075′	4° 16.732′	1226	Quetame Gr.	> 416	21	350	13.470 (927)	35.28 (2428)	3.5558 (3091)	23.2	5%	**8.3**	**0.5**
Z17	BV 196	73° 47.002′	4° 17.550′	2862	Quetame Gr.	> 416	38	420	26.636 (1705)	57.880 (3705)	4.3073 (3924)	0.0	50%	**11.4**	**1.1**
Z18	BV 194	73° 46.628′	4° 17.855′	3084	Chingaza Fm.	143 ± 2	27	297	14.885 (1058)	44.937 (3194)	4.8631 (3924)	61.4	3%	**9.8**	**0.6**
Z19	BV 283	73° 36.545′	4° 16.773′	1096	Buenavista Fm.	144 ± 2	20	231	187.07 (3799)	26.344 (535)	3.5478 (2766)	0.0	44%	**145.2**	**17.3**
Z20	BV 279	73° 40.141′	4° 9.743′	870	Buenavista Fm.	144 ± 2	20	204	185.783 (6244)	235.65 (792)	3.6288 (2766)	0.0	21%	**165.9**	**12.9**

[a] RhoS and Rho I are the spontaneous and induced tracks density measured, respectively (x 10^5 tracks/cm^2). NS and NI are the number of spontaneous and induced tracks counted for estimating RhoS and RhoI, respectively

[b] (χ^2) (%) is the chi-square probability (Galbraith, 1981; Green, 1981). Values greater than 5% are considered to pass this test and represent a single population of ages

[c] RhoD is the induced track density measured in the external mica detector attached to CN2 dosimetry glass (x 10^5 tracks/cm^2). ND is the number of induced tracks counted in the mica for estimating RhoD.

[d] Pooled (*central*) age for samples passing (*failing*) the χ^2test

Farther to the east, in the Eastern Cordillera's western fold-and-thrust belt, the timing for the onset of cooling is evaluated through our own thermal modeling of AFT data obtained by Gómez (2001) and Gómez et al (2003). These authors presented AFT ages of 66.2 ± 7.7 Ma and 61.5 ± 9.1 Ma for Upper Cretaceous and Lower Paleocene sandstones in the western flank of the Guaduas syncline (samples A02-A03, respectively; Fig. 3.3a). Indistinguishable cooling and depositional ages, a Ro value of ~0.6% (~100°C, Burnham and Sweeney, 1989) in the Upper Cretaceous Buscavidas Formation (Gómez 2001; Table B3), and a short mean track length (MTL=13.56 ± 1.40 μm; Figure 3.3b) suggest that AFT ages are partially reset. Along the same structure, samples A04 and A5, collected ~1 to 4 km shallower within the stratigraphic section from upper Paleocene and Oligocene sandstones and at higher elevations, yield cooling ages of 25.8 ± 3.8 Ma and 12.2 ± 2.3 Ma, respectively (Table 3.1). Although AFT ages are younger than depositional ages, a virtually invariable Ro value of ~0.6% throughout the Upper Cretaceous – lower Miocene section in the Guaduas syncline (Gómez, 2001; Table B3), suggests that ages are partially reset.

Based on thermal modeling of Upper Cretaceous and Paleocene samples, Gómez (2001) inferred that first cooling episode from peak temperatures of 100°-120 °C occurred sometime between 65 and 30 Ma. Also, this cooling event is interpreted to correlate with development of the regionally extensive angular unconformity at the base of middle Eocene deposits along the western foothills of the Eastern Cordillera and the Middle Magdalena Valley Basin (Gómez, 2001; Restrepo-Pace et al., 2004). To better document the timing for such a cooling episode, we performed thermal modeling on data from three partially reset sandstones ranging in age from Maastrichtian to late Paleocene (Samples A02, A03 and A04, Table 3.1). Modeling input parameters include AFT grain ages, track lengths, and Dpar measurements, as well as Ro values (see Appendix B for details). For samples with a discordant age, we divided the grains into populations based on AFT kinetic properties (Dpar or Cl content), and modeled the population with the maximum number of grains that yield a concordant age. We also guided the *t*-*T* paths by introducing constraints related to the time of deposition and, importantly, cooling sometime between 56 and 43 Ma, corresponding to the time gap associated with the angular unconformity (Gómez et al., 2005). Only one sample (A02) has a fair number of confined tracks (50) sufficient for modeling with moderate resolution (Fig. 3.3b). However, the other two samples with fewer tracks yielded similar results (not shown). Modeling results suggest very rapid cooling between peak temperatures and deposition, implying either a source area rapidly exhuming during the Late Cretaceous such as the Central Cordillera (e.g., Gómez, 2001; Villagómez et al., 2008), or potential contribution from volcanic sources. Although contemporaneous volcanism is not reported in Central Colombia, sparse layers of felsic tuff have been found interbedded within coal-bearing Paleogene deposits farther to the north, at ~10°N (Bayona et al., 2007). Therefore, a distal volcanic source may have provided volcanic minerals to non-tuffaceous Paleocene foreland deposits in the present Eastern Cordillera. Finally, the modeling results suggest the time for onset of cooling is constrained to sometime between 50 and 35 Ma.

3.5.2 Villeta Anticlinorium

Three ZFT samples were collected from Lower Cretaceous sedimentary units along the most deeply exhumed areas in the Villeta Anticlinorium (Samples Z02, Z03, Z04; Fig.3a). All samples have concordant ages ranging from 19.4 ± 1.1 to 24.0 ± 1.4 Ma (Table 3.3). A Ro value of 6.4% in Lower Cretaceous rocks nearby indicates a paleoburial temperature > 250° (Gómez, 2001). Concordant ages and peak burial temperature estimates thus indicate reset ZFT ages and imply that exhumation was ongoing by 25 Ma. AFT data from equivalent horizons yield reset ages of 6.6 ± 1.8 and 7.9 ± 3 Ma (Samples A06 and A07; Gómez 2001; Table 3.1).

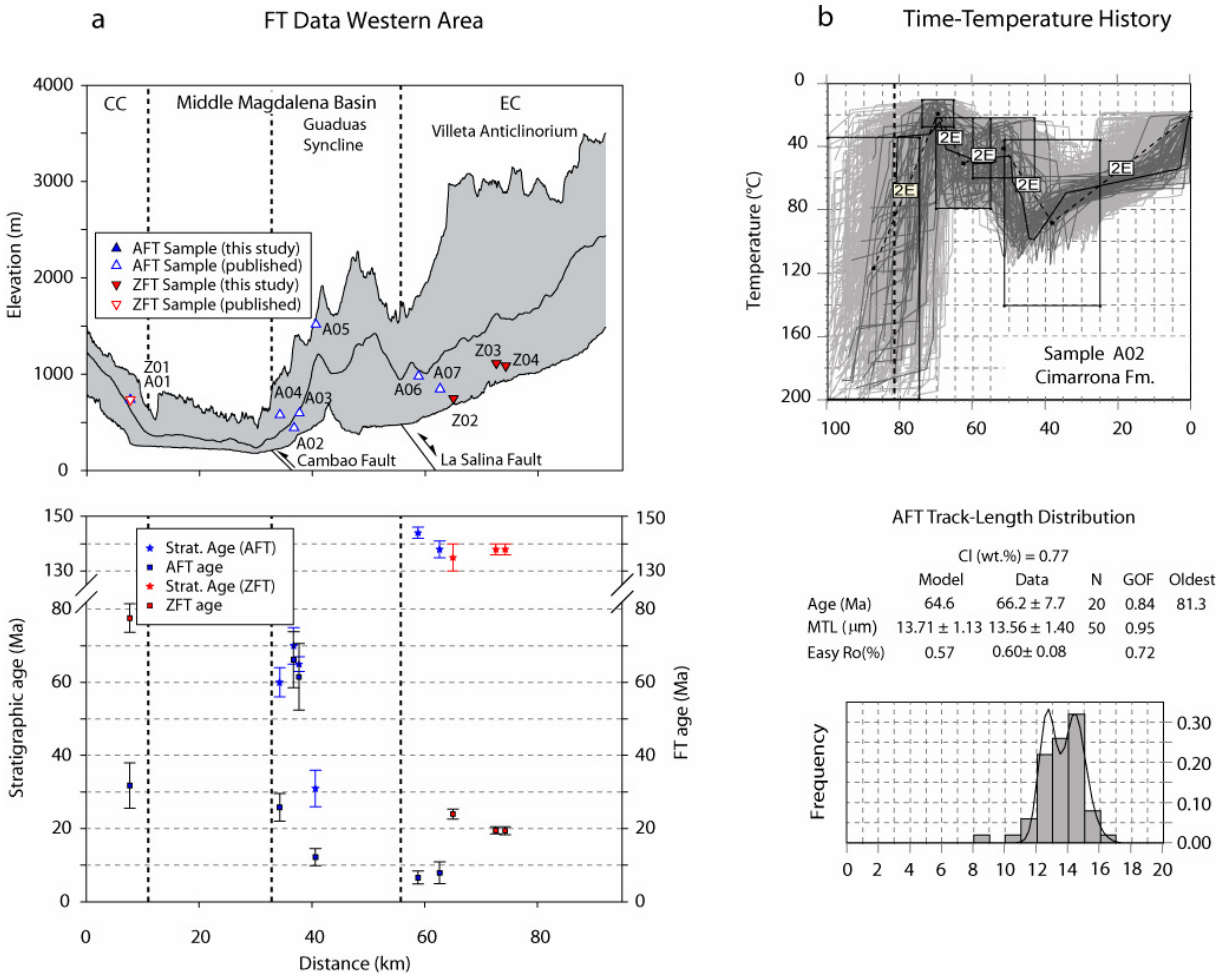

Figure 3.3. Topography, simplified structure and fission-track data from the Central Cordillera and the western sector of the Eastern Cordillera. **a**. 40-km-wide topographic swath (SRTM) profile showing maximum, mean and minimum elevation, as well as projected FT samples for the Western transect; see Fig. 3.1 for location. Cooling ages (1σ error) and depositional ages are shown in the lower panel. Note cooling ages significantly younger than stratigraphic ages in samples from the Villeta Anticlinorium, reflecting resetting. **b**. Results of thermal modeling of AFT data for Upper Cretaceous partially reset Sample A02. Time-temperature paths constrained by AFT and VR data, as well as known geologic constraints, suggest that initiation of cooling occurred sometime between ~45 and 25 Ma.

3.5.3. Axial Eastern Cordillera

Along the Northern transect, concordant AFT ages from Jurassic and Cretaceous sandstones of the hanging-wall block of the Soapaga Fault are significantly younger than depositional ages (9.6 ± 2.5 to 25.9.0 ± 2.2 Ma; Table 3.2; Fig. 3.4a). This result and Ro values of 0.7-1.0% in the Cretaceous units (Guadalupe and Une Formations, respectively; Table B3) show that ages are reset, and thus exhumation must have been active by ~26 Ma. A similar cooling versus depositional age relation is observed in the ZFT data obtained from a Jurassic sandstone and from Precambrian granite and gneiss beneath the Mesozoic sequence (ZFT ages = 68.2 ± 7.0 to 89.2 ± 13 Ma; Table 3.3). However, these ZFT ages are discordant and show large grain-age dispersion (42-105%). We thus interpret the ZFT ages as partially reset. Similar Cretaceous, partially reset ZFT ages have been reported in the Santander Massif, 100-150

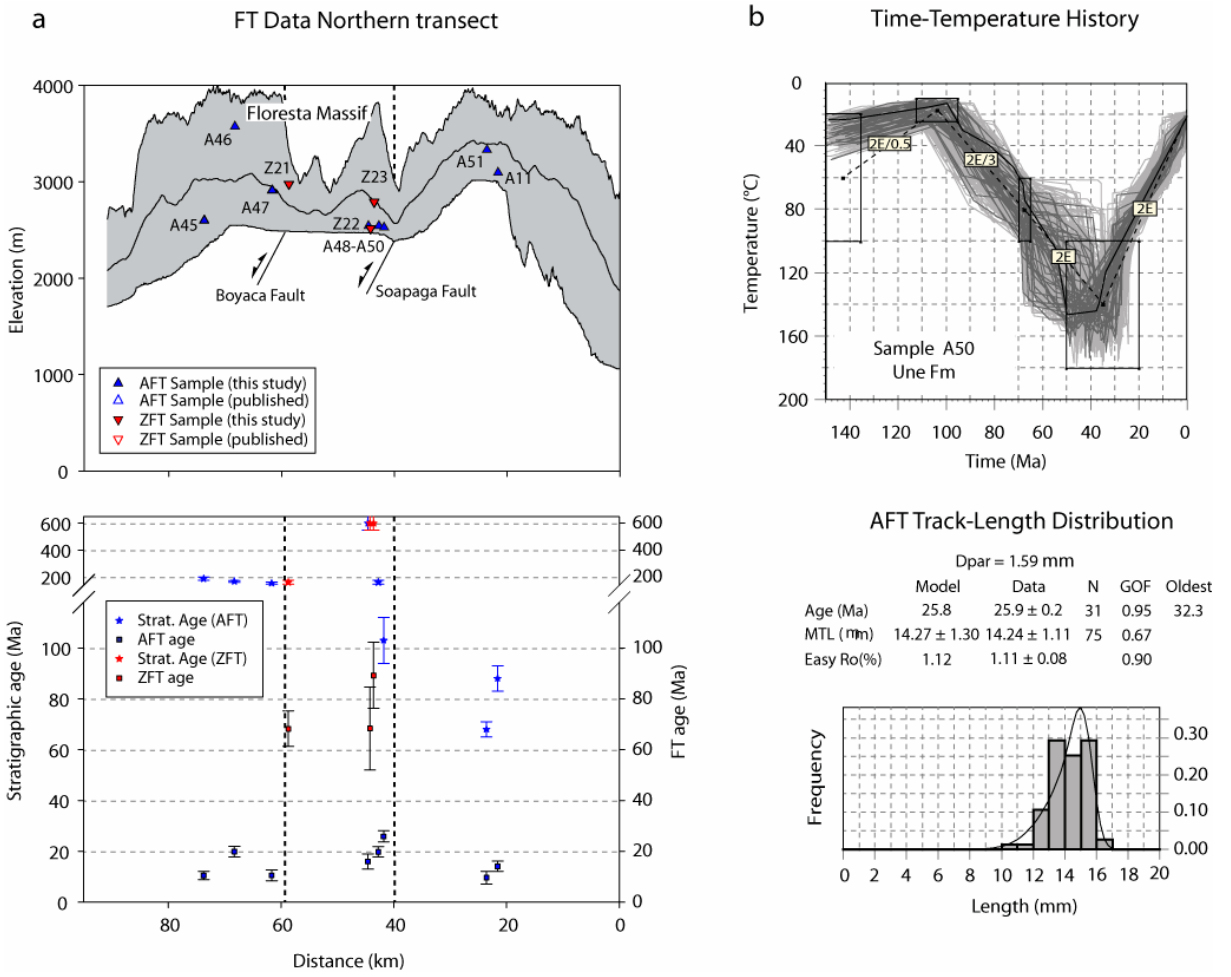

Figure 3.4. Topography, simplified structure and fission-track data from the Floresta Massif area in the axial sector of the Eastern Cordillera. **a**. 40-km-wide topographic swath (SRTM) profile showing maximum, mean and minimum elevation, as well as projected FT samples for the Northern transect; see Fig. 3.1 for location. Cooling ages (1σ error) and depositional ages are shown in the lower panel. Note Oligocene-Miocene reset AFT ages from Precambrian to Cretaceous units. Cretaceous ZFT ages are interpreted as partially reset (see text for discussion). **b**. Results of thermal modeling of AFT data for Upper Cretaceous partially reset Sample A09. Time-temperature paths constrained by AFT data, VR data, and known geologic constraints suggest that initiation of cooling occurred sometime between ~50 and 30 Ma.

km to the north (Shagam et al., 1984), reflecting insufficient burial for total annealing of zircon fission-tracks after Jurassic deposition in both the hanging- and footwalls of the former transtensional Santa-Marta-Bucaramanga fault. In order to investigate the approximate time for onset of cooling in the Floresta Massif, we performed thermal modeling in reset sample A50 from in the Lower Cretaceous Une Formation, combining AFT and Ro data (Ro =~1.0%). In this particular case, while AFT data constrain the cooling patterns (i.e. allowed cooling rates) in the range of temperatures at which fission tracks are preserved in the younger portion of the *t-T* path (< 120°C), peak burial temperatures based on Ro data (~150°C) allow extrapolation of this pattern into the older, initial cooling history. Good-fit t-T paths suggest a fairly constant cooling rate of ~ 3.0-3.5 °C/My from the ~110°C isotherm since 27 Ma (Fig. 3.4b). Thermal modeling extrapolates this rate into the previous cooling history and hence constrains the initiation of cooling to sometime between 50 and 30 Ma in the hanging-wall block of the contractionally reactivated Soapaga fault.

Farther to the south along the axial sector of the Eastern Cordillera, a low degree of exhumation has resulted in preservation of an important portion of the Mesozoic, rift-related and Cenozoic foreland sedimentary sequences in the area of the Bogotá Plateau. Thus, along our Central transect, exhumation is evaluated only through AFT dating and thermal modeling. Five sandstone samples from the late Paleocene-early Eocene Lower and Upper Socha Formations (Samples A08, A09, A13, A14 and A19) yield AFT ages ranging from 73.3 ± 3.6 to 38.0 ± 3.5 Ma (Table 3.2). All, but one of the ages (Sample A9) are discordant and all are close to or older than depositional ages (Fig. 3.5a). In addition, Ro values of 0.43-0.52% from these units (Mayorga and Vargas, 1995) correspond to peak-maximum temperatures of 80-95°C. Combined, this information indicates that samples were exhumed from depths above the total annealing isotherm and thus ages are partially reset. In all but one of these samples (A08) we measured sufficient confined track lengths for thermal modeling. Modeling was conducted by combining AFT grain ages, track lengths, and Dpar measurements, as well as Ro values (see Appendix B for details). In a similar style as thermal models from the Magdalena Valley basin, we used model constraints based on the known geological history of the region. Particularly, four constraints were used for each model: (1) (40°C-200°C) between 100-60 Ma, to allow a wide range of pre-depositional thermal histories, including residence both above and below the total annealing isotherm in the source areas of the Central Cordillera and the Guyana craton; (2) (10°-25°C) during deposition (late Paleocene-early Oligocene, 59-49 Ma); (3) (60°-130°C) between deposition and ~15 Ma, to allow heating due to burial reaching temperatures beyond peak burial temperature estimates; and (4) 20°C at present conditions. Acceptable- and good-fits for all models show a similar *t-T* path (Fig. 3.5b) that involves three stages. As these detrital apatites may be derived from multiple source areas, the first modeled cooling can not be definitively interpreted. Nevertheless, the first, very rapid cooling overlaps in time with the depositional age, indicating a potential volcanic contribution from the source area, which has been shown to correspond to the Central Cordillera (Gómez et al., 2003). Besides this rapid cooling, the oldest track given for the best-fit path in each model

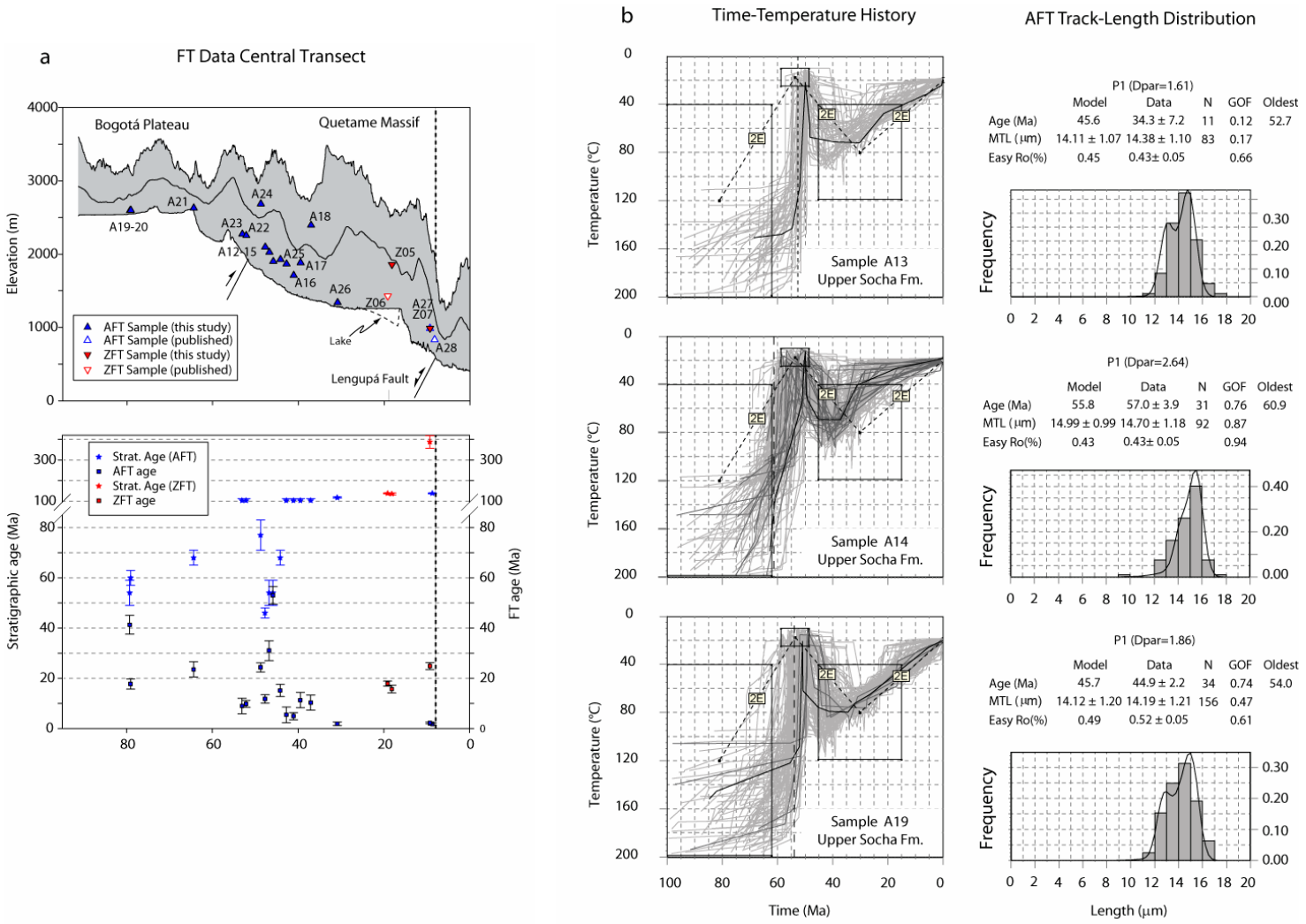

Figure 3.5. Topography, simplified structure and fission-track data from the axial sector Eastern Cordillera **a**. 40-km-wide swath-averaged maximum, mean and minimum topographic (SRTM) profiles for the Central transect (see Fig. 1 for location). Projected FT samples are shown. Cooling ages (1□ error) and depositional ages are plotted in the lower panel. Note similarity between cooling ages and depositional ages for the Paleocene and younger samples in the western half of the transect, indicating that ages are partially reset. **b**. Results of thermal modeling of AFT data for and Paleocene samples A13-A19. The portion of the thermal histories older than the oldest modeled track (indicated by vertical line in each model) is not resolved by our thermal input data; however, they are consistent with known geological constraints.

yield Campanian to Paleocene ages, suggesting a potential contribution of apatites from the uplifting Central Cordillera. Second, heating up to 90-105°C precedes the onset of cooling at some time between 45-30 Ma. Finally, the samples cooled to surface temperatures at moderate rates of 2°-5°C/My.

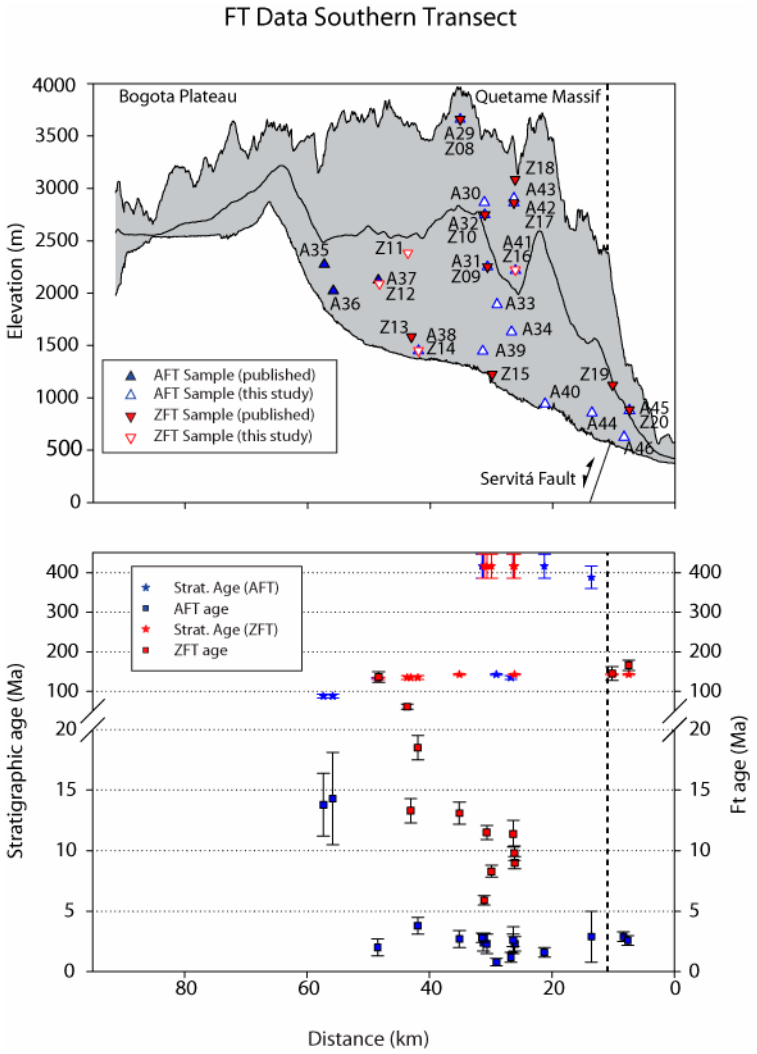

Figure 3.6. Topography, simplified structure and fission-track data from the axial sector Eastern Cordillera along the Southern transect (see Fig.1 for location). **a**. 40-km wide swath-averaged maximum, mean and minimum topographic (SRTM) profiles. Projected FT samples are shown. Cooling ages (1□ error) and depositional ages are plotted in the lower panel. Note overlapping depositional and cooling ages in the footwall of the Servitá fault, suggesting partial resetting. Miocene exhumation of the Quetame Massif is illustrated by ZFT and AFT ages younger than 20 Ma.

3.5.4 Quetame Massif

We present 14 new AFT ages and 11 new ZFT ages from samples collected along the Central and Southern transects in the eastern margin of the Eastern Cordillera (Fig. 3.1, tables 3.2 and 3.3). Most of the samples were collected in the hanging walls of the Servitá-Lengupá faults (Fig. 3.5 and 3.6). In a W to E direction the dataset includes 5 AFT samples from Upper Cretaceous sandstones (Chipaque Formation and Guadalupe Group), 9 AFT and 4 ZFT samples from Lower Cretaceous sandstone units, 1 ZFT sample from Upper Paleozoic sandstones, and 4 ZFT samples from Pre-Devonian low-grade meta-arenites. Finally, 2 ZFT samples were collected from the basal Cretaceous sandstones in the footwall of the Servitá fault (Figs. 3.1 and 3.2).

A first-order analysis is derived from comparison of ZFT ages from equivalent units in different tectonic blocks (Fig. 3.6a). First, two samples from basal Cretaceous sandstones in the hanging wall of

the Servitá fault have reset Miocene ages of 13.1 ± 0.9 and 9.8 ± 0.6 Ma (Samples Z08 and Z18). Second, another group of samples from the footwall of this fault yields discordant, partially reset ages similar to slightly older than the depositional age (Samples Z19 and Z20; 145.2 ± 17.3 and 165.9 ± 12.9 Ma, respectively). These results indicate that Lower Cretaceous rocks were buried at depths beneath the ZFT total annealing isotherm only in the western, former hanging-wall block of the extensional Servitá fault that formerly defined the eastern margin of the Mesozoic rift. Conversely, as suggested by Mora et al (2008b), nearly identical AFT ages of ~ 3 to 4 Ma in Lower Cretaceous and basement samples in the hanging wall (e.g., Samples A29 and A43) and footwall (e.g., Samples A45 and A46) blocks of the Servitá fault, suggest that Pliocene exhumation was accompanied by thrusting along a single block limited to the east by the Mirador short-cut fault (Fig. 3.7).

On the other hand, AFT reset ages from the whole set of Pre-Devonian to Upper Cretaceous samples are younger than 25 Ma and hence reveal ongoing exhumation by Oligocene time. In order to evaluate the time for the onset of exhumation, provided by the structurally shallowest sample beneath the lower boundaries of the now exhumed AFT and ZFT partial-annealing zones, we analyze the distribution of fission-track ages with respect to stratigraphic depth (e.g., Brandon et al., 1998; O'Sullivan and Wallace, 2002) for samples collected from the hanging-wall block of the Servitá and Lengupá faults in the Central and Southern transects, including both our new ages and published data (see Table B3). This approach constitutes an approximation to the age-elevation profiles that have been used to derive the timing and rates of exhumation in exhumed crustal sections (e.g., Fitzgerald et al., 1993; Reiners et al., 2003a) or the paleodepth-age profiles used in extensional settings (Stockli, 2005; Stockli et al., 2002). Figures 3.8a and 3.8b show the distribution of AFT and ZFT ages with respect to the stratigraphic datum defined by the angular unconformity at the base of the Lower Cretaceous rift deposits (See Table B3). On this plot, the distribution of AFT ages in the Central transect (Fig. 3.8a) defines a major break in slope between the top of the Upper Cretaceous Guadalupe Group and the Late Paleocene Lower Socha Formation (between 6000 and 6500 m above theunconformity), with an age between ~25 and ~40 Ma. Ro values of 0.6–0.7% at this stratigraphic depth suggest peak burial temperatures of 110-120 °C (after Burnham and Sweeney, 1989). This temperature range corresponds to the total annealing temperature for moderately rapidly cooled, fast-annealing apatites, typically characterized by Dpar values < 1.75 μm (Donelick et al., 2005), such as those observed in the Cretaceous samples along this transect (Fig. 3.8a, right panel). Collectively, the stratigraphic depth-age distribution for the kinetically homogeneous apatites and the Ro data thus suggest that the observed break in slope corresponds to an approximate location of the base of an exhumed AFT PAZ. However, since our analysis combines samples from different structural levels over a horizontal distance of ~70km, we use such an approximate location of the AFT PAZ to derive a conservative estimate of the time of onset of cooling. Our data suggest that cooling

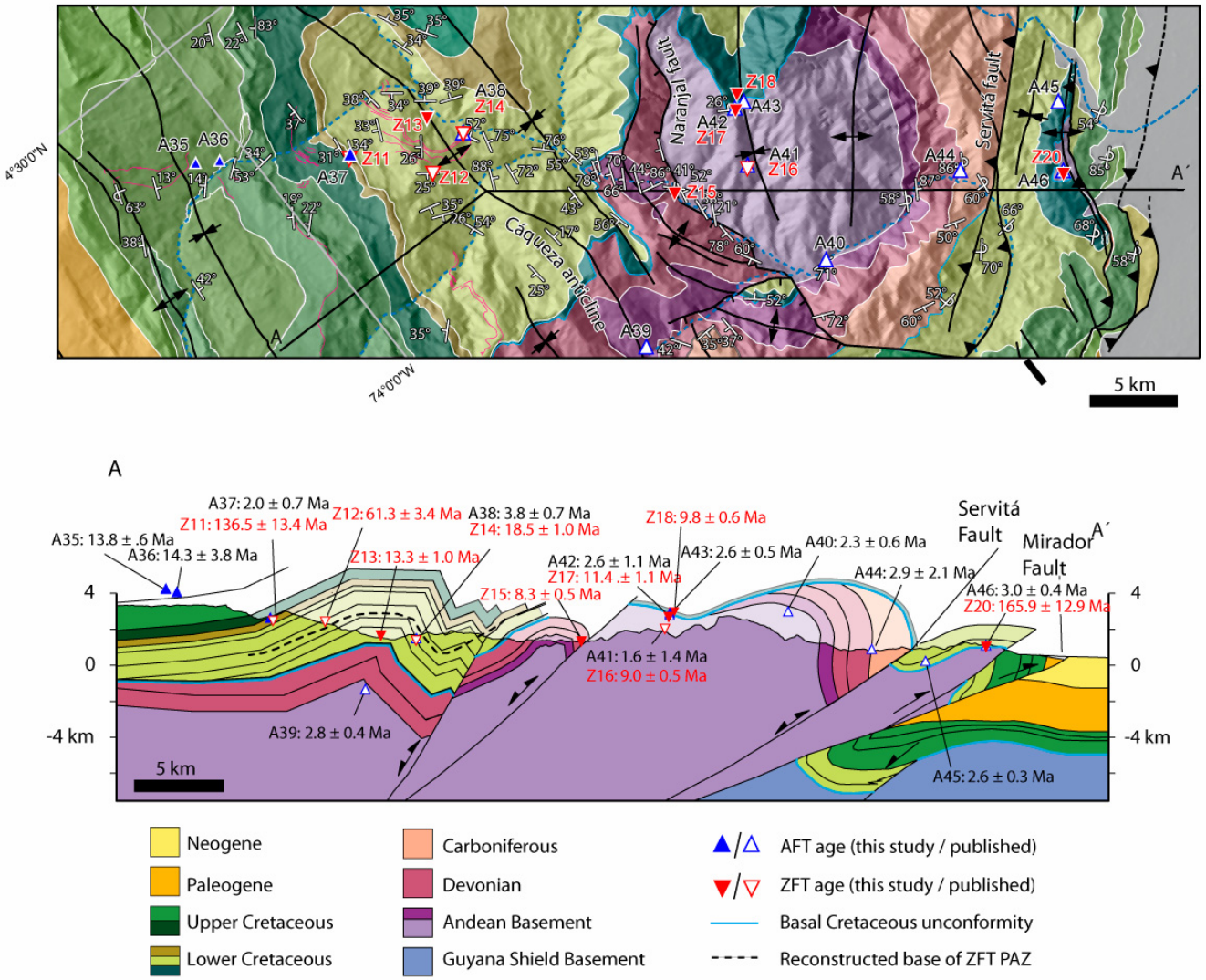

Figure 3.7. AFT and ZFT data collected along the Southern transect. The easternmost ZFT sample (Z20) collected from Lower Cretaceous sedimentary units in the footwall of the Servitá thrust (ST) yield a Cretaceous age, indicating a provenance age modified by partial annealing. On the contrary, ZFT samples from the hanging-wall of the thrust display a pattern of increasing ages toward shallower structural levels. The base of the partial-annealing zone for ZFT is located between Samples Z11 and Z12. See Fig. 3.5 and text for further discussion. Structural cross section after Mora et al, (2008b).

would have commenced sometime between 25 and 40 Ma. Furthermore, more resistant apatites (with larger Dpar values) in the overlying Paleocene samples (~6500-7000 m) have older ages, supporting our interpreted position for the base of the PAZ. Sample A12, obtained from the youngest unit in the profile, has an anomalously young age (11.7 ± 1.7 Ma) compared to nearby samples. We suspect this may arise from sample A12 residing in a distinct faulted unit not recognized in the field.

A similar analysis was conducted for ZFT samples collected along the Southern transect (Fig. 3.8b). Here, a major break in slope of a stratigraphic depth-age plot occurs within the Macanal Formation, between 1500 and 2200 m above the base of the Cretaceous units (Fig. 7b). Ro values > 3.5% for the Macanal Formation (e.g., (Mora et al., 2008b; Toro et al., 2004) suggest peak temperatures similar to that of total annealing for ZFT, and hence reveal the base of an exhumed zircon fission-track PAZ. In this transect, the structural configuration of the sampled section allows a closer approximation of the time for the initiation of cooling. As shown in Figure 3.7, we identify the position of the lower boundary of the PAZ based on the ages obtained in sandstones from the Macanal Formation cropping out in the core of the Cáqueza anticline within the hanging-wall block of the Naranjal fault. Here, samples Z11 and Z12 yield discordant ages of 136.5 ± 13.4 Ma and 61.3 ± 3.4 Ma, respectively; we interpret these ages as partially reset. In contrast, structurally deeper samples Z13 and Z14 yield concordant reset ages of 13.3 ± 1.0 Ma and 18.5 ± 1.0 Ma. Therefore, according to the pattern of reset ages from the lower part of the Macanal Formation and the underlying basement units, the age for onset of cooling must be very close to that of the uppermost totally annealed sample (Z14; 18.5 ± 1.0 Ma, 1510 m). We thus interpret that thrust-induced exhumation started at ~20 Ma in the hanging wall block of the Naranjal fault.

To better constrain the timing and apparent rates of exhumation, we constructed stacked pseudo-vertical profiles (e.g., Reiners et al., 2003b) combining AFT and ZFT data for the Central and Southern transects (Figs. 3.8c and 3.8d). While AFT ages are plotted in their actual stratigraphic position, elevations for ZFT data are shifted upward by an amount proportional to the difference between the depths of the total annealing isotherms for both thermochronometric systems. Using typical thermal parameters for convergent orogens within a stable thermal regime and moderate exhumation rates of 0.1-0.3 mm/yr, this difference has been estimated to be ~5.7 km (Reiners et al., 2003a). In the Eastern Cordillera of Colombia, however, accelerated Pliocene exhumation, as suggested by AFT data (Mora et al, 2008b; see Fig. 3.8), implies an unstable thermal regime due to compression of the isotherms and increase of the geothermal gradient by heat advection (e.g., (Mancktelow and Grasemann, 1997). Nevertheless, we use this depth difference of 5.7 km between the ZFT and AFT total annealing isotherms [equivalent to a difference of 115-140°C for geothermal gradients of 20-25°C, similar to the modern value in the proximal foredeep region (Bachu et al., 1995)], since the time window covered by our ZFT data largely predates the episode of Pliocene-Pleistocene accelerated exhumation.

Both stacked pseudo-vertical profiles show similar exhumation patterns (Fig. 3.8c and 3.8d) characterized by moderately rapid exhumation followed by much faster erosion beginning in the last ~4-5 Ma. Using the calculated pseudo-mean thicknesses, ZFT and AFT ages overlap in both profiles,

suggesting that the estimated depth difference between both isotherms is correct. A first break in slope at ~25-40 Ma in the northern profile and ~20 Ma to the south marks the timing for the onset of thrust-induced exhumation along the hanging wall of the Servitá-Lengupá faults. Based on a subset of 8 samples collected along the Southern transect (Fig. 3.8d), we derive an error-weighted pseudo-apparent exhumation rate of 0.3 ± 0.1 mm/yr between ~20 and ~9 Ma. Although this rate is not directly comparable with apparent exhumation rates derived from true age-elevation profiles, we use it as a minimum estimate as it assumes exhumation trajectories perpendicular to bedding, and hence neglects folding accompanying exhumation. A second break in slope observed in both transects places maximum constraints on the timing for the onset of accelerated exhumation at ~4-5 Ma. As noted by Mora et al. (2008b), based on a true AFT vertical profile, this episode of accelerated exhumation (1-2 mm/yr) was restricted to the eastern, windward flank of the Eastern Cordillera and suggests a positive feedback between the build-up of topography, focused orographic precipitation, and long-term exhumation rates.

3.6. DISCUSSION

3.6.1 Diachronous exhumation

In absence of other mechanisms that could have generated regional cooling in the Eastern Cordillera, such as post-magmatic cooling (e.g., Tagami and Shimada, 1996) or normal faulting driving tectonic exhumation (e.g., Ring et al., 1999), we interpret the cooling ages obtained in this study as a signal of erosional exhumation. Since erosion is facilitated by the creation of topography and the formation of pronounced relief contrasts accompanying reverse faulting in contractional orogens, the age for initial cooling in the study area constitutes a proxy for initial thrusting.

Figure 3.9 summarizes the spatiotemporal pattern of onset of thrust-induced exhumation across the eastern Colombian Andes. To the west, in the Central Cordillera, a ZFT age of ~78 Ma suggests that exhumation was active by late Cretaceous (Campanian) time. Existence of elevated topography in the area of the Central Cordillera in the Late Cretaceous has also been inferred from paleoflow data, sandstone and gravel petrography, and the character and direction of facies changes in Upper Cretaceous conglomerate and sandstone units in the Guaduas syncline (Gómez et al., 2003), and farther to the south, in the Upper Magdalena Valley basin (Montes et al., 2005; Ramon and Rosero, 2006). On the other hand, an AFT age of ~ 32 Ma (Gómez et al., 2003) places additional constraints on the Cenozoic cooling patterns in this sector of the Central Cordillera. Assuming total annealing temperatures of 250 ± 40 °C and 120 ± 10 °C for the ZFT and AFT, respectively, a geothermal gradient of 20°-25°C, surface temperatures of 20°C, and linear cooling, these ages indicate moderate exhumation rates of 0.1-0.25 mm/yr since the Late Cretaceous.

Eastward advance of the orogenic front is documented by the estimated age for initial cooling in the western fold-and-thrust belt of the Eastern Cordillera. Here, development of an angular unconformity between the late Paleocene Hoyón Formation and the middle Eocene San Juan de Rio Seco Formation brackets the initial time for rock uplift in the Guaduas syncline to 56-43 Ma (Gómez et al. 2003).

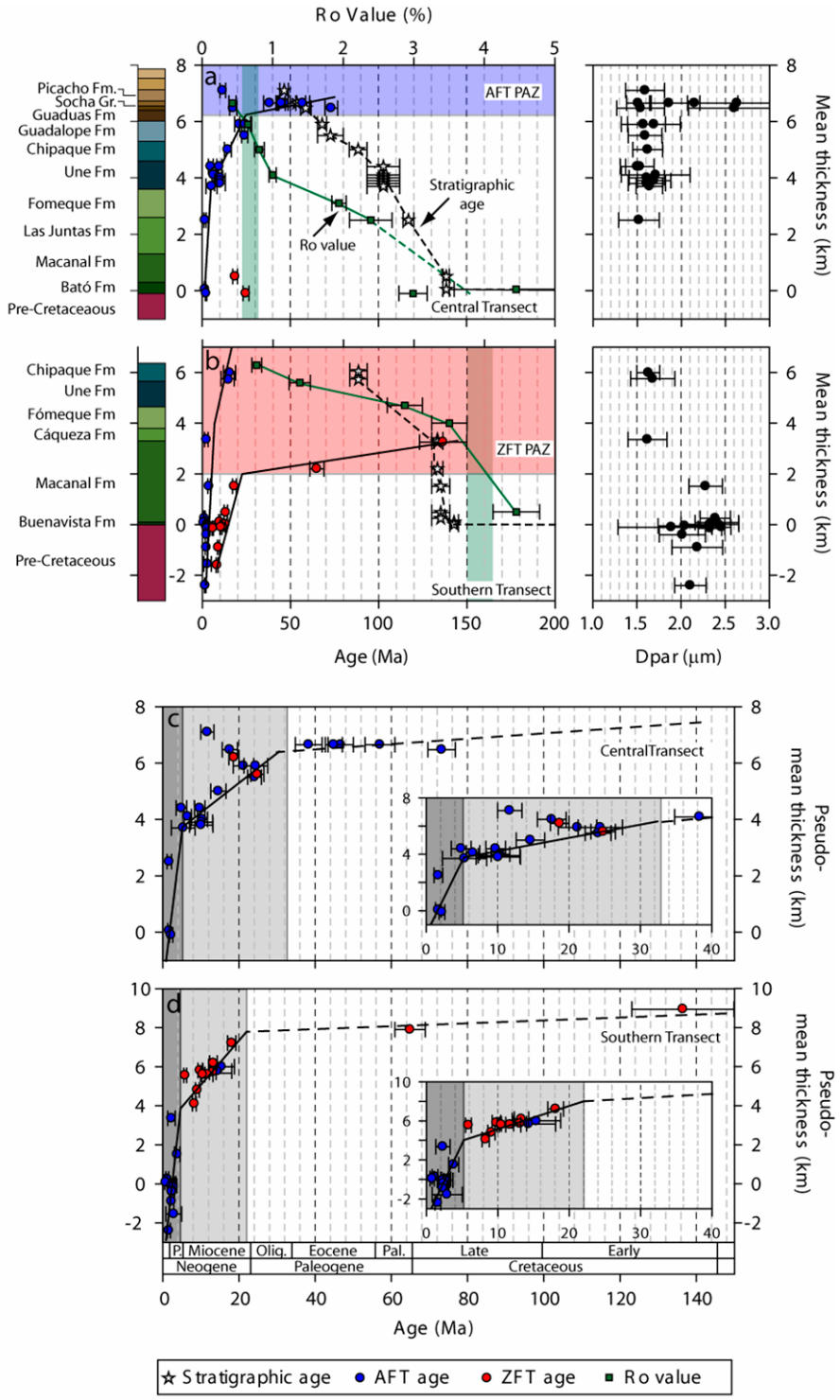

Figure 3.8. Fission-track data and vitrinite reflectance (Ro) values for samples from the Central **(a)** and Southern **(b)** transects plotted against the stratigraphic position referred to the base of the Cretaceous rift-related units (See Table B3 for details and Fig.1 for location. Stratigraphic thicknesses and ages are compiled from Ulloa and Rodríguez (1979) and Mora et al (2008b). Vertical green bars represent the range of Ro values that correspond to the temperature delimiting the base of the AFT (Central transect) and ZFT (Southern transect) partial annealing zones (blue and pink shaded areas, respectively). Stacked pseudo-vertical profiles are obtained for the Central **(c)** and Southern **(d)** transects. AFT data are plotted at their original stratigraphic position, as in Figure 3.8a and 3.8b, but ZFT data are offset upward by an amount proportional to the depth difference between the ZFT and the AFT isotherms, estimated to be 5.7 km. The first break in slope, denoted by vertical light gray band, at ~40-25 Ma (central profile) and 20 Ma (southern profile) marks the onset of thrust-induced cooling through the AFT and ZFT total annealing isotherms, respectively. See text for discussion.

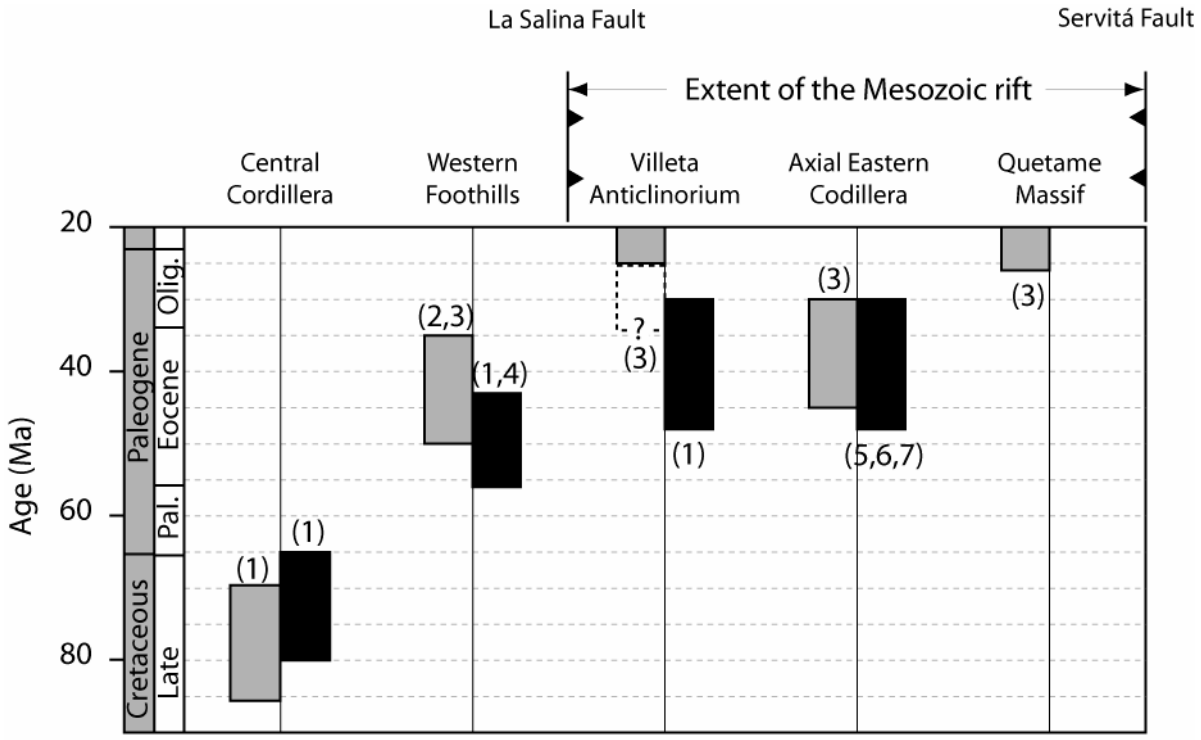

Figure 3.9. Summary of chronological indicators of the initiation of contractional deformation in the eastern Colombian Andes. Gray bars represent the maximum and minimum age estimates inferred from indicators of brittle deformation preserved in sedimentary basins across the range. Black bars represent indicators based on thermochronometric data. See text for discussion. Sources: 1 – Gómez et al (2003), 2 – Gómez (2001), 3 – this work, 4 – Restrepo-Pace et al. (2004), 5 – Julivert (1963), 6 – Gómez et al (2005), 7 – Parra et al (2008).

Likewise, farther to the NE, at ~ 6°N, west-verging thrusts are cut off beneath the angular unconformity at the base of the middle Eocene (Restrepo-Pace et al., 2004). Thermal modeling of partially reset AFT ages in an Upper Cretaceous sample from the western flank of the Guaduas syncline suggests that cooling began sometime between 50 and 35 Ma. Within this structure, AFT data by Gómez (2001) show an inverted pattern of younger AFT ages in stratigraphically shallower and topographically higher levels (See Fig. 3.3a). Along the same section, a similar burial temperature for the Upper Cretaceous (Buscavida Formation) to Miocene (Santa Teresa Formation) units is suggested by nearly invariable Ro values of ~0.6% throughout the entire stratigraphic section (Gómez et al. 2003; Table B2). We interpret this pattern as an indicator of pre-Miocene growth of the western flank of the Guaduas syncline, which would have prevented the stratigraphically deeper portion of the section from reaching burial beneath the full stratigraphic thickness.

Farther to the east, three reset ZFT ages of ~24-19 Ma from Lower Cretaceous units in the core of the Villeta Antilcinorium constrain the minimum age for thrust-driven exhumation associated with contractional reactivation of the La Salina fault. In this area, our data are not sufficient for delimiting the ZFT PAZ, which would require sampling shallower structural levels with partially reset ages. In addition, partially reset AFT age data which could aid in resolving the patterns of initial cooling through thermal

modeling are not available. However, growth strata within the middle Eocene to Oligocene San Juan de Rio Seco Formation in the eastern flank of the Guaduas syncline indicate a maximum age of ~43 Ma for initial deformation along the La Salina fault (Gómez et al., 2003). On the other hand, AFT cooling ages of 7-10 Ma in the core of the Villeta Anticlinorium reveal Miocene exhumation associated with thrusting of the La Salina fault. Simple calculations considering pooled ZFT and AFT ages, as well as assuming total annealing temperatures of 250 ± 40 °C and 120 ± 10°C for the ZFT and AFT systems, respectively, linear cooling, and horizontal isotherms suggest that long-term exhumation rates must have increased between 2 and 4-fold during the late Miocene - Pliocene.

In the axial sector of the Eastern Cordillera, our thermochronologic results from Jurassic and older basement rocks in the Floresta Massif show Miocene reset AFT ages (Samples A45-A49; ~11-20 Ma) and Cretaceous partially reset ZFT ages (Samples Z21-23) in all structural levels sampled. These results are strikingly similar to those obtained by Shagam et al. (1984) in the Santander Massif, ~100-150 km to the north, and demonstrate that Cretaceous to Cenozoic overburden was significantly thinner in the northern sector of the range than in the southern sector near the Quetame Massif, where ZFT ages are reset. In the Floresta Massif, Miocene reset cooling ages in Jurassic and older rocks and, in particular, an AFT reset age of ~26 Ma in a Lower Cretaceous sandstone from the Une Formation (Sample A50) reveal pre-late Oligocene initiation of exhumation in the Floresta Massif. Furthermore, this AFT reset age from Lower Cretaceous sandstones in the western, hanging-wall block of the Soapaga fault is older than cooling ages retrieved from coeval and younger units to the east, in its footwall (Une, Chipaque and Guadalupe Formations; samples A10, A11, A51; ~6-15 Ma). This pattern reveals that pre-late Oligocene exhumation was associated with motion on the Soapaga fault. Thermal modeling including estimates of peak burial temperatures for the reset AFT sample A50 limits the initiation of thrust-induced exhumation in the western, hanging-wall block of the Soapaga fault to Eocene-early Oligocene time (~50-30 Ma). Approximately 100 km to the south, along the Central transect, a similar middle Eocene-early Oligocene age (~45-30 Ma) for the onset of cooling is determined by AFT thermal modeling of partially reset late Paleocene sedimentary rocks from the Bogotá Plateau (Fig. 3.5). These ages for the onset of thrust-induced exhumation in the Bogotá Plateau and Floresta Massif coincide with the formation of middle Eocene-Oligocene growth strata south of the plateau (Regadera and Usme Formations; Gómez et al., 2005; Julivert, 1963). In addition, reconstruction of the subsidence history in the Medina wedge-top basin (Parra et al., 2008) and in the Llanos Basin at ~5.5 °N (Bayona et al, 2008) suggest a major increase in tectonic subsidence at around 30-35 Ma (late Eocene-early Oligocene). Parra et al (2008) interpreted this as reflecting eastward advance of the orogenic load and uplift of the Quetame Massif, based on the absence of any other discrete tectonic block to the west along a cross-section at ~4.5 °N. However, our extended thermochronologic dataset and growth strata in the area of the Bogotá Plateau support an Eocene-late Oligocene initiation of thrust-driven exhumation along the present-day axis of the Eastern Cordillera. To the north, in the Floresta Massif, this exhumation resulted from tectonic inversion of a Mesozoic half-graben basin limited to the east by the Soapaga fault. To the south, our structural cross-

section across the Bogotá Plateau suggests that there is no particular structure that can delimit a tectonic block associated with this Eocene-late Oligocene exhumation (Fig. 3.1b). We thus infer that contractional deformation in this location was accommodated along a previously unrecognized blind fault that would be located southward along the structural trend of the Soapaga fault. Taken together, our new thermochronologic data, the age range of synkinematic sediments in the Bogotá Plateau, and subsidence histories in the modern wedge-top and foredeep basins to the east suggest that the Soapaga fault and its southern continuation formed the leading edge of deformation in this sector of the northern Andes at 35-30 Ma.

Our thermochronologic data do not support a previous hypothesis that, based on the presence of unstable lithic fragments in Upper Paleocene and Miocene sandstones from the Eastern Cordillera, erosion of metamorphic basement in the Floresta Massif occurred in Paleocene to Miocene time (Bayona et al, 2008). Such a hypothesis implies an unrealistic scenario that requires erosional removal of ~5-6 km of Paleozoic, Jurassic and Cretaceous sedimentary overburden from the area of the present-day Floresta Massif in the early to middle Paleocene (~7 Myr), followed by negligible unroofing of basement rocks from late Paleocene time to the present, i.e., a time span of 56 Myr. Conversely, the Miocene reset AFT ages obtained in this study from Jurassic and basement units in the Floresta Massif (Samples A45-A49; ~ 11-20 Ma) imply that, for normal geothermal gradients of 20-25 °C/km, samples from Jurassic and older rocks were buried at a depth of 3 to 4 km during the Miocene, at the time of closure. A similar scenario for the igneous and metamorphic basement in the Santander Massif is inferred in light of the similar AFT and ZFT age patterns with respect to the Floresta Massif (Shagam et al., 1984). Considering the ~3 km of stratigraphic thicknesses for the Cretaceous section in the Floresta Massif (Etayo-Serna et al., 2003) the AFT cooling ages suggest unroofing of Cretaceous units during the Miocene. Such a Miocene erosion window exposing Cretaceous rocks in the axial Eastern Cordillera is further supported by the presence of recycled detritus of Cretaceous sedimentary rocks in the Oligocene-Miocene units of the Eastern Cordillera. Such Cretaceous recycled detritus include gravel clasts of glauconitic sandstone in conglomerates (Parra et al., 2007), fragments of chert and foraminifera-bearing siltstones in conglomerate and sandstone (Bayona et al., 2008; Céspedes and Peña, 1995), and Cretaceous palynomorphs within organic matter-rich siltstones and mudstones (Bayona et al., 2008; Carlos Jaramillo, pers. comm. 2008).

Farther eastward propagation of the actively exhuming areas is documented by the pattern of ZFT and AFT reset ages in the Quetame Massif. Age-stratigraphic depth profiles and the pattern of ZFT ages in the core of the Cáqueza anticline, to the west of the Naranjal fault, suggest an onset of exhumation at ~20 Ma. Ongoing Miocene exhumation associated with this fold is further confirmed by reset AFT ages of ~ 14 Ma in shallower structural levels within the Cretaceous section (Samples A35-A36). Farther to the east, we obtained reset ZFT ages as old as ~12 Ma in the structurally shallower levels exposed in the basement high. Therefore, our ZFT data cannot directly constrain the onset of cooling in the eastern, hanging-wall block of the Naranjal fault. Such information would require employing a higher-temperature thermochronometric system. However, here we discuss additional evidence based on geodynamic

modeling, sediment accumulation rates in the adjacent basins, and the structural configuration of the eastern margin of the Eastern Cordillera that suggest uplift of the Quetame Massif beginning in the early Miocene. First, two-dimensional flexural models require tectonic loads in the Quetame Massif to match the reconstructed middle Miocene flexural profile in the Llanos basin (Bayona et al., 2008). Second, an increase in the sediment accumulation rates recorded by the early to late Miocene Upper Carbonera Formation in the Medina wedge-top basin (Gómez et al., 2008; Parra et al., 2007; Parra et al., 2008) and the Llanos foredeep (Bayona et al, 2008) suggest an eastward advance of the orogenic front and the corresponding loads from their position along the axial Eastern Cordillera during the late Eocene-Oligocene. Finally, the offset of the basal Cretaceous unconformity across the Cenozoic faults, as noted by Mora et al. (2006, 2008a), illustrates that the Naranjal fault is one of many Mesozoic normal faults that have undergone only minor Cenozoic contractional reactivation (see Fig. 3.7). Instead, these inherited structures have been passively uplifted atop a major basement thrust along the formerly rift-bounding Servitá fault (Fig. 3.1b). This structural configuration suggests that orogenic loading in the Quetame Massif could only be generated by slip along this major basement thrust. Taken together, this suggests that contractional reactivation of the Naranjal fault may have been coeval with slip along the Servitá fault. This also corroborates the interpretation that thrust-related cooling of the entire hanging wall block of the Servitá fault began at approximately 20 Ma.

3.6.2 Pattern of orogenic front advance

The initiation of rock uplift associated with specific inherited structures, as well as the reconstruction of their retrodeformed palinspastic positions allows a calculation of the rate of migration of the orogenic front toward the foreland over time. First, the propagation rate of the orogen is the rate of its lengthening, which is obtained by dividing its present length in the transport direction by the time elapsed since the onset of shortening (DeCelles and DeCelles, 2001). In the Colombian Andes, we used the present distance between the eastern boarders of the Central and Eastern Cordilleras (~200 km), and the age of the thrust belt (82-74 Ma) to derive a long-term propagation rate of 2.5-2.7 mm/yr. Second, we evaluate the rate of propagation rates between adjacent structures in order to resolve the spatiotemporal pattern of orogen growth. The upper and lower limits for the amount of orogen lengthening between such structures is provided by the restored, and the present (i.e., shortened) distances between them, respectively (Table 3.4). We use the balanced structural cross-section from Mora et al. (2008a) to calculate the restored distances between the structures and a pin line defined at the surface trace of the most frontal structure, the Guaicaramo thrust (Fig. 3.10). To the west of the western end of the cross-section, we use the palinspastic reconstruction of Gómez et al (2003) to estimate the restored distance between the Central Cordillera's deformation front and the Cambao thrust. However, limited information on the deep structure and amount of shortening associated with deformation in the Central Cordillera precludes a more precise palinspastic reconstruction of this part of the orogen. A closer look at the spatiotemporal advance of the orogenic wedge suggests a three-stage evolution (Table 3.4 and Fig. 3.10).

First, after initial uplift of the Central Cordillera at ~82-74 Ma, deformation migrated to the Cambao fault and associated west-verging thrust systems at a rate of 0.5-2.1 mm/yr and continued at similar to slightly higher rates of 0.5-3.1 mm/yr during the late Paleocene-middle Eocene as deformation propagated westward to the La Salina fault. By that time the orogen had attained as much as 26 % of its present width. Second, a virtually simultaneous uplift along this fault and the axial sector of the Eastern Cordillera along the Soapagá fault during the middle-late Eocene (30-40 Ma) illustrates a rapid eastward jump of the deformation front. The broad age range for the onset of deformation is due to the low-resolution biostratigraphical age determinations of the growth strata result in a large uncertainty in the calculation of the rate of migration. However, the data suggest values of at least 100 mm/yr. Rapid eastward advance of the orogen into the foreland continued during the late Eocene-Oligocene, as deformation progressed to the Servitá fault at rates of 2.2-7.7 mm/yr. Taken together, average rates for the middle Eocene-early Miocene (~40-20 Ma) episode of faster advance of the orogenic deformation front that result from tectonic inversion of the Eastern Cordillera are 4.1-18.0 mm/yr. Our data illustrate that by the early Miocene (~20-25 Ma) the northern Andes had achieved ~86 % of their present width. Finally, time-averaged orogen-migration rates slowed since then to 1.2-2.1 mm/yr, as the deformation front remained stationary along the Servitá-Tesalia faults during the Miocene and propagated to the Guaicaramo fault only after ~5 Ma (Mora, 2007).

Table 3.4: Temporal evolution of orogenic width and orogenic migration rates

Fault	Age [1] (Ma)	1σ error (Ma)	Shortened distance (km) [2]	**Minimum mean propaga-tion rate (mm/yr) [3]**	**1σ error (mm / yr)**	% of orog. width	Restored distance (km) [4]	**Maximum mean propaga-tion rate (mm/yr) [5]**	**1s error (mm / yr)**	% of orog. width
Guaicaramo	4.0	1.5	0	**1.5**	**0.3**	100%	0	**1.8**	**0.3**	100%
Servita	22.0	3.0	27	**4.0**	**1.8**	86%	32	**5.3**	**2.4**	87%
Soapaga	35.0	5.0	79	**150**	**3100**	60%	101	**171**	**3100**	60%
Salina	35.5	7.5	156	**1.6**	**1.1**	21%	187	**1.8**	**1.3**	26%
Cambao	49.5	6.5	178	**0.7**	**0.2**	10%	213	**1.4**	**0.7**	16%
CC	77.6	3.9	197			0%	252			0%

[a]. Age for onset of deformation
[b]. Present (i.e shortened) distance to Guaicaramo thrust
[c]. Minimum error-weighted orogen propagation rate (Δ shortened distance/ Δ time)
[d]. Restored distance to Guaicaramo fault according to retrodeformed profile by Mora et al. (2008b) for the Eastern Cordillera, and Gómez et al. (2003) for the Central Cordillera
[e]. Maximum error-weighted orogen propagation rate (Δ restored distance/ Δ time)

Our observations demonstrate a non-systematic growth of the orogen in the northern Andes characterized by alternating periods of slow and rapid advance of the orogenic deformation front. Such episodic behavior is different from the growth patterns that would be expected during the self-similar growth of an orogenic wedge system (e.g., Dahlen, 1990; DeCelles and DeCelles, 2001). In orogenic wedges that deform according to critical Coulomb wedge mechanics and under constant accretionary

influx and erosive efflux rates, a systematic decrease in the rate of wedge propagation through time is expected because: (1) as the wedge enlarges, greater amounts of mass influx are required by the wedge to continue growing (DeCelles and DeCelles, 2001); and (2) as the wedge propagates into the foreland above a progressively gentler basal decollement, as is the case of many orogenic wedges (Boyer, 1995), greater amounts of convergence are absorbed as internal deformation in order to build taper, reducing therefore the amount of convergence consumed in orogenic advance (Boyer, 1995).

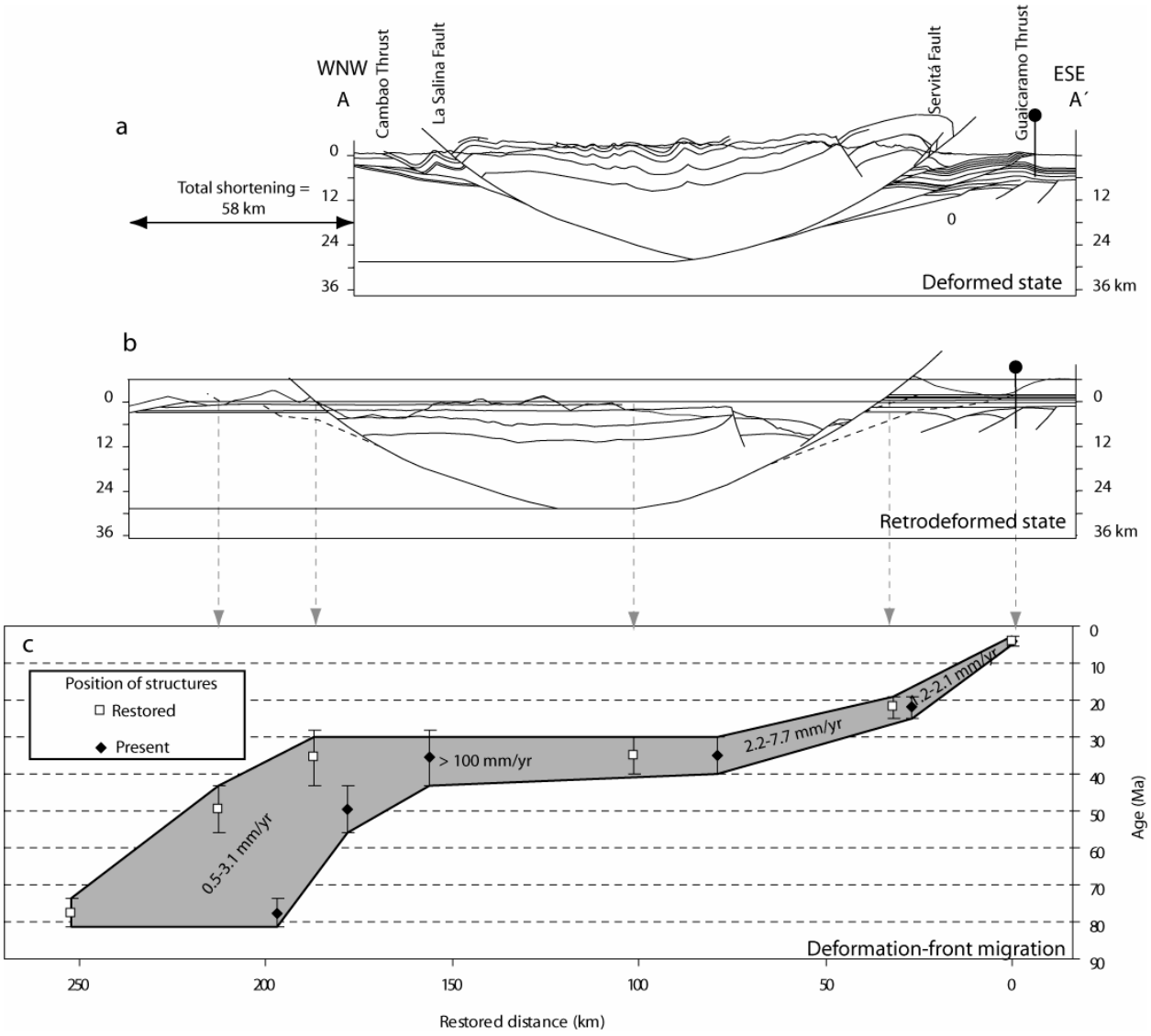

Figure 3.10. Spatial and temporal variation in the position of the deformation front of the northern Andes in central Colombia. a-b. Present-day and retrodeformed structural configuration along cross section A-A´ after Mora et al. (2008b; see location in Fig. 1). c. Rates of orogen propagation. The present (filled symbols) and restored (open symbols) distances of key structures with respect to the undeformed foreland beneath the Guiacaramo thrust are plotted versus their age of onset of deformation. Dotted lines with arrows indicate structures projected for the analysis (see Table 3.4). An episodic pattern of Cenozoic orogen-front migration shows three major stages. This configuration results from (1) a change from oblique and slow to orogen-perpendicular and faster convergence in the middle Eocene (~50 Ma), and (2) slip and deformation preferentially accommodated along former normal faults reactivated in contraction. See text for discussion.

Alternatively, changes in the rate of orogenic-front propagation may be related to variations in the mass-flux balance through time (e.g., Dahlen and Barr, 1989). This model predicts that either an increase in accretionary influx rates (for example by an increase in convergence rates) or a decrease in the erosive efflux through time promote attainment of supercritical conditions that favor faster orogenic advance (e.g., DeCelles and DeCelles, 2001). Although developed for internally homogeneous orogenic wedges, this concept of mass-flux balance as a major control in orogen width may also apply to those parts of orogens where the crust has been pervasively deformed in previous tectonic episodes and is hence predisposed to concentrate deformation along basement inhomogeneities (Hilley et al., 2005; Strecker et al., 2008), as is the case of the northern Andes. Based on these predictions, the observed increase in orogenic propagation rates in the middle Eocene in the central Colombian Andes, ~40 Myr after the initiation of orogenesis, should reflect an increase in the net mass-flux balance incorporated into the orogen. We suggest that such an increase may have resulted from (1) a middle Eocene (49-42 Ma) increase in the convergence rate between the Farallon-Nazca and South American plates (Pardo-Casas and Molnar, 1987), and (2) a change in the convergence direction (Pardo-Casas and Molnar, 1987; Pilger, 1984) that contributed to rotation of the paleostress orientation from a prevailing oblique, WSW-ENE direction prior to the middle Eocene to a subsequent, more orogen-perpendicular NW-SE orientation (Cortés et al, 2005). As a result of this change, an increase in the net component of convergence accommodated perpendicular to the structural grain may have resulted in faster advance of the orogenic deformation front.

On the other hand, a non-systematic pattern of orogenic propagation is expected in those settings where favorably oriented basement anisotropies within an orogen behave as weak structures that may favorably absorb shortening independent of wedge mechanics (e.g., Allmendinger et al.., 1983; DeCelles, 2004; Hilley, 2005; Jordan and Allmendinger, 1986; Marshak et al., 2000). Our data suggest that the extensional structures of the Mesozoic rift basin such as the Soapaga and Servitá faults were utilized and incorporated into the fold-and-thust belt during the middle Eocene-early Oligocene contraction. As a result of this predisposition to failure, the rate of orogenic propagation decreased during the Miocene, and deformation was absorbed along the Servitá fault, thus causing a stagnation of the lateral advance of the orogenic front. Finally, as shown by Mora (2007), despite the apparent increase in erosive efflux in the Pliocene documented by young AFT ages, the attainment of elevated topography in Eastern Cordillera must have increased the lithostatic stresses in the range and prompted an eastward jump of the deformation front to low elevation areas, where contractional reactivation and failure occurred along the Guaicaramo thrust.

3.7 SUMMARY AND CONCLUSIONS

Apatite and zircon fission-track thermochronology coupled with paleoburial estimates and published temporal indicators of brittle deformation allow a first regional evaluation of the spatiotemporal tectonic evolution of the orogenic wedge in the northern Andres of central Colombia. Different degrees of

thermal resetting in the Mesozoic rift-related and Cenozoic foreland-basin sedimentary units in this sector of the orogen enable us to employ fission-track thermochronology to constrain the exhumation history of the sedimentary basins.

Zircon fission-track reset ages were found in Lower Cretaceous and older units from the Eastern Cordillera in the southern part of the study area (~4.5°N). These reset ZFT ages are younger than 25 Ma (late Oligocene) and occur in the immediate hanging wall of the range-bounding reverse faults that limited a Mesozoic rift basin and were subsequently reactivated in contraction during the Cenozoic. To the north, in the Floresta and Santander massifs, and to the east, in the areas outside of the Mesozoic rift, postdepositional burial was insufficient to reset the ZFT thermochronometric system.

Reset apatite fission-track ages occur in the Upper Cretaceous and older units from the eastern sector of the Eastern Cordillera. Like the ZFT ages, reset AFT ages are younger than 25 Ma. An exception to this pattern was observed in the western foothills of the Eastern Cordillera, where ~ 66 Ma published AFT ages from Upper Cretaceous samples are partially reset (Gómez, 2001; Gómez et al., 2003). We interpret this pattern to be the result of the earlier incorporation of this sector of the range into the fold-and thrust-belt, which interrupted burial and prevented a full thermal resetting of Upper Cretaceous sandstones.

We interpret the thermochronogical ages as reflecting erosional exhumation triggered by mountain building associated with shortening. Our main thermochronologic results are summarized as follows: (1) Reset ZFT ages in the western sector of the Eastern Cordillera, along the Villeta Anticlinorium, reveal that exhumation began before 25 Ma in this sector of the range; (2) Farther to the east, reset AFT ages from the Lower Cretaceous strata in the Floresta Massif and thermal modeling of AFT data from partially reset Cenozoic sandstones in the axial Eastern Cordillera suggest initiation of cooling sometime between 40 and 30 Ma. (3) ZFT and AFT ages in the Quetame Massif, along with the structural relations of the contractionally reactivated faults, suggest onset of exhumation at ~20 Ma. (4) Samples from the Quetame Massif suggest that apparent exhumation rates during the Miocene were lower than in the Pliocene. Faster exhumation in the Pliocene has been independently documented in the Quetame Massif by means of apatite age-elevation profiles (Mora et al., 2008b). The consistency of these two results demonstrates the validity of our approach.

Long-term propagation of the northern Andes in central Colombia occurred at rates of 2.5-2.7 mm/yr. An integrated analysis of the new thermochronologic data with published structural, thermochronologic and geodynamic evidence of rock uplift reveal that this advance occurred in three stages. An initial Upper Cretaceous-early Eocene episode of orogen migration occurred at rates of 0.5-3.1 mm/yr (1σ error) and accounts for up to 26% of the present width of the orogen. This episode was followed by very rapid orogenic advance during the middle Eocene-early Miocene, at average rates of 4.1-18.0 mm/yr, which lead to the inversion of the Eastern Cordillera. We propose that this acceleration in the orogenic advance was produced by an increase in the accretionary flux that resulted from an increase in the plate convergence rate and a decrease in its obliquity with respect to the inherited

structural grain. By the end of this episode of fast propagation, the orogen had reached ~86% of its present width. Finally, slow propagation resulted from stagnation of the deformation front along the Servitá fault during the Miocene. Preferential accommodation of deformation along this crustal anisotropy inherited from the Mesozoic rifting resulted in rates of orogenic advance of 1.2-2.1 mm/yr.

Our data demonstrate that episodic orogenic advance may result from contractional reactivation of pre-strained basement in the orogenic foreland, whereby weak anisotropies inherited from previous tectonic events tend to concentrate slip and deformation. This mode of deformation and orogenic growth is apparently also represented in the Santa Barbara system and the northern Sierras Pampeanas of NW Argentina, where deformation tends to be accommodated along basement inhomogeneities inherited from previous tectonic events (e.g., Allmendinger et al., 1983; Hilley et al., 2005; Mortimer et al., 2007; Ramos et al., 2002; Strecker et al., 2008). In conclusion, our dataset illustrates the need for integrating structural reconstructions of uplifting mountain ranges with thermochronologic data to provide a comprehensive and more realistic account of the complex processes governing orogenic growth.

ACKNOWLEDGEMENTS

We are grateful to Hocol S.A and Ecopetrol for permission to publish the apatite fission-track data presented in this work. P. O´Sullivan from Apatite to Zircon Inc. conducted the unpublished AFT analyses and provided detailed methodologic information presented in Appendix B. Diane Seward (ETH Zurich) kindly provided information and advice on the zircon fission-track methodology and sample preparation. Elias Gómez and Ian Duddy (Geotrack International) kindly provided raw data from published AFT samples from the Magdalena Basin. We thank Brian Horton, Paolo Ballato and Carlos Jaramillo for helpful discussions and Birgit Fabian for graphic work. Exhaustive revisions of an earlier version of this work by two anonymous reviewers significantly improved the ideas discussed in this paper. We thank A. Velázquez, J.G. Vargas and Y. García for discussions and help during the field work. This study was supported by grants and fellowships from the German Academic Exchange Service (DAAD) to M Parra and A. Mora, the German Research Foundation (DFG), Str 373/19-1 to M. Strecker, funds from the Leibniz Center for Earth Surface and Climate Studies at Potsdam University, and Universidad Nacional de Colombia (Beca de Honor to M. Parra).

Chapter 4

Tectonic controls on Cenozoic foreland basin development in the north-eastern Andes, Colombia

ABSTRACT

In order to evaluate the relationship between thrust loading and sedimentary facies evolution, we analyzed gravel progradation in the retroarc foreland basin system of the north Andes of Colombia. We compare sedimentary facies distribution with one-dimensional Eocene to Recent sediment-accumulation rates in the Medina wedge-top basin and a three-dimensional sedimentary budget based on the interpretation of ~1800 km of industry-style seismic reflection profiles and borehole data. Age constraints are derived from a new chronostratigraphic framework based on palynology. The sedimentological data from the Medina Basin reveal rapid accumulation of fluvial and lacustrine sediments at rates of up to ~500 m/my during the Miocene. Provenance data based on gravel petrography and paleocurrents reveal that these Miocene fluvial systems were sourced from Upper Cretaceous and Paleocene sedimentary units exposed to the west, in the Eastern Cordillera. Peak sediment-accumulation rates in the upper Carbonera Formation and the Guayabo Group occur during episodes of coarse-grained facies progradation in the early and late Miocene proximal foredeep. We interpret this positive correlation between sediment accumulation and gravel deposition as the direct consequence of thrust activity in the Servitá-Lengupá faults. This contrasts with current models relating gravel progradation to episodes of tectonic quiescence in more distal portions of foreland basin systems.

4.1. INTRODUCTION

Grain-size trends and the basinwide distribution of coarse-grained strata in foreland basins have been used to interpret the tectonic and climate-related controls on foreland basin accumulation (e.g., Flemings and Jordan, 1990; Heller and Paola, 1992; Paola et al., 1992). Several mechanisms have been proposed to account for the progradation of coarse-grained sediments in foreland basins: (1) uplift of the source areas by either increased tectonic activity in the fold-and thrust belt (e.g., Burbank et al., 1988; Horton et al., 2004) or erosionally-driven isostatic rebound (e.g., Burbank, 1992); (2) an increase in the efficiency of erosion triggered by high-frequency global climatic oscillations (e.g., Molnar, 2004) or by orographic effects (Hoffman and Grotzinger, 1993; Masek et al., 1994); (3) tectonic quiescence favoring a decrease in subsidence and progradation of coarse-grained sediments to the distal part of the basin (e.g., Heller et al., 1988; Flemings and Jordan, 1990; Burbank, 1992; Heller and Paola, 1992); and (4) changes in the resistance to erosion of the source areas (e.g., DeCelles et al., 1991; Carroll et al., 2006). Numerical modeling has been used to evaluate the thresholds of these controlling factors on the overall distribution of coarse-grained facies in basins with different flexural rigidities (e.g., Flemings and Jordan, 1989, 1990; Sinclair et al., 1991; Paola et al., 1992). A critical

factor determining the sedimentary response in the basin to the above mentioned changes, however, involves a better knowledge of the time scales over which variations in the external forcings and associated erosional and depositional processes occur compared to an inherent background level of processes in the basin, which scale with basin length and diffusivity (Paola et al., 1992). While some debate has existed on the role of each of these factors in the distal portion of foreland basins (Burbank et al., 1988; Heller et al., 1988), combined field evidence and numerical models have demonstrated that coarse-grained sediments accumulate in the proximal part of foreland basins, usually within their flexural half-width, irrespective of the nature of the tectonic and climatic regimes (e.g., Flemings and Jordan, 1990; Jones et al., 2004). These inherent characteristics complicate a rigorous assessment of the role exerted by each of these competing factors on the accumulation of coarse-grained sediment in proximal sectors of foreland basins. Nevertheless, deconvolving such relations from the tectonically and climatically controlled forcing factors reflected in depositional characteristics are critical for understanding the tectonic and sedimentary processes of convergent orogenic belts as well as the spatiotemporal trends in orogenic processes. This is particularly true in the northern Andes, where contractional deformation and orogenic growth have been linked with reactivated long-lived basement anisotropies (Mora et al., 2008b; Parra et al., 2008) that have fundamentally influenced the loci of tectonic deformation, erosion and sediment dispersal.

In the eastern Andes of central Colombia, the sedimentary record of subduction orogenesis is preserved in Late Cretaceous to Cenozoic basins that extend east of the Central Cordillera, the present-day magmatic arc (Fig. 4.1). Late Cretaceous crustal thickening along this range was related to initial accretion and subsequent oblique subduction of the oceanic proto-Caribbean Plate associated with initial foreland-basin development (Cooper et al., 1995; Gómez et al., 2003; Gómez et al., 2005). A determining factor for the Cenozoic evolution of the Andean orogen north of ~2°N has been the presence of a Mesozoic rift basin in the area presently occupied by the Eastern Cordillera (e.g., Campbell and Bürgl, 1965; Mora et al., 2006; Sarmiento-Rojas et al., 2006). In the course of Cenozoic contraction, major inherited extensional faults became the locus for preferential accommodation of thrust loading and deformation (Mora et al., 2006; Mora et al., 2008b; Parra et al., 2008; see also Chapter 3). In particular, the major Mesozoic rift-bounding Servitá-Legupa faults, located ~30 km west of the presently active orogenic front, have focused protracted contractional deformation since at least early Miocene time (Parra et al., 2008; see Chapter 3) and therefore prevented a significant eastward advance of the orogenic front. This configuration has led to unroofing of progressively older structural levels from the eastern flank of the Eastern Cordillera and resulted in the coeval accumulation of sediments in the Llanos Basin broken foreland basin to the east. Plio-Pleistocene eastward advance of the orogen to the present-day frontal structure (Mora, 2007) has incorporated only the proximal part of this Mio-Pliocene foredeep into the orogen in the form of the Medina wedge-top basin. This exhumed foredeep offers a unique, yet aerially limited location where the sedimentary record of the late stages of Andean uplift and exhumation are well exposed. However, due to the

absence of radiometrically datable minerals and the paucity of published biostratigraphic markers, the sedimentary evolution and its relation with Andean tectonic and climatic evolution are still unclear.

In this study we present previously unreleased seismic reflection data that refine earlier estimates on the age of thrust initiation and unravel the tectono-sedimentary evolution along the eastern margin of the Eastern Cordillera. We also present new field-based sedimentological and provenance data and the first systematically acquired biostratigraphic database for the proximal foredeep deposits in this area, based on detailed palynology. In order to understand the causes of sedimentary facies distribution and to discriminate among multiple potential forcings, we compare one-dimensional Eocene to Pliocene sediment-accumulation rates in the Medina Basin with a three-dimensional sedimentary budget in an area of ~5000 km^2 based on the interpretation of ~1800 km of industry-style seismic reflection profiles and borehole data tied to the new biostratigraphic framework. Importantly, our data show that in contrast to many other mountain belts, episodes of coarse-grained sedimentation occur are coeval with rapid subsidence throughout basin history, illustrating that increased tectonic activity in the Eastern Cordillera has exerted a dominant control on the geometry and pattern of sediment distribution

4.2. GEOLOGIC BACKGROUND

4.2.1. Geodynamic and structural setting

The Medina Basin is a 90 × 25 km wedge-top depocenter located atop the most external east-verging thrust-sheet along the eastern margin of the Eastern Cordillera of the Colombian Andes (Fig. 4.1). This range is the easternmost branch of the retroarc fold-and-thrust belt related to Late Cretaceous to Cenozoic shortening resulting from the complex interaction between the Nazca, Caribbean and South American plates (e.g., Cooper et al., 1995; Taboada et al., 2000; Gómez et al., 2005; Parra et al., 2008). Late Cretaceous (~80 Ma) oblique accretion of relicts of a Pacific oceanic plateau (e.g., Kerr and Tarney, 2005; Vallejo et al., 2006) constitutes the Western Cordillera and triggered crustal shortening and thickening and initial mountain building along the present-day Central Cordillera (e.g., Cooper et al., 1995). The tectonic loading exerted by this range created a foreland-basin system east of the Central Cordillera (Cooper et al., 1995; Gómez et al., 2005). Subsequent deformation compartmentalized the foreland basin in a non-systematic manner due to the selective reactivation of crustal anisotropies inherited from Proterozoic and Paleozoic collision and subduction episodes (e.g., Restrepo-Pace et al., 1997; Cediel et al., 2003 and references therein). However, most important for the Cenozoic evolution of this region are extensional structures generated during Mesozoic rifting (e.g., Cooper et al., 1995; Mora et al., 2006; Sarmiento-Rojas et al., 2006). In this context, initial middle Eocene tectonic inversion of Mesozoic rift basins in the area of the present-day Eastern Cordillera disrupted the once contiguous foreland basin and formed two principal Cenozoic basins: the Middle Magdalena Valley Basin to the west, and the Llanos basin to the east (e.g., Gómez et al., 2003; Parra et al., 2008). During inversion, major rock uplift in the Eastern Cordillera occurred

through reverse slip along the formerly rift-bounding faults. These major faults are the east-dipping Bituima-La Salina faults, to the west, and the west-dipping Servitá-Lengupá faults to the east (Fig. 4.1). This has resulted in the formation of a bivergent thick-skinned fold-and-thrust belt with the loci of maximum exhumation coinciding with the proximal hanging-wall blocks of inverted Mesozoic normal faults whose orientation was favorable with respect to absorbing compressional stresses during the Andean orogeny (Mora et al., 2006). Prominent examples of the more deeply exhumed sectors in the Eastern Cordillera are the Villeta Anticlinorium on the western flank of the range, and the Floresta and Quetame basement massifs in the axial and eastern sectors. Outside of the Mesozoic rift domain, én-echelon arranged, northeastward stepping, thin-skinned Cenozoic thrust sheets with opposite vergence overthrust the Magdalena and Llanos basins above detachment surfaces within mechanically weak Cretaceous and Paleogene strata (e.g., Butler and Schamel, 1988; Cooper et al., 1995; Gómez et al., 2003; Mora et al., 2008b).

4.2.2. Stratigraphy of the Eastern Cordillera

Pre-Devonian low-to medium-grade phyllites, quartzites and schists, and sparse Paleozoic intermediate to acid intrusives characterize the basement rocks of the Quetame and Floresta massifs in the eastern flank the Eastern Cordillera (Segovia, 1965; Ulloa and Rodríguez, 1979, Ulloa and Rodríguez, 1982; Jiménez, 2000). In this region, metamorphic basement rocks are unconformably overlain by up to ~4 km of Devonian marginal marine mudstones and sandstones and Carboniferous nonmarine red beds (e.g., Ulloa and Rodríguez, 1979; Fig. 4.2). These units are in turn superseded by Mesozoic rift-related units including: (1) up to 2 km of Early to Late Jurassic lacustrine and volcanoclastic rocks, locally deposited in narrow half-graben basins in the western half of the present-day mountain range (e.g., Kammer and Sánchez, 2006; Sarmiento-Rojas et al., 2006); (2) up to ~5 km of synrift, predominantly mudstone-dominated platformal units of Early Cretaceous (Berriasian to Aptian) age, deposited in a wider rift basin whose limits approximately coincide with the margins of the present-day mountain range (Mora et al., 2006; Mora et al., 2008a); and (3) up to 2 km of postrift, shallow marine sandstones and mudstones, deposited within and beyond the structural limits of the rift, including areas of the Llanos and Magdalena basins (e.g., Cooper et al., 1995; Mora et al., 2006; Sarmiento-Rojas et al., 2006). In the Eastern Cordillera, these units include decimetric layers of glauconitic sandstones in the Une, Chipaque and Guadalupe Formations (Guerrero and Sarmiento, 1996; Vergara and Rodríguez, 1996), foraminifera-bearing siliceous siltstones and phosphatic sandstones (Guadalupe Group, e.g., Föllmi et al., 1992; Vergara and Rodríguez, 1996), which constitute lithologic important markers that help constrain the provenance of Cenozoic sedimentary units.

The onset of nonmarine to transitional sedimentation in the Eastern Cordillera is recorded by the up to 1100-m-thick coastal plain, estuarine, and fluvial sedimentary rocks of the late

Maastrichtian-early Paleocene Guaduas Formation (Sarmiento, 1992). This unit is interpreted as the distal equivalent of coarse-grained, westerly sourced synorogenic deposits of the Magdalena Valley

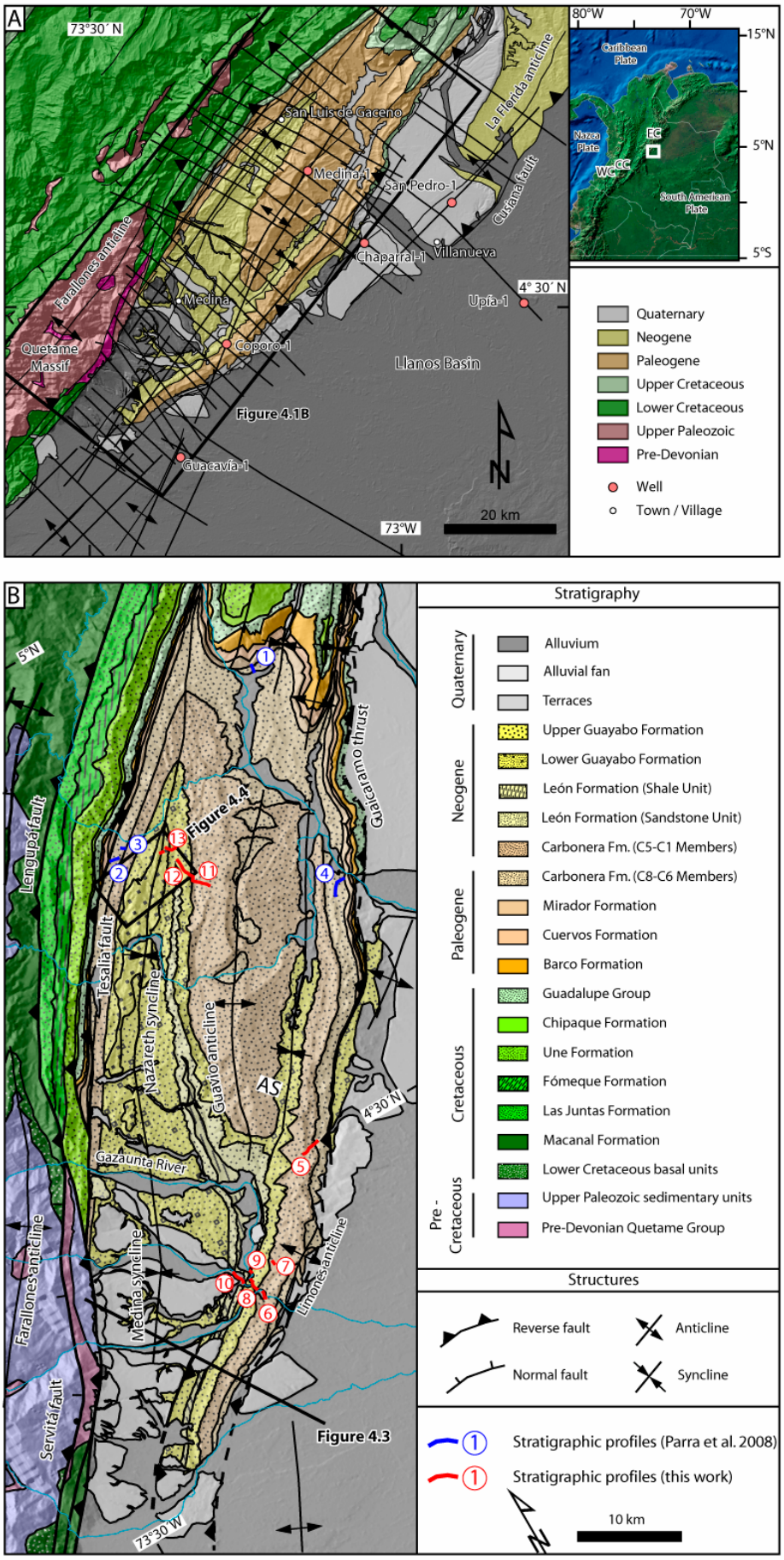

Figure 4.1. (A) Geologic map of the eastern flank of the Eastern Cordillera (after Mora et al., 2008b and Parra et al., 2008) showing main structures in the northern sector of the Quetame Massif and the adjacent Medina (black box) and Llanos basins. Locations of seismic lines and wells are indicated. Inset map denotes the location of the Western (WC), Central (CC) and Eastern (EC) cordilleras within the Colombian Andes. White box in inset indicates the location of the main map. **(B)** Geological map of the Medina Basin (location shown in Fig. 4.1A). Locations of growth strata (Figs. 4.3 and 4.4) and measured stratigraphic sections are shown.

(Gómez et al., 2005). In the Medina Basin, only ~60 m of the Guaduas Formation (Guerrero and Sarmiento, 1996) are preserved below a regional unconformity associated with forebulge erosion (Gómez et al., 2005) (Fig. 4.2). Here, the overlying Cenozoic units comprise two megasequences of late Paleocene and Eo-Pliocene age, respectively, that progressively onlap eastward onto the Mesozoic substratum of the Llanos Basin (Cooper et al., 1995; Fig. 4.2). The first sequence consists of up to ~700 m of estuarine and coastal plain deposits of the Barco and Los Cuervos (or Arcillolita del Limbo) Formations (Ulloa and Rodríguez, 1979; Cazier et al., 1995; Cooper et al., 1995; Guerrero and Sarmiento, 1996; Cazier et al., 1997; Jaramillo and Dilcher, 2000; Jaramillo et al., 2006). The second sequence comprises ~5-km-thick lower Eocene to Neogene strata that thin eastward and rest unconformably upon progressively older Paleocene and Cretaceous units toward the east, in the Llanos Basin. As a result, the chronostratigraphic gap below the basal sandstones of this sequence increases toward the Llanos Basin (Jaramillo et al., 2008; Fig. 4.2). This sequence comprises up to ~250 m of estuarine valley-fill and coastal-plain deposits (Cazier et al., 1997) of the lower to middle Eocene Mirador Formation (or Arenisca del Limbo Formation) that are superseded by up to ~3 km of estuarine and locally marine deposits of the Carbonera Formation (Cazier et al., 1995; Cooper et al., 1995; Cazier et al., 1997; Bayona et al., 2008; Parra et al., 2008). The Carbonera Formation consists of eight members (the C1-C8 members) of interlayered sandstone- and mudstone-dominated deposits (e.g., Cooper et al., 1995). Rapid sediment accumulation within an eastward-thinning sedimentary wedge with pronounced facies changes in the upper Eocene-Oligocene lower part of the Carbonera Formation can be inferred for the western part of the Medina Basin and has been related to initial uplift of the axial Eastern Cordillera (Parra et al., 2008; see Chapter 3). These strata are overlain by the approximately 500-m-thick León Formation (Cooper et al., 1995), which records lacustrine deposition with short-lived marine incursions (Bayona et al., 2008) prior to the onset of protracted nonmarine sedimentation documented by distal to proximal alluvial deposits of the Lower Guayabo and Upper Guayabo Formations (Cooper et al., 1995). The Upper Guayabo Formation intersects the present-day erosion surface and has an exposed minimum thickness of ~700 m. Our field observations and geologic mapping show that the spatial distribution of the upper Carbonera Formation and younger units is affected by numerous facies changes leading to a significantly different stratigraphic column for the eastern and western sectors of the Medina Basin. In this study we focus on the the Miocene-Pliocene stratigraphy of this broken foreland basin.

4.2.3 Structure

The Medina Basin constitutes the hanging wall of a thin-skinned thrust sheet that extends ~40 km east of the Tesalia fault (Fig. 4.1). Here, the Guavio anticline is a broad fault-bend fold related to the Guaicaramo thrust. Subsurface data and structural interpretation suggest that this thrust splays at depth from the Tesalia fault (Mora et al., 2006) and propagates along two decollement levels within the Lower Cretaceous Macanal Formation and the Upper Cretaceous Chipaque Formation (Rowan and

Linares, 2000). The thrust propagates to a higher decollement above an underlying normal fault and, farther east, has generated a fault-propagation fold (Limones anticline) in its hanging wall (Fig. 4.1b). In the northern part of the Medina Basin, west of the Guavio anticline, the Nazareth syncline is a highly asymmetric, east-verging fold that forms the westernmost structure in the area. The western limb is overturned and constitutes the northern extent of the western Medina syncline. The steepening of the western limb of the Medina syncline occurs where the deformation style changes at the eastern margin of the Quetame massif: in the south it is primarily accommodated by thrusting along the Servitá fault, whereas in the north deformation has resulted in fault-propagation folding (Fig. 4.1b). Farther east, in the footwall of the Guaicaramo thrust, follows the Llanos Plain in the modern foredeep depozone. Here, deformation is minor and results primarily from the southward propagation of the Cusiana fault and the associated hanging-wall La Florida anticline, a structure corresponding to a more frontal depocenter within the én-echelon segments of the eastern fold-and-thrust belt. To a lesser

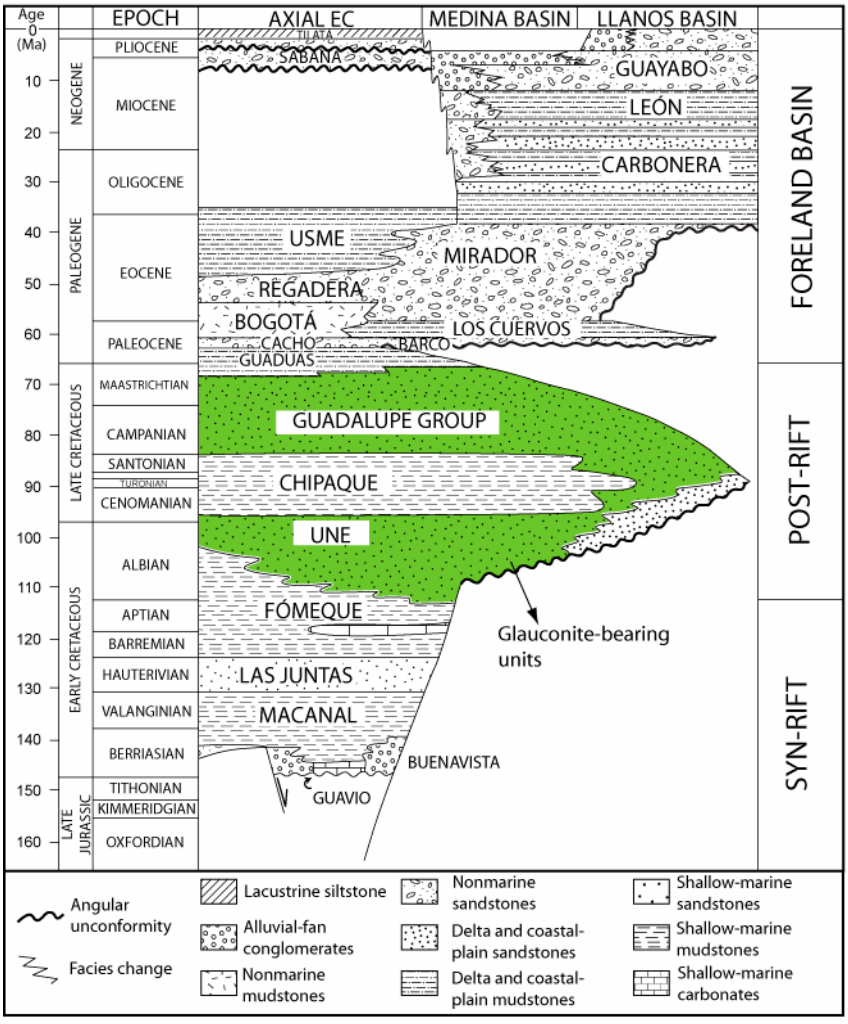

Figure 4.2. Chronostratigraphic diagram of the Cretaceous-Cenozoic strata in the eastern flank of the Eastern Cordillera (after Gómez, et al., 2005; Mora et al., 2008b; and Parra et al., 2008). Green shading represents lithostratigraphic units with glauconitic sandstones used to evaluate the unroofing of the source areas (see text for discussion).

degree, deformation is also associated with minor normal faulting within the Cenozoic deposits, imaged in seismic reflection profiles and interpreted to be related to forebulge extensional faulting (Bayona et al., 2008).

4.2.4 Chronology of foreland basin deformation

Crustal thickening in the Central Cordillera since Late Cretaceous time (~75-80 Ma) led to initial foreland-basin formation in Central Colombia (e.g., Cooper et al., 1995; Gómez et al., 2005). Eastward advance of the orogenic front has taken place episodically, with stages of fast advance associated with disruption of the basin through initial bivergent inversion of the Eastern Cordillera. This was triggered by an increase in the rate and decreasing obliquity of convergence in the middle-late Eocene (40-30 Ma; see Chapter 3). Likewise, stagnation of the deformation front has resulted from contractional deformation being preferentially accommodated along crustal inhomogeneities inherited from previous tectonic events (Mora et al., 2008b; Parra et al., 2008). In particular, this pattern has been documented for the contractionally reactivated Servitá-Lengupá faults along the eastern limit of the Quetame basement high. There, zircon fission-track data constrains the minimum age of initial deformation-related exhumation associated with slip along this fault as ~20 Ma (see Chapter 3). Subsequent deformation and erosion of the Cenozoic strata in the vicinity of the trace of the Lengupá fault has prevented the determination of tighter age constraints on initial deformation. However, despite these limitations, growth-strata relations in early Miocene units of the lower Carbonera Formation (described below) support previous interpretations of an early Oligocene-early Miocene onset of thrusting along this fault (see Chapter 3). Protracted deformation and tectonic loading along this structure is inferred from a Miocene increase in the tectonic subsidence of the Medina (Parra et al., 2008) and Llanos (Bayona et al., 2008) basins. Moreover, absence of growth strata in the Miocene-Pliocene strata in the footwall of the Guaicaramo thrust, as deduced from the analysis of industry seismic lines (Mora, 2007), provides a maximum age of ~5 Ma for initial thrusting along this fault. This pattern thus demonstrates Miocene-Pliocene stagnation of the deformation front along the long-lived crustal anisotropy of the Servitá-Lengupá faults and subsequent post-Pliocene migration of the deformation front to its present location along the Guaicaramo thrust (Mora, 2007; see also Chapter 3).

4.3. METHODS

Detailed mapping of an area of ~1500 km^2 provides the basis for stratigraphic profiling of Neogene foreland basin strata. We conducted sedimentary facies interpretation, paleocurrent and provenance determinations on 9 measured sections, totaling ~5.3 km, of the Carbonera Formation and the Guayabo Group exposed in the Medina Basin (Fig. 4.1). Correlations between measured sections either are based on tracing of laterally continuous lithostratigrahic units over distances of a few kilometers within individual limbs of folds or on subsurface extrapolation of outcrop exposures in

seismic reflection profiles where surface correlation is impossible due to erosion. A new chronological framework of sediment accumulation is provided on the basis of a palynological study performed on ~500 samples.

Paleocurrent directions were derived from imbricated clasts, channel-axis directions and trough cross-bedding. Sixteen conglomerate clast counts were conducted to reveal the unroofing history of the source areas. A minimum of 100 clasts were counted in individual, clast-supported conglomerate layers, using a 10 cm grid. Conglomerate petrography data are reported in Table 4.1.

We evaluate the spatial and temporal patterns of sediment accumulation in the Medina and Llanos basins by assessing both one-dimensional and volumetric sedimentary budgets. First, we reconstruct one-dimensional, decompacted sediment-accumulation rates along a composite stratigraphic section in the Medina wedge-top basin. A composite stratigraphic section of the Late Cretaceous–Pliocene units of the Medina Basin was constructed by combining the measured profiles of Mio-Pliocene units presented in this study and sections for older units presented by Parra et al. (2008) and Jaramillo and Dilcher (2000). Sediment-accumulation rates are estimated using thickness and age constraints based on the palynological biozonation. In order to account for anomalies in measured stratigraphic thicknesses derived from progressive loss of porosity with burial depth and inhomogeneous compaction of mechanically different lithologies, we used a porosity-depth relation to estimate decompacted thicknesses (Sclater and Christie, 1980). Decompaction parameters and detailed results are presented in Table C1 in Appendix C. Second, we estimate the volume of sedimentary strata accumulated for specific intervals in the Medina Basin and the proximal, western sector of the Llanos Basin by interpreting an extensive grid of ~1800 km of 2D industry seismic reflection data (Fig. 4.1). Mapped units were translated into the grid of seismic lines by direct extrapolation of surface outcrops in the Medina Basin. In addition, seismic reflectors were tied to the stratigraphy with data from seven hydrocarbon-exploration boreholes, especially in areas with no surface exposure within the footwall of the Guaicaramo thrust. The accumulated (compacted) volume of rock was estimated from the seismic data by converting the vertical time axis into depth. We used check-shot surveys from seven boreholes across the Medina and Llanos basins to evaluate the seismic velocities in Cenozoic strata. The near-surface velocity gradient decreases eastward from ~3900 m/s in the Medina Basin (Coporo-1 Well) to ~2800 m/s in the easternmost part of the study area in the Llanos Basin (Upia-1 Well; see Appendix C, Fig. C1). We therefore derived different depth-time relations for the hanging and footwalls of the Guicaramo thrust by combining information from available wells in each fault block.

4.4. RESULTS

4.4.1 Growth strata and growth unconformities

First, growth-strata relationships and unconformities are well preserved in different stratigraphic levels along the western margin of the Medina Basin. In seismic line MVI-1020, a

package of divergent reflectors in strata equivalent to the lower part of the C5-C2 members of the Carbonera Formation occurs within the western limb of the Medina syncline (Fig. 4.3). A westward decrease in stratal thickness and onlap geometries suggests contemporaneous sedimentation and tilting of the forelimb of the fault-propagation Farallones anticline (e.g., Riba, 1976). These geometries constrain a minimum, early Miocene age for the initiation of slip along the Lengupá fault. Second, in the northwestern part of the basin, growth strata and growth unconformities in strata of the upper Miocene-Pliocene Guayabo Group exist in the western flank of the Nazareth syncline at ~4° 40´ N (Fig. 4.1). There, an up-section decrease in dip angle of 50-60° is accompanied by erosional truncation of steeply southeastward-dipping conglomeratic strata of the top of the Lower Guayabo Formation (Fig. 4.4). This geometry reveals continued deformation through rotation of the Farallones anticline forelimb. Overall, these syncontractional stratal geometries in different stratigraphic intervals of the Mio-Pliocene units of the western Medina Basin document inversion, protracted reverse faulting, and fault-related folding associated with the long-lived Lengupá fault.

TABLE 4.1: GRAVEL PETROGRAPHY DATA FOE EOCENE-PLIOCENE UNITS OF MEDINA BASIN

Sample	UTM East	UTM North	Thickness	Unit	Quartz	Chert	Mdst	Sdst	Sil. Stst	Gl. Sdst	Phos. Sdst	Shale	Total
MP 603	1094728	1023645	0	C7	64	36	0	0	0	0	0	0	100
					64%	**36%**	**0%**	**0%**	**0%**	**0%**	**0%**	**0%**	**100%**
MP 605	1094989	1023198	300	C7-C6	61	36	3	0	0	0	0	0	100
					61%	**36%**	**3%**	**0%**	**0%**	**0%**	**0%**	**0%**	**100%**
MP 607	1095417	1023145	600	C7-C6	70	27	2	1	0	0	0	0	100
					70%	**27%**	**2%**	**1%**	**0%**	**0%**	**0%**	**0%**	**100%**
MP 608	1095567	1023223	870	C7-C6	65	25	8	0	2	0	0	0	100
					65%	**25%**	**8%**	**0%**	**2%**	**0%**	**0%**	**0%**	**100%**
MP 642	1078675	998906	1740	C5-C2	20	12	4	60	2	0	2	0	100
					20%	**12%**	**4%**	**60%**	**2%**	**0%**	**2%**	**0%**	**100%**
MP 610	1097950	1023786	2010	C5-C2	37	13	14	32	0	1	0	0	97
					38%	**13%**	**14%**	**33%**	**0%**	**1%**	**0%**	**0%**	**100%**
MP 611	1097703	1023225	2280	C5-C2	39	15	5	32	11	2	0	0	104
					38%	**14%**	**5%**	**31%**	**11%**	**2%**	**0%**	**0%**	**100%**
MP 612	1097436	1022554	2660	C5-C2	11	8	2	19	19	15	2	0	76
					14%	**11%**	**3%**	**25%**	**25%**	**20%**	**3%**	**0%**	**100%**
MP 613	1097406	1022196	2990	C1	15	4	3	64	10	4	0	0	100
					15%	**4%**	**3%**	**64%**	**10%**	**4%**	**0%**	**0%**	**100%**
MP 641	1081015	997960	3100	Lower Guayabo	0	0	0	100	0	0	0	0	100
					0%	**0%**	**0%**	**100%**	**0%**	**0%**	**0%**	**0%**	**100%**
MP 615	1097349	1021870	3210	Lower Guayabo	13	8	10	65	4	4	0	0	104
					13%	**8%**	**10%**	**63%**	**4%**	**4%**	**0%**	**0%**	**100%**
MP 616	1097646	1021490	3700	Lower Guayabo	0	2	4	102	0	0	0	0	108
					0%	**2%**	**4%**	**94%**	**0%**	**0%**	**0%**	**0%**	**100%**
MP 626	1100576	1021315	3750	Lower Guayabo	5	2	14	53	2	26	0	0	102
					5%	**2%**	**14%**	**52%**	**2%**	**25%**	**0%**	**0%**	**100%**
MP 618	1097677	1021210	3945	Upper Guavabo	0	0	0	70	0	30	0	0	100
					0%	**0%**	**0%**	**70%**	**0%**	**30%**	**0%**	**0%**	**100%**
MP 627	1099965	1021794	3990	Upper Guavabo	3	1	4	69	3	20	0	2	102
					3%	**1%**	**4%**	**68%**	**3%**	**20%**	**0%**	**2%**	**100%**
MP 623	1097582	1020934	4015	Upper Guavabo	0	2	4	86	0	8	0	0	100
					0%	**2%**	**4%**	**86%**	**0%**	**8%**	**0%**	**0%**	**100%**
MP 630	1099191	1021630	4700	Upper Guavabo	0	0	2	56	0	42	0	0	100
					0%	**0%**	**2%**	**56%**	**0%**	**42%**	**0%**	**0%**	**100%**

Counted gravel clasts and recalculated detrital modes. Sample coordinate system is Colombia Bogota Zone.

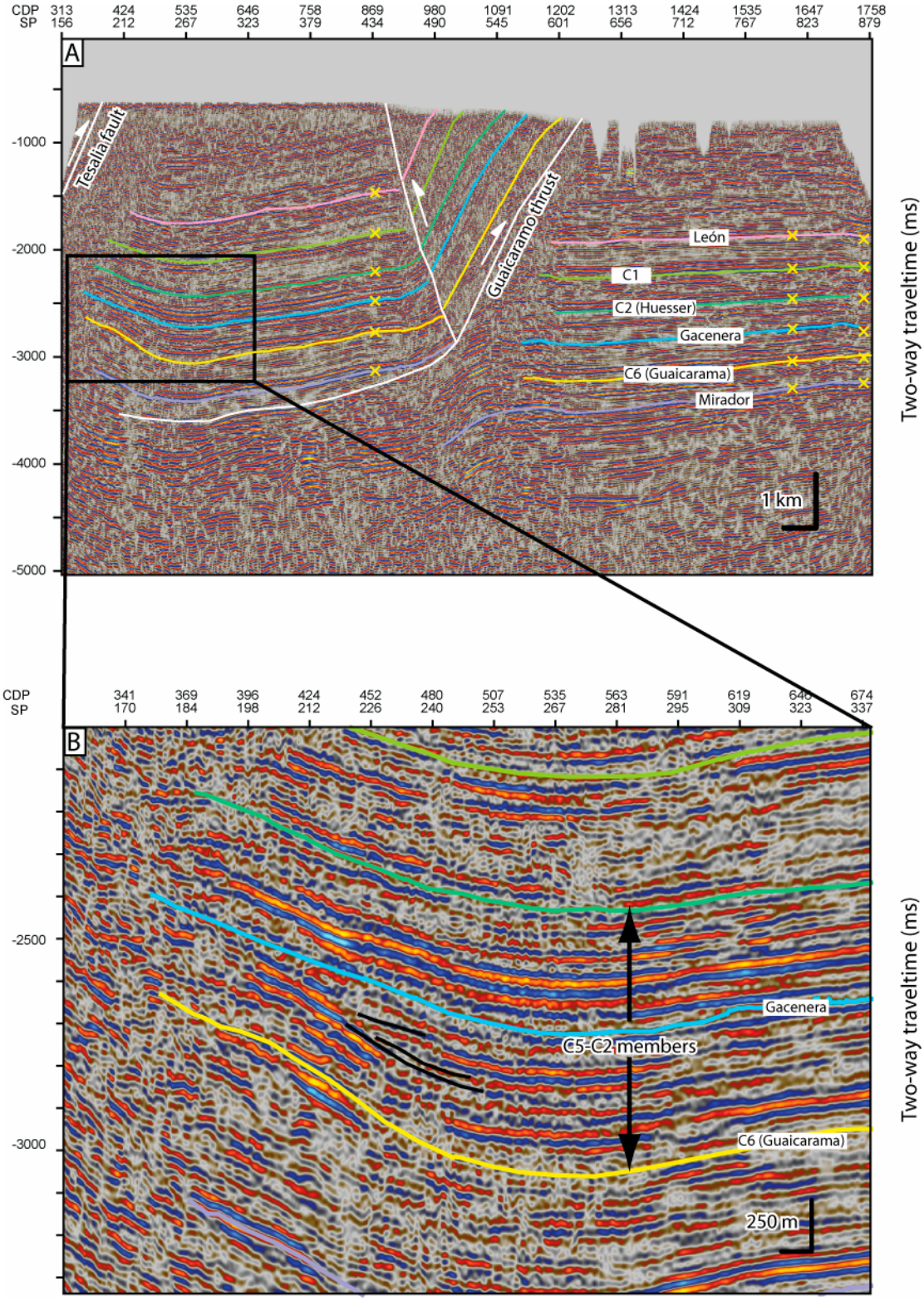

Figure 4.3. (A) Time-migrated seismic line MVI-1997-1070 across the southern sector of the Medina Basin depicting tops of interpreted Cenozoic units (see Figures 4.5, 4.6 and 4.8). For approximate vertical scale bar, vertical axis is based on a velocity correction of 4 km/s. Vertical exaggeration is 1.7X. **(B)** Detail of growth-strata geometries in the early Miocene C5-C2 members of the Carbonera Formation in the Medina syncline.

4.4.2. Sedimentary facies architecture of the Medina Basin

The upper Eo-Pliocene basin fill of the Medina Basin is reconstructed on the basis of 13 stratigraphic sections totaling ~7.4 km of strata which constitute the Carbonera (C8-C1 members), León, Lower Guayabo, and Upper Guayabo Formations. The characteristics of the lower 2.1 km of this record, comprising the C8-C5 members, has already been presented by Parra et al. (2008) based on four stratigraphic profiles with four facies associations that represent tidally-influenced deltaic, lacustrine, alluvial plain, and braided fluvial sedimentary environments. These four facies associations (FA1-FA4; Table 4.2) are also present in the upper members of the Carbonera Formation and overlying units that are the subject of this work. Therefore, here we build upon our previous work by complementing the description of the previously identified facies associations FA1-FA4 with new data from the upper Carbonera and León Formations. In addition, we add the description and interpretation of facies associations FA5 and FA6, which occur in the Upper Guayabo Formation. Facies associations are described on the basis of the recognition of sixteen lithofacies, following Parra et al. (2008). These descriptions are included in the supplementary material (Appendix C, Table C2). In the following section we focus on the interpretation of the spatial distribution of the six identified facies associations based on the measured stratigraphic profiles (Figs. 4.5 - 4.6), and the associated depositional processes and sedimentary environments.

4.4.2.1 Interpretation of facies associations

Facies Association 1 (coarsening-upward laminated sandstones)

Thin interbedded sandstone-mudstone couplets with lenticular and flaser lamination suggest tidal influence (Reineck and Wunderlich, 1968). The extensive areal extent of laterally continuous sandstone bodies with a variety of wavy, lenticular, flaser and cross lamination, as well as associated coal laminae and coal seams, suggests deposition in a transition zone between fluvial-marine and tide-dominated estuarine systems (e.g., Dalrymple et al., 1992; Dalrymple and Choi, 2007). The thickening- and coarsening-upward sequences evolve from laminated dark mudstones to wavy, lenticular, and finally to cross-stratified sandstones, suggesting an increase in current velocity (Collinson et al., 2006) and possibly indicating a decrease in water depth through time. This is compatible either with eustatically-controlled parasequences (e.g., Mitchum and Van Wagoner, 1991) or, alternatively, autogenic progradational successions, such as observed in delta-front deposits (e.g., Tye and Coleman, 1989; Coleman et al., 1998). Although dewatering structures, soft-sediment deformation, and growth faults indicate rapid deposition (Lowe, 1975; Owen, 1996) typical for deltaic enviroments (Coleman et al., 1998; Dalrymple et al., 2003), some allogenic control cannot be ruled out.

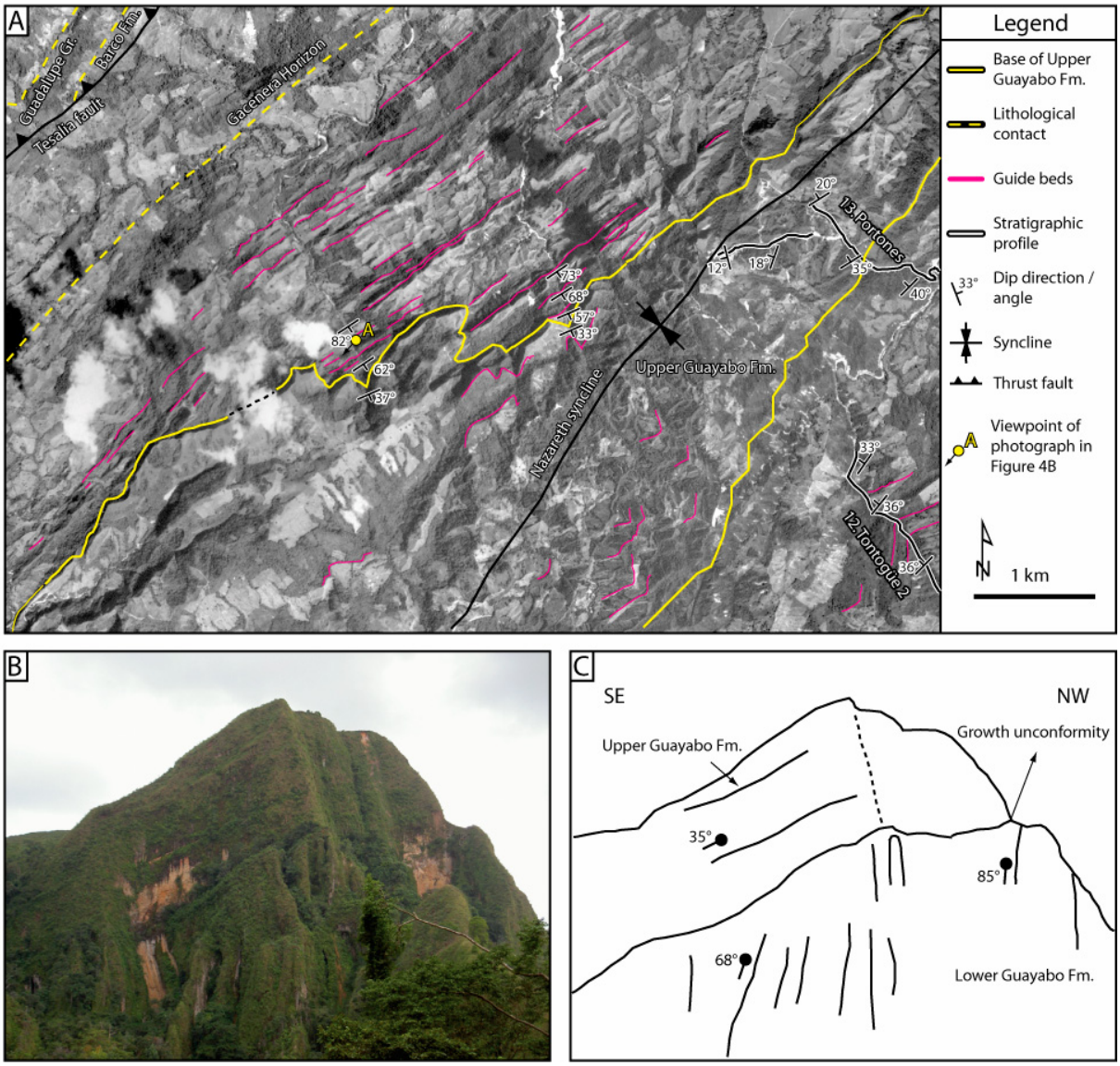

Figure 4.4. Growth-strata relationships in the northern Medina Basin. **(A)** Interpreted ortho-rectified aerial photograph depicting erosional truncation of steeply southeastward-dipping to subvertical conglomeratic units from the Lower Guayabo and older units, (lines in magenta to the left) below gently dipping conglomerates corresponding to the base of the base of the Upper Guayabo Formation (yellow line) in the western limb of the Nazareth syncline. Note erosion of progressively older units toward the southwest. (**B)** Photograph and **(C)** line drawing of conglomeratic growth geometries at the contact between the Lower Guayabo and Upper Guayabo Formations (viewpoint indicated in Figure 4.4 A). Note progressive up-section decrease in bedding dip, from subvertical in the lowermost strata (right) to ~ 60° at the top. Farther southeast (not shown) measured bedding dip is ~30° (see Figure 4.4 A).

Facies Association 2 (massive and laminated mudstones)

A marine influence is indicated by discrete thin levels with abundant microforaminiferal linings and dinoflagellates, including *Homotryblium floripes, Cordosphaeridium inodes, Polysphaeridium subtile, Achomosphaera, and Spiniferites*. The laterally continuous, dark-gray mudstone-dominated facies associated with thin, flaser-laminated sandstones and coal beds suggests deposition in a mud flat environment. This interpretation is supported by the presence of the bivalves

TABLE 4.2. SUMMARY OF EARLY MIOCENE-PLIOCENE FACIES ASSOCIATIONS

Facies Association	Description	Stratigraphic occurrence	Interpretation
FA 1 (coarsening-upward laminated sandstone)	Up to 8 m thick thickening- and coarsening-upwards intervals of tabular sandstone with minor thin interbeds of mudstone. Sandstone beds present non-erosive basal contacts and are frequently bioturbated. Laminae rich in organic-matter, plant remains. Thin pebble conglomerate commonly cap intervals at top. Typical lithofacies pattern includes, from base to top, Fm, Fl, Sw, Sf, Slc, Sr and Gco. Dewatering structures, convolute bedding and growth faults occur. Sandstone-mudstone couplets with wavy (Sw), lenticular (Slc), flaser (Sf) and oscilltory current ripple lamination (Sr).	Predominant lithofacies in C7, C5 and C3 members in the eastern margin of the basin. Common in lower part of C1.	Tidally-influenced deltaic environment. Growth faults, convolute bedding and water-escape structures suggest rapid accummulation. Possible allogenic control.
FA 2 (massive and laminated dark mudstone)	Thick intervals (up to 100 m) of dark-gray to greenish mudstone. Occasional minor bioturbation. Limited interbeds of trough cross-laminated sandstone, and up to 30-cm-thick coal seams. Occasional thin, disorganized bivalve-bearing shell-beds. Local microforaminiferal linings and dinoflagellates. Fragmented and disarticulated bivalves belonging to the genus *Pachydon, Anondondites* and *Mytylopsis,* and gastropods *Sheppardioncha (Fig. 4.7A)*. Discrete levels with microforaminiferal linings and dinoflagellates including *Homotryblium floripes, Cordosphaeridium inodes, Polysphaeridium subtile, Achomosphaera, and Spiniferites.*	In the eastern margin of the basin dominant facies in C8, C6, C4 and C2 members and in Leon Formation.	Mud flat in a deltaic plain. Coal indicates humid climate. Fragmented freshwater mollusk suggest a high-energy environment. Dinoflagellates and microforaminiferal linings indicate local marine influence
FA 3 (interbedded fluvial sandstones and conglomerates)	Medium- to thick-bedded, medium-to coarse grained, and pebbly sandstone. Gravel lags and mudstone intraclasts common at base of individual beds. Beds have erosive bases above mottled sandy mudstones and siltstones, and extend laterally up to few tens of meters. Commonly floating pebble clasts occur. Granule and pebble stringers loosely defining large-scale planar cross stratification occur rarely. Frequently, strata grade upward into variegated mudstone (FA4).	Interbedded with FA4 in Upper Carbonera (C5-C2 members) to the west, and in C1 and Lower Guayabo everywhere. Interbedded with FA5 and FA6 in Upper Guayabo Formation.	Stream flow deposits. Loosely defined large-scale, low-angle planar cross-stratification, absense of well defined normal grading and frequent floating pebbles suggest deposition in braided fluvial channels.
FA 4 (overbank fines)	Reddish to brown, massive to crudely stratified sandy mudstone and siltstone. Ubiquitous mottling and root traces (Fig. 4.7B). Sporadic mudcracks (Fig 4.7C) and iron nodules (Fig 4.7 D). Lenticular, normally graded, thin sandstone interbeds.	Dominant facies in C5-C2 members to the west and in C1 and Lower Guayabo to the east. Less frequent in Upper Guayabo.	Fluvial floodplain environment. Dissecation cracks, pervasive mottling and ferruginous nodules indicate pedogenesis during fluctuating wet-dry conditions.
FA 5 (granule to pebble conglomerates and sandstones)	Medium- to thick-bedded, clast-supported granule and pebble conglomerates. Individual beds have sheet-like and lenticular geometry, poor developed subhorizontal stratification and rarely low-angle through cross-stratification and clast imbrication. Moderate sorting. Flat, non erosional bases are common (Fig 4.7E). Interbedded with FA4 and FA3,	Occasionally in C1 member; Frequent in upper part of Lower Guayabo, and Upper Guayabo.	Stream flow deposits and hyperconcentrated flows in subaerial alluvial fans.
FA 6 (massive, coarse conglomerates and sandstones)	Up to 10 m-thick, dominantly clast-supported cobble and pebble conglomerate (Fig 4.7F). Subangular to well rounded clasts. Individual beds have ribbon-like geometry, latterally continuous for tens of metes and display basal scours. Moderate to poor sorting, ungraded to reverse grading and crude imbrication. Lenticular sandstone interbeds. Lithofacies Gcd, Gco, Sm. Interbedded with FA3 and FA4.	Exclusively in Upper part of lower Guayabo, and Upper Guayabo.	Gravel bars in fluvial channels on alluvial fan.

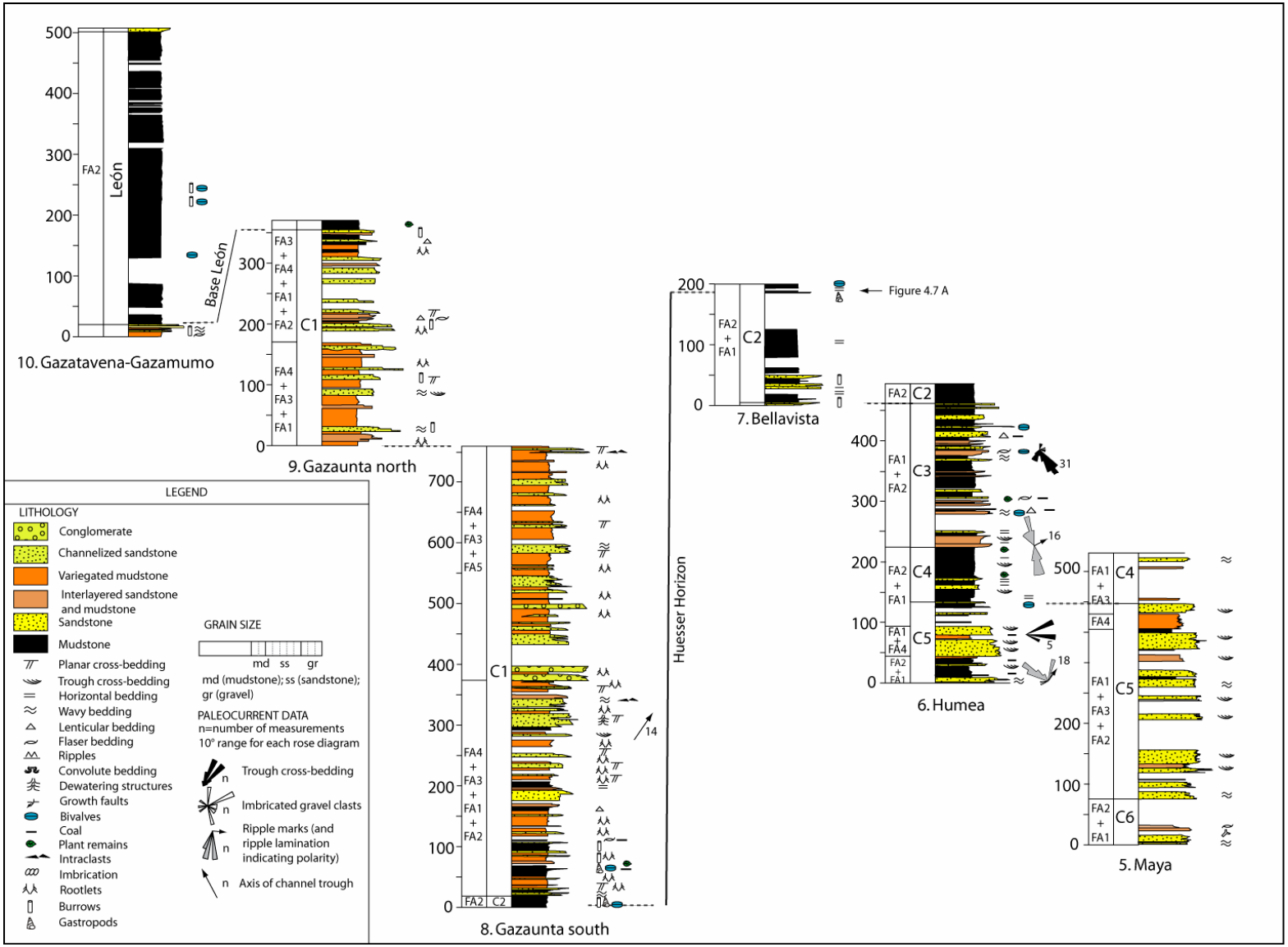

Figure 4.5. Measured straigraphic profiles of the Carbonera (C6-C1 members) and León Formations in the southeastern sector of the Medina Basin (locations in Fig. 4.1B), including lithostratigrahic correlation based on field-based and remote-sensing observations, interpreted facies associations and paleocurrent measurements. Locations of facies photographs of Fig 4.7 are shown.

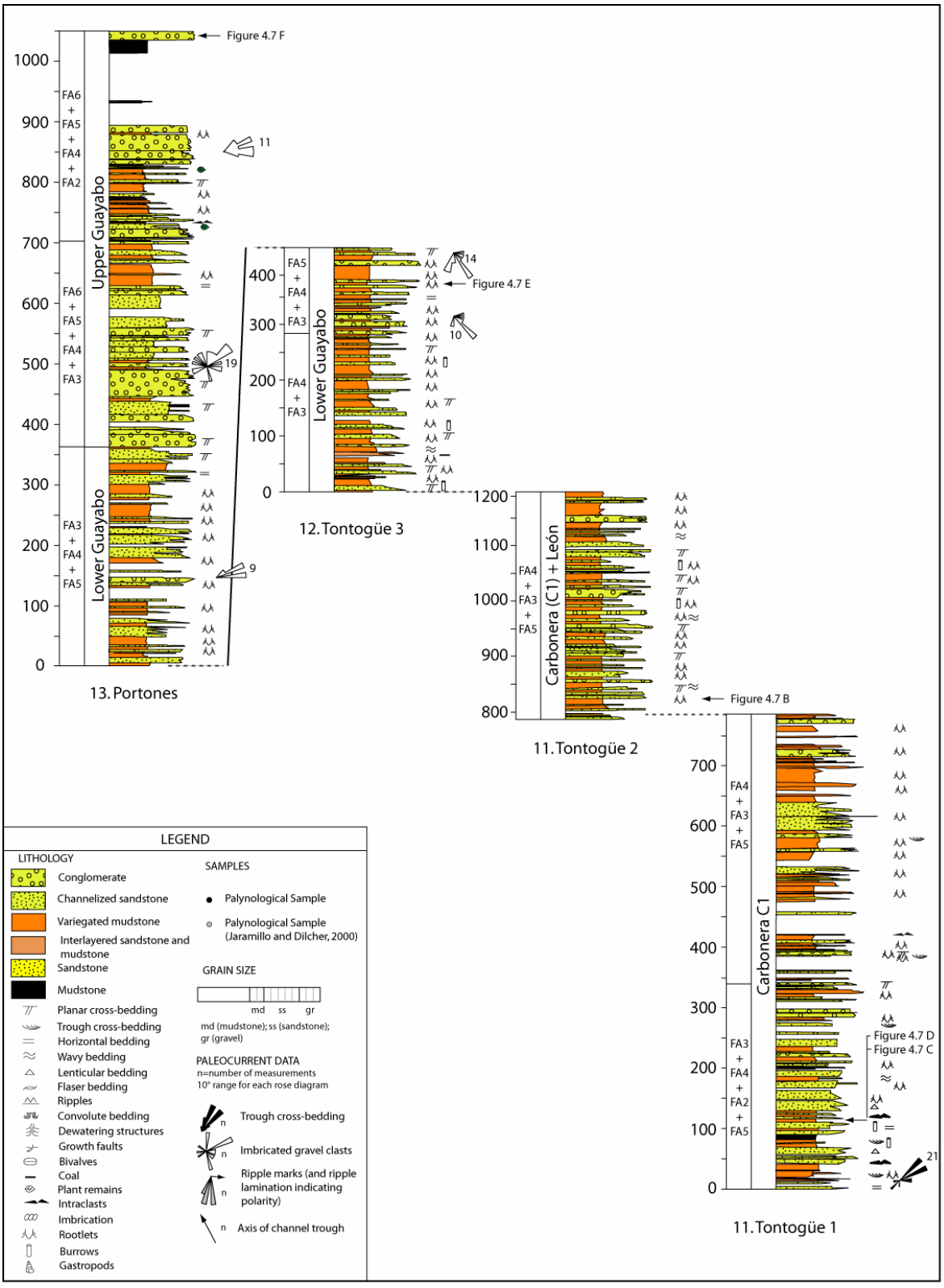

Figure 4.6. Measured straigraphic profiles of the Carbonera Formation and the Guayabo Group in the northwestern sector of the Medina Basin (locations in Fig. 4.1B), including lithostratigrahic correlation based on field-based and remote-sensing observations, interpreted facies associations and paleocurrent measurements. Locations of facies photographs of Fig 4.7 are shown.

Pachydon, Anondondites, and *Mytilopsis* (Gómez et al., 2008; Parra et al., 2008), which have been associated with fresh-water lacustrine systems (e.g., Nuttall, 1990; Wesselingh et al., 2002; Anderson et al., 2006; Wesselingh and Macsotay, 2006), as well as the occurrence of gastropods *Sheppardioncha* (Gómez et al., 2008; see also Fig. 4.7a). The fragmentation, corrosion and abrasion of gasteropoda and disarticulated bivalve shells reflect reworking in a high-energy environment. Finally, the sporadic occurrence of mudstone with negligible bioturbation is indicative of rapid accumulation (e.g., Dalrymple and Choi, 2007). Collectively, these observations suggest deposition in a transitional environment between freshwater lakes and estuary.

Facies Association 3 (braided fluvial sandstones and conglomerates)

Laterally restricted sandstone bodies with basal scours are characteristic of stream-flow deposition (e.g., Bridge, 2003). The lenticular morphology of the sandstone beds and the presence of erosive basal scour marks and muddy intraclasts suggests transport by traction (e.g., Collinson et al., 2006). The poorly defined large-scale, low-angle planar cross-stratification, absence of well defined normal grading and ubiquitous floating pebble clasts may represent deposition in braided fluvial channels (e.g., Miall, 1985; Bridge, 2003).

Facies Association 4 (overbank mudstones and siltstones)

Laterally continuous variegated mudstone and siltstone units represent deposition by suspended load in overbank areas. Pervasive mottling, and root traces (Fig. 4.7b) indicate repeated flooding in a fluvial floodplain environment (e.g., Bridge, 1984). Desiccation cracks (Fig. 4.7c) and sporadic ferruginous nodules (Fig. 4.7d) reflect pedogenesis during intermittent flooding and subaerial exposure and fluctuating wet-dry soil conditions (e.g., McCarthy et al., 1997; Kraus, 1999). In this scenario, the thin, wedge-shaped, fining-upward sandstone bodies may have been deposited as crevasse channel fills (e.g., Bridge, 1984).

Facies Association 5 (granule to pebble conglomerates and conglomeratic sandstones)

Clast-supported, granule and pebble conglomerates with organized fabrics, lack of muddy matrix, and dominantly sharp, non-erosive basal contacts (Fig. 4.7e) indicate waterlaid deposition by unconfined flow (e.g., Blair and McPherson, 1994; Blair, 1999a). Horizontal stratification suggests upper-flow regime conditions. These features represent sediment gravity flows, such as sheetflood or hyperconcentrated flows. The interbedding of this facies with facies association FA3 likely indicate deposition in distal sectors of waterlaid alluvial-fans (e.g., Blair, 1999a).

Facies Association 6 (cobble and boulder conglomerates)

Clast-supported, crudely stratified, pebble-to-boulder conglomerates (Fig. 4.7f) with ribbon-like geometry represent deposition by high-energy streamflows in moderately to well confined channels (e.g., Blair, 1999a). Occasional very poorly sorted, matrix-supported conglomerates organized in subtabular beds are diagnostic of debris-flow deposits (Nemec and Postma, 1993; Blair, 1999b). Taken together, these features represent deposition in proximal sector of alluvial fans.

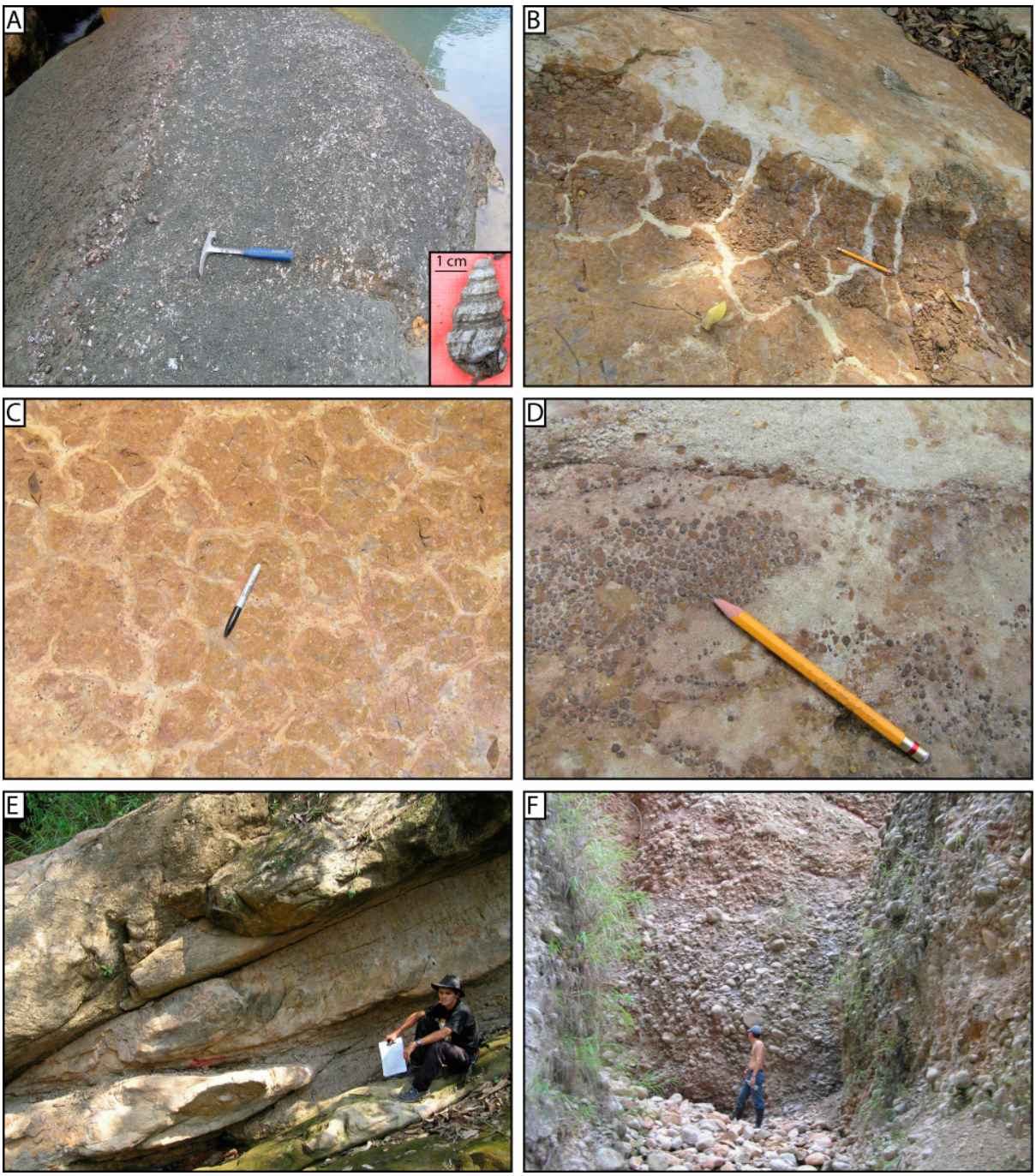

Figure 4.7. Photographs of representative sedimentary facies. Locations are indicated in Figures 4.5 and 4.6. **(A)** Mollusk-rich horizon at the top of C2 member (Huesser Horizon) in Profile 7 (Bellavista). Approximately 1.5 m-thick shell bed formed by densely packed specimens of gasteropod *Sheppardiconcha* (shown in inset) and molds of thin-shelled bivalve *Anondonites* (Gómez et al., 2008) embedded in muddy matrix (facies association FA1). Dip direction is to the left. **(B)** Well-developed mudcracks and root traces in pedogenically altered floodplain deposits (facies association FA4) of the C1 member in Profile 11 (Tontogüe 2). See pencil for scale. **(C)** Dessication cracks and **(D)** ferruginous nodules in massive, pedogenically altered floodplain siltstones and silty sanstones of the C1 member in Profile 11 (Tontogüe 1). **(E)** 2 m-thick, subtabular, granule to pebble conglomerate bed with non-erosive basal contact (facies association FA5) overlying floodplain siltstones in the Lower Guayabo Formation along Profile 12 (Tontogüe 3). **(F)** View toward the N of massive cobble and block conglomerates (facies association FA6) of the Upper Guayabo Formation in Profile 13 (Portones). Bedding dip is ~12° toward the SW (left).

4.4.2.2 Facies distribution

Both fine- and coarse-grained strata constitute the sedimentary fill of the Medina Basin. Coarse-grained fluvial deposits are commonly confined to the western border of the basin and appear in units as old as the laterally equivalent strata to the C6-C5 units from the eastern margin (Parra et al., 2008; Profiles 1-4; Fig. 4.8). Conversely, fine grained-lacustrine and marginal marine deposits are almost exclusively restricted to the eastern margin of the basin. There, the basin fill can be subdivided into two coarsening-upwards cycles, largely delineated by the eastward progradation of braided stream deposits that constitute the C1 member of the Carbonera Formation over areas previously dominated by estuarine systems (C5-C1 members; Fig. 4.8). Spatially extensive freshwater-lake deposition punctuated by short-lived marine incursions (facies association FA 2) of the Carbonera and León Formations exclusively occurs in the easternmost distal part of the basin. This facies association in the León Formatión is 450 m thick and marks the beginning of the uppermost coarsening-upward cycle. Progressively coarser-grained braided stream and sheetflood deposits become more abundant upsection. Finally, coarse alluvial-fan conglomerates prograded eastward and beyond the eastern margin of the basin toward the Llanos plains. A coeval increase in tectonic deformation rates in the Eastern Cordillera is suggested by the first occurrence of growth unconformities within the coarse conglomerates of the Upper Guayabo Formation (Fig. 4.4).

Paleocurrent indicators reflect a predominant easterly transport, locally varying from NE to SE directions (Fig. 4.5 and 4.6). The paleoflow pattern, the trend toward an eastward change of facies from alluvial to estuarine strata, and the presence of growth strata within the early Miocene to Pliocene strata clearly indicate syntectonic sedimentation related to uplift and denudation of mountainous terrain to the west of the basin.

4.4.3 Age constraints

We provide a new chronostratigraphic framework for the Carbonera (C5-C1 members), León, Lower Guayabo and Upper Guayabo Group based on palynomorphs, following standard methods (Traverse, 1988). In our analysis we follow the biostratigraphic zonal scheme developed by Jaramillo and Rueda (2004), Jaramillo et al. (2005) and Jaramillo et al., (2008). Palynological biozones from northern South America have been calibrated using foraminifera and nanoplankton from Venezuela (Germeraad et al., 1968; Muller et al., 1987), and stable carbon isotopes ($\Delta^{13}C$) from Colombia and Venezuela (Jaramillo et al., 2006; Jaramillo et al., 2007).

Our main results are summarized in Figure 4.10. Units C5 to Lower Guayabo were deposited within the palynological zones 31 to 35 (biozones after Jaramillo and Rueda, 2004), corresponding to early to Late Miocene (Fig. 4.5). Twelve samples from the Upper Guayabo Formation in Profile 13 (Portones) yield sufficient palynomorphs for analyses. The presence of *Echitricolporites spinosus, Fenestrites sp, Polypodiaceiosporites pseudopsilatus* and *Nikssenosporites fossulatus* indicates an Upper Miocene to Pliocene age (Da Silva 2006).

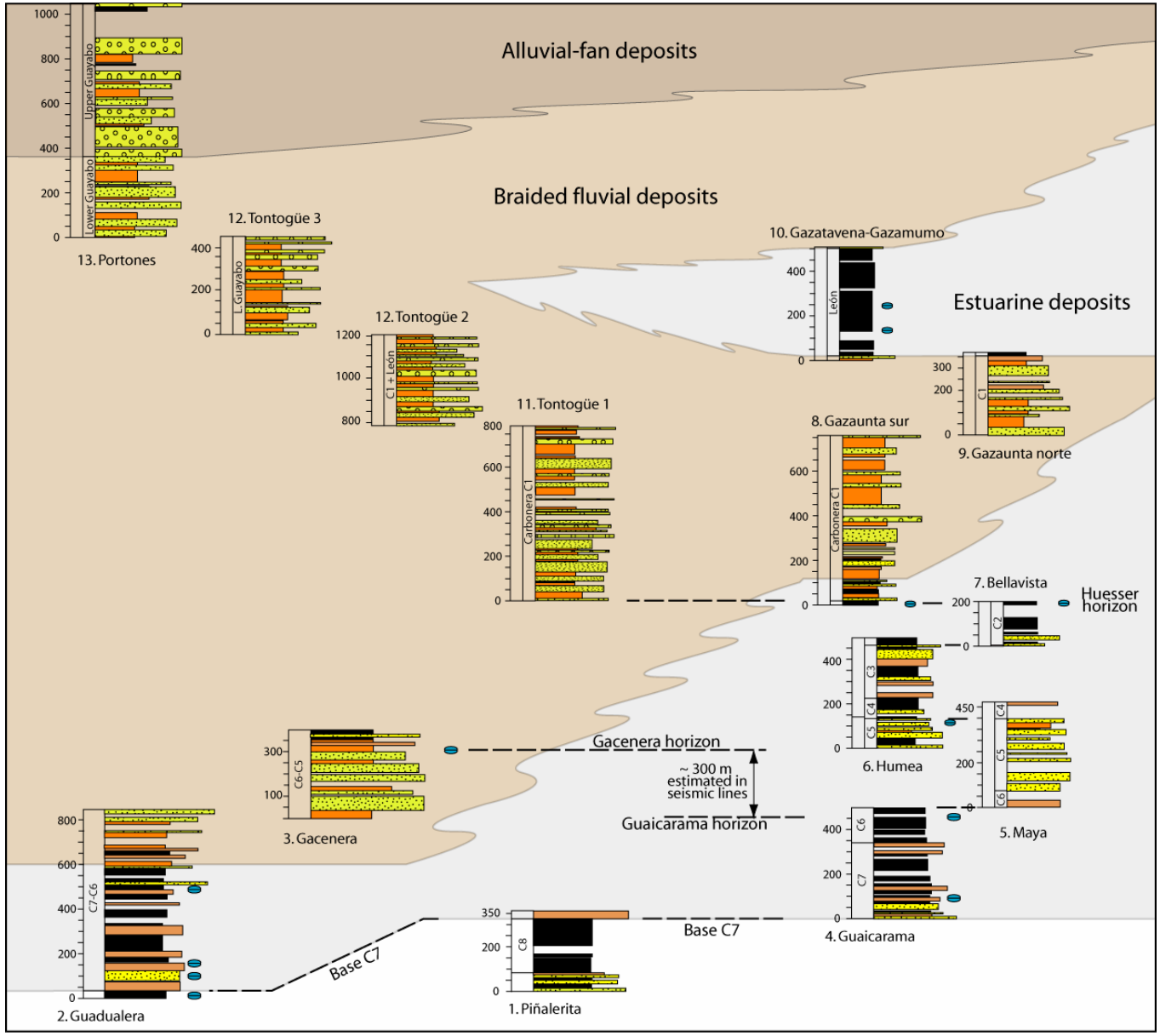

Figure 4.8. Scheme of facies distribution in the Medina Basin based on simplified representation of measured stratigraphic profiles 5-13 (this study) and 1-4 (Parra et al., 2008). Locations of profiles are shown in Figure 4.1. Easterly sourced coarse-grained fluvial strata in the Carbonera Formation occur mainly along the western sector of the basin and grade eastward to temporarily marine-influenced lacustrine deposits. The distribution of facies delineate two main coarsening upward cycles. See text for discussion.

4.4.4 Unroofing of Eastern Cordillera source areas

We evaluate the unroofing history of the basement-cored uplift of the Quetame Massif by tracking the occurrence of distinct conglomeratic clasts and in the Oligo-Miocene strata of the Medina Basin. Conglomerate clasts are composed of two main lithologies: vein quartz and sedimentary lithic fragments, with an increasing abundance of the latter upsection (Fig. 4.9). Conglomerate petrography documents a first appearance of Upper Cretaceous glauconitic sandstone fragments in the lower Miocene C2 Member of the Carbonera Formation (Fig. 4.9). Glauconitic sandstone gravel is present throughout the Miocene sediments and constitutes as much as ~40% of the bulk sedimentary composition. However, within the Miocene units we identified two peak intervals in the occurrence of glauconitic-sandstone clasts. A first peak occurs in the lower part of the Lower Guayabo Formation, and a second peak is seen in the Upper Guayabo Formation. These intervals are separated by sectors with only up to ~4% of glauconitic sandstone clasts. In addition, a small amount of phosphatic sandstones (up to 3%), and as much as 25% of siliceous siltstones are associated with the first peak of glauconitic sandstones in the lower sections of the Lower Guayabo Formation. Finally, redbed clasts, indicative of the Upper Paleozoic sedimentary units, are absent in the Oligo-Miocene sedimentary record of the basin. The first appearance of Paleozoic red sandstone clasts is seen in the undated lower alluvial terrace levels of the Humea and Gazaunta rivers of inferred Quaternary age (see Fig. 4.1 for location).

In the source area, the Upper Cretaceous glauconitic sandstone-bearing units (the Une, Chipaque and Guadalupe Formations) have been completely eroded from the basement-cored Farallones anticline and only crop out along its flanks (Fig. 4.1). From gravel petrography data we interpret a normal unroofing sequence that can be summarized as follows (Fig. 4.9): (1) absence of glauconitic sandstone clasts in the conglomerates of the C2 and C1 members and the coarse-grained strata laterally equivalent to the León Formation suggest dominant Paleogene sources; (2) an important fraction of the source area included glauconitic and phosphatic sandstones, and siliceous siltstones during middle Miocene accumulation of the lower portion of the Guayabo Group, suggesting erosion of the Guadalupe Group; (3) dominant exposure of the mudstone-rich Chipaque Formation compared to the glauconitic sandstones of the Guadalupe Group yields conglomerates devoid of glauconitic sandstones and siliceous siltstones during the accumulation of the upper portion of the Lower Guayabo Group; (4) renewed occurrence of glauconitic sandstone likely reflects unroofing of the Une Formation during accumulation of the strata of the Upper Guayabo Formation.

We thus derive apparent denudation rates on the basis of the thickness of the reconstructed erosion window (e.g., DeCelles et al., 1991) and the time of denudation as constrained by the statigraphic age of the appearance of clasts in the basin. Upper Cretaceous glauconite-bearing units typically have a thickness of ~1.5 to 2 km in the Eastern Cordillera (Mora et al., 2006). An upper limit for the thickness of the eroded rock is provided by the absence of Paleozoic clasts in the investigated Oligo-Miocene strata. Such a scenario limits the maximum value of eroded thickness to that of the

overlying Cretaceous section (6.5 km). We therefore estimate apparent long-term denudation rates of as much as 0.3 mm/yr for the area of the Quetame massif in the interval between ~23 and 2 Ma. Similar apparent exhumation rates have been inferred with thermochronological data in the Eastern Cordillera (see Chapter 3).

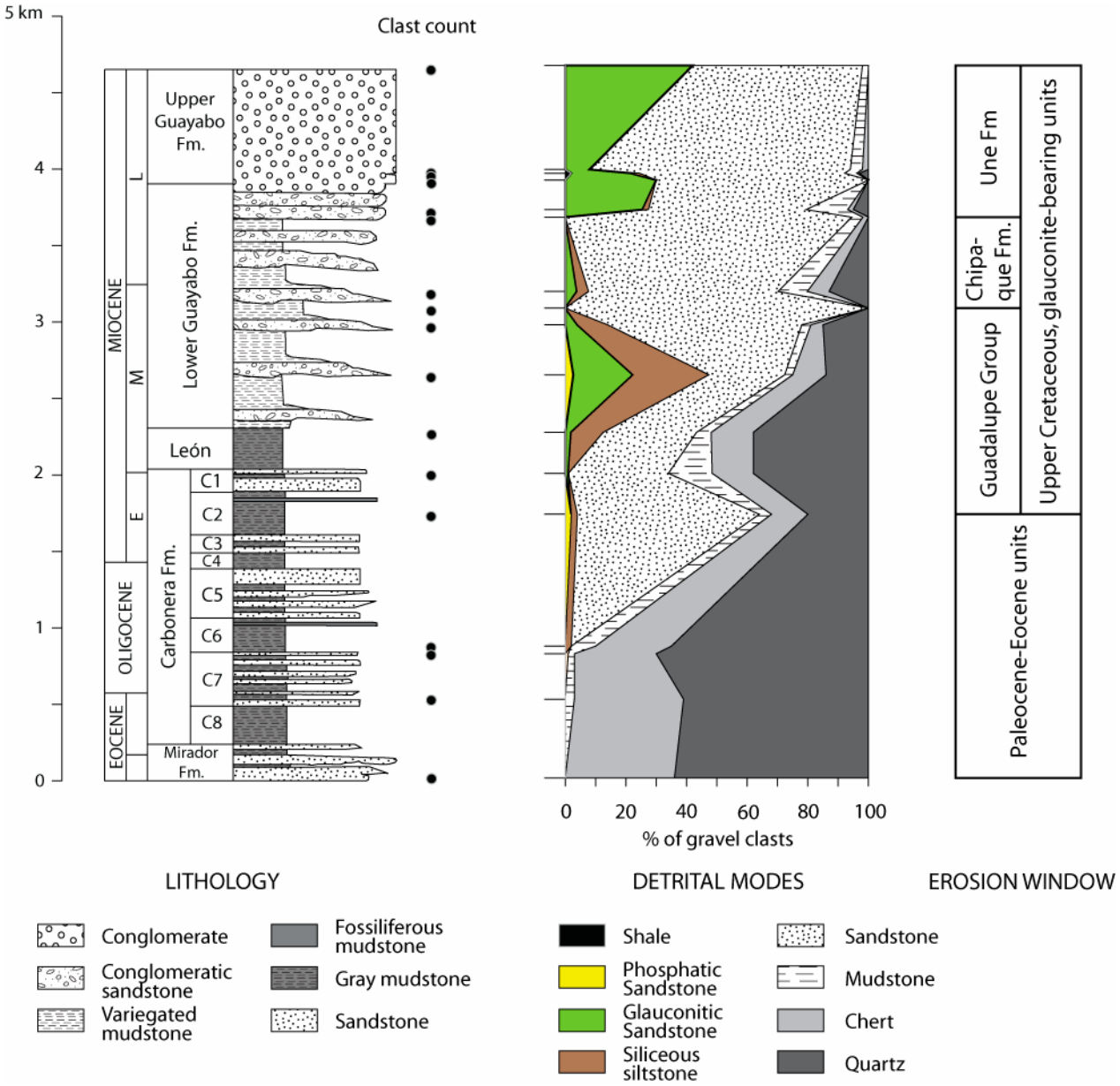

Figure 4.9. Compositional trends in Eocene-Pliocene conglomerates of the Medina Basin. Black circles denote the stratigraphic position of conglomeratic samples. Clasts of Upper Cretaceous glauconitic sandstone, phosphatic sandstone and siliceous siltstone occur in Miocene strata of the Carbonera Formation and Guayabo Group, documenting progressive unroofing of the Eastern Cordillera (right panel). Raw data and recalculated modes are reported in Table 4.1. See text for discussion.

4.4.5 Sediment-accumulation rates

4.4.5.1 One dimensional analysis

Sediment accumulation in the Medina Basin reflects a three-stage history characterized by an Eocene-early Oligocene episode of slow sediment accumulation with rates of 30-70 m/my that separates two periods of faster accumulation during Late Cretaceous-Paleocene (~100 m/my) and late Oligocene-Pliocene time (~220 m/my), respectively. In agreement with the distribution of Cenozoic sedimentary facies and unconformities in the southern Middle Magdalena Valley Basin (Gómez et al., 2005), plausible explanations for these sediment accumulation trends and tectonic subsidence rates have been explored by Parra et al. (2008). They interpret this pattern as the result of alternating episodes of cratonward and orogenward migration of the orogen-basin pair.

Here, we particularly consider the significance of the late Oligocene-Pliocene episode of rapid accumulation. A first increase in the rate of sediment accumulation occurs at the base of Biozone T-10, at ~30 Ma, which corresponds to the base of the C7 member of the Carbonera Formation in the Guadualera profile (Fig. 4.10). On the basis of a comprehensive examination of exhumation patterns derived from thermochronology and indicators of brittle deformation in the Eastern Cordillera, such an episode was likely associated with eastward migration of the tectonic loads to the present-day axial sector of the Eastern Cordillera, toward the Soapaga fault (see Chapter 3). Our new data reveal a second, more pronounced increase in rates of sediment accumulation at the beginning of the early Miocene Biozone 31 (~23 Ma). During the early Miocene, spanning ~7 my, accumulation of ~3350 m of sediments implies peak mean accumulation rates of ~480 m/my. Our data furthermore suggest that middle Miocene accumulation rates decline to values of ~100m/my during accumulation of the León and Lower Guayabo Formations. However, we interpret this result with extreme caution, since this part of the composite section is based on lithostratigraphic correlation of fluvial deposits in the Tontogüe section, in the northwest of the basin, with their distal, laterally equivalent lacustrine units in the southeast, spanning a distance of ~35 km along the structural termination of the Guavio anticline (Figs. 4.1 and 4.8). Despite these unavoidable difficulties imposed by the location of the best exposed sections in the densely vegetated area, our correlation suggests that rapid sediment accumulation prevailed throughout the Mio-Pliocene.

4.4.5.2 Three-dimensional sedimentary budget

In order to account for potential lateral thickness variations and to provide a more regionally meaningful assessment of the sedimentary budget, we interpret an extensive grid of ~70 2D industry seismic reflection profiles totaling ~1800 km. We translated 6 mapped lithostratigraphic limits into the seismic profiles intersecting the outcrop exposures close to the measured sections. We chose horizons which constitute easily traceable markers either exposed in the basin or in the seismic profiles. We trace stratigraphic limits southward along the hanging wall of the Guaicaramo thrust toward the area where the thrust loses displacement and finally terminates, allowing the interpreted horizons

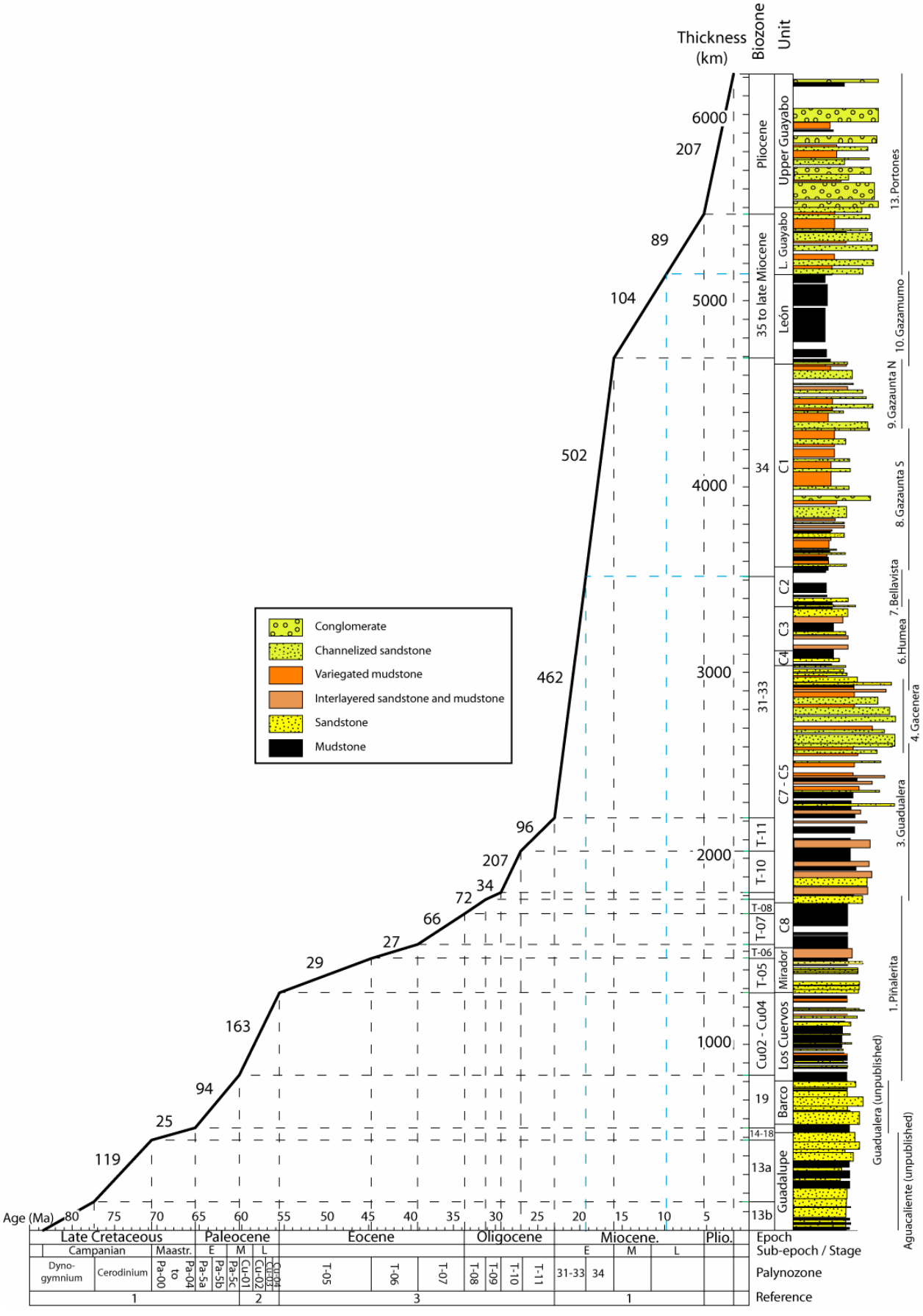
Thickness (km)
Biozone
Unit
6000
5000
4000
3000
2000
1000
207
89
104
502
462
96
207
34
72
66
27
29
163
94
25
119
Conglomerate
Channelized sandstone
Variegated mudstone
Interlayered sandstone and mudstone
Sandstone
Mudstone
Pliocene
35 to late Miocene
34
31-33
C7 - C5
T-11
T-10
T-08
T-07
T-06
T-05
Cu02 - Cu04
19
14-18
13a
13b
Upper Guayabo
L. Guayabo
León
C1
C2
C3
C4
C8
Mirador
Los Cuervos
Barco
Guadalupe
13. Portones
10. Gazamumo
9. Gazaunta N
8. Gazaunta S
7. Bellavista
6. Humea
4. Gacenera
3. Guadualera
1. Piñalerita
Guadualera (unpublished)
Aguacaliente (unpublished)
Age (Ma)
80 75 70 65 60 55 50 45 40 35 30 25 20 15 10 5
Late Cretaceous
Paleocene
Eocene
Oligocene
Miocene.
Plio.
Epoch
Campanian
Maastr.
E
M
L
Sub-epoch / Stage
Dyno-gymnium
Cerodinium
Pa-00 to Pa-04
Pa-5a
Pa-5b
Pa-5c
Cu-01
Cu-02
Cu03 Cu04
T-05
T-06
T-07
T-08
T-09
T-10
T-11
31-33
34
Palynozone
1
2
3
1
Reference

stratigraphy based on interpreted depths of well-defined horizons from borehole reports. We interpret five rock units bounded by the following horizons: (1) the top of the Eocene Mirador Formation sandstones; (2) the top of the C6 member, defined by the appearance of the fossiliferous Guaicarama horizon; (3) the top of the C2 member, defined by the outcrop of the fossiliferous Huesser horizon; (4) the top of the C1 member, defined by the change of fluvial overbank deposits and channelized sandstones to monotonously bedded, organic-rich mudstones of the León Formation; and (5) the top of the León Formation mudstones. Stratigraphic ages for these horizons are interpolated from the palynological zonation and are reported in Table 4.3.

Based on interpolations between seismic reflectors for each of these horizons, we constructed surfaces in two-way traveltime for the hanging- and footwall blocks of the Guaicaramo thrust. In order to avoid errors in areas of poor seismic-reflection coverage, we exclude the area in the footwall beneath the thrust sheet. Depth conversion was carried out for surfaces of each block using seismic velocities obtained from check-shots surveys. We average data from the Coporo-1 and Medina 1 wells in the hanging-wall block of the Guaicaramo fault, and from the Guacavía, Chaparral, San Pedro and Upía-1 wells in the footwall (see depth-time relations in Appendix C, Fig. C1). Finally, to reveal spatiotemporal variations in sediment-accumulation rates, we calculated an average sediment-accumulation rate (compacted) for each of the five interpreted rock-units, computed by dividing the volume of rock between successive depth-converted surfaces (evaluated within the 2D area of the smaller, usually upper surface of each rock package), by the 3D area of that surface. In addition, we derived sediment-accumulation rate maps, obtained by dividing isopach thicknesses by the geologic time represented by each unit. Parameters for volumetric calculations and results are reported in Table 4.3.

Figure 4.11 shows the middle Eocene-Holocene history of variation in sediment-accumulation rates. The sediment-budget pattern for the entire area resembles that of the one-dimensionally reconstructed basin history, albeit with a broader resolution resulting from the larger time windows into which the thickness data are binned. Subsequent to limited upper Eocene-early Oligocene accumulation, rapid sediment deposition at rates of 100 to 350 m/my (compacted thickness) have occurred since the Miocene, with an absolute minimum during accumulation of the middle Miocene León Formation. The more regionally meaningful, three-dimensional reconstruction of sediment accumulation reveals patterns not captured in the one-dimensional reconstruction. First, as a result of the lower resolution, the onset of rapid sediment accumulation at ~30 Ma is not portrayed in the 3D sedimentary budget. Second, the absolute maxima in mean sediment-accumulation rates occur during the youngest history of the basin, represented here as late-Miocene to Holocene. This pattern

Figure 4.10. Palynological biozonation and composite stratigraphic section of the Late Cretaceous-Pliocene strata of the Medina Basin based on stratigraphic sections by Jaramillo and Dilcher (2000), Parra et al., (2008), ECOPETROL (unpublished data) and this study. The slope of the curve indicates sediment-accumulation rates. Rates based on decompacted thickness are indicated (see text and Table C1). Assignment of biozones is based on Jaramillo et al. (2004), Jaramillo et al. (2005) and Jaramillo et al. (in press) (references coded in zonal scheme with numbers 1, 2 and 3, respectively). Time scale from Gradstein et al. (2004).

is independently captured in the sedimentary budget of each block of the Guaicaramo fault (Fig. 4.11). Third, higher sediment-accumulation rates occur in the western, hanging-wall block of the thrust throughout basin history. Finally, a local maximum in sedimentation rates restricted to the hanging-wall block of the thrust occurs during deposition of the C1 member.

TABLE 4.3: RESULTS FROM THREE-DIMENSIONAL SEDIMENTARY BUDGET OF EOCENE-HOLOCENE UNITS IN THE MEDINA AND LLANOS BASINS

Unit	Volume (km3)	2D Area at top (km2)	3D Area at top (km2)	Age at top (Ma)	Acc. rate min (m/my)	**Acc. rate mean (m/my)**	Acc. rate max (m/my)
Guaicaramo hanging wall (Medina Basin)							
Guayabo	1177	744	755	3.6 ± 1.8	144	**195**	300
Leon	347	734	759	11.6 ± 1.0	71	**104**	190
C1	522	876	924	16.0 ± 1.0	103	**188**	1129
C2-C5	1102	1165	1284	19.0 ± 1.5	101	**156**	344
C6-C8	1020	1462	1526	24.5 ± 1.5	32	**38**	48
Mirador				42.0 ± 2.0			
C1-C5	1624	876	924	16.0 ± 1.0	160	**207**	293
Guaicaramo footwall (western Llanos Basin)							
FW_Guayat	6793	3382	3386	0	159	**173**	189
FW_Leon	1153	3291	3380	11.6 ± 1.0	53	**78**	142
FW_C1	949	3351	3339	16.0 ± 1.0	52	**95**	569
FW_C2-C5	2118	3376	3387	19.0 ± 1.5	74	**114**	250
FW_C6-C8	939	3472	3628	24.5 ± 1.5	12	**15**	18
Mirador				42.0 ± 2.0			
C1-C5	3067	3351	3339	16.0 ± 1.0	84	**108**	153

The spatial distribution of sediment-accumulation rates for the five analyzed time windows displays a consistent pattern of eastward-decreasing rates without major along-strike variations (Fig. 4.12). Widespread increases in sedimentation rates during accumulation of the lower Miocene C5-C2 members of the Carbonera Formation and enhanced accumulation in the proximal, western part of the basin during deposition of the C1 member are portrayed by these analyses. Likewise, an overall increase in sedimentation rates is a characteristic since the late Miocene, but is slightly more pronounced in the northern part of the basin.

4.5. DISCUSSION

4.5.1 Early Miocene basin evolution

Integration of the multiple datasets presented in this study allows correlation of tectonic episodes in the orogen with the distribution and rates of sediment deposition in the adjacent basin. East of the basin, a minimum early Miocene age for initial deformation associated with motion on the Lengupá fault is supported by growth-strata relationships in rocks equivalent to the C5 member. An independent assessment of the timing of tectonic activity in the Eastern Cordillera is available from mineral cooling ages derived from apatite and zircon fission-track data from the eastern flank of the

Eastern Cordillera. This thermochronological information documents initial exhumation and uplift during the middle-Eocene to Oligocene (40-30 Ma) in its axial sector (Floresta Massif; Toro, 1990; see also Chapter 3), and during late Oligocene-early Miocene time (25-20 Ma) along its eastern flank (see Chapter 3)

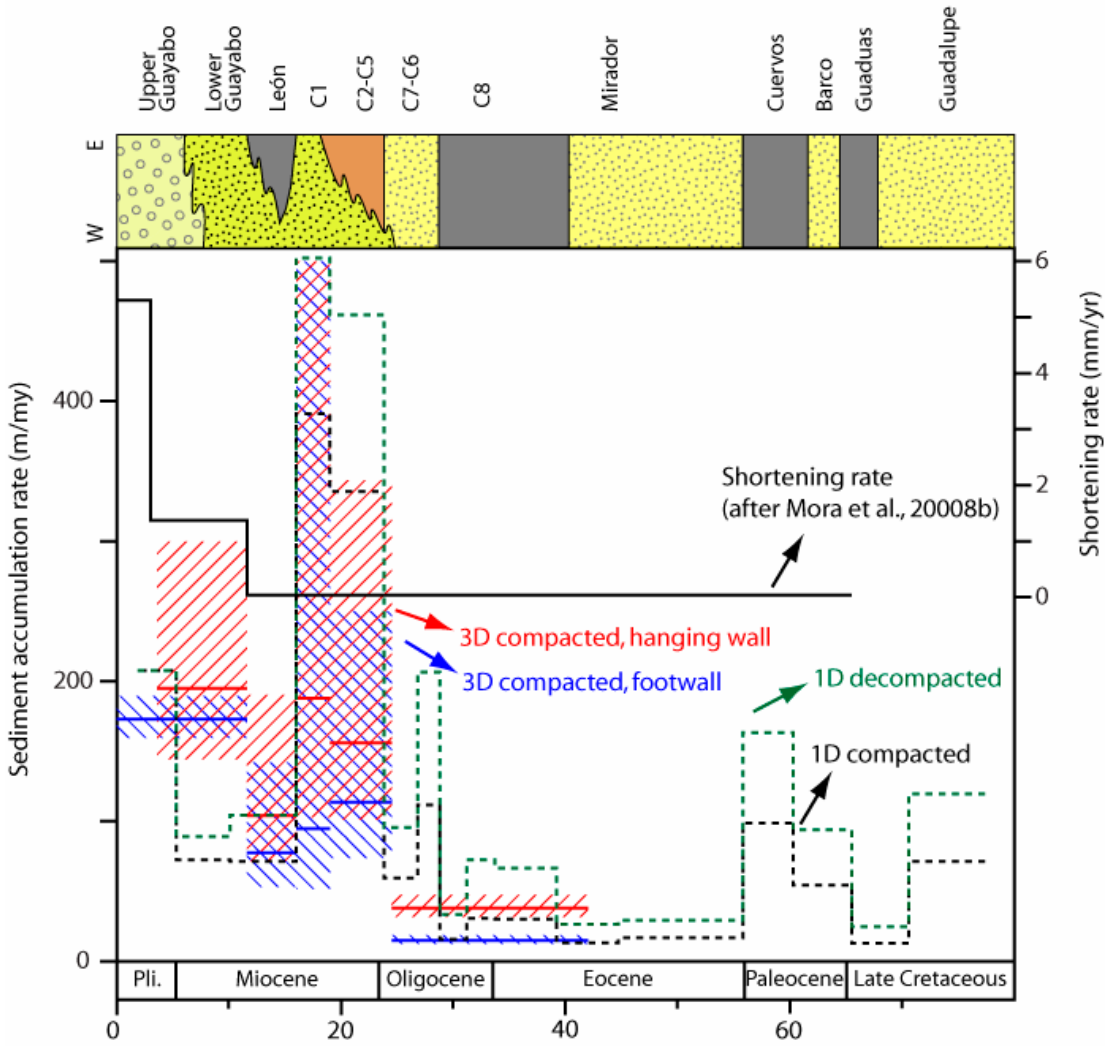

Figure 4.11. Reconstructed one-dimensional sediment-accumulation rates for the Medina Basin (green and black dotted lines), and three-dimensional sedimentary budgets for the Medina and proximal Llanos basins (blue and red lines, respectively). Errors in 3D accumulation rates are indicated by shaded areas. Episodes of faster accumulation are coeval to deposition of coarse-grained facies in both the western and eastern sectors of the basin, as indicated by lithologies in the upper panel (colors coded as in Fig. 4.5). Pliocene eastward progradation of coarse conglomerates is contemporaneous with faster shortening rates in the eastern flank of the Eastern Cordillera. See text for discussion.

An abrupt two- to four-fold increase in sediment-accumulation rates is observed at the base of the early Miocene lower Carbonera Formation (C6-C5 member) in the Medina Basin (Figs. 4.10-4.12), which in turn follows a period of rapid accumulation that commenced in the late Oligocene (~30 Ma). Sediment-accumulation rates are primarily affected by tectonic subsidence in foreland basins where accommodation space provided by lithospheric flexure is nearly filled or overfilled with

sediments (Burbank et al., 1988; Jordan, 1995). In the foreland of the Colombian Andes, a dominant orogen-perpendicular, eastward paleocurrent direction observed in Miocene units and lack of evidence of Miocene forebulge erosion (e.g., Bayona et al., 2008) point toward a filled to overfilled foreland basin and hence permit using sediment-accumulation rates as a proxy for tectonic subsidence. As suggested in foreland basin models, (e.g., Flemings and Jordan, 1989; DeCelles and Giles, 1996), an upsection increase in tectonic subsidence reflects the relative shift of the depositional site toward a more proximal sector within the foredeep depozone in response to the migration of the flexural profile accompanying growth and lateral propagation of the orogenic wedge. However, this effect of tectonically enhanced accommodation space is attenuated toward the distal part of the basin. As a result, farther away from the deformation front, such an increase in sedimentation rates is delayed with respect to thrusting (e.g., Flemings and Jordan, 1990; Jones et al., 2004). In the Medina Basin, synchronicity between the independently constrained ages of thrusting along the Lengupá fault and increase of tectonic subsidence in the Medina Basin suggest a causal relationship between these phenomena, as well as in-phase thrusting and rapid sediment accumulation ~20 km away of the deformation front.

In the Medina Basin, the C6-C1 members of the Carbonera Formation comprise an early Miocene coarsening upward cycle approximately 2500-m thick. We calculated average accumulation rates (1D, decompacted) of ~480 m/my (Fig. 4.10), which are within the upper limit of long-term accumulation rates determined for nonmarine foreland basins (Burbank et al., 1988; Meigs et al., 1995; Echavarria et al., 2003; Uba et al., 2007). Sedimentary facies and provenance analysis of the Carbonera Formation document accumulation of westerly sourced sediments derived from Mesozoic and Paleogene sedimentary rocks from the Eastern Cordillera along an eastward-sloping alluvial plain that transitioned to a low-energy, tidally influenced estuarine system. The distribution of sedimentary facies reveals earlier accumulation of fluvial deposits along the western margin of the basin (upper part of C7-C5 members; Guadualera-Gacenera profile; see Fig. 4.8 and also Parra et al., 2008) compared to the east (Guaicaramo and Maya sections; Figs. 4.5 and 4.8). Subsequent forelandward migration of coarser-grained, fluvial deposits resulted in accumulation of the C1 member at the eastern margin of the basin (Gazaunta section; Fig. 4.5 and 4.8). Despite insufficient resolution of the age constraints within the early Miocene units, our volumetric sedimentary budget reveals that such progradation of coarser-grained facies may have occurred during a period of peak accumulation and subsidence rates which was restricted to the realm of the Medina Basin in the latest early Miocene (~19 to 16 Ma). Farther east, in the footwall of the Guaicaramo fault, accumulation rates during deposition of the C1 member are slightly lower compared to those of the underlying early Miocene units (Fig. 4.11 and 4.12).

In light of the reconstructed position of the orogenic front, we interpret such a pattern as the result of an episode of tectonic thickening along a stationary deformation front located immediately to the west of the basin. Overall, the facies distribution and the reconstructed early Miocene

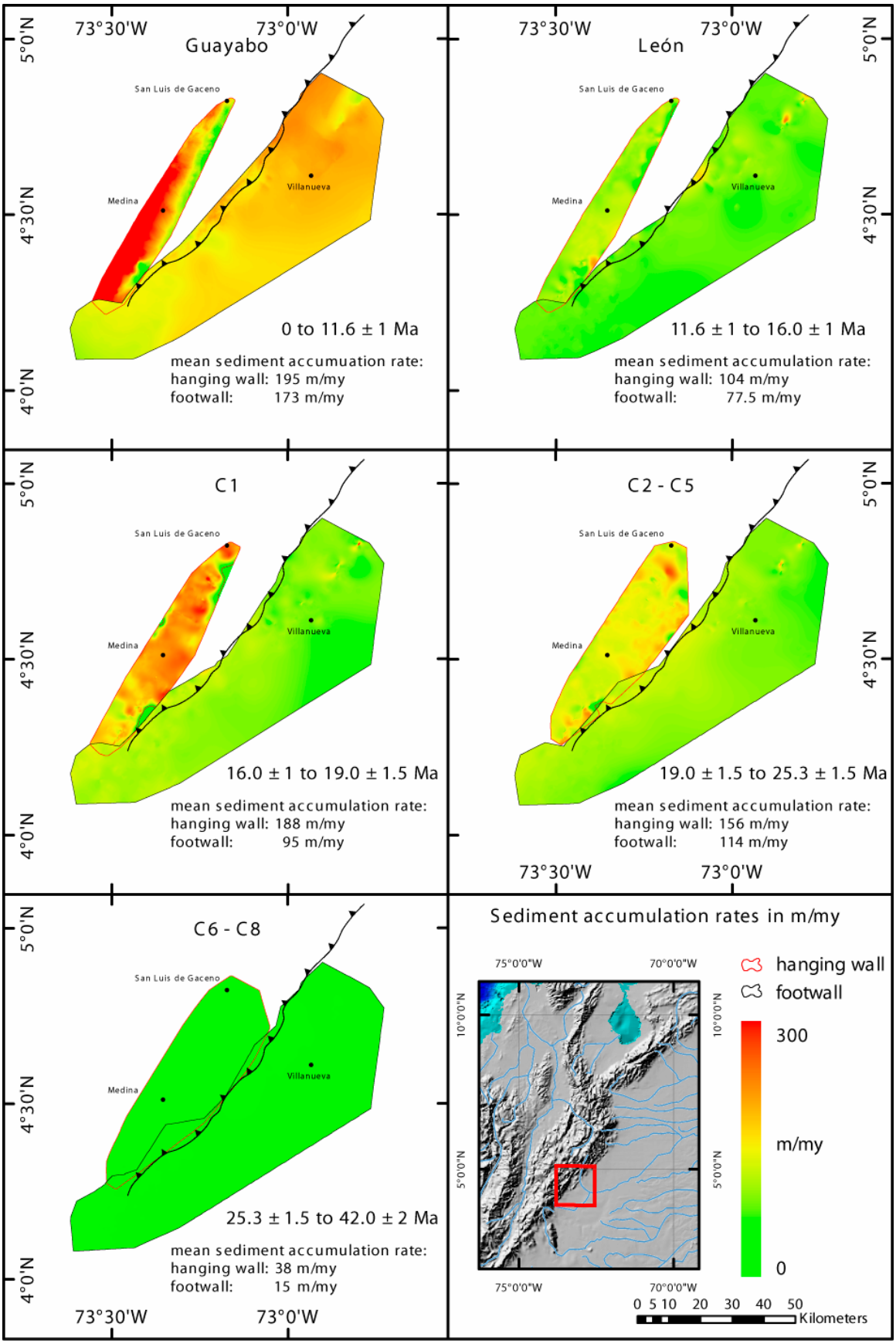

Figure 4.12. Spatial distribution of sediment-accumulation rates (compacted thickness) for five interpreted Eocene to Holocene stratigraphic units in the hanging wall (Medina Basin) and footwall (Llanos Basin) of the Guaicaramo thrust. Towns and the surficial trace of the thrust and indicated for reference. Inset shows location of the mapped area.

accumulation history of the Medina Basin support foreland-basin models that predict coeval thrusting and accumulation of coarser-grained facies in the proximal part of the foredeep depozone (e.g., Burbank et al., 1988). Our data suggest that this mechanism may have been active at multiple time scales. First, coarsed-grained facies of the C6-C1 members of the Carbonera Formation were deposited in the proximal foredeep during an episode of fast subsidence lasting ~7 m.y. during the early Miocene. Second, peak eastward progradation of these coarse-grained sediments toward the easternmost sector of the present-day Medina wedge-top basin (C1 member) seems to have occurred during episodes maximum local subsidence associated with active thrusting. However, the available age resolution for the C1 member renders this behavior still unclear.

4.5.2 Middle-late Miocene basin evolution

A second coarsening-upward cycle corresponds to the accumulation of the León Formation and the Guayabo Group (Fig. 4.8). As for the underlying coarsening-upward cycle of the upper members of the Carbonera Formation, this coarsening-upward pattern is more pronounced in the eastern sector of the basin, where the León Formation comprises tidally-influenced lacustrine deposits punctuated by short-lived marine incursions. A progressive westward change to laterally equivalent fluvial deposits in the eastern limb of the Nazareth syncline caused amalgamation of the lower portion of this cycle with the underlying sequence capped by the fluvial deposits of the C1 member, hence partially obscuring the coarsening-upward pattern (Fig. 4.8). A similar pattern of an eastward increase in the sand-to-mud ratio in the León Formation occurs approximately 100 km to the north along the western margin of the Llanos basin (Cooper et al., 1995). Potential causes of widespread accumulation of fine-grained sediments in temporarily marine-influenced, primarily lacustrine environments in proximal sectors of the foredeep may have included several factors. These entail eustatic sea level change (e.g., Van Wagoner, 1995), reduced erosion rate in the source area due to an arid or stable climate (e.g., Paola et al., 1992; Molnar, 2004), and exposure of erosion-resistant lithologies in the source area causing a general decrease in erosion rate and sediment supply leading to sediment starvation in the basin (e.g., Carroll et al., 2006). Alternatively, accumulation of fine-grained sediments may have resulted from waning tectonics (e.g., Jordan et al., 2001) or from exposure of nonresistant lithologies that are less likely to generate coarser sediments (DeCelles et al., 1991). Below, we explore each of these scenarios.

First, recently published sea-level curves (e.g., Kominz et al., 2008; and references therein) do not show any significant increase in eustatic level between early and middle Miocene time, arguing against a causal link between middle Miocene deposition of marine-influenced fine-grained sediments in the foreland of the Colombian Andes and eustatic sea-level changes (Cooper et al., 1995; Gómez et al., 2003). Second, whether regional climatic change drove accumulation of fine-grained sediments in the middle-Miocene is unclear, due to the paucity of detailed reconstructions of pre-middle Miocene climate conditions. However, high-resolution paleoclimate proxies in northern South America for the

last 13 m.y. suggest that a wetter than present-day climate punctuated by intermittent aridity promoted rapid erosion during the middle Miocene and Pliocene times (Harris and Mix, 2002). In contrast, an opposite climatic pattern, i.e., a relatively wetter and stable climate, prevailed during late Miocene time, which resulted in low erosion rates (Harris and Mix, 2002). It is hard to envision that this regional post-middle Miocene climatic pattern could have controlled the observed late Miocene coarsening-upward trend in the deposits of the Medina Basin. If climate had played an important role, diminished rates of sediment supply would have resulted in an opposite, fining-upward trend in middle to late Miocene strata. Third, our unroofing estimates document a middle Miocene to Pliocene erosion window in the Eastern Cordillera, with up to ~2 km glauconitic-bearing units (Fig. 4.9). Clast composition suggests that, within this unroofing sequence, a relatively higher contribution from the mud-rich, glauconitic-poor Chipaque Formation characterized the accumulation of the middle to late Miocene Lower Guayabo Formation. Overall, gravel petrography data do not support a correlation between erodability of the source-area lithologies and grain-size trends. Finally, both one- and three-dimensional reconstructions of the post-early Miocene sediment accumulation history suggest that sedimentation rates decline during deposition of fine-grained sediments of the León Formation. Subsequently, an increase in sediment accumulation accompanied the progradation of coarse-grained facies of the Guayabo Group (Figs. 4.8 and 4.11). This pattern resembles the syntectonic origin of coarse-grained facies progradation in the proximal foredeep observed in other areas (e.g., Burbank et al., 1988; Paola et al., 1992; Horton et al., 2004) and hence suggests that variability in tectonics, rather than climate, erodability or eustasy exerted the defining control on grain size trends.

Plausible tectonic scenarios that explain the decrease in accumulation (and subsidence) rates accompanying deposition of fine-grained strata of the León Formation are either backward stepping of thrust loads (e.g., DeCelles and Mitra, 1995) or waning tectonic activity (e.g., Flemings and Jordan, 1990). Geologic evidence supports the notion that both mechanisms are not mutually exclusive and may have operated virtually synchronously. Backward stepping of the tectonic loads by out-of-sequence thrusting in the interior of the orogen is supported by the cross-cutting relationships of the Soapaga and Pesca faults in the axial sector of the Eastern Cordillera. There, the Oligocene Concentración Formation east of the Floresta Massif is truncated to the west by the east-verging Soapaga Fault. Early Miocene apatite fission-track ages in the hanging-wall block (see Chapter 3) most likely reflect synchronous slip along this fault. Similar out-of-sequence reactivation in the interior of the Eastern Cordillera has been documented ~200 km farther north (Bayona et al., 2008). On the other hand, Flemings and Jordan (1990) and Sinclair et al. (1991) demonstrated that waning tectonic activity in the thrust wedge generate foreland basin accumulations with lens-shaped geometries, as opposed to wedge-like geometries developed during active thrusting. Based on subsurface data in the Llanos basin, Cooper et al. (1995) show that middle Miocene mudstones (their sequence T80) extend farther eastward onto the Guyana shield than any of the older foreland basin strata. In addition, our sedimentary budget shows that mean accumulation rates between the hanging

and footwall blocks of the Guaicaramo fault were more similar during the accumulation of the León Formation (104 vs. 78 m/my, respectively) than previously, during accumulation of the C5-C1 members (207 vs. 108 m/my, respectively; see Table 4.3 and Figs. 4.11 and 4.12). Such patterns reflect a more uniform distribution of tectonic subsidence along the foreland basin during accumulation of the León Formation than before, and thus are compatible with lens-shaped foreland strata. Taken together with the decline in rates of sediment accumulation, this suggests an episode of diminishing tectonic loading in the Eastern Cordillera.

4.5.3 Pliocene basin evolution

Coarse alluvial-fan conglomerates primarily sourced from Upper Cretaceous units from the Eastern Cordillera accumulated in the Medina Basin during the Pliocene, coeval with an episode of increasing sediment-accumulation rates (Figs. 4.8, 4.11 and 4.12). As in the underlying coarsening-upward cycle of the Carbonera Formation, such a parallel increase in both grain size and tectonic subsidence indicates a syntectonic origin for gravel progradation (e.g., Burbank et al., 1988; Heller and Paola, 1992). An increase in shortening rates in the eastern flank of the Eastern Cordillera during the last ~4 Ma (Mora et al., 2008b) furthermore supports increased tectonic activity as a fundamental forcing factor controlling gravel progradation (Fig. 4.11). In addition, the development of growth unconformities in the Upper Miocene-Pliocene strata of the Guayabo Group in the Nazareth syncline suggests that Pliocene uplift rates associated with fault-related folding of the Farallones anticline were greater than sediement-accumulation rates (e.g., Mora, 2007). In addition to faster shortening, concurrent rapid Pliocene-Holocene exhumation of the Quetame Massif revealed by AFT ages younger than ~3 Ma, and the asymmetric structure and topography of the range led Mora et al. (2008b) to propose a positive feedback mechanism between climatic and tectonic forcing. The trigger mechanism for this may have been ~1.5 to 2.5 km of surface uplift in the Eastern Cordillera between ~6 and 3 Ma (Van der Hammen et al., 1973; Wijninga, 1996; Hooghiemstra et al., 2006). This uplift established an orographic barrier that subsequently trapped westerly sourced, moisture-laden winds and focused precipitation, which ultimately enhanced erosional efficiency along the eastern flank of the orogen (Mora et al., 2008b). In this scenario, additional controls for Pliocene gravel progradation besides increasing tectonism may have included (1) an increase in topographic gradient induced by surface uplift in the source area; (2) an increase in sediment supply triggered by both enhanced water discharge and more pronounced source-area relief (Milliman and Syvitski, 1992); and (3) high-frequency global climatic oscillations (Molnar, 2004) . The simultaneous operation of fast shortening, efficient erosion, and an increase in topography prevents further deconvolving the contribution of each of these factors with respect to the progradation of coarse conglomerates during the Pliocene. However, a coeval increase in sediment-accumulation rates in a filled to overfilled basin reflects an increase in tectonic subsidence, and hence suggests that tectonics must have exerted a major control on the distribution of coarse-grained strata. Finally, rapid subsidence during the accumulation of the

Upper Guayabo Formation may also have been favored by enhanced sediment loading. Models predict that widening and deepening of the basin may occur when sufficient sediment flux is coupled with efficient mass transport, which produces significant sediment loading and generates additional subsidence, even beyond the flexural wave (Flemings and Jordan, 1989). In any case, the contribution of this factor has yet to be assessed by means of future two- and three-dimensional backstripping.

4.6. SUMMARY AND CONCLUSIONS

The stationary condition of the orogen-basin pair imposed by the inherited structural fabrics of the eastern border of the Eastern Cordillera provide an outstanding scenario for directly linking a long-lived history of exhumation of the Eastern Cordillera with the sedimentary record of the adjacent proximal foredeep. One- and three-dimensional reconstructions of sediment accumulation reveal that coarsening upward trends in sedimentary facies occur primarily as a result of increased tectonic activity in the Eastern Cordillera. Climate, eustasy and differential erodability of the source areas have played a minor role in determining the large-scale trends of facies distribution in the proximal sector foreland basin system of the Colombian Andes during most of the Neogene. However, proposed positive feedback mechanisms between surface uplift in the source areas, increased orographic precipitation and erosional efficiency, and faster shortening in the Eastern Cordillera during the last ~4 Ma may have conspired to result in rapid progradation of coarse conglomerates to more distal sectors of the foreland.

ACKNOWLEDGEMENTS

This study was supported by grants and fellowships from the German Academic Exchange Service (DAAD) to M Parra and A. Mora, the German Research Foundation (DFG), Str 373/19-1 to M. Strecker, funds from the Leibniz Center for Earth Surface and Climate Studies at Potsdam University, and Universidad Nacional de Colombia (Beca de Honor to M. Parra). Additional support was provided from the Colombian Petroleum Institute (ICP) and the Smithsonian Tropical Research Institute (STRI). The seismic data used in this work were released by an agreement with the Colombian National Hydrocarbons Agency (ANH). We are grateful to J. Cardona at ANH for his help in providing data for this study. Seismic interpretation was done in the PETREL™ software package through an academic license kindly provided by Schlumberger. J. Sayago at Potsdam University is thanked for her help and advice during seismic interpretation. C. Caldana is greatly acknowledged for her help with graphic work. The ideas presented here benefited from informative discussions with P. Ballato, B. Horton, and T. Gaona. We thank S. Morón, L. Quiroz, A. Rodríguez, and O. Romero for their help during field work.

Chapter 5
Conclusions

Within the retroarc foreland basin system of the Colombian Andes, the Cenozoic history of the Eastern Cordillera exemplifies the prime role of tectonic inheritance in the style and tempo of foreland basin evolution. In this dissertation I investigated the pattern of orogen advance in the northern Andes by reconstructing the exhumation patterns along the eastern flank of the Eastern Cordillera and the coeval sedimentary history of the adjacent retroarc foreland basin.

In the present-day Medina wedge-top basin, to the east of the deeply exhumed areas of the Eastern Cordillera, new sedimentological and provenance data, and a new chronological framework based on palynology reveal a three-stage history of tectonic subsidence and sediment accumulation. An initial Late Cretaceous to Paleocene episode of moderate subsidence preceded limited accommodation from Eocene through early Oligocene time and was subsequently followed by an episode of rapid early Oligocene to Pliocene subsidence. During the latter episode, tectonic subsidence increased in the Miocene-Pliocene interval. Using a comparison with published data on the early history of Cenozoic orogenesis to the west, in the Central Cordillera and Magdalena Valley Basin, I correlate the first stage with a late Paleocene eastward advance of the orogenic deformation front. This was, however, followed by Eocene to early Oligocene westward retreat of the foreland-basin system. Similarly, I interpret the second episode of faster tectonic subsidence in late Oligocene-Pliocene time to result from the eastward advance of the deformation front toward the eastern flank of the Eastern Cordillera. Rapid subsidence in the Medina Basin starting at ca. 30 Ma and the concomitant deposition of an eastward-thinning sedimentary wedge with pronounced facies changes suggests initial deposition in the proximal sectors of a foredeep depozone. This consequently reveals an eastward advance of the orogenic front to the area of the present-day Eastern Cordillera. Furthermore, growth-strata relationships in early Miocene to Pliocene strata from the western margin of the basin, as well as the lower degree of thermal maturation of these units compared to their lateral equivalents to the east, document folding due to protracted deformation along the reactivated faults that delimit the basin to the west.

In order to better identify the precise location of orogenic loads in time and space, I used apatite and zircon fission-track thermochronology coupled with paleo-burial estimates and published temporal indicators of brittle deformation and exhumation. I identified zircon fission-track (ZFT) reset ages in Lower Cretaceous and older units from the southern part of Eastern Cordillera (~4.5°N). These reset ZFT ages are younger than 25 Ma (late Oligocene) and occur in the immediate hanging wall of the range-bounding reverse faults that limited Mesozoic rift basins and were subsequently reactivated in contraction during the Cenozoic. To the north, in the Floresta and Santander massifs, and to the east, in the areas outside of the Mesozoic rift, post-depositional burial was insufficient to reset the ZFT thermochronometric system. Reset apatite fission-track (AFT) ages occur in the Upper Cretaceous and

older units from the eastern sector of the Eastern Cordillera. Like the ZFT ages, reset AFT ages are younger than 25 Ma. I interpret the thermochronogical ages as reflecting erosional exhumation triggered by mountain building associated with shortening. My main thermochronologic results are summarized as follows: (1) Reset ZFT ages in the western sector of the Eastern Cordillera, along the Villeta Anticlinorium, reveal that exhumation began before 25 Ma in this sector of the range; (2) farther east, reset AFT ages from the Lower Cretaceous strata in the Floresta Massif and thermal modeling of AFT data from partially reset Cenozoic sandstones in the axial Eastern Cordillera suggest initiation of thrust-related cooling sometime between 40 and 30 Ma. A coeval increase in sediment accumulation rates in the Medina Basin (~ 30 Ma) points to a causal link between orogenic loading along the axial sector of the Eastern Cordillera and enhanced tectonic subsidence in the adjacent basin; (3) ZFT and AFT ages in the Quetame Massif, along with the structural relationships of the contractionally reactivated faults, document the onset of exhumation at ~20 Ma. This episode of loading in the more external sector of the inverted Mesozoic rift generated the more pronounced increase in the tectonic subsidence in the Medina Basin; (4) finally, a suite of stratigraphically and structurally constrained samples from the Quetame Massif suggests that apparent exhumation rates during the Miocene were lower than in the Pliocene. Faster exhumation in the Pliocene has been independently documented in the Quetame Massif by means of AFT age-elevation profiles (Mora et al., 2008b) and may be linked to increased, climate-controlled erosional exhumation.

I derived rates of oroenic advance by superposing the new chronological constrains of deformation on a retrodeformed structural section across the central Colombian Andes. This analysis reveals that long-term propagation of this sector of the orogen occurred at rates of 2.5-2.7 mm/yr. However, an integrated analysis of the new thermochronologic data with published structural, thermochronologic, and geodynamic evidence of rock uplift reveals an episodic advance comprising three stages. An initial Upper Cretaceous-early Eocene episode of orogen migration occurred at rates of 0.5-3.1 mm/yr (1σ error) and accounts for up to 26% of the present width of the orogen. This episode was followed by very rapid orogenic advance during the middle Eocene-early Miocene, at average rates of 4.1-18.0 mm/yr, which resulted from tectonic inversion of the Eastern Cordillera. I correlate this acceleration in the orogenic advance with an increase in the accretionary flux that followed an increase in both, plate convergence rate and perpendicularity with respect to the inherited structural grain. By the end of this episode of fast propagation, the orogen had reached ~86% of its present width. Finally, slow propagation resulted from stagnation of the deformation front along the Servitá-Lengupá faults during the Mio-Pliocene. Preferential accommodation of deformation along these crustal anisotropies inherited from Mesozoic rifting resulted in rates of orogenic advance of 1.2-2.1 mm/yr.

This stationary condition of the orogen-basin pair imposed by the inherited structural fabrics of the eastern border of the Mesozoic rift provide an outstanding scenario for directly linking a long-lived history of exhumation of the Eastern Cordillera with the sedimentary record of the adjacent

proximal foredeep. One- and three-dimensional reconstructions of sediment accumulation reveal that coarsening upward trends in sedimentary facies occur primarily as a result of increased tectonic activity in the Eastern Cordillera. Climate, eustasy and differential erodability of the source areas have played a minor role in determining the large-scale trends of facies distribution in the proximal sector foreland basin system of the Colombian Andes during most of the Neogene. However, proposed positive feedback mechanisms between surface uplift in the source areas, increased orographic precipitation and erosional efficiency, and faster shortening in the Eastern Cordillera during the last ~4 Ma may have conspired to result in rapid progradation of coarse conglomerates to more distal sectors of the foreland.

My data demonstrate that episodic orogenic advance and unsteadiness in foreland basin development in the Colombian Andes have resulted from a reorganization of the orogenic loads primarily controlled by the inherited crustal characteristics of the orogen. Rather than responding to systematic adjustments of a wedge that deforms following Coulomb criteria, my data document that the loci or deformation in the central Colombian Andes are strongly modulated by the contractional reactivation of pre-strained basement in the orogenic foreland. Therefore, thrust motions along weak anisotropies inherited from previous tectonic events can fundamentally dictate the geometry of the adjacent foreland basin and thus influence the generation and migration of hydrocarbons and water in these environments.

References

Allen, P. A., and Allen, J. R., 2005, Basin Analysis: Principles and Applications: Oxford, Blackwell Science, 549 p.

Allmendinger, R. W., Ramos, V. A., Jordan, T. E., Palma, M., and Isacks, B. L., 1983, Paleogeography and Andean structural geometry, northwest Argentina: Tectonics, v. 2, no. 1, p. 1-16.

Anderson, L. C., Hartman, J. H., and Wesselingh, F., 2006, Close evolutionary affinities between freshwater corbulid bivalves from the Neogene of western Amazonia and Paleogene of the northern Great Plains, USA: Journal of South American Earth Sciences, v. 21, no. 1-2, p. 28-48.

Angevine, C. L., Heller, P. L., and Paola, C., 1993, Quantitative Sedimentary Basin Modeling, American Association of Petroleum Geologists Course Note Series 32, 132 p.

Bachu, S., Ramon, J. C., Villegas, M. E., and Underschultz, J. R., 1995, Geothermal regime and thermal history of the Llanos Basin, Colombia: American Association of Petroleum Geologists Bulletin, v. 79, no. 1, p. 116-129.

Barker, C. E., and Pawlewicz, M. J., 1993, An empirical determination of the minimum number of measurements needed to estimate the mean random vitrinite reflectance of disseminated organic matter: Organic Geochemistry, v. 20, no. 6, p. 643-651.

Barrientos, A., and Torres, R., 1994, Análisis paleoambiental de la secuencia del Terciario Inferior, Aguaclara, Casanare (Colombia) [BSc thesis]: Bogotá, Universidad Nacional de Colombia, 80 p.

Batt, G. E., Braun, J., Kohn, B., and McDougall, I., 2000, Thermochronological analysis of the dynamics of the Southern Alps, New Zealand: Geological Society of America Bulletin, v. 112, no. 2, p. 250-266.

Bayona, G., Cortés, M., Jaramillo, C., Ojeda, G., Aristizabal, J. J., and Reyes-Harker, A., 2008, An integrated analysis of an orogen-sedimentary basin pair: Latest Cretaceous-Cenozoic evolution of the linked Eastern Cordillera orogen and the Llanos foreland basin of Colombia: Geological Society of America Bulletin, v. 120, no. 9/10, p. 1171-1197.

Bayona, G., Lamus, F., Cardona, A., Jaramillo, C., Montes, C., and Tchegliakova, N., 2007, Procesos orogénicos para la Cuenca de Ranchería (Guajira, Colombia) y áreas adyacentes definidos por análisis de procedencia: Geología Colombiana, v. 32, p. 21-46.

Bayona, G., Reyes-Harker, A., Jaramillo, C. A., Rueda, M., Aristizabal, J., Cortés, M., and Gamba, N., 2006, Distinguishing tectonic versus eustatic surfaces in the Llanos Basin of Colombia, and implications for stratigraphic correlations, *in* Extended Abstracts, IX Simposio Bolivariano de Exploración Petrolera en las Cuencas Subandinas, Cartagena de Indias, Colombia, p. 13.

Beaumont, C., 1981, Foreland basins: Geophysical Journal, Royal Astronomical Society, v. 65, no. 2, p. 291-329.

Bernet, M., and Garver, J. I., 2005, Fission-track analysis of detrital zircon, *in* Reiners, P. W., and Ehlers, T. A., eds., Low Temperature Thermochronology: Techniques, Interpretations, and Applications: Reviews in Mineralogy and Geochemistry, v. 58: Washington D.C, Mineralogical Society of America, p. 205-238.

Bertotti, G., Mosca, P., Juez, J., Polino, R., and Dunai, T., 2006, Oligocene to present kilometres scale subsidence and exhumation of the Ligurian Alps and the Tertiary Piedmont Basin (NW Italy) revealed by apatite (U-Th)/He thermochronology: Correlation with regional tectonics: Terra Nova, v. 18, no. 1, p. 18-25.

Blair, T. C., 1999a, Sedimentary processes and facies of the waterlaid Anvil Spring Canyon alluvial fan, Death Valley, California: Sedimentology, v. 46, no. 5, p. 913-940.

Blair, T. C., 1999b, Sedimentology of the debris-flow-dominated Warm Spring Canyon alluvial fan, Death Valley, California: Sedimentology, v. 46, no. 5, p. 941-965.

Blair, T. C., and McPherson, J. G., 1994, Alluvial fans and their natural distinction from rivers based on morphology, hydraulic processes, sedimentary processes, and facies assemblages: Journal of Sedimentary Research A: Sedimentary Petrology & Processes, no. A64, p. 3.

Blythe, A. E., Burbank, D. W., Carter, A., Schmidt, K., and Putkonen, J., 2007, Plio-Quaternary exhumation history of the central Nepalese Himalaya: 1. Apatite and zircon fission track and apatite [U-Th]/He analyses: Tectonics, v. 26, no. 3.

Boyer, S. E., 1995, Sedimentary basin taper as a factor controlling the geometry and advance of thrust belts: American Journal of Science, v. 295, no. 10, p. 1220-1254.
Brandon, M. T., Roden-Tice, M. K., and Carver, J. I., 1998, Late Cenozoic exhumation of the Cascadia accretionary wedge in the Olympic Mountains, northwest Washington State: Geological Society of America Bulletin, v. 110, no. 8, p. 985-1009.
Bray, R. J., Green, P. F., and Duddy, I. R., 1992, Thermal history reconstruction using apatite fission track analysis and vitrinite reflectance: a case study from the UK East Midlands and southern North Sea, *in* Hardman, R. S. P., ed., Exploration Britain: Geological Insights for the Next Decade, Geological Society Special Publications, v. 67, p. 3-25.
Bridge, J. S., 1984, Large-scale facies sequences in alluvial overbank environments: Journal of Sedimentary Petrology, v. 54, no. 2, p. 583-588.
Bridge, J. S., 2003, Rivers and Floodplains: Forms, Processes and Sedimentary Record: Oxford, Blackwell Science, 487 p.
Burbank, D. W., 1992, Causes of recent Himalayan uplift deduced from depositional patterns in the Ganges basin: Nature, v. 357, p. 680-682.
Burbank, D. W., and Raynolds, R. G. H., 1988, Stratigraphic keys to the timing of thusting in terrestrial foreland basins: Applications to the northwestern Himalaya, *in* Kleinspehn, K. L., and Paola, C., eds., New Perspectives in Basin Analysis: Frontiers in Sedimentary Geology: New York, Springer-Verlag, p. 331-352.
Burbank, D. W., Verges, J., Munoz, J. A., and Bentham, P., 1992, Coeval hindward- and forward-imbricating thrusting in the south- central Pyrenees, Spain: timing and rates of shortening and deposition: Geological Society of America Bulletin, v. 104, no. 1, p. 3-17.
Burke, K., 1988, Tectonic evolution of the Caribbean: Annual Reviews of Earth and Planetary Sciences, v. 16, p. 201-230.
Burnham, A. K., and Sweeney, J. J., 1989, A chemical kinetic model of vitrinite maturation and reflectance: Geochimica et Cosmochimica Acta, v. 53, no. 10, p. 2649-2657.
Butler, K., and Schamel, S., 1988, Structure along the eastern margin of the Central Cordillera, upper Magdalena Valley, Colombia: Journal of South American Earth Sciences, v. 1, no. 1, p. 109-120.
Campbell, C. J., and Bürgl, H., 1965, Section throught the Eastern Cordillera of Colombia, South America: Geological Society of America Bulletin, v. 76, p. 567-590.
Cardozo, N., 2005, OSXBackstrip: 1D Backtripping of Geological Strata, available at: http://homepage.mac.com/nfcd/work/programs.html.
Cardozo, N., and Jordan, T., 2001, Causes of spatially variable tectonic subsidence in the Miocene Bermejo Foreland Basin, Argentina: Basin Research, v. 13, no. 3, p. 335-357.
Carrapa, B., Strecker, M. R., and Sobel, E. R., 2006, Cenozoic orogenic growth in the Central Andes: Evidence from sedimentary rock provenance and apatite fission track thermochronology in the Fiambalá Basin, southernmost Puna Plateau margin (NW Argentina): Earth and Planetary Science Letters, v. 247, no. 1-2, p. 82-100.
Carrera, N., Muñoz, J. A., Sàbat, F., Mon, R., and Roca, E., 2006, The role of inversion tectonics in the structure of the Cordillera Oriental (NW Argentinean Andes): Journal of Structural Geology, v. 18, no. 11, p. 1921-1932.
Carroll, A. R., Chetel, L. M., and Smith, M. E., 2006, Feast to famine: Sediment supply control on Laramide basin fill: Geology, v. 34, no. 3, p. 197-200.
Catuneanu, O., Beaumont, C., and Waschbusch, P., 1997, Interplay of static loads and subduction dynamics in foreland basins: Reciprocal stratigraphies and the "missing" peripheral bulge: Geology, v. 25, no. 12, p. 1087-1090.
Catuneanu, O., Hancox, P. J., and Rubidge, B. S., 1998, Reciprocal flexural behaviour and contrasting stratigraphies: A new basin development model for the Karoo retroarc foreland system, South Africa: Basin Research, v. 10, no. 4, p. 417-439.
Cazier, E. C., Cooper, M. A., Eaton, S. G., and Pulham, A. J., 1997, Basin development and tectonic history of the Llanos Basin, Eastern Cordillera, and Middle Magdalena Valley, Colombia: Reply: American Association of Petroleum Geologists Bulletin, v. 81, no. 8, p. 1332-1338.
Cazier, E. C., Hayward, A. B., Espinosa, G., Velandia, J., Mugniot, J.-F., and Leel, W. G., 1995, Petroleum geology of the Cusiana Field, Llanos Basin foothills, Colombia: American Association of Petroleum Geologists Bulletin, v. 79, no. 10, p. 1444-1463.

Cediel, F., Shaw, R., and Cáceres, C., 2003, Tectonic assembly of the northern Andean Block, *in* Bartolini, C., Buffler, R. T., and Blickwede, J., eds., The Circum-Gulf of Mexico and the Caribbean: Hydrocarbon habitats, basin formation and plate tectonics, American Association of Petrolum Geologists Memoir 79, p. 815-848.

Céspedes, S., and Peña, L., 1995, Relaciones estratigráficas y ambientes de depósito de las formaciones del Terciario Inferior aflorante entre Tunja y Paz de Río, Boyacá: Bogotá, Universidad Nacional de Colombia, 50 p.

Coleman, J. M., Roberts, H. H., and Stone, G. W., 1998, Mississippi River delta: An overview: Journal of Coastal Research, v. 14, no. 3, p. 698-716.

Colletta, B., Hebrard, F., Letouzey, J., Werner, P., and Rudkiweicz, J. L., 1990, Tectonic style and crustal structure of the Eastern Cordillera, Colombia from a balanced cross section, *in* Letouzey, J., ed., Petroleum and Tectonics in Mobile Belts: Paris, Editions Technip, p. 81-100.

Collinson, J., Mountney, N., and Thompson, D., 2006, Sedimentary Structures, Terra Publishing, 304 p.

Colmenares, L., and Zoback, M. D., 2003, Stress field and seismotectonics of northern South America: Geology, v. 31, p. 721-724.

Coney, P. J., and Evenchick, C. A., 1994, Consolidation of the American Cordilleras: Journal of South American Earth Sciences, v. 7, no. 3-4, p. 241-261.

Cooper, M. A., Addison, F. T., Álvarez, R., Coral, M., Graham, R. H., Hayward, S. H., Martínez, J., Naar, J., Peñas, R., Pulham, A. J., and Taborda, A., 1995, Basin development and tectonic history of the Llanos Basin, Eastern Cordillera, and Middle Magdalena Valley, Colombia: American Association of Petroleum Geologists Bulletin, v. 79, no. 10, p. 1421-1443.

Corredor, F., 2003, Eastward extent of the Late Eocene-Early Oligocene onset of deformation across the northern Andes: Constraints from the northern portion of the Eastern Cordillera fold belt, Colombia: Journal of South American Earth Sciences, v. 16, no. 6, p. 445-457.

Cortés, M., and Angelier, J., 2005, Current states of stress in the northern Andes as indicated by focal mechanisms of earthquakes: Tectonophysics, v. 403, no. 1-4, p. 29-58.

Cortés, M., Angelier, J., and Colletta, B., 2005, Paleostress evolution of the northern Andes (Eastern Cordillera of Colombia): Implications on plate kinematics of the South Caribbean region: Tectonics, v. 24, no. 1, p. 1-27.

Cortés, M., Colletta, B., and Angelier, J., 2006, Structure and tectonics of the central segment of the Eastern Cordillera of Colombia: Journal of South American Earth Sciences, v. 21, no. 4, p. 437-465.

Coutand, I., Carrapa, B., Deeken, A., Schmitt, A. K., Sobel, E. R., and Strecker, M. R., 2006, Propagation of orographic barriers along an active range front: Insights from sandstone petrography and detrital apatite fission-track thermochronology in the intramontane Angastaco basin, NW Argentina: Basin Research, v. 18, no. 1, p. 1-26.

Coutand, I., Cobbold, P. R., De Urreiztieta, M., Gautier, P., Chauvin, A., Gapais, D., Rossello, E. A., and López-Gamundi, O., 2001, Style and history of Andean deformation, Puna plateau, northwestern Argentina: Tectonics, v. 20, no. 2, p. 210-234.

Crowhurst, P. V., Green, P. F., and Kamp, P. J. J., 2002, Appraisal of (U-Th)/He apatite thermochronology as a thermal history tool for hydrocarbon exploration: An example from the Taranaki Basin, New Zealand: American Association of Petroleum Geologists Bulletin, v. 86, no. 10, p. 1801-1819.

Da Silva, S., 2006, Palynological biozonation of the Upper Guayabo Formation, Eastern Cordillera, Colombia: Smithsonian Tropical Research Institute, Internal Report, 16 p.

Dahlen, F. A., 1990, Critical taper model of fold-and-thrust belts and accretionary wedges: Annual Reviews of Earth and Planetary Sciences, v. 18, p. 55-99.

Dahlen, F. A., and Barr, T. D., 1989, Brittle frictional mountain building. 1. Deformation and mechanical energy budget: Journal of Geophysical Research, v. 94, no. B4, p. 3906-3922.

Dahlen, F. A., Suppe, J., and Davis, D., 1984, Mechanics of fold-and-thrust belts and accretionary wedges: Cohesive Coulomb theory: Journal of Geophysical Research, v. 89, no. B12, p. 10087-10101.

Dalrymple, R. W., Baker, E. K., Harris, P. T., and Hughes, M., 2003, Sedimentology and stratigraphy of a tide-dominated, foreland-basin delta (Fly River, Papua, New Guinea), *in* Sidi, F. H., Nummedal, D., Imbert, P., Darman, H., and Posamentier, H. W., eds., Tropical Deltas of

Southeast Asia - Sedimentology, Stratigraphy and Petroleum Geology: Society for Sedimentary Geology Special Publication, vol. 76, p. 147-173.
Dalrymple, R. W., and Choi, K., 2007, Morphologic and facies trends through the fluvial-marine transition in tide-dominated depositional systems: A schematic framework for environmental and sequence-stratigraphic interpretation: Earth-Science Reviews, v. 81, no. 3-4, p. 135-174.
Dalrymple, R. W., Zaitlin, B. A., and Boyd, R., 1992, Estuarine facies models : conceptual basis and stratigraphic implications: Journal of Sedimentary Petrology, v. 62, no. 6, p. 1130-1146.
Damanti, J. F., 1993, Geomorphic and structural controls on facies patterns and sediment composition in a modern foreland basin, *in* Marzo, M., and Puigdefábregas, C., eds., Alluvial sedimentation, International Association of Sedimentologists Special Publication, v. 17, p. 221-233.
Dávila, F. M., and Astini, R. A., 2003, Early Middle Miocene broken foreland development in the southern Central Andes: Evidence for extension prior to regional shortening: Basin Research, v. 15, no. 3, p. 379-396.
Davis, D., Suppe, J., and Dahlen, F. A., 1983, Mechanics of fold-and- thrust belts and accretionary wedges: Journal of Geophysical Research, v. 88, no. B2, p. 1153-1172.
DeCelles, P. G., 2004, Late Jurassic to Eocene evolution of the Cordilleran thrust belt and foreland basin system, western U.S.A: American Journal of Science, v. 304, no. 2, p. 105-168.
DeCelles, P. G., and Currie, B. S., 1996, Long-term sediment accumulation in the Middle Jurassic-early Eocene Cordilleran retroarc foreland-basin system: Geology, v. 24, no. 7, p. 591-594.
DeCelles, P. G., and DeCelles, P. C., 2001, Rates of shortening, propagation, underthrusting, and flexural wave migration in continental orogenic systems: Geology, v. 29, no. 2, p. 135-138.
DeCelles, P. G., Gehrels, G. E., Quade, J., Ojha, T. P., Kapp, P. A., and Upreti, B. N., 1998, Neogene foreland basin deposits, erosional unroofing, and the kinematic history of the Himalayan fold-thrust belt, western Nepal: Geological Society of America Bulletin, v. 110, no. 1, p. 2-21.
DeCelles, P. G., and Giles, K. A., 1996, Foreland basin systems: Basin Research, v. 8, no. 2, p. 105-123.
DeCelles, P. G., Gray, M. B., Ridgway, K. D., Cole, R. B., Srivastava, P., Pequera, N., and Pivnik, D. A., 1991, Kinematic history of a foreland uplift from Paleocene synorogenic conglomerate, Beartooth Range, Wyoming and Montana: Geological Society of America Bulletin, v. 103, no. 11, p. 1458-1475.
DeCelles, P. G., Langford, R. P., and Schwartz, R. K., 1983, Two new methods of paleocurrent determination from trough cross- stratification: Journal of Sedimentary Petrology, v. 53, no. 2, p. 629-642.
DeCelles, P. G., and Mitra, G., 1995, History of the Sevier orogenic wedge in terms of critical taper models, northeast Utah and southwest Wyoming: Geological Society of America Bulletin, v. 107, no. 4, p. 454-462.
Deming, D., Nunn, J. A., and Evans, D. G., 1990, Thermal effects of compaction-driven groundwater flow from overthrust belts: Journal of Geophysical Research, v. 95, no. B5, p. 6669-6683.
Dengo, C. A., and Covey, M. C., 1993, Structure of the Eastern Cordillera of Colombia: implications for trap styles and regional tectonics: American Association of Petroleum Geologists Bulletin, v. 77, no. 8, p. 1315-1337.
Dickinson, W. R., 1974, Plate tectonics and sedimentation, *in* Dickinson, W. R., ed., Tectonics and Sedimentation: Tulsa, Oklahoma, Society of Economic Paleontologists and Mineralogists Special Publications, v. 22, p. 1-27.
Dimaté, C., Rivera, L. A., Taboada, A., Delouis, B., Osorio, A., Jiménez, E., Fuenzalida, A., Cisternas, A., and Gómez, I., 2003, The 19 January 1995 Tauramena (Colombia) earthquake: geometry and stress regime: Tectonophysics, v. 363, no. 3-4, p. 159-180.
Donelick, R., and Miller, D. S., 1991, Enhanced TINT fission track densities in low spontaneous track density apatites using 252Cf-derived fission fragment tracks. A model and experimental observations: Nuclear Tracks and Radiation Measurements, v. 18, no. 3, p. 301-307.
Donelick, R. A., Ketcham, R. A., and Carlson, W. D., 1999, Variability of apatite fission-track annealing kinetics: II. Crystallographic orientation effects: American Mineralogist, v. 84, no. 9, p. 1224-1234.
Donelick, R. A., O'Sullivan, P. B., and Ketcham, R. A., 2005, Apatite fission-track analysis, *in* Reiners, P. W., and Ehlers, T. A., eds., Low Temperature Thermochronology: Techniques,

Interpretations, and Applications: Reviews in Mineralogy and Geochemistry, v. 58: Washington D.C, Mineralogical Society of America, p. 49-94.
Dumitru, T. A., 1993, New computer-automated microscope stage system for fission-track analysis: Nuclear Tracks and Radiation Measurements, v. 21, no. 4, p. 575-580.
Dunkl, I., 2002, Trackkey: A windows program for calculation and graphical presentation of fission track data: Computers and Geosciences, v. 28, no. 1, p. 3-12.
Duque-Caro, H., 1990, The Choco Block in the northwestern corner of South America: Structural, tectonostratigraphic and paleogeographic implications: Journal of South American Earth Sciences, v. 3, p. 71-84.
Echavarria, L., Hernández, R., Allmendinger, R., and Reynolds, J., 2003, Subandean thrust and fold belt of northwestern Argentina: Geometry and timing of the Andean evolution: American Association of Petroleum Geologists Bulletin, v. 87, no. 6, p. 965-985.
Ehlers, T. A., 2005, Crustal thermal processes and the interpretation of thermochronometer data, *in* Reiners, P. W., and Ehlers, T. A., eds., Low Temperature Thermochronology: Techniques, Interpretations, and Applications: Reviews in Mineralogy and Geochemistry, v. 58: Washington D.C, Mineralogical Society of America, p. 315-350.
Einsele, G., 2000, Sedimentary Basins: Evolution, Facies and Sedimentary Budget: Heidelberg, Springer Verlag, 781 p.
Erslev, E. A., 1986, Basement balancing of Rocky Mountain foreland uplifts (USA): Geology, v. 14, no. 3, p. 259-262.
Etayo-Serna, F., 1968, El sistema Cretáceo en la región de Villa de Leiva y zonas próximas: Geología Colombiana, v. 5, p. 5-74.
Fabre, A., 1983, La subsidencia de la Cuenca del Cocuy (Cordillera Oriental de Colombia) durante el Cretáceo y el Terciario Inferior. Primera parte: Estudio cuantitativo de la subsidencia: Geología Norandina, v. 8, p. 22-27.
Fitzgerald, P. G., Stump, E., and Redfield, T. F., 1993, Late Cenozoic uplift of Denali and its relation to relative plate motion and fault morphology: Science, v. 259, no. 5094, p. 497-499.
Fleischer, R. L., Price, P. B., and Walker, R. M., 1975, Nuclear Track in Solids: Principles and Applications: Berkeley, University of California.
Flemings, P. B., and Jordan, T. E., 1989, A synthetic stratigraphic model of foreland basin development: Journal of Geophysical Research, v. 94, no. B4, p. 3851-3866.
Flemings, P. B., and Jordan, T. E., 1990, Stratigraphic modeling of foreland basins: interpreting deformation and lithosphere rheology: Geology, v. 18, p. 430-435.
Föllmi, K. B., Garrison, R. E., Ramirez, P. C., Zambrano-Ortiz, F., Kennedy, W. J., and Lehner, B. L., 1992, Cyclic phosphate-rich successions in the upper Cretaceous of Colombia: Palaeogeography, Palaeoclimatology, Palaeoecology, v. 93, no. 3-4, p. 151-182.
Forster, C., and Smith, L., 1989, The influence of groundwater flow on thermal regimes in mountainous terrain: a model study: Journal of Geophysical Research, v. 94, no. B7, p. 9439-9451.
Galbraith, R. F., 1981, On statistical models for fission-tracks counts: Mathematical Geology, v. 13, no. 6, p. 471-478.
Gansser, A., 1973, Facts and theories on the Andes: Journal of the Geological Society, v. 129, p. 93-131.
Garver, J. I., Reiners, P. W., Walker, L. J., Ramage, J. M., and Perry, S. E., 2005, Implications for timing of Andean uplift from thermal resetting of radiation-damaged zircon in the Cordillera Huayhuash, northern Peru: Journal of Geology, v. 113, no. 2, p. 117-138.
Germeraad, J. H., Hopping, C. A., and Muller, J., 1968, Palynology of Tertiary sediments from tropical areas: Review of Palaeobotany and Palynology, v. 6, p. 189-348.
Gleadow, A. J. W., 1981, Fission-track dating methods: what are the real alternatives?: Nuclear Tracks, v. 5, no. 1-2, p. 3-14.
Gleadow, A. J. W., Duddy, I. R., Green, P. F., and Lovering, J. F., 1986, Confined fission track lengths in apatite: a diagnostic tool for thermal history analysis: Contributions to Mineralogy and Petrology, v. 94, no. 4, p. 405-415.
Godin, L., Parrish, R. R., Brown, R. L., and Hodges, K. V., 2001, Crustal thickening leading to exhumation of the Himalayan metamorphic core of Central Nepal: Insight from U-Pb geochronology and 40Ar/39Ar thermochronology: Tectonics, v. 20, no. 5, p. 729-747.

Gómez, A., Jaramillo, C., Parra, M., and Mora, A., 2008, Huesser Horizon: A lake and marine incursion in northwestern South America during the early Miocene: Palaios v. in press.

Gómez, E., 2001, Tectonic controls on the Late Cretaceous to Cenozoic sedimentary fill of the Middle Magdalena Valley Basin, Eastern Cordillera and Llanos Basin, Colombia [Ph.D thesis]: Ithaca, New York, Cornell University, 619 p.

Gómez, E., Jordan, T. E., Allmendinger, R. W., and Cardozo, N., 2005a, Development of the Colombian foreland-basin system as a consequence of diachronous exhumation of the northern Andes: Geological Society of America Bulletin, v. 117, no. 9-10, p. 1272-1292.

Gómez, E., Jordan, T. E., Allmendinger, R. W., Hegarty, K., and Kelley, S., 2005b, Syntectonic Cenozoic sedimentation in the northern middle Magdalena Valley Basin of Colombia and implications for exhumation of the Northern Andes: Geological Society of America Bulletin, v. 117, no. 5-6, p. 547-569.

Gómez, E., Jordan, T. E., Allmendinger, R. W., Hegarty, K., Kelley, S., and Heizler, M., 2003, Controls on architecture of the Late Cretaceous to Cenozoic southern Middle Magdalena Valley Basin, Colombia: Geological Society of America Bulletin, v. 115, no. 2, p. 131-147.

Gómez, J., Nivia, A., Montes, N. E., Tejada, M. L., Jiménez, D. M., Sepúlveda, M. J., Osoria, J. A., Gaona, T., Diederix, H., Mora, M., and Uribe, H., 2007, Geologic Map of Colombia: INGEOMINAS, scale 1:500,000: Bogotá.

Gradstein, F. M., Ogg, J. G., Smith, A. G., Bleeker, W., and Lourens, L. J., 2004, A new Geologic Time Scale, with special reference to Precambrian and Neogene: Episodes, v. 27, no. 2, p. 83-100.

Green, P. F., 1981, A new look at statistics in fission-track dating: Nuclear Tracks, v. 5, p. 77-86.

Green, P. F., Duddy, I. R., Gleadow, A. J. W., Tingate, P. R., and Laslett, G. M., 1986, Thermal annealing of fission tracks in apatite 1. A qualitative description: Chemical Geology, v. 59, no. 4, p. 237-253.

Green, P. F., Duddy, I. R., Laslett, G. M., Hegarty, K. A., Gleadow, A. J. W., and Lovering, J. F., 1989, Thermal annealing of fission tracks in apatite 4. Quantitative modelling techniques and extension to geological timescales: Chemical Geology (Isotope Geoscience Section), v. 79, no. 2, p. 155-182.

Guerrero, J., and Sarmiento, G., 1996, Estratigrafía física, palinológica, sedimentológica y secuencial del Cretácico Superior y Paleoceno del Piedemonte Llanero. Implicaciones en exploración petrolera: Geología Colombiana, v. 20, p. 3-66.

Guidish, T. M., Kendall, C. G. S. C., Lerche, I., Toth, D. J., and Yarzab, R. F., 1985, Basin evaluation using burial history calculations: An overview.: American Association of Petroleum Geologists Bulletin, v. 69, no. 1, p. 92-105.

Hain, M. P., and Strecker, M. R., 2008, The control of Cretaceous extension and pre-existing basement structures upon position and style of Andean shortening - A case study from the Valle de Lerma, Salta, NW Argentina, *in* XVII Congreso Geológico Argentino, San Salvador de Jujuy, Argentina.

Haq, B. U., Hardenbol, J., and Vail, P. R., 1987, Chronology of fluctuating sea levels since the Triassic: Science, v. 235, no. 4793, p. 1156-1167.

Harris, S. E., and Mix, A. C., 2002, Climate and tectonic influences on continental erosion of tropical South America, 0-13 Ma: Geology, v. 30, no. 5, p. 447-450.

Hasebe, N., Barbarand, J., Jarvis, K., Carter, A., and Hurford, A. J., 2004, Apatite fission-track chronometry using laser ablation ICP-MS: Chemical Geology, v. 207, no. 3-4, p. 135-145.

Heller, P. L., Angevine, C. L., Winslow, N. S., and Paola, C., 1988, Two-phase stratigraphic model of foreland basin sequences: Geology, v. 16, p. 501-504.

Heller, P. L., and Paola, C., 1992, The large-scale dynamics of grain-size variation in alluvial basins, 2: Application to syntectonic conglomerate: Basin Research, v. 4, p. 91-102.

Helmens, K. F., 1990, Neogene-Quaternary Geology of the High Plain of Bogotá, Eastern Cordillera, Colombia (Stratigraphy, Paleoenvironments and Landscape Evolution) [Ph.D thesis], University of Amsterdam, 202 p.

Helmens, K. F., and Van der Hammen, T., 1994, The Pliocene-Quaternary of the high plain of Bogotá: a history of tectonic uplift, basin development and climatic change: Quaternary International, v. 21, p. 41-61.

Hilley, G. E., Blisniuk, P. M., and Strecker, M. R., 2005, Mechanics and erosion of basement cored uplift provinces: Journal of Geophysical Research, Solid Earth, v. 110, B12409, doi:10. 1029/2005JB0003704, 2005.

Hilley, G. E., Strecker, M. R., and Ramos, V. A., 2004, Growth and erosion of fold-and-thrust belts with an application to the Aconcagua fold-and-thrust belt, Argentina: Journal of Geophysical Research B: Solid Earth, v. 109, B01410, doi:10.1029/2002JB002282.

Hoffman, P. F., and Grotzinger, J. P., 1993, Orographic precipitation, erosional unloading, and tectonic style: Geology, v. 21, no. 3, p. 195-198.

Hooghiemstra, H., Wijninga, V. M., and Cleef, A. M., 2006, The Paleobotanical record of Colombia: Implications for biogeography and biodiversity: Annals of the Missouri Botanical Garden, v. 93, p. 297-325.

Hoorn, C., Kaandorp, M. C. N., and Roele, J., 1987, Tertiary sediments of the Usme Valley, Colombia: a palynological and stratigraphical approach, Hugo de Vries Laboratory, Amsterdam, 31 p.

Horton, B. K., 1999, Erosional control on the geometry and kinematics of thrust belt development in the central Andes: Tectonics, v. 18, no. 6, p. 1292-1304.

Horton, B. K., 2005, Revised deformation history of the central Andes: Inferences from Cenozoic foredeep and intermontane basins of the Eastern Cordillera, Bolivia: Tectonics, v. 24, no. 3, p. 1-18.

Horton, B. K., Constenius, K. N., and DeCelles, P. G., 2004, Tectonic control on coarse-grained foreland-basin sequences: An example from the Cordilleran foreland basin, Utah: Geology, v. 32, no. 7, p. 637-640.

Horton, B. K., Hampton, B. A., and Waanders, G. L., 2001, Paleogene synorogenic sedimentation in the Altiplano plateau and implications for initial mountain building in the Central Andes: Bulletin of the Geological Society of America, v. 113, no. 11, p. 1387-1400.

Hoth, S., Adam, J., Kukowski, N., and Onken, O., 2005, Influence of erosion on the kinematics of bivergent orogens: Results from scaled sandbox simulations, *in* Willet, S. D., Hovius, N., Brandon, M. T., and Fisher, D., eds., Tectonics, Climate, and Landscape Evolution: Penrose Conference Series, Geological Society of America, Special Paper 398, p. 201-225.

Hubbard, M. S., and Harrison, T. M., 1989, 40Ar/39Ar age constraints on deformation and metamorphism in the Main Central Thrust zone and Tibetan Slab, eastern Nepal, Himalaya: Tectonics, v. 8, no. 4, p. 865-880.

Huntington, K. W., Ehlers, T. A., Hodges, K. V., and Whipp, D. M., 2007, Topography, exhumation pathway, age uncertainties, and the interpretation of thermochronometer data: Tectonics, v. 26, TC4012, doi:10.1029/2007TC002108.

Hurford, A. J., and Green, P. F., 1983, The zeta age calibration of fission-track dating: Isotope Geoscience, v. 1, no. 4, p. 285-317.

Jaramillo, C., and Dilcher, D. L., 2000, Microfloral diversity patterns of the late Paleocene-Eocene interval in Colombia, northern South America: Geology, v. 28, no. 9, p. 815-818.

Jaramillo, C., and Dilcher, D. L., 2001, Middle Paleogene palynology of Central Colombia, South America: a study of pollen and spores from tropical latitudes: Palaeontographica B, v. 258, p. 87-213.

Jaramillo, C., Muñoz, F., Cogollo, M., and Parra, F., 2005, Quantitative biostratigraphy for the Paleocene of the Llanos Foothills, Colombia: Improving palynological resolution for oil exploration, *in* Powell, A. J., and Riding, J., eds., Recent Developments in Applied Biostratigraphy: London, The Micropalaeontological Society Special Publications, v. 1, p. 145-159.

Jaramillo, C., Pardo-Trujullo, A., Rueda, M., Harrington, G., Bayona, G., Torres, V., and Mora, G., 2007, Palynology of the Upper Paleocene Cerrejon Formation, Northern Colombia: Palynology, v. 31, p. 153-189.

Jaramillo, C., and Rueda, M., 2004, Impact of biostratigraphy in oil exploration, *in* Abstracts, III Convención Técnica de la Asociación Colombiana de Geólogos y Geofísicos del Petróleo, Bogotá, p. 6.

Jaramillo, C., Rueda, M., Bayona, G., Santos, C., Florez, P., and Parra, F., 2008, Biostratigraphy breaking paradigms: dating the Mirador Formation in the Llanos Basin of Colombia, *in*

Demchuk, T., and Waszczak, R., eds., Geologic Problem Solving with Microfossils, Society for Sedimentary Geology Special Publication TMS001 (in press).
Jaramillo, C., Rueda, M., and Mora, G., 2006, Cenozoic plant diversity in the Neotropics: Science, v. 311, p. 1893-1896.
Jiménez, D., 2000, Filitas y Esquistos de Busbanzá, Catálogo de las Unidades Litoestratigráficas de Colombia: Bogotá, INGEOMINAS, p. 19.
Jones, M. A., Heller, P. L., Roca, E., Garcés, M., and Cabrera, L., 2004, Time lag of syntectonic sedimentation across an alluvial basin: Theory and example from the Ebro Basin, Spain: Basin Research, v. 16, no. 4, p. 467-488.
Jordan, T. E., 1981, Thrust loads and foreland basin evolution, Cretaceous, western United States: American Association of Petroleum Geologists Bulletin, v. 65, p. 2506-2520.
Jordan, T. E., 1995, Retroarc Foreland and Related Basins, *in* Busby, C. J., and Ingersoll, R. V., eds., Tectonic of Sedimentary Basins: Cambridge, MA, Blackwell Science, p. 331-362.
Jordan, T. E., and Allmendinger, R. W., 1986, The Sierras Pampeanas of Argentina: a modern analogue of Rocky Mountain foreland deformation: American Journal of Science, v. 286, no. 10, p. 737-764.
Jordan, T. E., Allmendinger, R. W., Damanti, J. F., and Drake, R. E., 1993, Chronology of motion in a complete thrust belt: the Precordillera, 30-31°S, Andes Mountains: Journal of Geology, v. 101, no. 2, p. 135-156.
Jordan, T. E., Flemings, P. B., and J.A, B., 1988, Dating thrust fault activity by use of foreland-basin strata, *in* Kleispehn, K. L., and Paola, C., eds., New Perspectives in Basin Analysis: New York, Springer Verlag, p. 307-330.
Jordan, T. E., Isacks, B. L., Allmendinger, R. W., Brewer, J. A., Ramos, V. A., and Ando, C. J., 1983, Andean tectonics related to geometry of subducted Nazca plate: Geological Society of America Bulletin, v. 94, no. 3, p. 341-361.
Jordan, T. E., Schlunegger, F., and Cardozo, N., 2001, Unsteady and spatially variable evolution of the Neogene Andean Bermejo foreland basin, Argentina: Journal of South American Earth Sciences, v. 14, no. 7, p. 775-798.
Julivert, M., 1963, Los rasgos tectónicos de la región de la Sabana de Bogotá y los mecanismos de la formación de las estructuras: Boletín de Geología, Universidad Industrial de Santander, v. 13-14, p. 5-102.
Kammer, A., 2003, La Formación Tilatá en los alrededores de Chocontá: Marco tectónico y ambientes deposicionales: Análisis Geográficos, v. 26, p. 69-100.
Kammer, A., and Sánchez, J., 2006, Early Jurassic rift structures associated with the Soapaga and Boyacá Faults of the Eastern Cordillera, Colombia: Sedimentological inferences and regional implications: Journal of South American Earth Sciences, v. 21, no. 4, p. 412-422.
Kerr, A. C., and Tarney, J., 2005, Tectonic evolution of the Caribbean and northwestern South America: The case for accretion of two Late Cretaceous oceanic plateaus: Geology, v. 33, no. 4, p. 269-272.
Ketcham, R. A., 2005, Forward and inverse modeling of low-temperature thermochronometry data, *in* Reiners, P. W., and Ehlers, T. A., eds., Low Temperature Thermochronology: Techniques, Interpretations, and Applications: Reviews in Mineralogy and Geochemistry, v. 58: Washington D.C, Mineralogical Society of America, p. 275-314.
Ketcham, R. A., Carter, A., Donelick, R. A., Barbarand, J., and Hurford, A. J., 2007a, Improved measurement of fission-track annealing in apatite using c-axis projection: American Mineralogy, v. 92, no. 5-6, p. 789-798.
Ketcham, R. A., Carter, A., Donelick, R. A., Barbarand, J., and Hurford, A. J., 2007b, Improved modeling of fission-track annealing in apatite: American Mineralogy, v. 92, no. 5-6, p. 799-810.
Ketcham, R. A., Donelick, R. A., and Carlson, W. D., 1999, Variability of apatite fission-track annealing kinetics: III. Extrapolation to geological time scales: American Mineralogist, v. 84, no. 9, p. 1235-1255.
Kley, J., Monaldi, C. R., and Salfity, J. A., 1999, Along-strike segmentation of the Andean foreland: causes and consequences: Tectonophysics, v. 301, no. 1-2, p. 75-94.

Kominz, M. A., Browning, J. V., Miller, K. G., Sugarman, P. J., Mizintseva, S., and Scotese, C. R., 2008, Late Cretaceous to Miocene sea-level estimates from the New Jersey and Delaware coastal plain coreholes: An error analysis: Basin Research, v. 20, no. 2, p. 211-226.

Kraus, M. J., 1999, Paleosols in clastic sedimentary rocks: Their geologic applications: Earth Science Reviews, v. 47, no. 1-2, p. 41-70.

Lowe, D. R., 1975, Water escape structures in coarse-grained sediments: Sedimentology, v. 22, p. 15-204.

Mancktelow, N. S., and Grasemann, B., 1997, Time-dependent effects of heat advection and topography on cooling histories during erosion: Tectonophysics, v. 270, no. 3-4, p. 167-195.

Marshak, S., Karlstom, K., and Timmons, J. M., 2000, Inversion of Proterozoic extensional faults: An explanation for the pattern of Laramide and Ancestral Rockies intracratonic deformation, United States: Geology, v. 28, no. 8, p. 735-738.

Martínez, J., 2006, Structural evolution of the Llanos foothills, Eastern Cordillera, Colombia: Journal of South American Earth Sciences, v. 21, no. 4, p. 510-520.

Masek, J. G., Isacks, B. L., Gubbels, T. L., and Fielding, E. J., 1994, Erosion and tectonics at the margins of continental plateaus: Journal of Geophysical Research, v. 99, no. B7, p. 13,941-13,956.

Mayorga, M., and Vargas, M., 1995, Caracterización geoquímica y facial de las rocas potencialmente generadoras de hidrocarburos del Cretáceo y Terciario inferior de la Cordillera Oriental y Piedemomte [BSc thesis]: Bogota, Colombia, Universidad Nacional de Colombia, 150 p.

McCarthy, P. J., Martini, I. P., and Leckie, D. A., 1997, Anatomy and evolution of a Lower Cretaceous alluvial plain: Sedimentology and palaeosols in the upper Blairmore Group, south-western Alberta, Canada: Sedimentology, v. 44, no. 2, p. 197-220.

McClay, K. R., and Whitehouse, P. S., 2005, Analog modeling of doubly vergent thrust wedges, *in* McClay, K. R., ed., American Association of Petrolum Geologists Memoir 82, p. 184-206.

McCourt, W. J., Aspden, J. A., and Brook, M., 1984, New geological and geochronological data from the Colombian Andes: continental growth by multiple accretion: Journal of the Geological Society, v. 141, no. 5, p. 831-845.

Meigs, A. J., Burbank, D. W., and Beck, R. A., 1995, Middle-late Miocene (>10 Ma) formation of the Main Boundary Thrust in the western Himalaya: Geology, v. 23, no. 5, p. 423-426.

Miall, A. D., 1996, The Geology of Fluvial Deposits: sedimentary facies, basin analysis, and petroleum geology: New York, Springer, 582 p.

Milliman, J. D., and Syvitski, J. P. M., 1992, Geomorphic/tectonic control of sediment discharge to the ocean: the importance of small mountainous rivers: Journal of Geology, v. 100, no. 5, p. 525-544.

Mitchum, R. M. J., and Van Wagoner, J. C., 1991, High-frequency sequences and their stacking patterns: sequence-stratigraphic evidence of high-frequency eustatic cycles: Sedimentary Geology, v. 70, no. 2-4, p. 131-160.

Mojica, J., Kammer, A., and Ujueta, G., 1996, El Jurásico del sector noroccidental de Suramérica: Geología Colombiana, v. 21, p. 3-40.

Mojica, J., and Villarroel, C., 1984, Contribución al conocimiento de las unidades paleozoicas del área de Floresta (Cordillera Oriental Colombiana, Departamento de Boyacá) y en especial de la Formación Cuche: Geología Colombiana, v. 13, p. 55-80.

Molnar, P., 2004, Late Cenozoic increase in accumulation rates of terrestrial sediment: How might climate change have affected erosion rates?: Annual Review of Earth and Planetary Sciences, v. 32, p. 67-89.

Mon, R., and Salfity, J. A., 1995, Tectonic evolution of the Andes of northern Argentina, *in* Tankard, A. J., Suarez, R., and Welsink, H. J., eds., Petroleum Basins of South America: Tulsa, American Association of Petroleum Geologists Memoir 62, p. 269-283.

Montes, C., Hatcher Jr., R. D., and Restrepo-Pace, P. A., 2005, Tectonic reconstruction of the northern Andean blocks: Oblique convergence and rotations derived from the kinematics of the Piedras-Girardot area, Colombia: Tectonophysics, v. 399, no. 1-4, p. 221-250.

Montgomery, D. R., Balco, G., and Willett, S. D., 2001, Climate, tectonics, and the morphology of the Andes: Geology, v. 29, no. 7, p. 579-582.

Mora, A., 2007, Inversion tectonics and exhumation processes in the Eastern Cordillera of Colombia [PhD thesis]: Potsdam, Universität Potsdam, 133 p.

Mora, A., Gaona, T., Kley, J., Montoya, D., Parra, M., Quiroz, L. I., Reyes, G., and Strecker, M., 2008a, The role of inherited extensional fault segmentation and linkage in contractional orogenesis: A reconstruction of Lower Cretaceous inverted rift basin in the Eastern Cordillera of Colombia: Basin Research, v. in press.

Mora, A., Parra, M., Strecker, M. R., Kammer, A., Dimaté, C., and Rodríguez, F., 2006, Cenozoic contractional reactivation of Mesozoic extensional structures in the Eastern Cordillera of Colombia: Tectonics, v. 25, no. 2.

Mora, A., Parra, M., Strecker, M. R., Sobel, E. R., Hooghiemstra, H., Torres, V., and Vallejo-Jaramillo, J., 2008b, Climatic forcing of asymmetric orogenic evolution in the Eastern Cordillera of Colombia: Geological Society of America Bulletin, v. 120, no. 7, p. 930-949.

Mortimer, E., Carrapa, B., Coutand, I., Schoenbohm, L., Sobel, E. R., Gomez, J. S., and Strecker, M. R., 2007, Fragmentation of a foreland basin in response to out-of-sequence basement uplifts and structural reactivation: El Cajón-Campo del Arenal basin, NW Argentina: Geological Society of America Bulletin, v. 119, no. 5-6, p. 637-653.

Muller, J., Di Giacomo, E., and Van Erve, A., 1987, A palynologic zonation for the Cretaceous, Tertiary and Quaternary of northern South America: American Association of Stratigraphic Palynologist, Contribution Series, v. 19, p. 7-76.

Nemec, W., and Postma, G., 1993, Quaternary alluvial fans in southwestern Crete: sedimentation processes and geomorphic evolution, *in* Marzo, M., and Puigdefábregas, C., eds., Alluvial sedimentation, International Association of Sedimentologists Special Publication, v. 17, p. 235-276.

Nio, S. D., and Yang, C., 1991, Diagnostic attributes of clastic tidal deposits: a review, *in* Smith, D. G., Reinson, G. E., Zaitlin, B. A., and Rahmani, R. A., eds., Clastic Tidal Sedimentology: Canadian Society of Petroleum Geologists Memoir 16, p. 3-27.

Nuttall, C. P., 1990, A review of the Tertiary non-marine molluscan faunas of the Pebasian and other inland basins of north-western South America: Bulletin - British Museum (Natural History), Geology Series, v. 45, no. 2, p. 165-371.

O'Sullivan, P. B., 1999, Thermochronology, denudation and variations in palaeosurface temperature: A case study from the North Slope foreland basin, Alaska: Basin Research, v. 11, no. 3, p. 191-204.

O'Sullivan, P. B., and Wallace, W. K., 2002, Out-of-sequence, basement-involved structures in the Sadlerochit Mountains region of the Arctic National Wildlife Refuge, Alaska: Evidence and implications from fission-track thermochronology: Geological Society of America Bulletin, v. 114, no. 11, p. 1356-1378.

Ojeda, G. Y., Bayona, G., Pinilla, J., Cortés, M., and Gamba, N., 2006, Subsidence and geodynamic analysis of the Llanos Basin: Linking mountain building and basin filling processes, *in* Extended Abstracts, IX Simposio Bolivariano de Exploración Petrolera en las Cuencas Subandinas, Cartagena de Indias, Colombia.

Owen, G., 1996, Experimental soft-sediment deformation: Structures formed by the liquefaction of unconsolidated sands and some ancient examples: Sedimentology, v. 43, no. 2, p. 279-293.

Paola, C., Heller, P. L., and Angevine, C. L., 1992, The large-scale dynamics of grain-size variation in alluvial basins, 1: Theory: Basin Research, v. 4, p. 73-90.

Pardo-Casas, F., and Molnar, P., 1987, Relative motion of the Nazca (Farallon) and South American plates since Late Cretaceous time: Tectonics, v. 6, no. 3, p. 233-248.

Pardo-Trujillo, A., Jaramillo, C., and Oboh-Ikuenobe, F. E., 2003, Paleogene palynostratigraphy of the Eastern Middle Magdalena Valley,Colombia: Palynology, v. 27, p. 155-178.

Parra, M., Mora, A., Jaramillo, C., Strecker, M. R., and Sobel, E. R., 2007, Cenozoic exhumation history in the northeastern Andes: new data based on low-T thermochronology and basin analysis in the Eastern Cordillera of Colombia: Geophysical Research Abstracts, v. 9, 07197.

Parra, M., Mora, A., Jaramillo, C., Strecker, M. R., Sobel, E. R., Quiroz, L. I., Rueda, M., and Torres, V., 2008, Orogenic wedge advance in the northern Andes: Evidence from the Oligocene-Miocene sedimentary record of the Medina Basin, Eastern Cordillera, Colombia: Geological Society of America Bulletin, v. in press.

Pfiffner, O. A., Ellis, S., and Beaumont, C., 2000, Collision tectonics in the Swiss Alps: Insight fro geodynamic modeling: Tectonics, v. 19, no. 6, p. 1065-1094.

Pilger, R. H., 1981, Plate reconstructions, aseismic ridges, and low-angle subduction beneath the Andes: Geological Society of America Bulletin, v. 92, no. 7, p. 448-456.
Pilger, R. H., 1984, Cenozoic plate kinematics, subduction and magmatism: South American Andes: Journal of the Geological Society, v. 141, no. 5, p. 793-802.
Raasveldt, H. C., 1956, Mapa geológico de la República de Colombia, Plancha L9 (Girardot): Instituto Geológico Nacional, scale 1:200,000: Bogotá.
Rahn, M. K., Brandon, M. T., Batt, G. E., and Garver, J. I., 2004, A zero-damage model for fission-track annealing in zircon: American Mineralogist, v. 89, no. 4, p. 473-484.
Ramón, J. C., and Rosero, A., 2006, Multiphase structural evolution of the western margin of the Girardot subbasin, Upper Magdalena Valley, Colombia: Journal of South American Earth Sciences, v. 21, no. 4, p. 493-509.
Ramos, V. A., Cristallini, E. O., and Pérez, D. J., 2002, The Pampean flat-slab of the Central Andes: Journal of South American Earth Sciences, v. 15, no. 1, p. 59-78.
Reineck, H. E., and Wunderlich, F., 1968, Classification and origin of flaser and lenticular bedding: Sedimentology, v. 11, p. 99-104.
Reiners, P. W., and Brandon, M. T., 2006, Using thermochronology to understand orogenic erosion: Annual Reviews of Earth and Planetary Sciences, v. 34, p. 419-466.
Reiners, P. W., Ehlers, T. A., Mitchell, S. G., and Montgomery, D. R., 2003a, Coupled spatial variations in precipitation and long-term erosion rates across the Washington Cascades: Nature, v. 426, no. 6967, p. 645-647.
Reiners, P. W., Zhou, Z., Ehlers, T. A., Xu, C., Brandon, M. T., Donelick, R. A., and Nicolescu, S., 2003b, Post-orogenic evolution of the Dabie-Shan, eastern China, from (U-Th)/He and fission-track thermochronology: American Journal of Science, v. 303, no. 6, p. 489-518.
Restrepo-Pace, P. A., Colmenares, F., Higuera, C., and Mayorga, M., 2004, A fold-and-thrust belt along the western flank of the Eastern Cordillera of Colombia. Style, kinematics, and timing constraints derived from seismic data and detailed surface mapping, *in* McClay, K. R., ed., Thrust Tectonics and Hydrocarbon Systems: Tulsa, American Association of Petroleum Geologists Memoir 82, p. 598-613.
Restrepo-Pace, P. A., Ruiz, J., Gehrels, G., and Cosca, M., 1997, Geochronology and Nd isotopic data of Grenville-age rocks in the Colombian Andes: New constraints for Late Proterozoic-Early Paleozoic paleocontinental reconstructions of the Americas: Earth and Planetary Science Letters, v. 150, no. 3-4, p. 427-441.
Riba, O., 1976, Syntectonic unconformities of the Alto Cardener, Spanish Pyrenees: a genetic interpretation: Sedimentary Geology, v. 15, no. 3, p. 213-233.
Richardson, N. J., Densmore, A. L., Seward, D., Fowler, A., Wipf, M., Ellis, M. A., Yong, L., and Zhang, Y., 2008, Extraordinary denudation in the Sichuan Basin: Insights from low-temperature thermochronology adjacent to the eastern margin of the Tibetan Plateau: Journal of Geophysical Research B: Solid Earth, v. 113, no. 4.
Ring, U., Brandon, M. T., Willett, S. D., and Lister, G. S., 1999, Exhumation processes, *in* Ring, U., Brandon, M. T., Lister, G. S., and Willett, S. D., eds., Exhumation Processes; Normal faulting, Ductile Flow and Erosion, Geological Society Special Publication, v. 154, p. 1-27.
Rivers, T., 1997, Lithotectonic elements of the Grenville Province: Review and tectonic implications: Precambrian Research, v. 86, no. 3-4, p. 117-154.
Rowan, M. G., and Linares, R., 2000, Fold-evolution matrices and axial-surface analysis of fault-bend folds: Application to the Medina anticline, Eastern Cordillera, Colombia: American Association of Petroleum Geologists Bulletin, v. 84, no. 6, p. 741-764.
Russo, R. M., and Silver, P. G., 1996, Cordillera formation, mantle dynamics, and the Wilson cycle: Geology, v. 24, no. 6, p. 511-514.
Sarmiento-Rojas, L. F., 2001, Mesozoic Rifting and Cenozoic Basin Inversion History of the Eastern Cordillera, Colombian Andes [Ph.D thesis]: Amsterdam, Vrije University, 295 p.
Sarmiento-Rojas, L. F., Van Wess, J. D., and Cloetingh, S., 2006, Mesozoic transtensional basin history of the Eastern Cordillera, Colombian Andes: Inferences from tectonic models: Journal of South American Earth Sciences, v. 21, no. 4, p. 383-411.
Sarmiento, G., 1992, Estratigrafía y medios de deposito de la Formación Guaduas: Boletín Geológico, Ingeominas Bogotá, v. 32, no. 1, p. 3-44.

Sclater, J. G., and Christie, P. A. F., 1980, Continental stretching: an explanation of the post Mid-Cretaceous subsidence of the central North Sea basin: Journal of Geophysical Research, v. 85, p. 3711-3739.

Segovia, A., 1965, Mapa Geológico de la plancha L-12 (Medina) de la República de Colombia: Servicio Geológico Nacional, scale 1:250,000: Bogotá.

Shagam, R., Kohn, B. P., Banks, P. O., Dasch, L. E., Vargas, R., Rodríguez, G. I., and Pimentel, N., 1984, Tectonic implications of Cretaceous-Pliocene fission-track ages from rocks of the circum-Maracaibo Basin region of western Venezuela and eastern Colombia, *in* Bonini, W. E., Hargraves, R. B., and Shagam, R., eds., The Caribbean-South American plate boundary and regional tectonics, Geological Society of America Memoir 162, p. 385-412.

Sinclair, H. D., 1997, Tectonostratigraphic model for underfilled peripheral foreland basins: An Alpine perspective: Geological Society of America Bulletin, v. 109, no. 3, p. 324-346.

Sinclair, H. D., and Allen, P. A., 1992, Vertical versus horizontal motions in the Alpine orogenic wedge: stratigraphic response in the foreland basin: Basin Research, v. 4, p. 215-232.

Sinclair, H. D., Coakley, B. J., Allen, P. A., and Watts, A. B., 1991, Simulation of foreland basin stratigraphy using a diffusion model of mountain belt uplift and erosion: an example from the central Alps, Switzerland: Tectonics, v. 10, no. 3, p. 599-620.

Sobel, E. R., and Strecker, M. R., 2003, Uplift, exhumation and precipitation: Tectonic and climatic control of Late Cenozoic landscape evolution in the northern Sierras Pampeanas, Argentina: Basin Research, v. 15, no. 4, p. 431-451.

Spikings, R. A., Winkler, W., Seward, D., and Handler, R., 2001, Along-strike variations in the thermal and tectonic response of the continental Ecuadorian Andes to the collision with heterogeneous oceanic crust: Earth and Planetary Sciences Letters, v. 186, no. 1, p. 57-73.

Steinmann, M., Hungerbühler, D., Seward, D., and Winkler, W., 1999, Neogene tectonic evolution and exhumation of the southern Ecuadorian Andes: A combined stratigraphy and fission-track approach: Tectonophysics, v. 307, no. 3-4, p. 255-276.

Stockli, D. F., 2005, Application of low-temperature thermochronometry to extensional tectonic settings, *in* Reiners, P. W., and Ehlers, T. A., eds., Low Temperature Thermochronology: Techniques, Interpretations, and Applications: Reviews in Mineralogy and Geochemistry, v. 58: Washington D.C, Mineralogical Society of America, p. 411-448.

Stockli, D. F., Surpless, B. E., Dumitru, T. A., and Farley, K. A., 2002, Thermochronological constraints on the timing and magnitude of Miocene and Pliocene extension in the central Wassuk Range, western Nevada: Tectonics, v. 21, no. 4, 1028, doi:10.1029/2001TC001295.

Storti, F., Salvini, F., and McClay, K., 2000, Synchronous and velocity-partitioned thrusting and thrust polarity reversal in experimentally produced, doubly-vergent thrust wedges: Implications for natural orogens: Tectonics, v. 19, no. 2, p. 378-396.

Strecker, M. R., Alonso, R. N., Bookhagen, B., Carrapa, B., Hilley, G. E., Sobel, E. R., and Trauth, M. H., 2007, Tectonics and climate of the southern central Andes, Annual Review of Earth and Planetary Sciences, p. 747-787.

Strecker, M. R., Hilley, G. E., and Sobel, E. R., 2008, Structural, geomorphic and depositional characteristics of contiguous vs. broken foreland basins: examples from the eastern flanks of the central Andes, southern Bolivia and northwestern Argentina., *in* Busby, C. J., and Ingersoll, R. V., eds., Tectonics and Sedimentation.

Taboada, A., Rivera, L. A., Fuenzalida, A., Cisternas, A., Philip, H., Bijwaard, H., Olaya, J., and Rivera, C., 2000, Geodynamics of the northern Andes: Subductions and intracontinental deformation (Colombia): Tectonics, v. 19, no. 5, p. 787-813.

Tagami, T., Galbraith, R. F., Yamada, R., and Laslett, G. M., 1998, Revised annealing kinetics of fission tracks in zircon and geological implications, *in* Van den Haute, P., and De Corte, F., eds., Advances in Fission-track Geochronology: Dordrecht, Kluwer Academic Publishers, p. 99-112.

Tagami, T., and O'Sullivan, P. B., 2005, Fundamentals of fission-track thermochronology, *in* Reiners, P. W., and Ehlers, T. A., eds., Low Temperature Thermochronology: Techniques, Interpretations, and Applications: Reviews in Mineralogy and Geochemistry, v. 58: Washington D.C, Mineralogical Society of America, p. 19-47.

Tagami, T., and Shimada, C., 1996, Natural long-term annealing of the fission track annealing of the fission-track system around a granitic pluton: Journal of Geophysical Research, v. 101, no. 4, p. 8245-8255.

Tessier, B., Archer, A. W., Lanier, W. P., and Feldman, H. R., 1995, Comparison of ancient tidal rhythmites (Carboniferous of Kansas and Indiana, USA) with modern analogues (the Bay of Mont-Saint-Michel, France): Tidal signatures in modern and ancient sediments, p. 259-271.

Thiede, R. C., Bookhagen, B., Arrowsmith, J. R., Sobel, E. R., and Strecker, M. R., 2004, Climatic control on rapid exhumation along the Southern Himalayan Front: Earth and Planetary Science Letters, v. 222, no. 3-4, p. 791-806.

Tippett, J. M., and Kamp, P. J. J., 1993, Fission track analysis of the late Cenozoic vertical kinematics of continental Pacific Crust, South Island, New Zealand: Journal of Geophysical Research, v. 98, no. B9, p. 16,119-16,148.

Tissot, B. P., Pelet, R., and Ungerer, P., 1987, Thermal history of sedimentary basins, maturation indices, and kinetics of oil and gas generations: American Association of Petroleum Geologists Bulletin, v. 71, no. 12, p. 1445-1466.

Toro, J., 1990, The termination of the Bucaramanga fault in the Cordillera Oriental, Colombia [M.Sc thesis]: Tucson, University of Arizona, 53 p.

Toro, J., Roure, F., Bordas-Le Floch, N., Le Cornec-Lance, S., and Sassi, W., 2004, Thermal and kinematic evolution of the Eastern Cordillera fold-and-thrust-belt, Colombia, *in* Swennen, R., Roure, F., and Granath, J. W., eds., Deformation, fluid flow, and reservoir appraisal in foreland fold and thrust belts, American Association of Petroleum Geologists Hedberg Series, v. 1, p. 79-115.

Traverse, A., 1988, Paleopalynology: New York, Academic Press, 600 p.

Trenkamp, R., Kellogg, J. N., Freymueller, J. T., and Mora, H. P., 2002, Wide plate margin deformation, southern Central America and northwestern South America, CASA GPS observations: Journal of South American Earth Sciences, v. 15, no. 2, p. 157-171.

Tye, R. S., and Coleman, J. M., 1989, Depositional processes and stratigraphy of fluvially dominated lacustrine deltas: Mississippi delta plain: Journal of Sedimentary Petrology, v. 59, no. 6, p. 973-996.

Uba, C. E., Heubeck, C., and Hulka, C., 2006, Evolution of the late Cenozoic Chaco foreland basin, Southern Bolivia: Basin Research, v. 18, no. 2, p. 145-170.

Uba, C. E., Strecker, M. R., and Schmitt, A. K., 2007, Increased sediment accumulation rates and climatic forcing in the central Andes during the late Miocene: Geology, v. 35, no. 11, p. 979-982.

Ulloa, C., and Rodríguez, E., 1979, Geología del Cuadrángulo K12, Guateque: Boletín Geológico, Ingeominas Bogotá, v. 22, no. 1, p. 3-55.

Ulloa, C., and Rodríguez, E., 1982, Intrusivos ácidos ordivícicos y post-devónicos en La Floresta (Boyacá), *in* IV Congreso Colombiano de Geología, Cali, p. 17-18.

Vallejo, C., Spikings, R. A., Luzieux, L., Winkler, W., Chew, D., and Page, L., 2006, The early interaction between the Caribbean Plateau and the NW South American Plate: Terra Nova, v. 18, no. 4, p. 264-269.

Van der Hammen, T., 1958, Estratigrafía del Terciario y Maestrichtiano Continentales y tectogénesis de los Andes Colombianos: Boletín Geológico, Ingeominas Bogotá, v. 6, no. 1-3, p. 67-128.

Van der Hammen, T., Werner, J. H., and Dommelen, v., 1973, Palynological record of the upheaval of the Nothern Andes: a study of the Pliocene and Lower Quaternary of the Colombian Eastern Cordillera and the early evolution of its High-Andean biota: Reviews of Paleobotany and Palynology, v. 16, p. 1-122.

Van Wagoner, J. C., 1995, Sequence stratigraphy and marine to nonmarine facies architecture of foreland basin strata, Book Cliffs, Utah, USA: Sequence stratigraphy of foreland basin deposits, p. 137-223.

Vergara, L., and Rodríguez, G., 1996, The Upper Cretaceous and Lower Paleocene of the Eastern Bogotá Plateau and Llanos Thrustbelt, Colombia: Alternative appraisal to the nomenclature and sequence stratigraphy: Geología Colombiana, no. 22, p. 41-63.

Villagómez, D., Spikings, R., Seward, D., Magna, T., Winkler, W., and Kammer, A., 2008, Thermotectonic history of the Northern Andes, *in* 7th International Symposium on Andean Geodynamics, Nice, p. 573-576.

Wagner, G. A., and Reimer, G. M., 1972, Fission track tectonics: The tectonic interpretation of fission track apatite ages: Earth and Planetary Science Letters, v. 14, no. 2, p. 263-268.
Wagner, G. A., and van den Haute, P., 1992, Fission-Track Dating: Dordecht, Kluwer Academic Publishers, 285 p.
Waples, D. W., 1980, Time and temperature in petroleum formation: application of Lopatin´s method to petroleum exploration: American Association of Petroleum Geologists Bulletin, v. 64, p. 916-926.
Waschbusch, P. J., and Royden, L. H., 1992, Episodicity in foredeep basins: Geology, v. 20, no. 10, p. 915-918.
Watts, A. B., Karner, G. D., and Steckler, M. S., 1982, Lithospheric flexure and evolution of sedimentary basins: Philosophical Transactions of the Royal Society of London. Series A, Mathemathical and Physical Sciences, v. 305, p. 249-281.
Wesselingh, F., Räsänen, M. E., Irion, G., Vonhof, H. B., Kaandorp, R., Renema, W., Romero-Pitman, L., and Gingras, M., 2002, Lake Pebas: A palaeoecological reconstruction of a Miocene long-lived lake complex in western Amazonia: Cainozoic Research, v. 1, no. 1-2, p. 35-81.
Wesselingh, F. P., and Macsotay, O., 2006, Pachydon hettneri (Anderson, 1928) as indicator for Caribbean-Amazonian lowland connections during the Early-Middle Miocene: Journal of South American Earth Sciences, v. 21, no. 1-2, p. 49-53.
Whiting, B. M., and Thomas, W. A., 1994, Three-dimensional controls on subsidence of a foreland basin associated with a thrust-belt recess: Black Warrior Basin, Alabama and Mississippi: Geology, v. 22, no. 8, p. 727-730.
Wijninga, V. M., 1996, Palynology and paleobotany of Neogene sediments from the high plain of Bogotá (Colombia): evolution of the Andean flora from an ecological perspective [Ph. D thesis], University of Amsterdam, 370 p.
Willett, S., Beaumont, C., and Fullsack, P., 1993, Mechanical model for the tectonics of doubly vergent compressional orogens: Geology, v. 21, no. 4, p. 371-374.
Zhao, G., Cawood, P. A., Wilde, S. A., and Sun, M., 2002, Review of global 2.1-1.8 Ga orogens: Implications for a pre-Rodinia supercontinent: Earth-Science Reviews, v. 59, no. 1-4, p. 125-162.

APPENDIX A

A1. PALYNOLOGY: METHODS

The palynologic samples were prepared by the standard procedure of digesting the sample in HF and HCl, separating organic matter by heavy liquids, and oxidizing (Traverse, 1988). Slides were mounted with Polyvinyl alcohol and Canada Balsam. Carl Zeiss light microscopes were used for palynologic analyses. At least one complete oxidized slide per sample was scanned with a 40x Zeiss planapochromatic objective and 200 palynomorphs per slide were counted when possible. Examination of the fossil taxa was done using a 100x Zeiss oil immersion planapochromatic objective. Photographs were taken using a Nikon digital camera. Identification of fossil taxa was done through comparison with published photographs and descriptions, and the holotype material in the palynological collections of University of Amsterdam (Holland), PETROBRAS in Rio de Janeiro (Brazil), PDVSA in Caracas (Venezuela), and the Instituto Colombiano del Petróleo (ICP) in Bucaramanga (Colombia). A detailed report including all the species identified for each stratigraphic profile is presented in Parra et al. (2008; Data Repository)

A2. BACKSTRIPPING: METHODS AND PARAMETERS USED.

One-dimensional backstripping was performed for the Cenozoic foreland section of the Medina and Middle Magdalena Valley basins. We follow the method described by Allen and Allen (2005), implemented in the program OSXBackstrip v. 1.7 (N.Cardozo, available at http://homepage.mac.com/nfcd/work/programs.html). This method involves obtaining the total subsidence signal by (1) decompacting the observed stratigraphic thickness, assuming an exponentially decreasing porosity-depth relation; (2) subtracting the amount of subsidence caused by the load of the decompacted sediments, assuming local isostatic compensation (Airy isostasy); and (3) estimating tectonic subsidence by correcting for water loading and adjusting the obtained depth to basement to a datum (i.e., the present-day sea level), which involves a correction for variation in both paleobathymetry and global eustatic sea level. Parameters for backstripping are presented in Table A1.

TABLE A1: ANALYSIS OF THE CENOZOIC SEDIMENTARY SECTION OF THE MEDINA AND SOUTHERN MIDDLE MAGDALENA VALLEY BASINS INPUT PARAMETERS FOR GEOHISTORY

(Bio) Stratigraphic unit	Lithology †	Depth to base (m)	Age (Ma)	Grain density (kg/m3)	c (1/km)	Initial Porosity	Water Depth (m; at the base of interval)	Absolute sea level (m) ‡
Medina Basin (based on Composite Section, Figure 6)								
Ca-8-Guayabo	ss, cg, ms	4300	5.3-22.1	2675	0.38	53%	-150 ± 150	120
Ca7-Ca8	ss, ms, cg	5038 ± 17.0	22.1-23.8	2680	0.37	59%	-150 ± 150	80
T-11	ms, ss	5229 ± 5.4	23.8-26.8	2705	0.45	60%	0 ± 10	65
T-10	ss, ms	5482 ± 4.4	26.8-28.8	2698	0.4	63%	0 ± 10	95
T-09	ms	5499 ± 5.2	28.8-31.2	2720	0.51	64%	0 ± 10	180
T-08	ms	5566 ± 5.2	31.2-33.7	2720	0.51	61%	0 ± 10	150
T-07	ms	5714 ± 3.0	33.7-39.2	2720	0.51	63%	0 ± 10	175
T-06	ms, ss	5823 ± 10.8	39.2-44.7	2685	0.39	63%	10 ± 10	190
T-05	ss, ms,cg	6007 ± 9.9	44.7-55.8	2669	0.34	63%	10 ± 10	150
Late Paleocene	ms, ss	6492	55.8-59.7	2692	0.41	50%	0 ± 10	170
Southern Middle Magdalena Valley Basin (data from Gómez et al., 2005)								
Santa Teresa	ms, ss	0-430	12.7-17	2692	0.41	57%	-250 ± 250	150
La Cruz Mb	ss, ms	430-923	17-26	2654	0.28	50%	-250 ± 250	200
Almácigos mb	ms, ss	923-2095	26-35.5	2692	0.41	57%	-250 ± 250	205
Armadillos Mb	ss, mm	2095-2973	35.5-43	2654	0.28	50%	-250 ± 250	195
LKCU §		2973-2973	43-56				-1500 ± 150(	200
Hoyon	cg, ss, mm	2973-4400	56-63	2671	0.34	53%	-250 ± 250	210

† ss = sandstone; ms (mudstone); cg (conglomerate)
‡ Estimated at the the base of each interval based on the global long-term eustatic curve (Haq et al., 1997)
§ LKCU: late Cretaceous-Cenozoic unconformity (Gómez et al., 2005a)

APPENDIX B

B1. ANALYTICAL PROCEDURES

B1.1 Apatite fission-track analyses

Apatite preparation and analysis were done by Apatite to Zircon Inc. Apatite and zircon grains were concentrated following conventional heavy liquids and magnetic separation procedures. Apatite grains were then immersed in an epoxy resin and cured at 90°C for 1 h. After grinding and polishing to expose internal surfaces, the apatites were etched in 5.5 HNO_3 for 20.0 s (±0.5 s) at 21°C (±1°C) to reveal spontaneous tracks. The mounts were then scanned to search for suitable apatite grains for age dating and those grain locations digitally recorded. For each suitable grain, representative kinetic parameters (Dpar) were measured, and the natural fission-track densities were counted. These grain localities were then revisited using the LA-ICP-MS; spot analyses to determine the concentration of U were completed on the identical areas of each grain from which the natural fission-track densities were first counted. The grain mounts were then irradiated with approximately 10^7 tracks/cm^2 fission fragments from a 50 μCi (activity as of July, 1996) ^{252}Cf source in a vacuum chamber in order to enhance the number of confined tracks available for measurement (e.g. Donelick and Miller, 1991; Donelick et al., 2005). Irradiated grain mounts were then re-immersed in 5.5N HNO_3 for 20.0 seconds (± 0.5 seconds) at 21°C (± 1°C) to reveal any horizontal, confined fission tracks, and the freshly-exposed confined tracks were then measured. Both track lengths and the angle to the *c*-axis were measured using unpolarized light.

For each apatite grain from which fission-track age or length data were collected, an arithmetic mean value for the kinetic parameter Dpar (Donelick et al., 2005) was determined from 1 to 4 measurements. Analyses by P. O´Sullivan were completed using 2000x magnification (100x dry objective, 1.25x projection tube, 16x oculars). Natural fission tracks form as a result of the spontaneous nuclear fission of trace amounts of ^{238}U within an apatite or zircon grain. Using a modified version of the radioactive decay equation, the fission-track age of an apatite or zircon grain can be calculated using the ratio of the number of fission tracks intersecting the surface over a unit area in the grain to the amount of ^{238}U present in the grain. Laser ablation inductively coupled plasma-mass spectrometer (LA-ICP-MS) was used to determine the ^{238}U concentrations by measuring the ratio of ^{238}U to ^{43}Ca for apatite from the exact regions on the individual grains from which the spontaneous tracks were initially counted (see Hasebe et al., 2004; Donelick et al., 2005). Operating details for the analyses are listed in Table B1. The fundamental assumption is made that Ca occurs in stoichiometric amounts in all apatite grains analyzed by the LA-ICP-MS. The isotope ^{43}Ca is used as the indicator of the volume of apatite ablated. Samples are ablated in a helium atmosphere to reduce condensation and elemental fractionation.

Spot analyses were used with the laser centered on a fixed point. A total of 30 scans for ^{238}U, ^{232}Th, ^{147} Sm, and ^{43}Ca (apatite) were performed for each spot analyzed. Of these scans, approximately

10 were performed while the laser was warming up and was blocked from contacting the grain surface. During this time, background counts were collected. Once the laser was permitted to hit the grain surface, a cylindrical pit was excavated to a depth beyond which uranium did not contribute fission tracks to the etched grain surface. Between 15 and 20 scans performed during pit excavation were required to reach this depth. The depths of a representative number of these pits were measured and the $^{238}U/^{42}Ca$ value for the pit as a whole was determined based on the weighted mean of the $^{238}U/^{43}Ca$ value for individual scans relative to the depths from which the ablated material was derived.

TABLE B1: ICP-MS and laser operating conditions and data acquisition parameters

ICP-MS: operating conditions	
Instrument	Finnigan Element II Magnetic Sector ICP-MS
Forward power	1.25 kW
Reflected power	<5 W
Plasma gas	Ar
Coolant flow	15 l/min
Carrier flow	1.0 l/min (Ar) 0.8 l/min (He) – optimized daily
Auxiliary flow	0.9 l/min
ICP-MS: acquisition parameters	
Dwell time	18 milliseconds per peak point
Points per peak	4
Mass window	5%
Scans	30
Data acquisition time	22 sec
Data acquisition mode	electronic scanning
Isotopes measured	^{43}Ca (apatite) or ^{29}Si (zircon), ^{238}U, ^{232}Th, and ^{147} Sm
Laser: operating conditions	
Laser type	New Wave UP213 (Nd: YAG)
Wavelength	213 nm
Laser mode	Q switched
Laser output power	8 J/cm
Laser warm up time	6 sec
Shot repetition rate	5 Hz
Sampling scheme	spot (16 μm apatite, 12 μm zircon)

All laser ablation of samples for age analyses were performed under the direction of Paul B. O'Sullivan at the Washington State University School of Earth and Environmental Sciences GeoAnalytical Laboratory in Pullman, Washington

The fission track ages and errors were calculated using: (a) the ratio of the density of natural fission tracks present in the grain to the amount of ^{238}U present, and (b) a modified version of the radioactive decay equation that includes a LA-ICPMS zeta calibration factor (see equations 1b for age equation and 2b for error calculation in Donelick et al., 2005). This zeta calibration factor is determined for each sample analyzed during each LA-ICP-MS session by analyzing the U:Ca ratio (for apatite) or U:Si ratio (for zircon) of apatite or zircon calibration standards with known ages at the beginning and end of each session on the LA-ICP-MS. The standards used are Durango apatite, 30.6±0.3 Ma, and Fish Canyon zircon, 28.5±0.3 Ma. Ages are reported at the 1σ level.

B 1.2 Zircon fission-track analyses

Zircon tracks analyses were conducted at the University of Potsdam. Individual zircon samples were split into two to four aliquots and each aliquot etched separately in the eutectic mixture of NaOH/KOH at 220°C for periods between 8 and 72 h. Analytical procedures followed the external detector method (Gleadow, 1981). Samples were irradiated at the Oregon State University research reactor. Following irradiation, mica monitors were etched with 40% hydrofluoric acid at 21°C for 45 min. Samples were counted at a magnification of 1600× (dry objective) using a Leica DMRM microscope with drawing tube located above a digitizing tablet, and a Kinetec ^{TM} computer-controlled stage driven by the FTStage program (Dumitru, 1993). Ages and errors were calculated using the zeta calibration method (Hurford and Green, 1983) with the software Trackkey (Dunkl, 2002), and are reported at the 1σ level. Zeta calibration factor is 121.8 ± 5.2 for zircon (CN2 glass; M.Parra).

B2. THERMAL MODELING

Inverse thermal modeling of AFT data was performed with the program HeFTy v. 1.5.4 (Reiners et al., 2003a; Ketcham, 2005) using the apatite annealing kinetics model of (Ketcham et al., 2007b). We used LA-ICPMS-derived age data, and *c*-axis corrected track lengths (Ketcham et al., 2007a) for kinetically homogeneous populations. To further constrain the number of allowed *t-T* paths, burial temperatures derived from vitrinite reflectance (Table B2) according to the correlation model of Burnham and Sweeney (1989) were introduced into the models. Additional constraints based on the known geological history of the samples were also introduced in each model (see section 3.5.1 and 3.5.3). Two randomly spaced, monotonic consistent half-segments (2E) between adjacent constraints were used. We ran 2,500 to 150,000 iterations using a Monte Carlo search method until a number between 5 (Sample A19) and 100 good fits was achieved.

TABLE B2 Vitrinite reflectance (Ro) data used in this study

Western transect (Guaduas syncline and Villeta Antilcinorium)

Unit	Stratigraphic height (m) [a]	Vitrinite reflectance data [b] Ro(%)	Source [c]
Santa Teresa Fm.	5200	0.54	1
Santa Teresa Fm.	5100	0.6	1
San Juan de Rio Seco Fm.	4700	0.64	1
San Juan de Rio Seco Fm.	3200	0.58	1
Buscavidas Fm	200	0.6	1
Pinzaima Fm	-6800	6.4	1

Northern transect (Floresta Massif)

Unit	Stratigraphic height (m) [b]	Vitrinite reflectance data [b] Ro(%)	Source [c]
Concentración Fm.		0.65	3
Guadalupe Gr.		0.7	3
Une Fm.		0.99 ± 0.07	2

Central Transect (northern Quetame Massif)

Unit	Stratigraphic height (m) [b]	Vitrinite reflectance data [b] Ro(%)	Source [c]
Upper Socha Fm.	6650	0.43 ± 0.03	2
Guadalupe Gr.	5900	0.69 ± 0.04	2
Chipaque Fm.	5000	0.81 ± 0.07	3
Une Fm.	4100	0.99 ± 0.07	2
Fómeque Fm.	3100	1.94 ± 0.10	2
Las Juntas Fm.	2500	2.39 ± 0.30	4
Bata Fm.	50	4.45 ± 0.88	5
Farallones Gr.	-100	2.99 ± 0.20	4

Southern Transect (southern Quetame Massif)

Unit	Stratigraphic height (m) [b]	Vitrinite reflectance data [b] Ro(%)	Source [c]
Chipaque Fm.	6200	0.77 ± 0.07	5
Une Fm.	5600	1.38 ± 0.15	5
Une Fm.	4700	2.87 ± 0.25	4
Fómeque Fm.	4000	3.50 ± 0.25	5
Macanal Fm.	500	4.45 ± 0.33	4

[a] Stratigraphic position with respect to the Late Cretaceous-Cenozoic unconformity (Gomez, 2001).
[b] Stratigraphic position with respect to the basal Cretaceous unconformity.
[c] Data sources are: 1. Gómez, 2001; 2 - Mayorga and Vargas (1995); 3 - Repsol, (unpublished data); 4 - Ecopetrol (unpublished data); 5 - Mora et al (2008b).

Table B3: Samples used in the stratigraphic position - age plots (Fig. 3.8)

Central Transect				*Southern Transect*			
ID	Sample	Unit	Stratigraphic depth [a]	ID	Sample	Unit	Stratigraphic height [a]
A12	AM 01	Picacho Fm.	7100	A35	BV MP3 F	Chipaque Fm.	6000
A13	AM 03	Upper Socha Fm.	6650	A36	BV MP7 F	Chipaque Fm.	5700
A14	AM 04	Upper Socha Fm.	6650	A37	BV120 F	Cáqueza Fm.	3350
A08	RG 06	Bogota Fm.	6650	Z11	BV 121	Cáqueza Fm.	3250
A19	RG 16	Upper Socha Fm.	6650	Z12	BV 65	Macanal Fm.	2200
A20	RG14	Cacho Fm.	6475	A38-Z14	BV 151	Macanal Fm.	1510
A09	M4 04	Lower Socha Fm.	6475	Z13	BV 126	Macanal Fm.	480
A15	AM 05	Guadalupe Gr.	5900	A34	SJ 2A	Macanal Fm.	250
A21	T2 018	Guadalupe Gr.	5900	Z18	BV 194	Chingaza Fm.	100
A24	T 012	Guadalupe Gr.	5500	A33	SJ 3	Buenavista Fm.	80
A11	RW 2	Chipaque Fm.	5000	A29-Z08	FT 1	Chingaza Fm.	10
A16	AM06	Une Fm.	4400	A43	BV 195	Quetame Gr.	-50
A23	T2 013	Une Fm.	4400	A42-Z17	BV 196	Quetame Gr.	-100
A10	T4 032	Une Fm.	4100	A31-Z09	SJ 5	Quetame Gr.	-100
A17	T3 004	Une Fm.	4000	A32-Z10	SJ 1	Quetame Gr.	-150
A18	T3 003	Une Fm.	3900	A30	FT 6	Quetame Gr.	-400
A22	T2 660	Une Fm.	3800	A40-Z16	BV 192	Quetame Gr.	-900
A25	T2 019	Une Fm.	3700	A39	BV 90	Quetame Gr.	-900
A26	AM07	Las Juntas Fm.	2500	A44	WPT	Farallones Gr.	-1550
Z06	MA 13	Macanal Fm.	500	Z15	BV 86	Quetame Gr.	-1600
A27	MA 18	Bata Fm.	50	A41	BV 423	Quetame Gr.	-2400
A28-Z07	MA 16	Farallones Gr.	-100				

[a] Stratigraphic position with respect to the basal Cretaceous unconformity.

APPENDIX C

C1. DECOMPACTION

Decompaction of the Upper Cretaceous-Pliocene stratigraphy of the Medina Basin was conducted following the method described in Allen and Allen (2005), implemented in the program OSXBackstrip v. 1.7 (N.Cardozo, available at http://homepage.mac.com/nfcd/work/programs.html). Parameters used and results of one-dimensional sediment accumulation rates are reported in Table C1.

TABLE C1: INPUT PARAMETERS FOR DECOMPACTION OF THE CENOZOIC STRATA OF THE MEDINA BASIN

(Bio) Stratigraphic unit	Lithology †	Depth to base (m)	Age (Ma)	Grain density (kg/m3)	c (1/km) ‡	Initial Porosity ‡	Compacted		Decompacted	
							Thickness (m)	Sed. Rate (m/my)	Thickness (m)	Sed. Rate (m/my)
Pliocene	cg, ss, ms	726	5.3-1.8	2671	0.34	53%	726	207	726	207
35-Late Miocene (Caja)	ss,ms,cg	1074	5.3-10.1	2679	0.37	55%	348	72	429	89
35-Late Miocene (Leon)	ms	1495	10.1-16.0	2720	0.51	63%	421	71	616	104
34	ss, ms,cg	2668	16.0-19.0	2679	0.37	55%	1173	391	1507	502
31-33	ss, ms	3969	19.0-23.0	2685	0.41	57%	1301	325	1847	462
T-11	ms, ss	4148	23.0-26.8	2705	0.45	60%	179	47	363	96
T-10	ss, ms	4372	26.8-28.8	2680	0.39	56%	224	112	413	207
T-09	ms	4408	28.8-31.2	2692	0.44	59%	36	15	81	34
T-08	ms	4485	31.2-33.7	2720	0.51	63%	77	31	181	72
T-07	ms	4650	33.7-39.2	2720	0.51	63%	165	30	365	66
T-06	ms, ss	4723	39.2-44.7	2680	0.39	56%	73	13	146	27
T-05	ss, ms,cg	4908	44.7-55.8	2669	0.34	51%	185	17	323	29
Cu02-Cu04	ms, ss	5353	55.8-60.3	2692	0.41	50%	445	99	735	163
19	ss,ms	5636	60.3-65.5	2659	0.31	51%	283	54	488	94
14-18	ss, ms	5702	65.5-70.6	2668	0.34	53%	66	13	127	25
13a	ss, st, ms	6033	70.6-?	2671	0.35	54%	485	71	812	119
13b	ss, ms	6187	?-77.4	2659	0.31	51%				

† ss = sandstone; ms (mudstone); cg (conglomerate)
‡ Based on lithology, after Sclater and Christie (1980)

C2. DEPTH CONVERSION

Mapped units in the Medina Basin were translated into an extensive grid of seismic lines by direct extrapolation of surface outcrops in the Medina Basin using the software package Petrel™. In addition, seismic reflectors were tied to the stratigraphy with data from seven hydrocarbon-exploration boreholes, especially in areas with no surface exposure within the footwall of the Guaicaramo thrust. Seismic surfaces were generated in Petrel™ by interpolation of interpreted horizons in different lines. Following interpolation, the accumulated (compacted) volume of rock between successive units was estimated from by converting the vertical time axis into depth. We used check-shot surveys from

seven boreholes in the Medina and Llanos basins to evaluate the seismic velocities in Cenozoic strata. Figure C1 depicts the depth vs. time relations obtained from the check shots. The velocity gradient decreases eastward from ~3900 m/s in the Medina Basin (Coporo-1 Well) to ~2800 m/s in the easternmost part of the study area in the Llanos Basin (Upia-1 Well). We therefore derived two different depth-time relations for hanging and footwalls of the Guicaramo thrust by combining information from available wells in each fault block. We average data from the Coporo-1 and Medina 1 wells in the hanging-wall block of the Guaicaramo fault, and from the Guacavía, Chaparral, San Pedro and Upía-1 wells in the footwall.

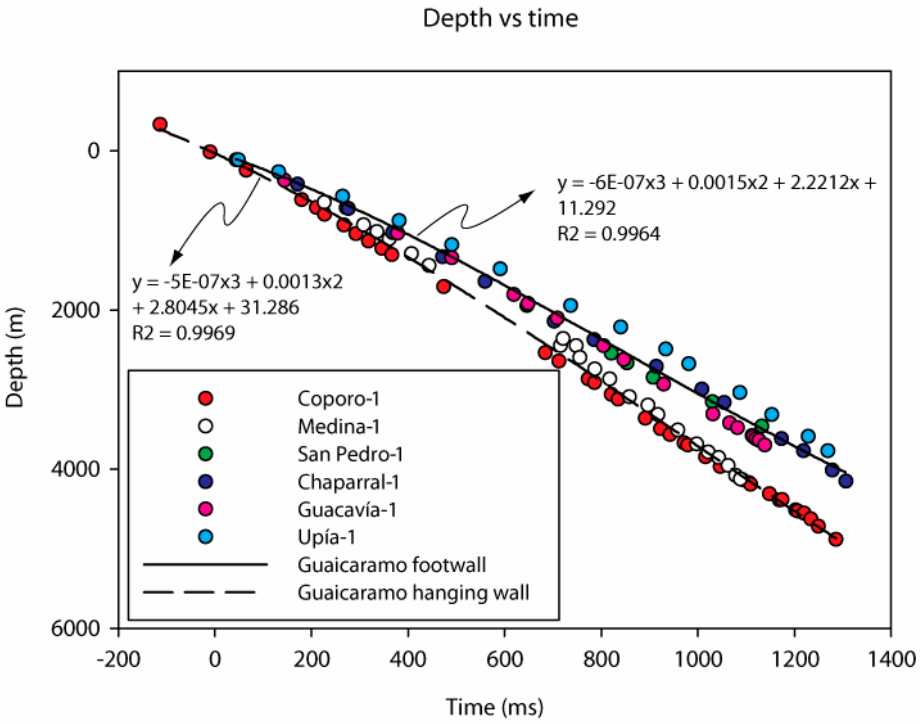

Figure C1. Velocity models for seven boreholes in the Medina and Llanos basins. Locations of wells are shown in Figure 4.1 A. Models are based on check-shot surveys measuring the seismic traveltime from the surface to known depths. Since velocity gradient decreases eastward toward the Llanos basin, we used an average values for each block of the Guaicaramo thrust. See text for further explanation.

C3. LITHOFACIES

Fifteen lithofacies were identified based on lithology, sedimentary structures, pedogenic features and fossils. We follow lithofacial classifications by Miall (1985) and Einsele (2000). Table C2 shows identified lithofacies.

TABLE C2: DESCRIPTION AND INTERPRETATION OF LITHOFACIES (after Miall,1996; Einsele, 2000)

Code	Description	Interpretation
Gcd	Disorganized clast-supported conglomerates, cobbles and pebbles	Clast-rich noncohesive debris flow
Gco	Organized, clast-supported conglomerates, cobbles and pebbles. Weak imbrication	Longitudinal bedforms, lag deposits
St	Trough cross-stratified sandstone, fine to coarse	3D dunes
Sp	Planar cross-stratified sandstone, fine to very coarse, often pebbly	Transverse and linguoid bedforms (2D dunes)
Sr	Ripple marks and small-scale cross stratification	Ripples (lower-flow regime)
Sf	Flaser bedded sandstone	Alternating suspension settling and lower-flow regime
Sw	Wavy bedded sandstone	Alternating suspension settling and lower-flow regime
Slc	Lenticular bedded sandstone	Alternating suspension settling and lower-flow regime
Sc	Convoluted bedded sandstone	Deformation by diferential loading or dewatering
Sm	Massive sandstone	Sediment gravity-flow deposits
Fl	Laminated mudstone and siltstone	Suspension-load deposits.
Fm	Massive mudstone and siltstone	Suspension deposits, overbank or abandoned channels
Fs	Disorganized shell-dominated mudstone	Upper-flow regime
Fb	Variegated mudstone and siltstone. Commonly sandy, intense mottling	Overbank or abandoned channels
Fo	Mudstone and siltstone with organic matter-rich laminae	Suspension settling deposits
C	Coal	Organic-rich swamp deposits